Development and Performance Evaluation of the Wavelength-shifting Optical Module for the IceCube Upgrade

---

Yuriy Popovych

October 6, 2025

Development and Performance Evaluation of the Wavelength-shifting Optical Module for the IceCube Upgrade

Dissertation

submitted for the award of the title

“Doctor of Natural Sciences”

to the Faculty of Physics, Mathematics and Computer Science
of Johannes Gutenberg-Universität
in Mainz

Yuriy Popovych

Born in Wyschnewe

Mainz, October 6, 2025

Yuriy Popovych
Development and Performance Evaluation of the Wavelength-shifting Optical Module for the IceCube Upgrade
Dissertation, October 6, 2025
Date of Defense: October 1, 2025

Johannes Gutenberg-Universität
AG Böser
Institute of Physics - ETAP
Department of Physics
Staudingerweg 7
55128 Mainz

Abstract

The IceCube Neutrino Observatory excels at detecting high-energy neutrinos via Cherenkov light in glacial ice. At lower energies, however, the high dark noise of the optical sensors dominates the signal, severely limiting sensitivity to astrophysical events such as supernovae. The Wavelength-shifting Optical Module (WOM) provides an elegant solution by improving detection efficiency and extending sensitivity into the ultraviolet (UV) range, which is largely inaccessible to standard IceCube optical modules. The WOM features a cylindrical wavelength-shifting tube that absorbs UV-photons and re-emits them at longer wavelengths, which are then guided via total internal reflection to photomultiplier tubes (PMTs) located at both ends. This design enhances UV sensitivity and reduces noise by decoupling the photosensitive area from the PMTs. These features are particularly beneficial for the upcoming IceCube Upgrade, the next development to IceCube, with a denser instrumentation optimized to lower the energy threshold of detected neutrinos.

This thesis presents the complete development cycle of the WOM, from simulation-based design and material selection to laboratory characterization and in-situ integration studies. A comprehensive performance evaluation is included, covering PMT quantum efficiency, time resolution, angular response, and effective area. In addition, an optimized production process and extensive optical and environmental testing demonstrate the WOM's suitability for deployment in the IceCube Upgrade. While its performance varies across different Upgrade use cases, it shows strong potential for broader applications, particularly in low-background or UV-sensitive detection environments.

Contents

List of Acronyms

ADC Analog-to-Digital Converter

ALG Adiabatic Light Guide

ALGO Adiabatic Light Guide Optimizer

CFD Constant Fraction Discriminator

DAC Digital-to-Analog Converter

DOM Digital Optical Module

DVT Design Verification Testing

EPDM Ethylene Propylene Diene Monomer

FAT Final Acceptance Testing

FPGA Field Programmable Gate Array

FWHM Full Width at Half Maximum

HAL Hardware Abstraction Layer

HV High Voltage

ICM Ice Comms Module

LLG Liquid Light Guide

LOM Long Optical Module

MB Mainboard

MC Monte-Carlo

MCU Micro Controller Unit

mDOM Multi-PMT Digital Optical Module

MPE Multi Photon Emission

MMB Mini-Mainboard

NSR Noise-to-Signal Ratio

NTS Northern Testing System

PCA Penetrator Cable Assembly

PDF Probability Density Function

PE Photo Electron

PEMA PolyEthylMethylAcrylate

PFPE Perfluoropolyether

PMMA PolyMethylMethAcrylate

PMT Photomultiplier Tube

QE Quantum Efficiency

SMT Simple Multiplicity Trigger

SNR Signal-to-Noise Ratio

SPAT South Pole Acceptance Test

SPE Single Photon Emission

TIR Total Internal Reflection

TTS Transit Time Spread

UV ultraviolet

WLS Wavelength Shifter

WLS wavelength-shifting

WOM Wavelength-shifting Optical Module

Author's Contributions

1 Introduction

The observable Universe is home to a wide range of extreme and yet unexplored phenomena—ranging from cosmic accelerators that produce particles with energies far beyond those achievable in terrestrial laboratories, to the violent explosions of dying stars, and even to subtle fluctuations in the cosmic microwave background that offer glimpses into the early Universe.

To study these events, which often occur thousands or even millions of light-years away, we rely on different types of cosmic messengers that reach Earth from various directions and energy ranges. Among these, **neutrinos** are particularly valuable: their extremely weak interaction with matter allows them to travel vast distances almost unimpeded, and remain unaffected by magnetic deflection. This makes them unique probes of the distant and dense regions where other signals such as protons are either absorbed or deflected—offering the possibility of tracing them back to their sources.

One of these possible sources are **core-collapse supernovae**. When a massive star exhausts its nuclear fuel and collapses under its own gravity, approximately 99% of its binding energy is released as neutrinos. These low-energy particles, located in the MeV regime, can escape the dense stellar interior before any photons, making them ideal messengers for early detection. In fact, neutrino observatories can serve as a supernova early warning system: upon detecting a characteristic neutrino burst, they can trigger optical follow-up observations to locate and study the corresponding supernova. Such multimessenger observations offer unique insights into the complex processes governing the life and death of massive stars. Since the detection of neutrinos from supernova SN1987A [1], neutrinos have been recognized as powerful probes for studying stellar collapse and explosion mechanisms.

Detecting neutrinos is challenging due to their extremely weak interactions, requiring detectors with large instrumented volumes to observe secondary particles via the Cherenkov effect [2]. The **IceCube Neutrino Observatory** [3] is currently the largest of its kind, instrumenting one cubic kilometer of Antarctic ice with optical modules equipped with Photomultiplier Tubes (PMTs) to detect high-energy neutrinos in the TeV–PeV range. In addition, IceCube provides sensitivity to lower energies, which will be further improved with the **IceCube Upgrade** [4], aiming to lower the energy threshold to the GeV scale.

IceCube relies on a collective increase in the photon count rates across its optical modules for the detection of core-collapse supernovae. One of the challenges of this detection strategy is its sensitivity to the rate of unrelated photons triggering the photomultiplier, the so called dark noise. This constrain currently limits IceCube's supernova sensitivity to events within the Milky Way galaxy. Simulation studies have identified several key requirements to extend this sensitivity to extragalactic supernovae producing neutrinos in the $10\,\mathrm{MeV}$ range. These include a denser sensor spacing and a maximum noise rate of approximately $50\,\mathrm{Hz}$ per meter of instrumented volume, or $350\,\mathrm{mHz}$ per cm^2 of effective photosensitive area [5]. Meeting these noise constraints is well beyond the capabilities of current optical modules, highlighting the need for the development of innovative sensors that combine high efficiency with low noise characteristics.

An effective approach to meeting the requirements for low-energy neutrino detection is the use of wavelength-shifting technology, as implemented in the **Wavelength-shifting Optical Module (WOM)** [6] which will be deployed in the IceCube Upgrade in 2025/26. The WOM leverages the principles of wavelength-shifting and total internal reflection to decouple the photosensitive area from the PMTs. This allows for a significant increase in the effective photon collection area without a proportional increase in dark noise, yielding in a much higher signal-to-noise ratio. In addition, the WOM is sensitive to ultraviolet (UV) photons, enabling it to exploit the high-intensity region of the emission spectrum of Cherenkov light—a capability that distinguishes it from conventional sensors limited to the visible wavelength range.

This thesis provides detailed insight into the complex development process of the WOM, covering everything from the conceptual considerations for optimized performance to the engineering challenges required to meet the operational constraints within IceCube. We introduce the module's design and motivating the key design decisions in Chapter 4. This is followed by an in-depth discussion of the optimization and characterization of critical components in Chapter 5. We then analyze and model the performance of the WOM in terms of timing resolution (Chapter 6), efficiency, and effective area (Chapter 7). Finally, we focus on the production and performance evaluation of the WOMs intended for deployment in the IceCube Upgrade. This includes optical performance evaluation and quality control covered in Chapter 8, as well as the mechanical requirements and handling of the full module discussed in Chapter 9, where we assess mechanical stability and explore potential improvements for future module generations.

Theoretical Basics

2

This chapter introduces key concepts from optics and Astroparticle Physics that are essential for understanding optical detection methods. It covers fundamental principles as well as general detector components such as wavelength shifters and optical sensors, providing the necessary background for the following chapters.

2.1 Neutrinos and their Detection

In the Standard Model of particle physics neutrinos are massless, electrically neutral leptons which only interact via the gravitational and the weak force. For each lepton generation of electron, muon and tau there is a corresponding neutrino namely ν_e, ν_μ and ν_τ. Neutrinos were postulated in 1930 by Wolfgang Pauli in order to explain the continuous energy spectrum of the electron resulting from the β-decay $n \to p + e^- + \bar{\nu}$. [7]
Detection of neutrinos may only be done indirectly by detecting their interaction products using processes like the inverse β-decay $\bar{\nu_e} + p \to n + e^+$ (illustrated in Fig. 2.1) which lead to the first experimental neutrino discovery in 1956 [8].

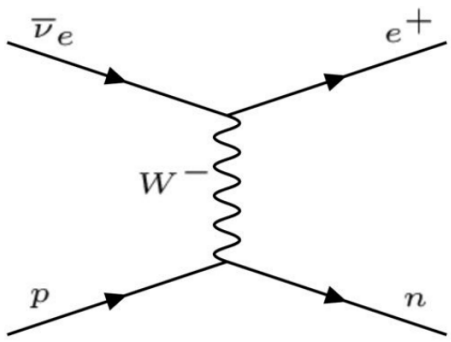

Fig. 2.1.: **Feynman diagram of the inverse β-decay [9].** An anti-electron neutrino $\bar{\nu_e}$ interacts with a proton p inside a nucleus outputting a neutron n and a positron e^+.

In the field of Astroparticle Physics neutrinos are of special interest as messenger particles. Due to their very low cross-section with matter of $\mathcal{O}(10^{-38}\,\mathrm{cm}^2)$ for GeV energies, neutrinos can cross large parts of our universe without being deflected by neither magnetic fields nor heavy objects allows tracking them back to their sources [10].
Besides the high-energy astrophysical neutrinos, which can give insight into extreme astrophysical sources, neutrinos over their whole energy spectrum (see Fig. 2.2) are important subjects of study such as Supernova neutrinos as early warning systems [1], solar neutrinos which give insight into the process of star lifetimes [11] or atmospheric neutrinos that help us study neutrino oscillations [12].

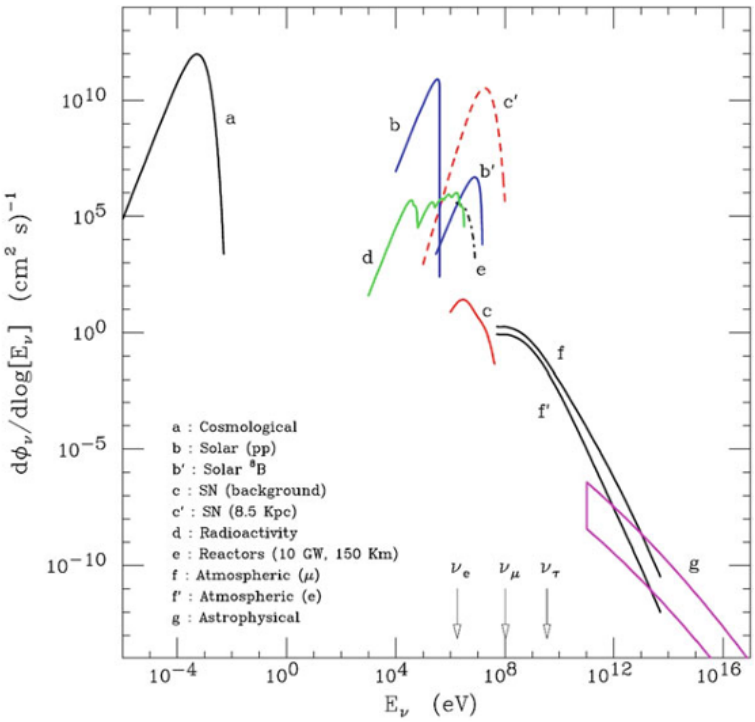

Fig. 2.2.: **Flux of neutrinos at the surface of the Earth [13].** Astrophysical neutrinos g are of special interest in high energy studies. Their very low flux requires detectors of large volumes.

2.2 Cherenkov Radiation

A common indirect detection method for neutrinos is the use of Cherenkov radiation. Cherenkov light is emitted whenever a charged particle traverses a dielectric medium with refractive index n with a velocity $v > c_n = \frac{c_0}{n}$, with c_n being the speed of light

in that medium and c_0 being the speed of light in vacuum. The emitted light forms a **Cherenkov Cone** with the opening angle θ_C, given by [2]

$$\cos\theta_C = \frac{c_n}{v} = \frac{1}{\beta \cdot n}. \tag{2.1}$$

The emission of Cherenkov radiation can be interpreted as a "shock" wavefront, analogous to a sonic boom as illustrated in Fig. 2.3. According to Huygens' principle of elementary waves a moving particle induces spherical waves propagating at c_n. In the case of $v > c_n$ these elementary waves interfere constructively forming a wavefront behind the particle known to us as the Cherenkov Cone. [14]

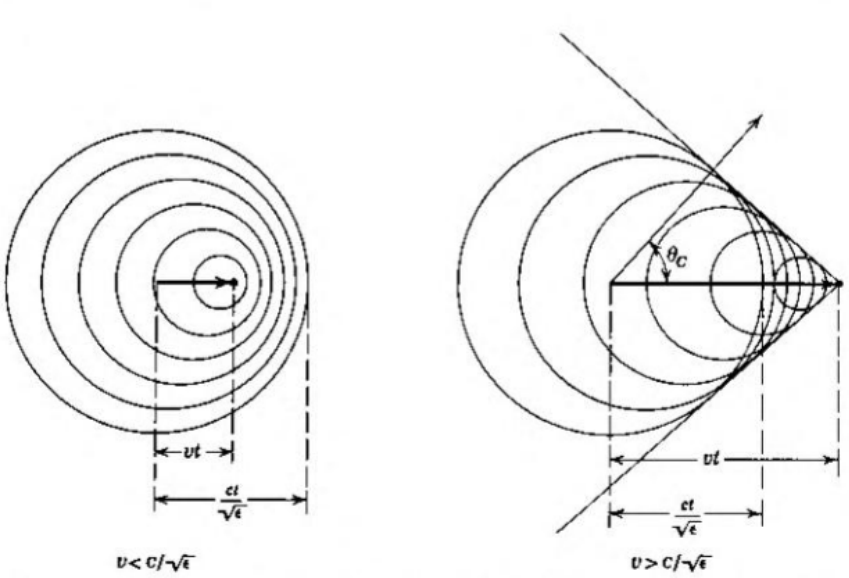

Fig. 2.3.: **Visualization of Cherenkov radiation[14].** Left: $v < c_n$, no radiation emission. Right: $v > c_n$, Elementary waves interfere forming wavefront behind the moving particle. $c_n = c/\sqrt{\epsilon}$.

The number of photons N per unit length dx and wavelength range $d\lambda$ is given by [15]:

$$\frac{d^2N}{dxd\lambda} = \frac{2\pi\alpha q}{\lambda^2}\left(1 - \frac{c_0^2}{n^2(\lambda)v^2}\right). \tag{2.2}$$

q is the electric charge of the particle, α the fine structure constant and c_0 is the speed of light in vacuum. An example of a Cherenkov spectrum is shown in Fig. 2.4.

We can approximate the relation $N \sim \frac{1}{\lambda^2}$ which would locate most of the Cherenkov photons in the UV-range. Light sensors in the detector medium however, measure only $\frac{dN}{d\lambda}$ for a fixed pathlength x determined by the distance between sensor

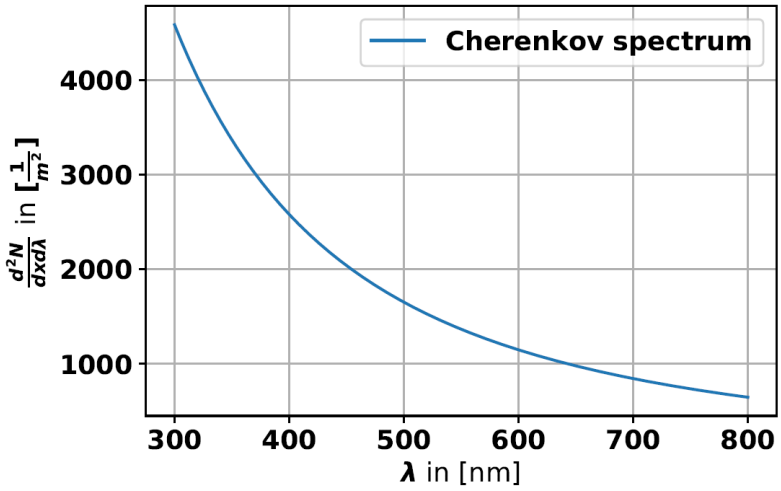

Fig. 2.4.: **Cherenkov radiation spectrum in ice with n=1.31 [16].** As the spectrum goes approximately with $1/\lambda^2$ it peaks in the UV region. However, this does not consider the propagation of photons through this medium which affects photons of each λ differently.

and particle interaction. As photons are differently affected by attenuation inside the medium depending on their wavelength we would expect a shift of the peak position.

2.3 Light Propagation and Attenuation

The Cherenkov photons have to propagate a certain distance until they reach the detector while undergoing different interactions with matter. This section introduces the effects of light attenuation in matter and the transitions between different optical media.

2.3.1 Absorption and Scattering

Depending on the wavelength of a photon propagating through matter, different effects may occur. If the photon's energy matches the energy of an electron transition the atom will absorb the photon, entering the excited state [17]. This process is referred to as **Absorption**.

The distance dependent decrease in intensity $I(d)$ of the propagating light can be modeled by the **Beer-Lambert law** such as scattering assuming the output is limited to a small spot. [18]:

$$I(d) = I_0 \cdot e^{-\mu \cdot d} = I_0 \cdot e^{-\frac{d}{\lambda_{\text{abs}}}} \tag{2.3}$$

I_0 is the initial intensity and μ is the **absorption coefficient** which is reciprocal to the the **absorption length** λ_{abs}. Further, λ_{abs} depends on the wavelength of the propagating light.

If the energy of the propagating photon is too low to cause a transition to a higher energy level the photon could cause the electron cloud to vibrate with respect to the positive nucleus while remaining in its ground state. This forms a dipole oscillator oscillating with same frequency as the photon which leads to the emission of a photon of the same frequency (and therefore energy). In this case, we observe the process of **elastic scattering** with a random scattering angle assuming unpolarized light. [17]

Assuming we have light propagating through matter with two different attenuation effects such as absorption and scattering with the corresponding attenuation lengths λ_{abs} and λ_{scat}, we can calculate the intensity $I(d)$ at thickness d by applying the Beer-Lambert law from Eq. 2.3 twice:

$$I(d) = I_0 \cdot e^{-\frac{d}{\lambda_{\text{abs}}}} \cdot e^{-\frac{d}{\lambda_{\text{scat}}}} = I_0 \cdot e^{-d \cdot \left(\frac{1}{\lambda_{\text{abs}}} + \frac{1}{\lambda_{\text{scat}}}\right)} = I_0 \cdot e^{-\frac{d}{\lambda_{\text{att}}}} \tag{2.4}$$

Therefore, one can combine the absorption and scattering length to the overall attenuation length λ_{att} given by[1]:

$$\frac{1}{\lambda_{att}} = \frac{1}{\lambda_{abs}} + \frac{1}{\lambda_{scat}} \tag{2.5}$$

This relation can be applied for any number of different attenuation effects such as combining several processes leading to absorption or scattering.

In the Antarctic deep ice, UV-light of $\lambda \approx 330\,\text{nm}$ displays a low scattering length of approximately $0.5\,\text{m}$ while having a relatively high absorption length of $100\,\text{m}$. Light in the visible region with $\lambda \approx 530\,\text{nm}$ behaves the other way around ($\lambda_{\text{scat}} \approx 50\,\text{m}, \lambda_{\text{abs}} \approx 20\,\text{m}$). [19]

[1] In this case we assume that every scattered photon is *lost*. Depending on the exact setup this might not always be the case as it could be possible for scattered photons to still hit the detector.

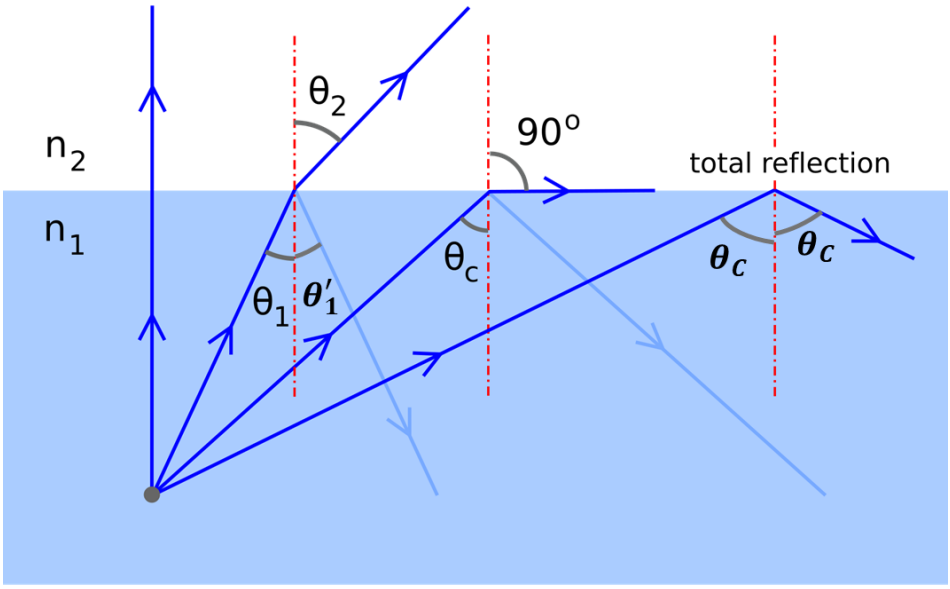

Fig. 2.5.: **Light ray behavior on interface for different inclination angles[@21].** If θ_1 becomes larger than the critical angle θ_C, all photons are reflected at the interface. This phenomenon is called Total Internal Reflection.

2.3.2 Interface Interaction

As light passes from one medium to another it is split into a **reflected** and a **refracted** ray (see Fig. 2.5). The reflection angle θ_1' relative to the normal vector of the interface equals the incoming angle θ_1 [20]:

$$\theta_1' = \theta_1. \tag{2.6}$$

The refraction angle θ_2 is given by **Snell's Law** [20]:

$$\frac{\sin\theta_1}{\sin\theta_2} = \frac{n_2}{n_1}. \tag{2.7}$$

n_1 and n_2 being the refractive indices of the two media.

To calculate the fraction of reflected and refracted light one can use the *Fresnel Equations* [20]. For this we calculate the **Reflectance R** and the **Transmittance T**. For s-polarized light we get:

$$R_s = \left(\frac{n_1\cos\theta_1 - n_2\cos\theta_2}{n_1\cos\theta_1 + n_2\cos\theta_2}\right)^2 \quad T_s = \left(\frac{2n_1\cos\theta_1}{n_1\cos\theta_1 + n_2\cos\theta_2}\right)^2 \cdot \frac{n_2\cos\theta_2}{n_1\cos\theta_1}. \tag{2.8}$$

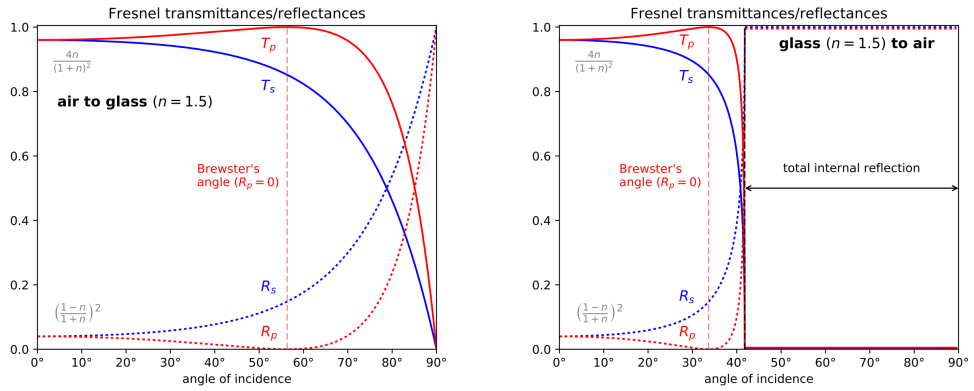

(a) Air to glass [@22]. (b) Glass to air [@23].

Fig. 2.6.: Reflectance and Transmittance for light on the interface between air ($n = 1.0$) and glass $n = 1.5$ for different inclination angles. We can see that transmission dominates for small (steep) angles while reflection increases for larger (shallow) angles.

And for p-polarized light[2]:

$$R_p = \left(\frac{n_1 \cos\theta_2 - n_2 \cos\theta_1}{n_1 \cos\theta_2 + n_2 \cos\theta_1} \right)^2 \quad T_p = \left(\frac{2n_1 \cos\theta_1}{n_1 \cos\theta_2 + n_2 \cos\theta_1} \right)^2 \cdot \frac{n_2 \cos\theta_2}{n_1 \cos\theta_1}. \tag{2.9}$$

As we only consider reflection and refraction, the conservation of energy implies that:

$$T_s = 1 - R_s \qquad T_p = 1 - R_p. \tag{2.10}$$

In the cases where light is unpolarized we use the mean from both equations:

$$R = \frac{1}{2}(R_s + R_p) \qquad T = \frac{1}{2}(T_s + T_p). \tag{2.11}$$

R and T are illustrated in Fig. 2.6 for different inclination angles.

In Fig. 2.6b we observe that above a certain angle the transmitted fraction goes to 0 while the reflected fraction becomes 1. This is the effect of **Total Internal Reflection (TIR)** which occurs when light passes to an optically less dense medium with an inclination angle above the **critical angle** θ_C given by [20]:

$$\theta_C = \arcsin\left(\frac{n_2}{n_1}\right). \tag{2.12}$$

[2]Both equations assume non-magnetic media with magnetic permeability $\mu_r = 1$ and ideal dielectrics resulting in a non-complex refractive index. This is a reasonable assumption for the material and frequencies that will be featured in this thesis.

Therefore, for $\theta > \theta_C$ the reflectance goes to 1 which can be also seen in the right part of Fig. 2.5.
An important application for TIR are optical fibers. Here, light is guided by total internal reflection due to the difference in refractive indices between the core and the cladding of the fiber. Due to its cylindrical symmetry the light is captured inside once it fulfills the requirement for TIR and can be guided to the end of the fiber. [20]

2.3.3 Ray Tracing

Optical simulations are widely used to model complex optical systems, including optical elements and photodetectors. However, simulating every emitted photon would be computationally infeasible. To conduct fast and efficient photon propagation simulations we use **Ray Tracing** [24] algorithms originating from 3D computer graphics.

The algorithm is visualized in Fig. 2.7. From a certain observer, rays are emitted to every pixel on a screen. From each pixel, the algorithm determines the intersections between the ray and the underlying geometry. The ray is only traced up until the intersection point closest to the screen and the pixel therefore displays the color of the object at said intersection point. This reversed way of light propagation saves on large amounts of computing time by only calculating the light rays that are actually seen by the observer.

The recursive use of this algorithm and the implementation of basic optical effects such as reflection, refraction and attenuation is used in computer graphics to generate photo realistic images. But it can also be used to simulate complex optical systems and detector geometries with high statistics very efficiently.

2.4 Wavelength Shifters

Wavelength Shifters (WLS) have broad use in different experiments in particle and astroparticle physics since the wavelength distribution of the signal oftentimes does not overlap well with the sensor's wavelength acceptance. They operate according to the **scintillation** principle, where molecules are excited by ionizing radiation to later re-emit the absorbed energy as photons [26].

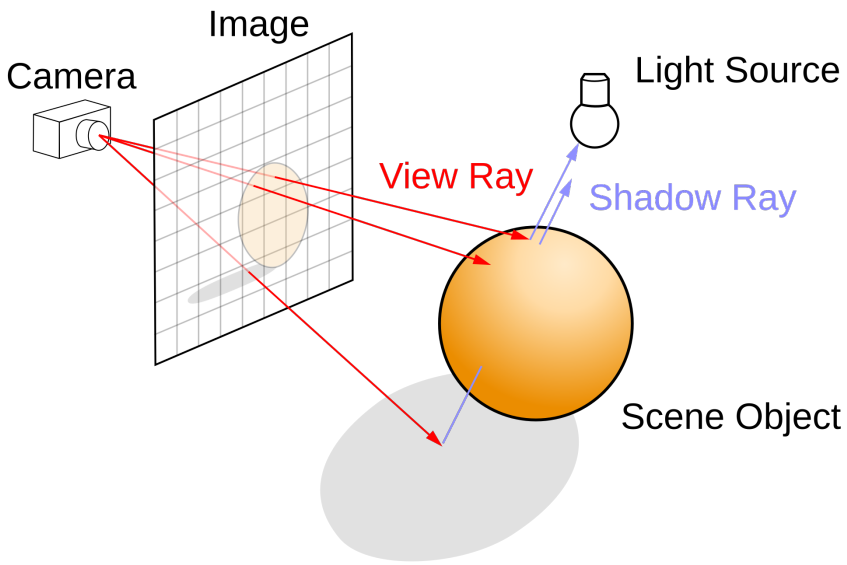

Fig. 2.7.: **Visualization of the Ray Tracing algorithm [@25].** We can further use it to trace the rays of light sources within the given geometry visualizing the shadow of an object.

In this thesis, we will focus on **organic** WLS. They are based on organic molecules with a so called π-electron structure. As shown in Fig. 2.8, each energy state – namely S_0, S_1, S_2, S_3 – is subdivided into several vibrational states such as S_{11}, S_{12}, S_{13}. An absorbed incoming photon results in an excitation from the ground state S_{00} to any of the vibrational states in a higher energy state depending on the photon's energy. Molecule electrons in higher vibrational states like S_{11}, S_{12} quickly loose vibrational energy due to not being in thermal equilibrium with their neighbors resulting in a radiationless transition to S_{10}. From there, transition to any of the vibrational ground states can happen ($S_{00}, S_{01}, S_{02}, S_{03}$) under emission of *fluorescent* light of different wavelengths. This decay follows the exponential relation

$$I(t) = I_0 \cdot e^{-t/\tau} \tag{2.13}$$

with I being the intensity and τ the decay constant which is typically in the order of ns. [26]

The process explained above results in the WLS having an apparently continuous absorption and emission spectrum (see Fig. 2.9). As for most transitions the emitted energy is below the initial energy of the absorbed photon, the light is shifted to higher wavelengths. The spectral distance between emission and absorption spectrum is called **Stokes Shift**. Further, the emitted wavelength does not depend on the wavelength of the absorbed photon, because the fluorescent transition will always start from the S_{10} state independently on the absorbed photon's energy.

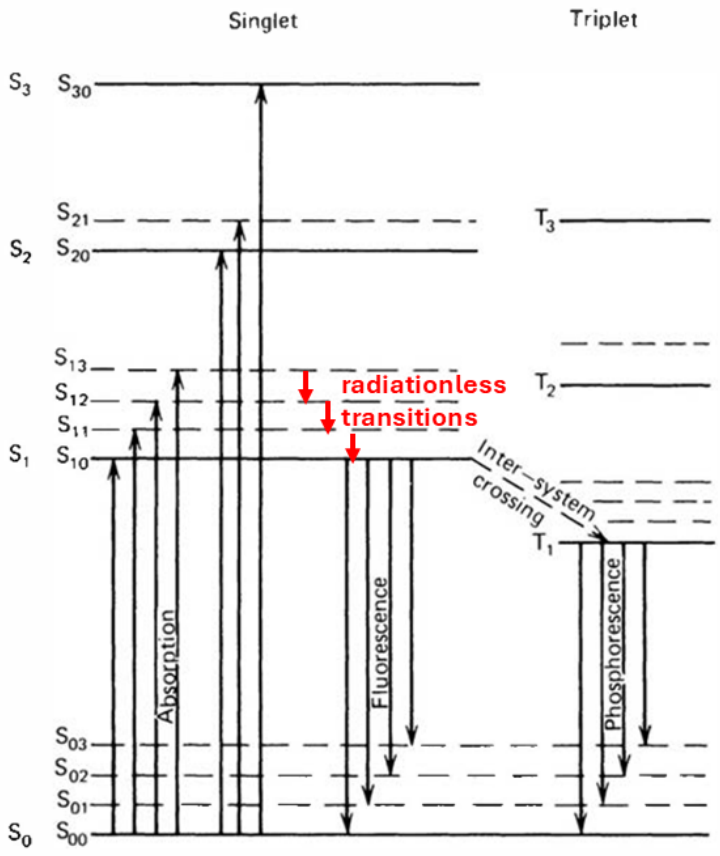

Fig. 2.8.: **Energy levels of an organic molecule with π-electron structure (adapted from [27]).** Excited molecules first relax to the S_{10} state before they transit to one of the vibrational ground states via fluorescence.

For an optimized WLS, one would aim for a high Stokes Shift and a minimal overlap between absorption and emission spectrum[3]. This increases the probability of emitted photons being shifted again reducing the efficiency and effectively cutting off a part of the emission spectrum.

An example for the applications of WLS are liquid argon detectors which can be used for either neutrino detection such as DUNE [@29] or the search of Dark Matter [@30]. The scintillation light from Argon at $128\,\mathrm{nm}$ is shifted to be detected by optical photo sensors [31]. Further, studies on supernova neutrinos such as with Hyper-Kamiokande [@32] or IceCube (see Chapter 3) can profit from WLS techniques. A large detector volume could be covered much more price-efficient compared to the use of conventional optical modules. Additionally, more Cherenkov

[3] An overlap between absorption and emission spectrum is possible, because most WLS consist of multiple complex molecules with different WLS spectra which we see the sum of.

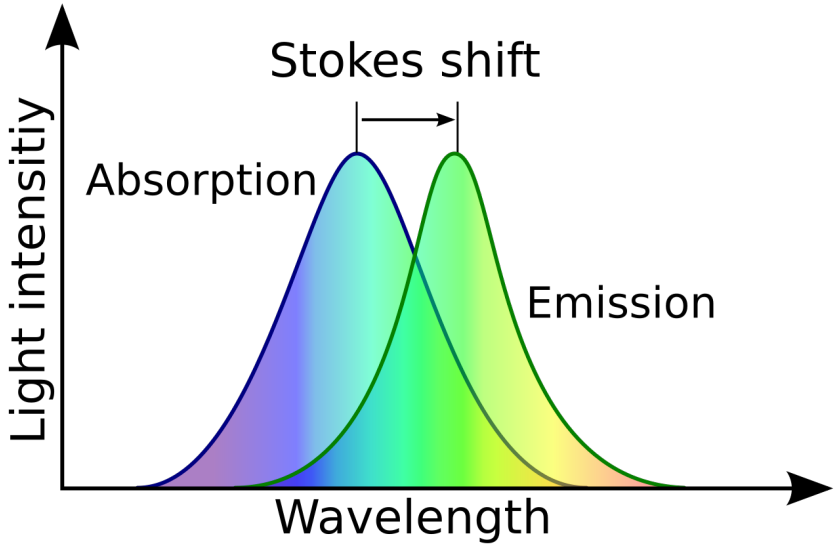

Fig. 2.9.: **Visualization of the Stokes Shift between the absorption and emission spectrum of a WLS[@28].** We see an overlap in both spectra resulting in the possibility of shifted light remaining in the absorption region. This light will be then shifted again by hitting the WLS another time.

photons per event would be detected which enchances the overall analysis possibilities [33].

2.5 Photomultiplier Tubes

To detect very faint light signals down to single photons amplification devices such as **Photomultiplier Tubes (PMTs)** are used. The working principle of a PMT is illustrated in Fig. 2.10. A photon hits the photocathode located inside a vacuum tube resulting in the emission of an electron according to the **Photoelectric Effect** [34]. The emitted electron is accelerated towards the first dynode by an applied **High Voltage (HV)** generating an electric field. Upon hitting the dynode multiple new electrons are emitted, which are then accelerated towards the second dynode. Repeating this process several times results in an avalanche of electrons eventually hitting the anode resulting in an overall amplification of typically $10^6 - 10^7$ and therefore a measurable electric signal. [35]

When the photocathode is hit by a photon it transfers its energy to an electron in the valence band of the cathode which results in the emission of an electron. The probability to emit one electron for one incident photon is called the **Quantum Efficiency (QE)** of the PMT. This value is dependent on the wavelength of the

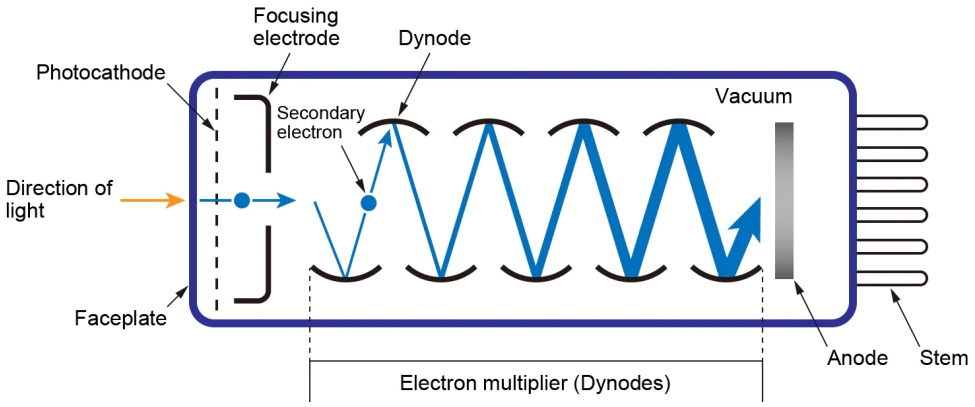

Fig. 2.10.: **Working principle of a PMT [@36].** An incoming photon results in the emission of an electron which is multiplied several time until you get a measurable electric signal.

incoming photon and can be optimized with the right choice of the photocathode material reaching peak values of up to 43% (see Fig. 2.11). We want the QE to be as high as possible as it is the limiting factor in the PMT's efficiency. The efficiency of a PMT can be also characterized by using the **Radiant Sensitivity**, which indicates the PMT's photocurrent for an incident photon flux. [35, 37]

The amplification factor, also referred to as the **Gain**, can be determined from the measured **Single Photon Emission (SPE)** spectrum, which is constructed by extracting the charge of a large number of single photons of every waveform (see Fig. 2.12) and creating a histogram[4]. The resulting spectrum as shown in Fig. 2.13 features the distribution of the deposited charge for all measured waveforms. The first peak around 0 results from waveforms containing only electrical noise from the PMT and readout and no actual signal[5]. The second, wider peak is the SPE or 1 **Photo Electron (PE)** peak resulting from the deposited charge upon detecting exactly one photon (and exactly one electron being emitted from the photo cathode). Smearing effects like electric noise or electrons missing the dynodes result in a non discrete peak.

The minimum between the noise and SPE peak is referred to as the **Valley** and marks the threshold above which the waveforms are dominated by signal rather than noise. While measuring light with PMTs one wants to set the threshold within the valley to detect most of the signal while getting rid of most noise hits. The valley is normally located at around 0.25 PE, it has become common practice within IceCube

[4]It has to be ensured that the PMT sees single photons primarily, otherwise we would get a **Multi Photon Emission (MPE)** spectrum instead. This can be achieved by illuminating the PMT with a dimmed light source.

[5]Using a threshold trigger would result in the peak being (partially) cut off.

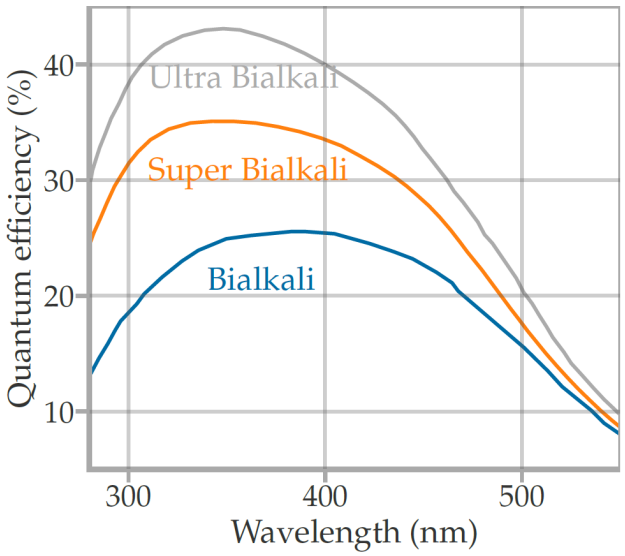

Fig. 2.11.: PMT QEs of different photocathodes [38]. The most efficient *Ultra Bialkali* cathodes reach peak QEs of over 40%. The more common used *Bialkali* go typically up to 25%.

to set the trigger to this threshold. However, the relative position of the valley changes depending on the electric noise of the PMT and its readout electronics.

The Gain G is determined using the 1 PE charge Q with

$$G = Q/e \tag{2.14}$$

with e being the elementary charge. As the applied HV U changes the kinetic energy of the accelerated photons and therefore the number of emitted electrons on each dynode we can model the gain by a power-law [35]:

$$G(U) = A \cdot U^B \tag{2.15}$$

with different A and B for each PMT depending on the material and structure of the photocathode and the underlying electric circuit.

Even without any incoming light the PMT will output signals indistinguishable from a photon signal. There are several reasons for that so called **Dark Rate** or **Dark Current** [35]. The most dominant effects are also visualized in Fig. 2.14.

- **Thermionic emission:** Electrons are spontaneously emitted from the photocathode and the dynodes as their thermal energy goes above the work function of the cathode and dynode. These electrons are multiplied as any other elec-

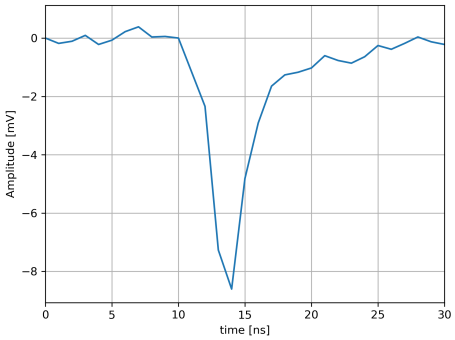

Fig. 2.12.: **PMT waveform resulting from one detected photon.**

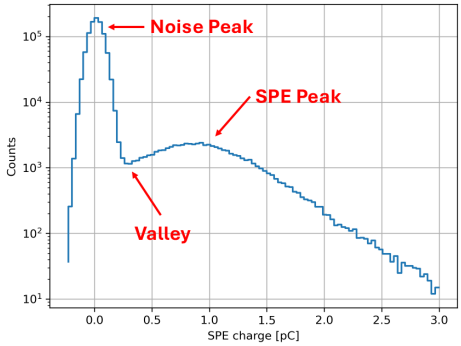

Fig. 2.13.: **SPE spectrum of a PMT featuring Noise Peak, SPE Peak at around** 1.0 **pC and Valley.** The position and shape of the SPE peak changes with the HV while the Noise peak stays constant.

trons resulting from an incoming photon. This effect is temperature dependent and can therefore be suppressed by operating the PMTs at low temperatures.

- **Radioactive decay:** Most glasses used for PMTs contains the radioactive isotope ^{40}K which emits β and γ-rays contributing to the dark rate. The amount depends on the exact manufacturing process of the glass. Further, γ-rays emitted from the close environment (e.g. glass coupled to the PMT) would also influence the dark rate.

- **External electric fields:** Strong external electric fields would result in electrons being deflected from their original trajectory eventually hitting the glass envelope followed by the emission of scintillating photos to be detected. This can be counteracted by applying a conductive carbon layer around the envelope of the PMT and connecting it to the cathode pin, also referred to as **HA-treatment** [35].

- **Field emission:** Operating the PMT at an excessive HV could result in electrons being emitted from the dynodes by a strong electric field increasing the dark rate abruptly.

- **Leakage current:** As PMTs are operated at high voltages while handling low currents of nA to μA an imperfect insulation could cause a leakage current in the magnitude of nA. As the dark rate resulting from thermionic emission scales with the HV and temperature the leakage current becomes the more dominant effect at low HVs or low temperatures.

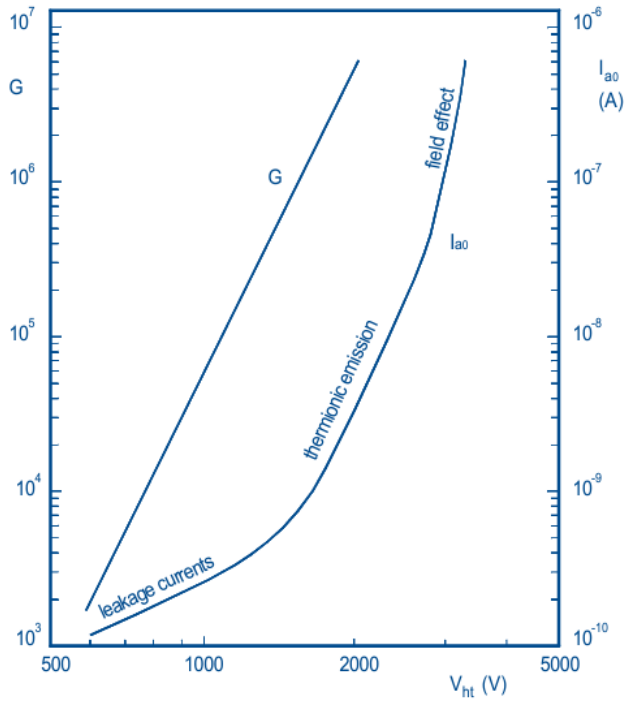

Fig. 2.14.: **Gain G and Dark Current I_{a0} as functions of the HV [39].**

- **Activation:** After being exposed to light the dark rate of the PMT decreases over time while being operated in the dark. So a PMT should be kept in the dark for some time before starting the actual operation. Further, the dark rate decreases over several years after the manufacturing of the PMT [40].

The time it takes for a PE to transverse between photocathode and anode is referred to as the **transit time**. As the trajectories between two dynodes differ of each electron the time between the incoming photons hitting the cathode and the output electric signal has a certain spread different for each PMT depending on its underlying geometry. This is called the **Transit Time Spread (TTS)** which is typically in the ns range and is an important characteristic for timing related PMT studies determining the PMT's timing resolution. [35]

2.6 Effective Area

Optical modules come in different sizes and shapes making the evaluation of their performance non trivial. Using the efficiency ϵ defined as the ratio between incoming and detected photons would create a false balance as it does not consider the probability of the module being hit by photons. Like this, a very small module with

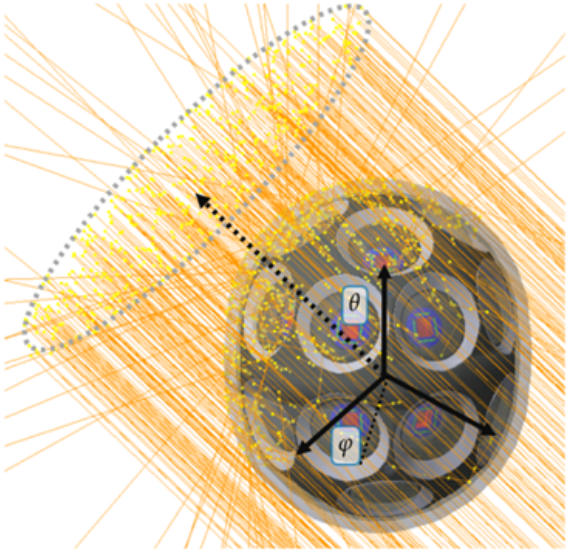

Fig. 2.15.: **Optical simulation to determine the effective area of the mDOM [38].** Photons are simulated perpendicular to a disk equal to the projected area of the module which is rotated for different θ and ϕ. For more information on IceCube modules see Chapter 3.

high efficiency would perform better than a large module with low efficiency while the absolute number of detected photons would be higher for the second case. For a better characterization we use the **effective area** $\boldsymbol{A_{\text{eff}}}$ which takes the photosensitive area A_{photo} and the efficiency into account [38]:

$$A_{\text{eff}}(\theta,\phi) = A_{\text{photo}} \cdot \epsilon(\theta,\phi) = A_{\text{photo}} \cdot \frac{N_{det}(\theta,\phi)}{N_{hit}}. \tag{2.16}$$

We get the effective area for detected photons of a certain zenith θ and azimuth angle ϕ.

To determine the effective area for non-trivial geometries, a simulation can be used to generate photons on the projected area of the module and determine the the number of detected photons while rotating the disk around the module (see Fig. 2.15). Then, the average A_{eff} is calculated using the area of the disk as A_{photo}.

The number of detected photons depends on different properties of the module such as the transmission efficiency and PMT acceptance, which depends on the photon's wavelength λ. So the wavelength dependency of A_{eff} needs also to be considered (see Fig. 2.16).

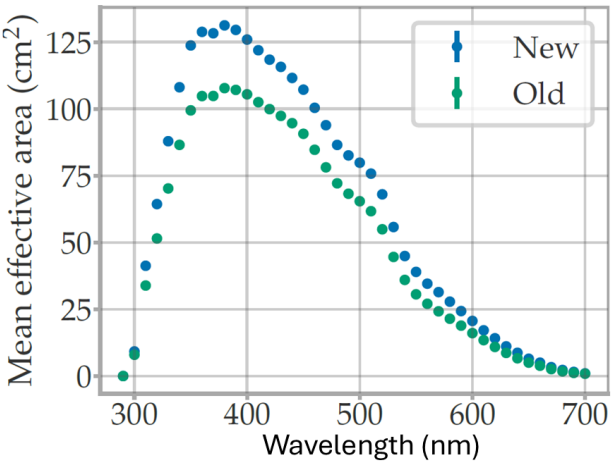

Fig. 2.16.: **Wavelength dependence of the effective area for an mDOM in ice[38].**

As we expect Cerenkov photons to hit our module we can also calculate the **Cherenkov-averaged** effective area $\bar{A_{\text{eff}}}$ valid for small distances [41]:

$$\bar{A_{\text{eff}}} = \frac{\int A_{\text{eff}}(\lambda P(\lambda))d\lambda}{\int P(\lambda)d\lambda} \qquad with \qquad P(\lambda) = \frac{2\pi\alpha}{\lambda^2}\left(1 - \frac{1}{\beta^2 n(\lambda)^2}\right) \tag{2.17}$$

with $P(\lambda)$ being the Cherenkov spectrum.

The IceCube Neutrino Observatory

3

The IceCube Neutrino Observatory [3, @42] is the largest neutrino detector instrumenting $1\,\mathrm{km}^3$ Antarctic ice of detector volume for the detection of high-energy neutrinos. The detector is separated into different segments for corresponding applications (as seen in Fig. 3.1) making IceCube very versatile in its use: Current research features among others the search for neutrino sources [43], studies on neutrino oscillations [44], Cosmic Ray Physics [45], search for supernovae [46]. IceCube contributes even beyond the field of Particle and Astroparticle physics, with fields such as glaciology [47]. This chapter will give insight into the instrumentation

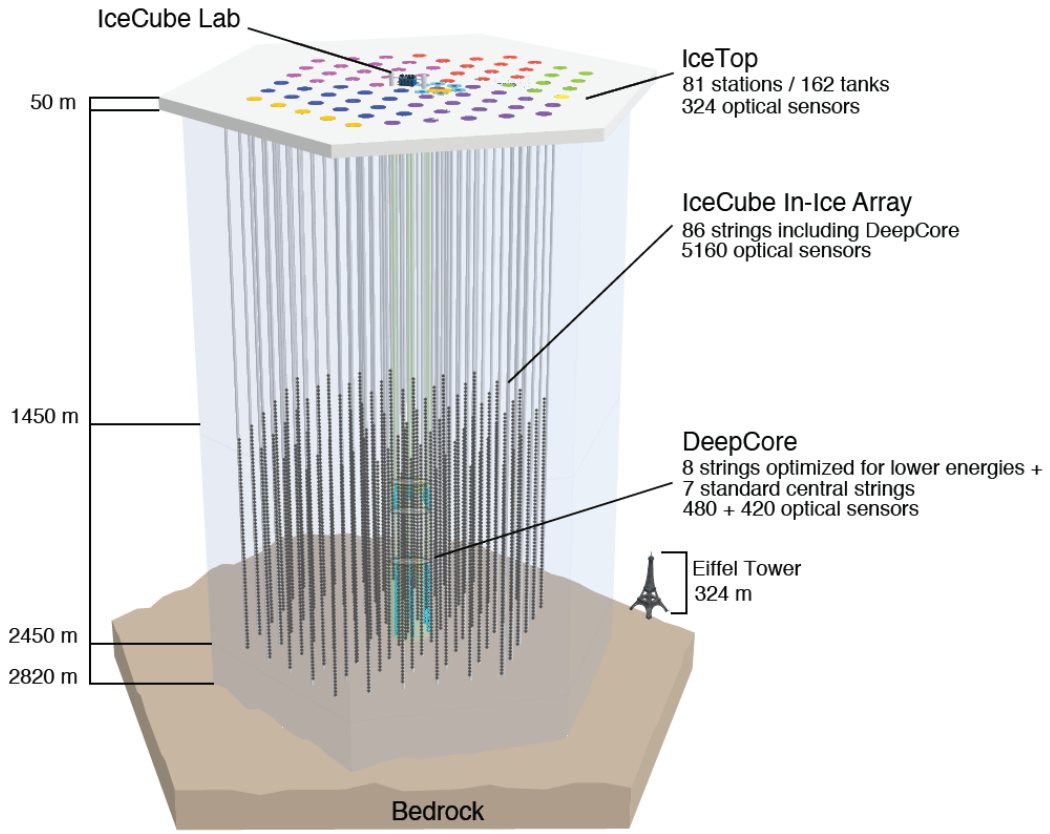

Fig. 3.1.: The IceCube Neutrino Observatory [3]. It consists of the in-ice array and several surface extensions including IceTop. See the following sections for more information on it.

of the IceCube detector and will talk about ongoing operation and prospects in the near and far future.

3.1 Instrumentation and Event Topologies

The IceCube instrumentation consists of 5,160 Digital Optical Modules (DOMs), which are deployed on 86 vertical strings at depths between $1450\,\mathrm{m}$ and $2450\,\mathrm{m}$ [3]. This deep deployment serves a dual purpose: the overlying ice provides effective shielding against cosmic-ray-induced muons, and the glacial ice at these depths exhibits excellent optical properties, including long absorption and scattering lengths, which significantly enhance the quality of data acquisition and event reconstruction [19].

The strings are arranged in a hexagonal grid pattern, which optimizes both spatial and angular coverage and facilitates efficient triangulation of Cherenkov light signals—crucial for accurately determining the direction and energy of incoming neutrinos. The DOMs are spaced $125\,\mathrm{m}$ apart horizontally and $17\,\mathrm{m}$ vertically, a design compromise that balances the need to instrument a large detection volume—essential for capturing rare high-energy neutrino events—with the requirement to collect sufficient Cherenkov light for precise reconstruction. This configuration enables IceCube to be sensitive to neutrinos in the energy range of approximately $\mathcal{O}$(TeV - PeV). [3]

Each DOM (see Fig. 3.2) houses a 10" PMT operated at a gain of 10^7, making it sensitive to even faint Cherenkov light signals. In addition, each module contains onboard digitization electronics and calibration systems, all sealed within a pressure-resistant glass sphere designed to withstand the extreme conditions in the deep Antarctic ice. The PMTs are oriented downward to enhance the sensitivity to up-going neutrinos, which have traversed the Earth and are more likely to be of astrophysical origin. At the same time, this orientation reduces sensitivity to the dominant background of down-going atmospheric muons, thereby improving the overall signal-to-noise ratio of the detector. [3, 48]

The **DeepCore** subarray [49] refers to a denser, low-energy extension located near the center of the IceCube array. It employs DOMs with higher QE than those used in the main detector and features reduced module spacing: on average $72\,\mathrm{m}$ horizontally and $7\,\mathrm{m}$ vertically. This compact geometry significantly lowers the energy threshold to the GeV scale, enabling the study of atmospheric neutrino oscillations and enhancing sensitivity to potential signals from dark matter [50].

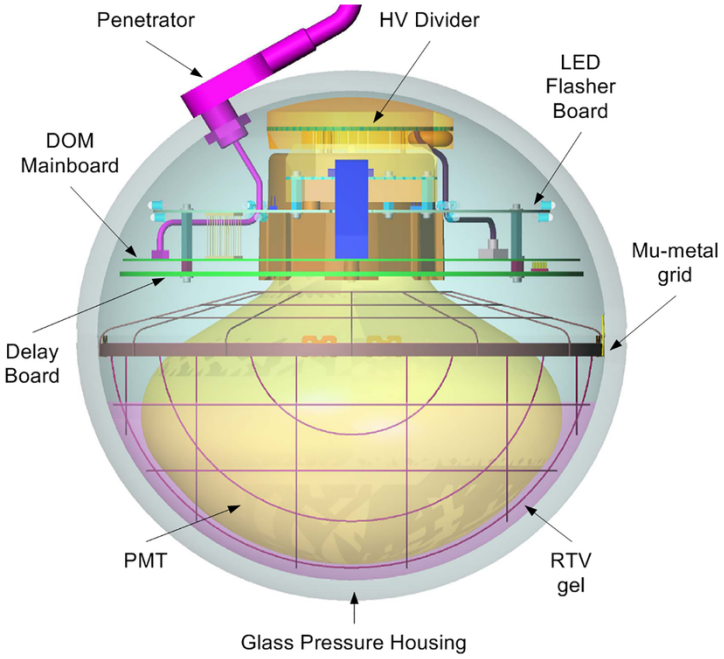

Fig. 3.2.: **Components of an IceCube DOM [48].** The PMT is optically coupled to the pressure housing using optical gel. The mu-metal grind shields the module against the earth's magnetic field.

Upon triggering, each DOM records charge and timing information, enabling the reconstruction of characteristic event signatures depending on the underlying neutrino interaction with the ice (see Fig. 3.3).

Track-like events arise primarily from charged-current interactions of muon neutrinos (ν_μ), producing relativistic muons that travel long distances through the detector. These tracks allow for excellent angular resolution due to their extended geometry, but accurate energy estimation is limited if the muon enters or exits the detector volume without being fully contained.

Cascade events result either from neutral-current interactions of all neutrino flavors or from charged-current interactions of electron and tau neutrinos (ν_e, ν_τ). These interactions produce short, localized showers of secondary particles, primarily through electromagnetic processes like Bremsstrahlung in the case of electrons. Unlike muons, these particles deposit their energy quickly, making cascades typically fully contained within the detector. This allows for good energy resolution, but the limited spatial extension and the relatively large inter-DOM spacing make directional reconstruction more challenging, as the light distribution appears nearly isotropic. The ν_τ can also produce unique signatures. However, due to the short lifetime of the resulting τ lepton ($12\,\mathrm{ps}$), it usually decays before producing a resolvable track in IceCube. At higher energies, rare *double-bang* signatures—featuring two cas-

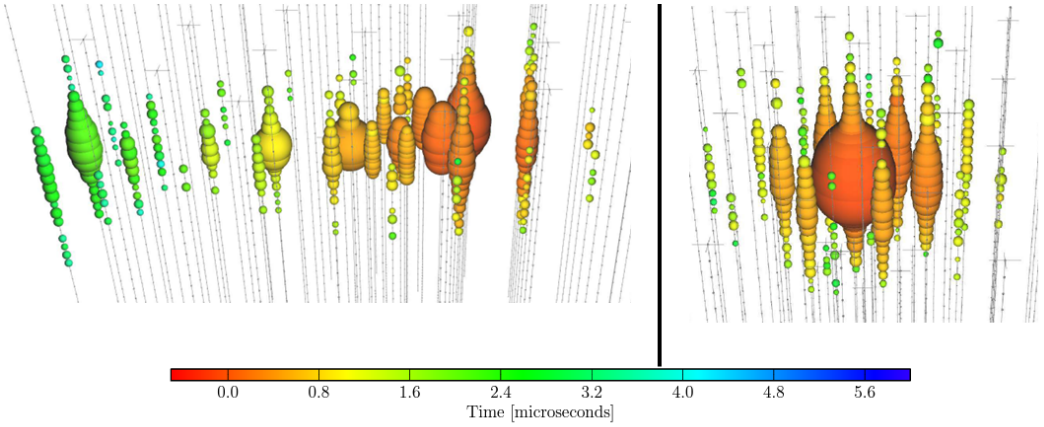

Fig. 3.3.: **Comparison between a track-like (left) and a cascade (right) neutrino event in IceCube (adapted from [52]).** Every circle represents one DOM. The size illustrates the detected number of photons and the color coding describes the relative hit times of each module.

cades separated by the τ propagation distance—can be observed, but these require energies in the PeV range and are thus extremely rare. [51]

Besides the in-ice modules, IceCube also includes several surface extensions like **IceTop** [53], **IceAct** [54] or **radio antennas** [55]. They can be used for cross-calibrations with the in-ice array. Further, the surface detectors are applied to multiple analyses on high energy cosmic rays such as measurements of the Cosmic Ray Spectrum around the knee region [56] or studies on Cosmic Air Showers.

3.2 IceCube Upgrade

The **IceCube Upgrade** is an in-ice extension for IceCube which will be deployed in austral summer 2025/26. The geometry of the Upgrade is shown in Fig. 3.4. It will feature approximately 600 new sensors on seven new strings located between already existing IceCube and DeepCore strings. The so called **physics region**, located between $2100\,\mathrm{m}$ and $2450\,\mathrm{m}$, will have a horizontal spacing of $20\,\mathrm{m}$ and a vertical spacing of $3\,\mathrm{m}$ which would effectively lower the energy threshold of IceCube down to $1\,\mathrm{GeV}$. The deployed modules will include new optical modules with multiple PMTs such as the D-Egg [41] and the Multi-PMT Digital Optical Module (mDOM) [57], but also calibration modules to calibrate the ice and positioning of devices such the acoustic module [58] or the POCAM [59].

On depths between $1300\,\mathrm{m}$ and $1900\,\mathrm{m}$ as well as bellow $2450\,\mathrm{m}$ the **shallow region** will be located with a vertial spacing of $17\,\mathrm{m}$. It will mainly serve for calibration and R&D purposes. [4, 60]

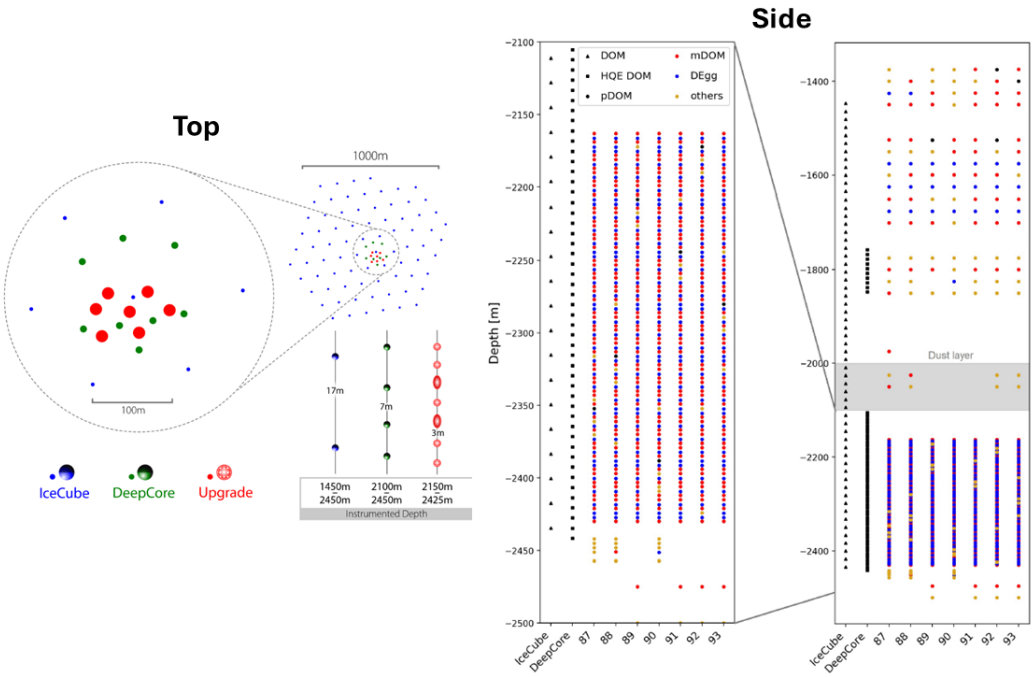

Fig. 3.4.: **Geometry of the IceCube Upgrade (adapted from [4, 60]).** The position of the Upgrade strings relative to IceCube and DeepCore is shown in red (left). The colors of the dots visualize the position of the different Upgrade modules (right). The **dust layer** indicates an ice volume with significantly increased absorption and scattering [61].

The mDOM (shown in Fig. 3.5) uses a total of 24 3" PMTs arranged symmetrically in an ellipsoid allowing for an efficient coverage of the solid angle. Further, this multi PMT design is going to enhance the directional event reconstruction compared to single-PMT DOMs. The mDOM has an effective area of over $100\,\mathrm{cm}^2$ which is more than triple the effective area of a single-PMT DOM. However, using many PMTs comes with the price of a high dark rate of about $15\,\mathrm{kHz}$ [38] which can be effectively reduced by the use of local coincidences within the module. [57]

The D-Egg (see Fig. 3.6) on the other hand uses two 8" PMTs pointing up and downwards extending the vision of a module to the area above compared to a conventional DOM. Additionally, it uses UV-transparent glass for the pressure vessel, which transmits photons with wavelengths down to $350\,\mathrm{nm}$ with almost 100% efficiency. With this additional coverage in its acceptance spectrum the D-Egg gets an effective area 2.8 times larger than a DOM while maintaining a relatively low dark rate of $1\,\mathrm{kHz}$. [41]

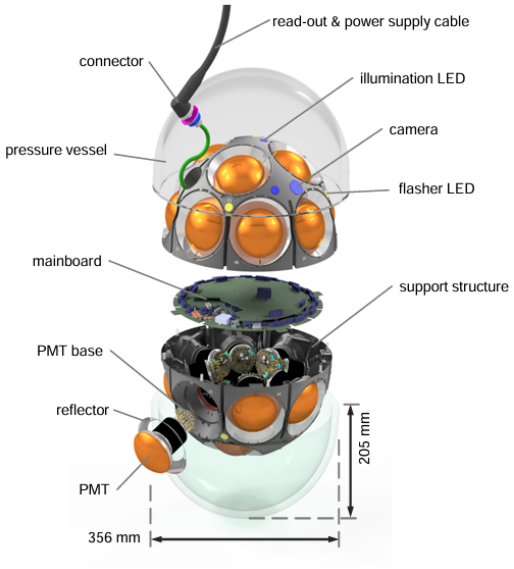

Fig. 3.5.: **Design of the mDOM [57].** It features 24 small PMTs arranged in all directions for better directional resolution.

Fig. 3.6.: **Design of the D-Egg [41].** Is uses two large PMTs pointing up and downwards.

Every optical module is equipped with fully calibrated LED flashers with adjustable brightness for a better calibration of the ice. These LEDs operate either in optical wavelengths of $405\,\mathrm{nm}$ or in the UV-range ($365\,\mathrm{nm}$). Besides optical baseline modules and calibration devices there are also different *R&D* modules to be deployed in small numbers. They consist of different sensor concepts to be probably considered for the future **Gen2** detector.

3.3 IceCube Gen2

The IceCube Gen2 detector [62, @63] is an envisioned large scale, high-energy extension for IceCube which is currently in its conceptual phase. It will consist of an extended in-ice and surface array, as well as a new large radio array. The overall goal of Gen2 is to enhance IceCube's sensitivity for high energy neutrinos and increase the upper energy threshold.

The optical in-ice array will extend the detector volume up to $8\,\mathrm{km}^3$. A total of 9600 optical sensors on 120 new strings with horizontal distances of $240\,\mathrm{m}$ are going to be deployed. This will presumably increase the rate of detected neutrinos above energies of $30\,\mathrm{TeV}$ by five to ten times.

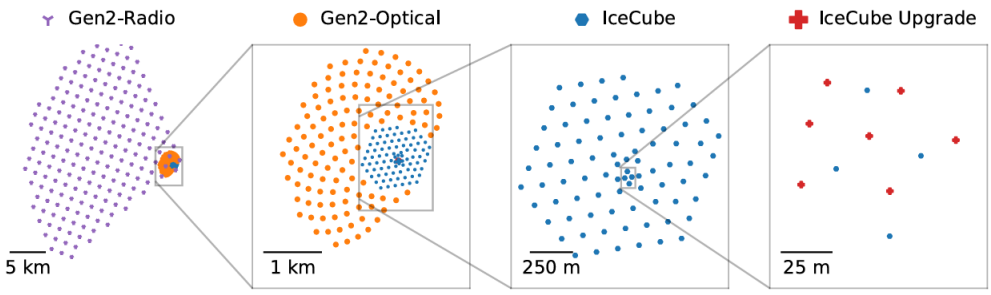

Fig. 3.7.: **Size comparison of the Gen2 geometry compared to current IceCube [62].** The optical in-ice array is to be deployed on same depths as IceCube with a vertical spacing of $16\,\mathrm{m}$.

The new extended surface array would be able to provide a veto against down-going muons and atmospheric neutrinos. Further, studies on the composition of cosmic rays in energy regions of $30\,\mathrm{PeV}$ to several EeV could be conducted. This region denotes the transition between galactic to extragalactic cosmic ray sources. [@63]

The Gen2 radio array will consist of $\sim$ 500 radio stations covering an area of $\sim 500\,\mathrm{km}^2$ (see Fig. 3.7 for a size comparison). Making use of the Askaryan effect [64] it can detect emitted radio waves from neutrinos interactions in the ice. Compared to optical sensors radio technology benefits in terms of effective area, resolution, cost-efficiency and background suppression. The detector would provide sensitivity for ultra-high-energy neutrinos for energies of $10^{17}\,\mathrm{eV}$ to $10^{19}\,\mathrm{eV}$. [65]

As already mentioned in Section 3.2 some of the optical modules planned for Gen2 will first be deployed in the Upgrade. The main Gen2 optical sensor is the Long Optical Module (LOM). It comes in two designs using either 16 or 18 4" PMTs (namely LOM16 and LOM18, see Fig. 3.8). As the Gen2 drilling holes will be $5\,\mathrm{cm}$ smaller compared to the Upgrade holes the LOM design has to be compact. The LOMs have effective areas around $110\,\mathrm{cm}^2$ at $400\,\mathrm{nm}$ which are similar to the mDOM and improve significantly of the Gen1 DOMs. [66]

After having introduced the detector we will now talk about one specific Upgrade module which could be also applied to Gen2.

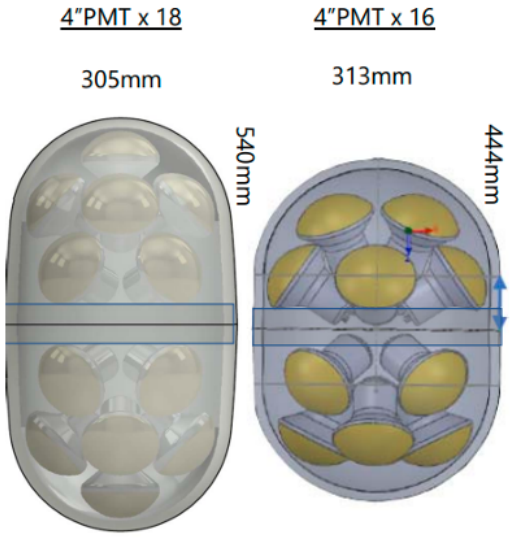

Fig. 3.8.: **The two LOM designs, LOM16 and LOM18 [66].** Currently, both LOM versions are developed and will be deployed in the Upgrade, but most likely one of them will be chosen as the Gen2 design.

4 The Wavelength-shifting Optical Module

Because of the borosilicate cover glass used for the PMTs of conventional IceCube modules, their sensitivity for Cherenkov light below $300\,\mathrm{nm}$ is cut off. Additionally, a low noise rate is essential for low energy studies as the ones going to be conducted with the Upgrade. However, as we are dealing with small photon numbers we also require a high effective area. This could prove a challenge as the PMT dark rate scales with its photosensitive area.

A possible way to solve both of these issues is the concept of the Wavelength-shifting Optical Module (WOM) [6] which is an R&D module to be deployed in the IceCube Upgrade. Its working principle is illustrated in Fig. 4.1. The main component is a cylindrical tube coated with wavelength-shifting (WLS)-paint. UV-photons hitting the tube are absorbed and isotopically re-emitted at longer wavelengths. A fraction of these photons is eventually captured inside the tube by TIR. Due to the WOM's cylindrical symmetry once captured, the photons will remain within the TIR angles while propagating to the ends of the tube with two coupled PMTs for detection.

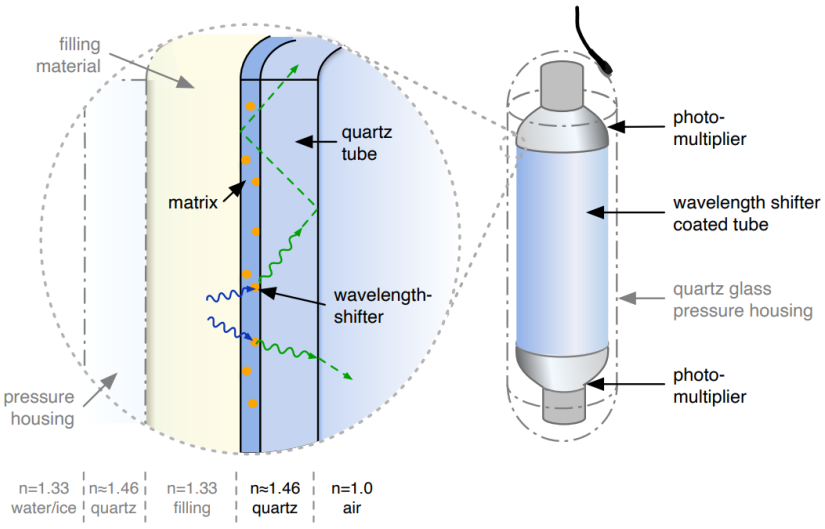

Fig. 4.1.: **Working principle of the WOM [6].** UV-photons are shifted, captured and propagated to the ends of the tube for detection.

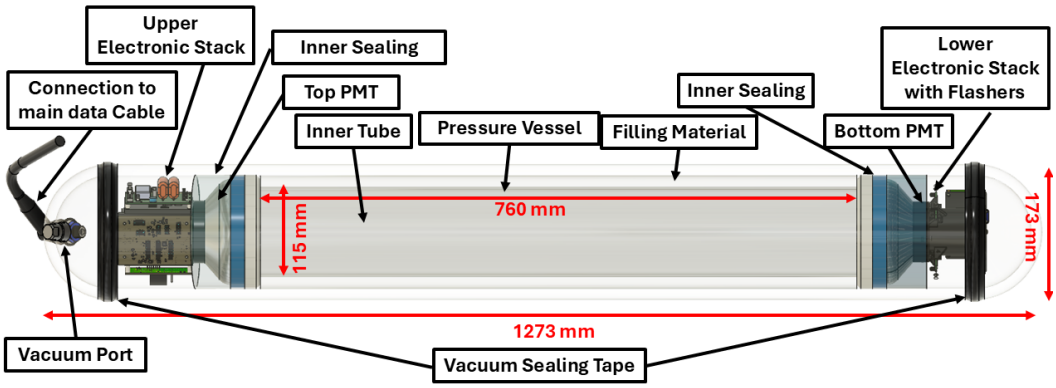

Fig. 4.2.: **CAD model of the full Upgrade WOM module.** The Harness is not shown to highlight the components inside the pressure vessel. See Fig. 4.13 for a picture with included Harness.

This design makes the module sensitive to wavelengths in the deep UV-region as the wavelength acceptance depends only on the absorption spectrum of the WLS-paint and not on the acceptance of the PMTs. Further, the WOM decouples the photosensitive area, represented by the outer surface of the WLS tube, from the area of the PMTs. By increasing the tube length it is possible to increase the photosensitive area, while the noise rate is dominated by the unaltered size of the photocathode. This allows for an increase in the signal-to-noise ratio for the WOM module compared to bare PMTs[1] resulting in a high Signal-to-Noise Ratio (SNR).

To operate the WOM under the harsh conditions at the South Pole and integrate it properly into the IceCube infrastructure many different things needs to be considered resulting in a much more complex overall design (see Fig. 4.2). To withstand high pressures of up to $700\,\mathrm{bar}$ the optical components have to be located inside a thick pressure vessel. To optimize the number of photons reaching the WLS-tube we introduce a filling material maximizing the transmission efficiency. The built-in electronics supply the module with power and allow for autonomous data readout. Finally, the WOM needs to be properly mounted to the string to survive deployment procedure without risking being damaged or destroyed.

A total of 10 WOMs will be deployed in the IceCube Upgrade with 5 of them already completed and shipped to the South Pole. This chapter will introduce the design and functionality of the single WOM components in the context of the IceCube Upgrade.

[1] Naturally, there are limitations of how much you can increase the size of the tube while remaining PMTs of the same size as there are attenuation losses and limitations in the size of IceCube modules. See Chapter 5 for more details on it.

4.1 Optical Design

This section will focus on the optical components of the WOM, which includes the WLS-tube and paint, the PMTs as well as the transmission layers consisting of the pressure vessel and the filling material.

4.1.1 Wavelength-shifting Tube

The inner WLS-tube (further referred to as "inner tube") is made out of the quartz glass material HSQ300 [67]. Quartz is known to have high a temperature resistance and high transmission for optical and UV-photons. The specific HSQ300 glass stands out by being especially chemically pure resulting in low radioactive noise making it a fitting component for a low-noise module such as the WOM. The inner tube has a length of $760\,\mathrm{mm}$, an outer diameter of $115\,\mathrm{mm}$ and a wall thickness of $2.5\,\mathrm{mm}$. These values were optimized in terms of effective area and cost-efficiency (see Chapter 5 for more details).

The WLS-paint layer applied on the tube needs to fulfill several requirements for optimal performance of the WOM [6]:

- Maximum overlap between emission spectrum and the high quantum efficiency regime of the PMT.
- Minimal overlap in the absorption and emission spectrum to prevent losses due to self absorption (see Section 4.5.3).
- Transparency to light within the emission spectrum to reduce light losses during propagation to the PMTs.
- Similar refractive index as the inner tube (1.46) to reduce Fresnel losses.
- Good adhesion to the tube.
- Optical thickness reaching a flat absorption spectrum with close to 100% absorption efficiency.

To satisfy these requirements we use a WLS mixture of PolyEthylMethylAcrylate (PEMA) [68] with the two solved WLS Bis-MSB ($1.3\,\mathrm{g\,kg^{-1}}$) [69] and p-Terpehnyl ($2.6\,\mathrm{g\,kg^{-1}}$) [70]. These two wavelength shifters complement each other well: the emission spectrum of p-Terphenyl overlaps particularly well with the absorption range of Bis-MSB between $300\,\mathrm{nm}$ and $400\,\mathrm{nm}$ [71]. This combination results in an effective absorption spectrum that extends into the deep UV, down to $250\,\mathrm{nm}$

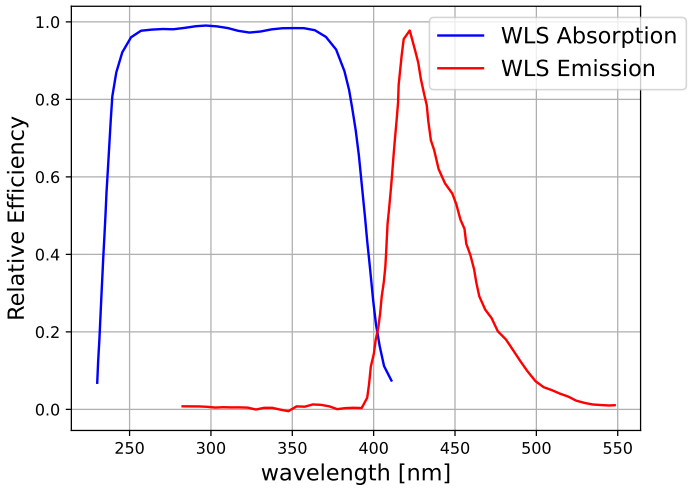

Fig. 4.3.: **Absorption and emission spectrum of the WLS-paint.** It was determined by a measurement using a coated quartz slide. See [72, 73] for more details on the measurement.

and below, while the emission always corresponds to the characteristic spectrum of Bis-MSB—independent of the wavelength of the initially absorbed photon (see Fig. 4.3). First, a liquid paint mixture is produced by solving these components in Toluene. The liquid paint is then applied onto the inner tube, where the Toluene evaporates at room temperature creating a PEMA matrix.

As the absorption drops down to 0 over most of the emission's spectrum wavelength range the paint is highly transparent to shifted light. However, there is a small overlap of the absorption and emission spectrum at $400\,\mathrm{nm}$. It results in the possibility of photons being shifted multiple times as the wavelength of the emitted photon could still remain within the absorption spectrum effectively cutting off re-emitted photons of certain wavelengths. As emission of shifted light happens isotropic, a shifted photon could be scattered out of the tube by not fulfilling the TIR condition after a second shift resulting in an efficiency loss. More details on this process, referred to as **self-absorption** can be found in [74].

The inner tube is **dip-coated** on the outside using the setup shown in Fig. 4.4. The tube is plugged from both sides to prevent the paint from getting inside the tube. Then it is immersed inside the paint vessel vertically and pulled out at a constant speed using a motor to ensure a homogeneous paint layer. The toluene of the paint sticking to the tube evaporates over several days eventually creating a thin layer of

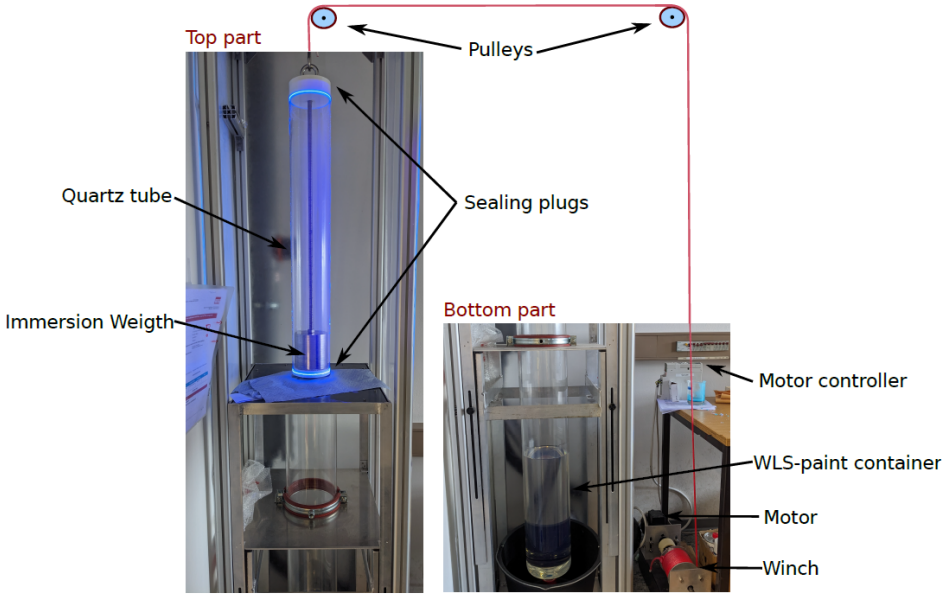

Fig. 4.4.: WOM dip-coating setup [71]. The tube is vertically emerged inside the paint and then pulled out at a constant speed. The outer paint layer then dries by the evaporation of toluene at room temperature.

plastic on top of the glass[2]. More details on the coating procedure can be found in [71].

The paint layer thickness can be adjusted by varying the speed under which the tube is pulled out of the paint vessel (further referred to as **coating speed**). This correlation can be modeled by the **Derjaguin-Model** [73, 75]:

$$d_0 = 0.8 \cdot \sqrt{\frac{\eta U_0}{\rho g}}. \tag{4.1}$$

d_0 is the paint layer thickness, η and ρ are the viscosity and density of the liquid paint respectively and U_0 is the coating speed. This model could be successfully verified for our specific coating setup (see Fig. 4.5). More details on the study can be found in [73].

The currently used coating speed for the WOM-tubes is $2.9\,\mathrm{mm\,s^{-1}}$ resulting in paint layers between $15\,\mu\mathrm{m}$ and $21\,\mu\mathrm{m}$. This is motivated by considering different aspects such as efficiency and handling further explained in Section 8.2.

[2]Considering this procedure and the compositions of the paint illustrates another advantage of using glass tubes instead of plastic ones like PolyMethylMethAcrylate (PMMA). As the paint does not damage or deform the glass the paint can be washed off and the tube could be reused. Using a PMMA tube would result in the paint merging into the tube as the plastic is partly dissolved as it comes into contact with toluene.

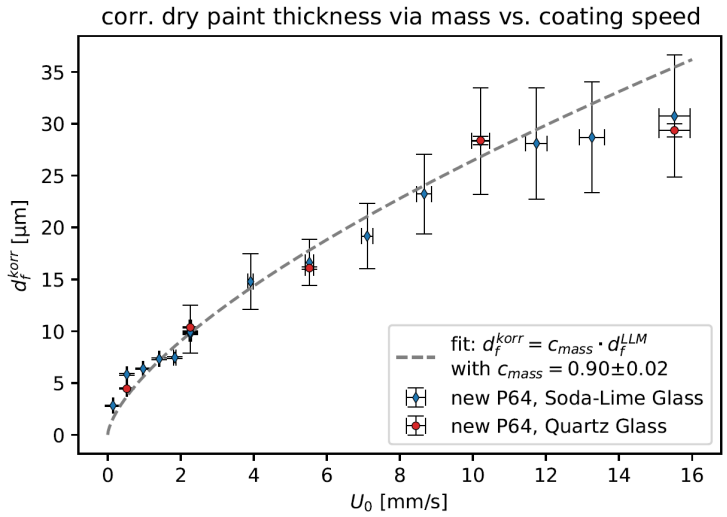

Fig. 4.5.: Paint layer thickness measurement with fit to coating model [73]. The measurement was done with glass slides coated at different speeds. The "true" value for thickness was derived from the mass difference before and after coating.

4.1.2 PMTs

Once the shifted photons reach the ends of the tube they need to be coupled into the PMTs. Best coupling is achieved by using flat PMTs considering a flat tube end surface. Using round PMTs would require shaping the tube accordingly. For good coupling this work would need to be performed very precisely which lead to limited success in the past [76]. Further, the processing of quartz could prove difficult and in turn risk damage or destruction of the tube in the process. So using flat, head-on PMTs is the logical choice here. These PMTs need to have an area large enough to cover the whole area of the tube's end surfaces. A previous idea was the use of an Adiabatic Light Guide (ALG) mounted at the tube's ends which effectively reduces the diameter of the tube. Like this, one would be able to use smaller PMTs which would additionally reduce the WOM's dark rate. However, simulation studies showed that using an ALG would significantly reduce the efficiency due to photons loosing their forward direction after entering the ALG therefore being back reflected and eventually absorbed [77, 78].

That leaves a very limited choice of possible PMTs resulting in choosing the **ET9390B Series** [79] as the WOM's PMTs. They have a photosensitive area of $115\,\mathrm{mm}$ and an overall front surface area of $130\,\mathrm{mm}$, which is larger than the inner tube while still fitting into the pressure vessel. Its spectral response in the wavelength range between $300\,\mathrm{nm}$ and $630\,\mathrm{nm}$ is overlapping well with the emission spectrum of the WLS-paint (see Fig. 4.6).

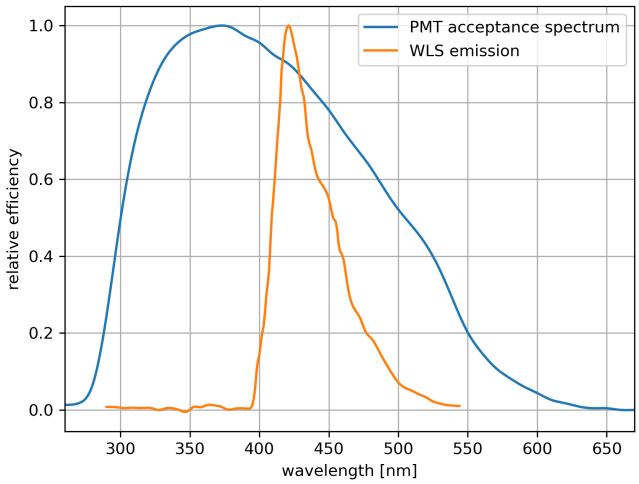

Fig. 4.6.: Acceptance curve of ET9390B PMTs compared to WLS-emission spectrum. As the WLS-emission spectrum is completely enclosed we do not expect certain wavelengths to be cut off due to PMT acceptance.

An alternative PMT originally considered for the WOM was the **Hamamatsu R877** [80] as it has the same front surface area. The ET PMTs were preferred, because of their larger sensitive area and the ability to reach the required gain of 10^7, which is required to reach a satisfying sensitivity for faint light signatures.

4.1.3 Pressure Vessel

Before hitting the inner tube and being shifted the photons need to be transmitted through the pressure vessel and the filling material. Just as the inner tube, the pressure vessel needs to be transparent for UV-photons so quartz glass was chosen for it. Specifically, we use the glass type *Heraeus HLQ 210* [81]. It shows a high transmission efficiency for deep UV-photons close to 100% and a low noise rate due to radioactivity which was measured to be $6\,\mathrm{Hz\,kg^{-1}}$ [6]. Besides the optical transparency another requirement for the pressure vessel is to withstand an outer pressure of up to $700\,\mathrm{bar}$ which is expected deep inside the ice.

The pressure vessel consists of three parts. The cylindrical center piece has an outer diameter of $173\,\mathrm{mm}$, a wall thickness of $14\,\mathrm{mm}$ and a length of $1100\,\mathrm{mm}$. The two endcaps are half-spheres with the same diameter and wall thickness. Both endcaps have vacuum ports mounted to them, used to evacuate the module. The top endcap has an additional hole for the cable feedthrough. A Penetrator Cable Assembly (PCA) is used to connect the electronics inside the module to the main

IceCube data cable. The overall weight of the pressure vessel is $20\,\mathrm{kg}$ resulting in a considerable low noise contribution of $120\,\mathrm{Hz}$.

4.1.4 Filling Material

The filling material is located between the pressure vessel and the inner tube. It is used to minimize the Fresnel losses for transmitted UV-light. For optimal transmission it needs to have a refractive index of about 1.3 and high UV-transparency. Further, it needs to be chemically inert to not dissolve the WLS-paint it touches directly as well as being insulating in order to not damage the electronics in case of a leakage. Additionally, it needs to be resistant to low in-ice temperatures down to $-40\,^{\circ}\mathrm{C}$.

A very suitable filling material is Perfluoropolyether (PFPE) [82]. It is a liquid over all relevant temperature ranges with a refractive index of 1.3[3]. Further it is chemically inert, insulating and has a transmission efficiency of almost 100% in the deep UV-region above $300\,\mathrm{nm}$. Combining it with the vessel transmission considering the given layer thicknesses we get a transmission efficiency as shown in Fig. 4.7. It is at almost 100% for $\lambda > 300\,\mathrm{nm}$, but falls down for lower UV-wavelengths.

The PFPE is filled in the central compartment on a height of $760\,\mathrm{mm}$ between pressure vessel and inner tube resulting in a filling volume of $\sim 4.66\,\mathrm{L}$. Considering its thermal expansion coefficient of $0.0011\,^{\circ}\mathrm{C}^{-1}$ [82] one would need to fill $4.97\,\mathrm{L}$ of PFPE at room temperature inside for the WOM to be completely filled at $-40\,^{\circ}\mathrm{C}$ in the ice. The PFPE compartment is sealed off from the rest of the WOM to prevent leakage in other parts of the module (see Section 4.4.1).

4.2 Electronics

The WOM electronics consists of different custom made boards used for supplying the PMTs with high voltage, reading out the data, communication and timing as well as devices for calibration purposes. The electronic design needs to fulfill certain requirements to be integrated properly into IceCube's infrastructure. An overview over all boards and their interconnectivity is shown in Fig. 4.8. The functionality of every board will be explained in this section.

[3] A detailed study of the optimal refractive index can be found in Chapter 7.

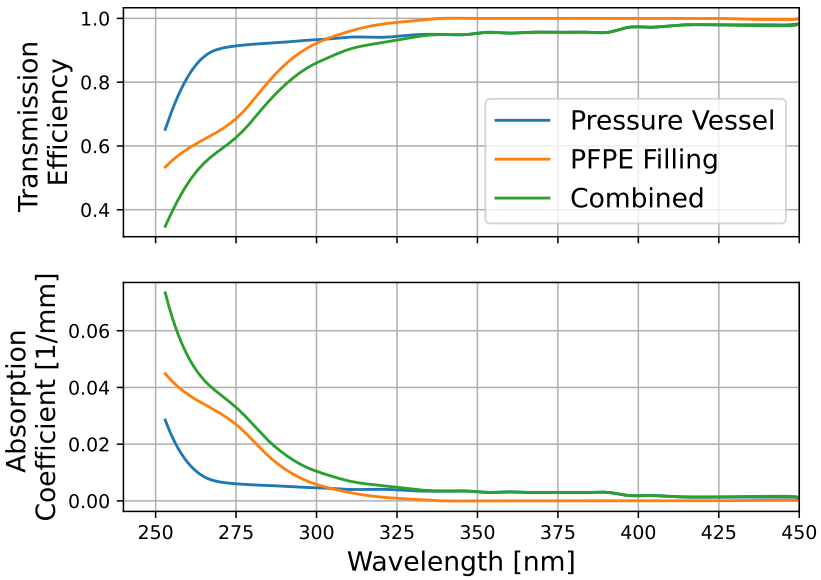

Fig. 4.7.: **Transmission efficiency through $14\,\mathrm{mm}$ thick pressure vessel and $15\,\mathrm{mm}$ thick PFPE filling and corresponding absorption coefficients (data from [81, 83]).** Data is scaled to the given layer thicknesses assuming vertical transmission of light. The calculated absorption coefficients μ_{abs} are independent on layer thickness. Additional efficiency factors as Fresnel losses or photons missing the next layer are not considered and will be discussed in Chapter 7.

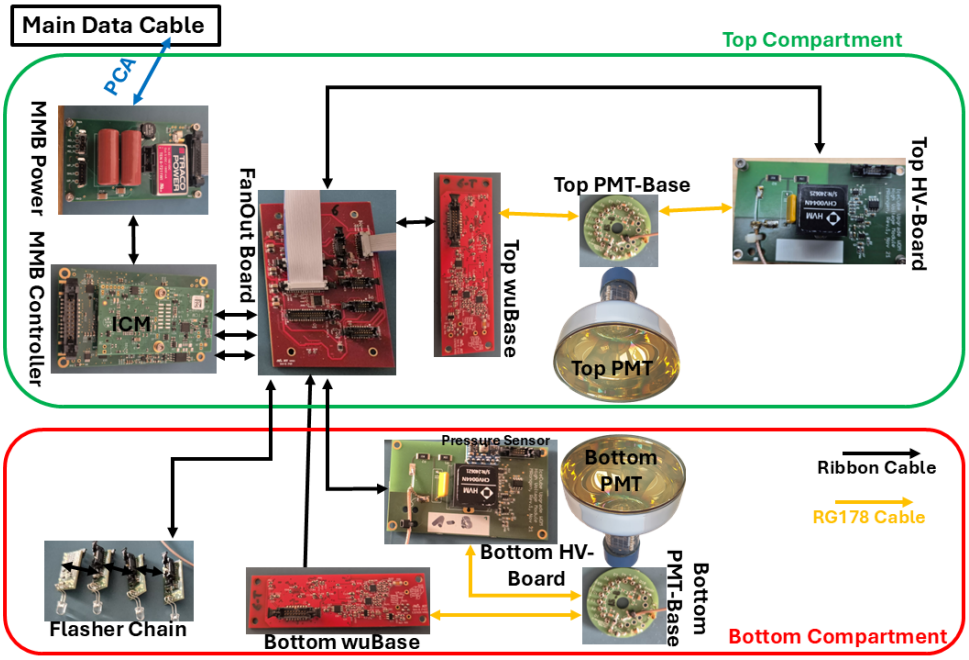

Fig. 4.8.: **Schematic of the WOM's electronic arrangement and cabling.** Every arrow represents a cable connection. Mostly, ribbon cables are used with the exception of the HV-board's and the wuBase's connection to the PMT-Base which is done by a RG176 coax cable.

The **Mini-Mainboard (MMB)** [84] is the central controller unit of the module. It splits into the power and the controller board. The power board handles electrical interference with the data cable, sets a hardware address for the modules and supplies the controller board and further connected peripherals with power. It connects directly to the main data cable via the PCA. The controller board contains an STM32H7 [85] Micro Controller Unit (MCU) for command and data handling as well as the Ice Comms Module (ICM) [86] for power distribution, timing, synchronization and communication with the surface. It is equipped with a Xilinx Field Programmable Gate Array (FPGA) Spartan-7 [87] which transmits signals received from the surface and processes them to the corresponding components. Further, several sensors are installed on the MMB to monitor the external environment. These contain pressure and temperature sensors as well as a magnetometer and an accelerometer which gives information on the tilt of the module. Both the MCU and ICM can be programmed with a firmware and updated remotely which provides an infrastructure for communication between the different boards in the module.

The MMB is connected to the **FanOut Board**. It functions as a hub for all remaining boards subdividing the signal from the MMB and generating the flasher pulses. It is closely modeled to the LOM FanOut [88] and provides connection to the two wuBases, HV-boards and flashers. As not all triggered signals are directly sent to the surface the board features the possibility of buffering data in flash memory of two SD-Cards (also referred to as *hitspool*). The board can receive software commands like turning certain boards on and off by supplying them with power.

The WOM **wuBase** acts as the readout system for the PMT pulses and was modelled based on the LOM wuBase [89, 90]. Contrary to the LOM version, which combines the functionality of HV-supply and readout, only the readout part is used for the WOM. The wuBase is equipped with a MCU and FPGA for triggering and low level waveform processing. An incoming PMT pulse entering the wuBase is first amplified and shaped using a low-pass filter and then digitized using a 12-bit Analog-to-Digital Converter (ADC) at $60\,\mathrm{MHz}$. The use of delay modules in the FPGA records allow a trigger timestamps precision of down to $1\,\mathrm{ns}$. An example of digitized waveforms is shown in Fig. 4.9. Further, the WOM wuBase is also used to control the HV of the PMTs.

The HV for the PMTs is generated on the **High Voltage (HV)-board** which uses a HVM SMHV0520N DC-DC converter [91] similar to other Upgrade modules. It generates voltages between 0 and $2000\,\mathrm{V}$ and an electric current up to $500\,\mu\mathrm{V}$ which is transmitted to the PMT-Base via a soldered RG178 coax cable. The HV can be set using a 12-bit Digital-to-Analog Converter (DAC) which is operated over

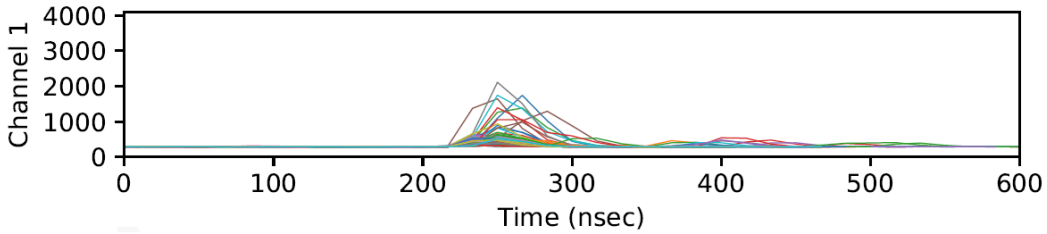

Fig. 4.9.: **PMT waveforms digitized by the WOM wuBase.** Amplitude in ADC Counts. The waveforms get wider due to shaping. The LOM features an additional **low-gain** channel (Channel 2) which is not used for the WOM.

the wuBase[4]. It is also possible to set a limit for the maximum received current. Exceeding this set value would result in the PMT's HV dropping down to protect the PMTs from being damaged due to exorbitant light exposure. The bottom HV-board is additionally equipped with an MPRLS Pressure Sensor [92] which provides pressure monitoring in the bottom compartment (see Section 4.4.2 for more information on the pressure inside the WOM).

The PMT HV Divider, or **PMT-Base** divides the HV received from the HV-board between all dynodes of the PMT. It is custom modeled based on the schematic of the C647 divider [@93] from ET-Enterprises. The signal output is connected to the wuBase using a RG178 signal cable. To prevent creepage current capacitors are covered in epoxy resin.

To calibrate ice properties a chain of four **LED Flashers** [94] is installed in the bottom compartment pointing radially outwards with $90°$ angles between them. Three of the flashers use $365\,\mathrm{nm}$ LEDs unique to the WOM to characterize the ice for wavelengths the WOM is sensitive to. The 4th flasher has a $395\,\mathrm{nm}$ LED which is also used for the flashers of other optical modules. For the Upgrade, a **WOM subarray** is planned which will have 5 WOMs close by. There, a flash originating from one WOM could be detected by another WOM giving more insight on ice properties. The flashers have adjustable brightness by varying the bias voltage using a 16-bit DAC and an underlying absolute calibration between bias voltage and the number of emitted photons.

The electronic boards are mounted on 3D printed plastic holding structures (see Fig. 4.10). The holders feature a two part construction having an inner cylinder molded into the sealing (see Section 4.4.1) and an outer part containing the boards which can be freely mounted and unmounted afterwards. To connect the top and

[4]This way of operation results from using the same software infrastructure as the LOM which uses a combined wuBase with HV-supply and readout.

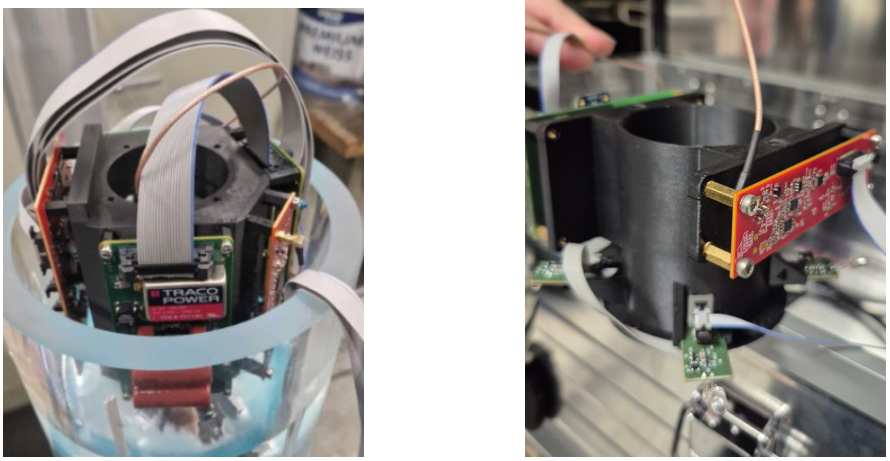

(a) Top compartment. (b) Bottom compartment.

Fig. 4.10.: **WOM Electronics mounted in the holder inside the module.** The boards are screwed on a 3D printed plastic structure which is then mounted onto an inner cylinder molded inside the sealing.

bottom compartment three ribbon cables need to be guided along the WLS-tube resulting in a small shadowing effect.

4.3 Software

For lab testing the communication to the module functions over a **mini-FieldHub** [95]. Up to six modules can be connected to it via wire-pairs. The FieldHub is used as a server which communicates with the connected devices via network using the **domnet** software package [@96]. It is used to send basic commands to the ICM or MCU like turning the wire-pair on and off, updating the image of the ICM or enabling or disabling certain interlocks.

For processes which operate directly on the MCU we use **IceBoot** [@97] for lab testing. It controls the hardware through the Hardware Abstraction Layer (HAL) and has a python interface. A version of IceBoot is flashed on the MMB. To determine the type of module we set the corresponding jumper setting on the board beforehand. Once the board is powered up and an **IceBoot Session** is created. IceBoot imports the corresponding python class depending on the jumper settings. This class provides default functions for the MMB as well as module specific functions for operation and testing. The WOM uses mainly functions provided by the LOM-Software.
The MCU of the wuBase can also be flashed with corresponding firmware which provides tools for triggering, HV-control and readout [@98]. For data readout, a

setup script is run, which sets the HVs and turns on the wuBases. Then, the actual datataking script can be run. Due to a limited bandwidth, only datataking with frequencies up to $178\,\mathrm{Hz}$ per wuBase is possible without loosing information.

For the operations of the modules after deployment another software infrastructure called **xDOMApp** [@99] will be used, which will not be discussed here in detail.

4.4 Mechanical Design

This section will explain the different mechanical considerations to keep the WOM mechanically stable and to ensure it survives the harsh conditions during transportation and deployment.

4.4.1 Sealing

The inner tube in combination with the two PMTs glued to both sides (see Section 5.3 for details on the gluing procedure) is referred to as the **inner assembly** which needs to be fixed inside the pressure vessel. This sealing needs to be leaktight from PFPE and withstand possible push and pull forces such as pressure differences throughout the module.

For the sealing, a three-layer design is used, which consists of one layer of foam and two layers of silicone. The first layer of foam is applied to the PMTs before they are glued to the inner tube with a custom designed mold. The two components foam mixture **FlexFoam-iT! V** [100] is poured inside and the volume expands by a factor of 11 forming a several mm thick foam layer around the PMTs (see Fig. 4.11). The elasticity of the foam allows the inner assembly to be easily pushed into the pressure vessel and to keep its position inside as long as there are no external push-pull forces.

However, the foam is not leaktight,so a second sealing layer is required. After the inner assembly is placed inside the pressure vessel – with routed cables connecting the top and bottom compartment – a few cm thick layer of **Mold Star 16 FAST** [101] is poured on top of the foam. It hardens within $30\,\mathrm{min}$ which is fast enough for the silicone to not leak through the foam.

While the Mold Star silicone forms a leak tight layer, its coupling to the glass is not optimal which could result in the sealing getting torn off by enough pushing

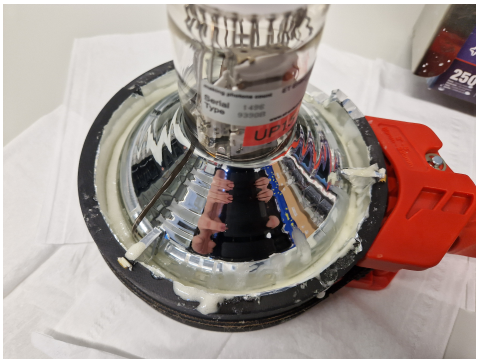

Fig. 4.11.: **PMT foam sealing inside mold.** The foam layer for the top PMT contains a sealed in straw to pour in the PFPE after the inner assembly is sealed in.

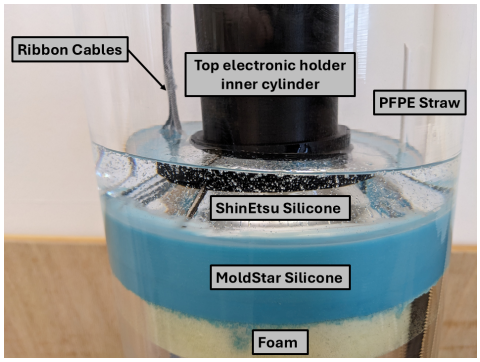

Fig. 4.12.: **Full WOM sealing on top side.** The top side is poured while the module is tilted to one side so the overflowing PFPE can flow back in by itself.

force or vibrations. So a third sealing layer consisting of **ShinEtsu** silicone [102] is poured on top. The ShinEtsu silicone has a low temperature resistance and high coupling to glass. It is mainly used to generate an optical coupling and is used for other optical Upgrade modules such as the mDOM, but for the WOM it is used exclusively for its mechanical properties. Its long hardening time of 3 days would result in the liquid silicone to leak through the foam if applied before the Mold Star silicone.

The final result is shown in Fig. 4.12. The inner part of the electronic holder is also sealed into the ShinEtsu silicone to keep the electronics in place. Further, the top sealing layer is poured under a slope so if PFPE leeaks into the upper compartement, it will flow back gravitationally. This sealing solution was tested for different environmental conditions (see Chapter 9). As it showed several faults in the design will be reworked for the WOMs produced in the future.

4.4.2 Evacuation

The modules deployed in IceCube are evacuated on the inside to prevent the module from opening up during plane transportation, where outer pressures down to $0.6\,\mathrm{bar}$ are expected. Evacuating the module also has the advantage of coupling the endcaps to the center part of the pressure vessel preventing the vessel to break while being exposed to high outer pressure due to weak spots. The sealing was tested to be airtight which isolates the top and middle compartment from the bottom

compartment[5]. To prevent any push-pull forces inside the module resulting from pressure differences between the compartments, the top and bottom compartment are evacuated at the same time to the same pressure. The pressure of evacuation was chosen to be $0.3\,\mathrm{bar}$ which results from different considerations further explained in Section 9.2. To minimize the air humidity inside, which could lead to the damaging of electronics, the module is flushed with nitrogen multiple times in the evacuation process[6].

To prevent air from leaking inside the module the two interface areas between endcaps and center piece are sealed off using **Teroson** sealing tape [103]. The Teroson is additionally protected by several layers of *3M Scotch Rap* [104]. Both tapes are highly resistant against low temperatures and harsh weather conditions. The pressure is required to be kept for at least one year which is the estimated time between production and deployment of the WOMs.

4.4.3 Harness

The Harness acts as the mechanical interface between the module and the string. It is designed to hold the WOM to the steel rope and withstand a safety weight of up to $150\,\mathrm{kg}$ (five times the weight of the WOM to compensate for vibrations and shocks during deployment). The rope itself is rated for a vertical load of $4250\,\mathrm{kg}$ which is five times the load of a full Upgrade string. The Harness also needs to withstand cold temperatures as well as temperature shocks which can occur when the module is dropped into the melted ice. A schematic of the WOM Harness is shown in Fig. 4.13.

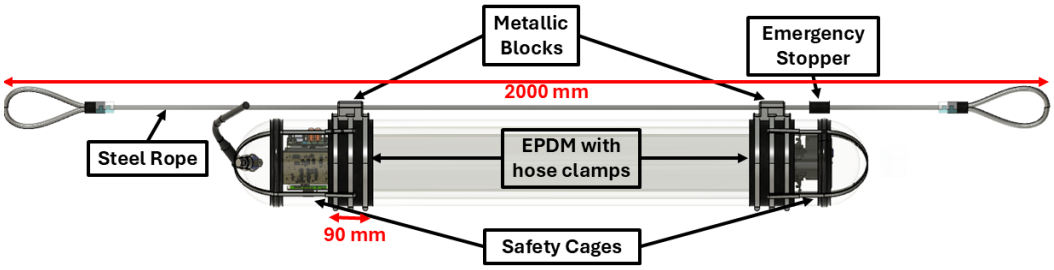

Fig. 4.13.: **Schematic of the WOM with attached Harness.** The layers of EPDM are covering the inner sealing.

[5]The top and middle compartment are connected by the PFPE straw.
[6]The flushing was not preformed for the first batch of WOMs, but will be implemented for the coming modules.

The WOM is encased by $9\,\mathrm{cm}$ wide Ethylene Propylene Diene Monomer (EPDM) rubber at the top and the bottom. EPDM has proven to have a high adhesion to the glass ensuring a proper mechanical coupling. The rubber is placed directly above and below the inner tube to not cover any of the photosensitive area.
Onto each EPDM strip a custom 3-piece metallic block is mounted using three hose clamps each. These blocks have a roughened surface area to couple better to the EPDM. The other part of the blocks contain a feedthrough to hang the module to the $2\,\mathrm{m}$ long steel rope. The top block is tightly fixed to the rope while the bottom block enables the rope to move freely through it.
Below the bottom block, a metallic stopper is mounted to the rope which will stop the WOM from sliding further down the rope in case the top block does not clamp to the rope properly. If the blocks slide down the EPDM, the WOM will be caught by metallic safety cages on the top and bottom which are fixed to one of the hose clamps and tightly coupled to the pressure vessel.

This harness design was tested to withstand the required load, low temperatures and temperature changes as well as $700\,\mathrm{bar}$ overpressure. Technical details on the Harness can be found in [105].

4.5 Optical Modeling

Several frameworks and models were developed to describe and study different optical properties of the WOM such as timing and efficiency. In this section, different simulation tools and analytical models will be introduced.

4.5.1 Simulation Tools

The propagation of photons through the WLS-tube needs to be properly modeled to calculate its efficiency and being able to optimize certain parameters.
One of these simulation tools is **WOMRaT** [77], a customized Ray Tracing simulation in C++ using CUDA GPUs. It implements the geometry of a cylinder with elliptic surfaces. Light is emitted vertically onto the tube. Upon hitting the tube the light is absorbed and isotropic re-emitted with 100% efficiency. Each light ray is traced until the next interface area (between tube and outside), where its reflection or refraction is calculated (depending on its angle relative to the surface area). Further, absorption and scattering are implemented into the simulation and these criteria are also checked for each photon. This loop is repeated until the photon is

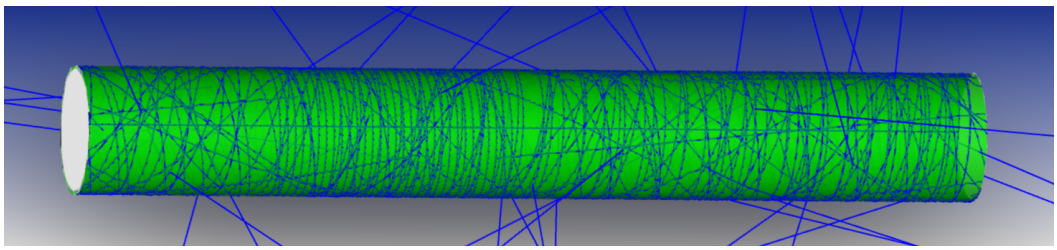

Fig. 4.14.: **Visualization of propagated photons through the inner WOM tube using Zemax.** One can see captured rays as well as rays which are scattered out of the tube.

either scattered out, absorbed or until it reaches the end of the tube and is hereby *terminated*. This results in a distribution of xyz-coordinates and spherical angles of all photons as well as the propagated distance. As the propagation of every photon happens independently, this algorithm can be parallelized on GPUs to simulate millions of photons within a few seconds.
For an easier usability the python wrapper **Adiabatic Light Guide Optimizer (ALGO)** [78] was implemented which will be used preferably in this thesis. It provides a practical way of running the simulation multiple times for certain optimization or timing studies (see Chapter 6).

Additionally, the commercial light simulation software **Zemax OpticStudio** [@106] is used in this thesis. Compared to ALGO this software provides much more flexibility in the implemented geometry. One can define a light source and a light detector of arbitrary shapes as well as any number of bodies for light transition made out of different materials. Besides simulating the propagation through the inner tube, Zemax can be also used to simulate the transmission through the vessel as well as to implement the wavelength-shifting process and light of different wavelengths. Further, Zemax provides a built-in visualization of the propagated rays which provides insight into different, less-obvious effects (see Fig. 4.14). However, the flexibility of Zemax comes with a significantly increased computation time with several minutes for 10000 photons compared to a few seconds for 10^6 photons with ALGO. That makes statistics limited.

4.5.2 Flattened Efficiency Model

The efficiency of the inner WLS tube can be approximated analytically by the **flattened model** [16]. The hollow cylinder is approximated as a "flattened out" cuboid neglecting its curvature (see Fig. 4.15). The width equals the tube circumference U and the height corresponds to the tube's wall thickness b. We look at a photon

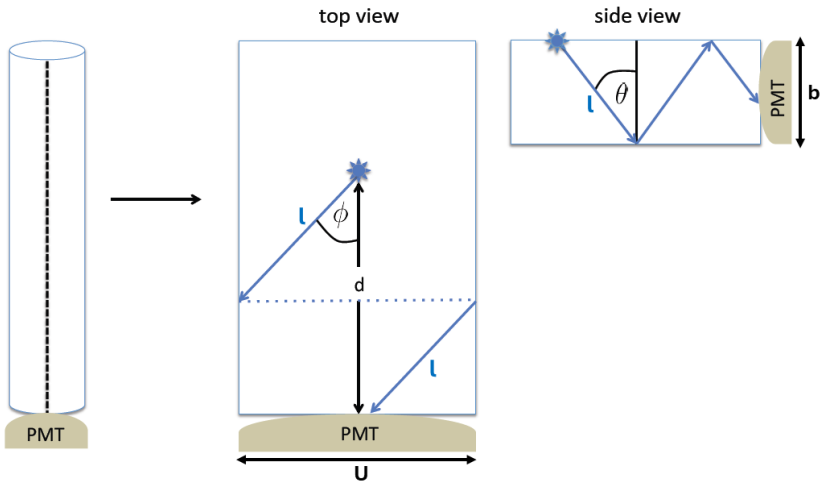

Fig. 4.15.: **Photon propagation through flattened out WOM tube [16].** The photon trajectory can be described by the two angles θ and ϕ. In the top view, the photon propagates in a straight line while being reflected in the side view while conserving the angle θ.

originating at a distance d from the PMT with θ being the forwarding angle and ϕ as the polar angle.

From geometrical considerations we get for the traveled photon distance l:

$$l = \frac{d}{\cos(\theta)\cos(\phi)}. \tag{4.2}$$

Using the Beer-Lambert-Law we can determine the angular dependent efficiency ϵ given the attenuation length λ_{att}:

$$\epsilon(d,\theta,\phi) = \exp\left(-l/\lambda_{att}\right) = \exp\left(-\frac{d}{\lambda_{att}\cos(\theta)\cos\phi}\right). \tag{4.3}$$

To get the overall distant dependent efficiency, we integrate this expression over all possible angles θ, ϕ. The range the θ is limited to the photon staying within the TIR angle θ_C

$$\epsilon(d) = \frac{1}{4\pi}\int_{-\theta_C}^{\theta_C}\int_{-\pi/2}^{\pi/2}\exp\left(-\frac{d}{\lambda_{att}\cos(\theta)\cos(\phi)}\right)\cos(\theta)d\phi d\theta. \tag{4.4}$$

Due to cylindrical symmetry the efficiency does not depend on the the azimuthal injection angle.

The flattened model was verified using WOMRaT (and ALGO) for tubes of different sizes (see Fig. 4.16) [77]. While the model captures all photons within the TIR angle it does not consider for photons being emitted close to the tube's end

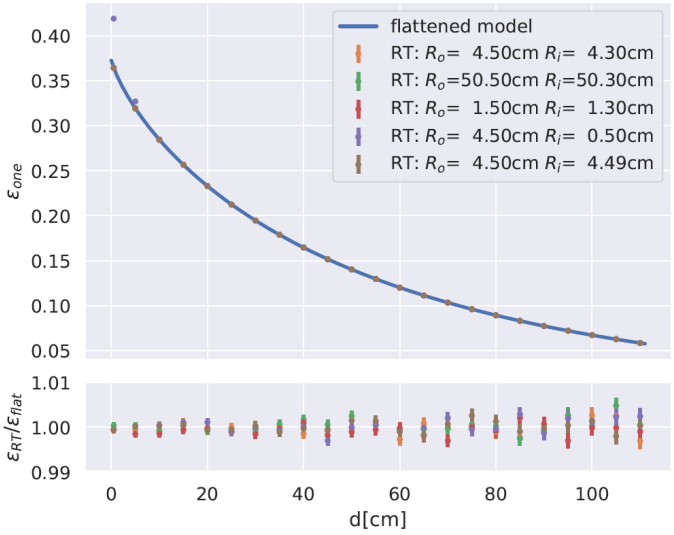

Fig. 4.16.: Comparison between flattened model and WOMRaT simulation [77]. The comparison for tubes of different inner and outer radii R_o, R_i shows a deviation <0.01% verifying our analytical model.

hitting the PMT even through $\theta < \theta_C$ (direct hits). Similarly, the possibility of an non-captured photon which is scattered towards the PMT is not considered. These effects have proven to be small and only relevant for small $d < 10\,\text{cm}$. Therefore we can conclude that the used approximation is of sufficient precision for the given tube parameters.

4.5.3 Self-Absorption Model

The flattened model and the simulation both do not distinguish between the tube and paint layer as both are modeled as bulk with one refractive index and attenuation length. Therefore, they are not able to model systematics related to the paint exclusively, one of them being the **self-absorption** of the paint [74]. As we notice from Fig. 4.3 we have a small overlap between its absorption and emission spectrum around $400\,\text{nm}$. This leads to some shifted photons being absorbed again to be shifted to even higher wavelengths. This effect can be observed in Fig. 4.17 which shows the emission spectrum being cut off more with increasing distance. Therefore, one would get a decreased efficiency for distances close to the tube's end.

An analytical modeling of the self-absorption expands the flattened model by introducing a wavelength dependency to the efficiency $\epsilon(d, \theta, \phi, \lambda)$ of each propagated photon which is changing depending on the traveled distance. The details on the

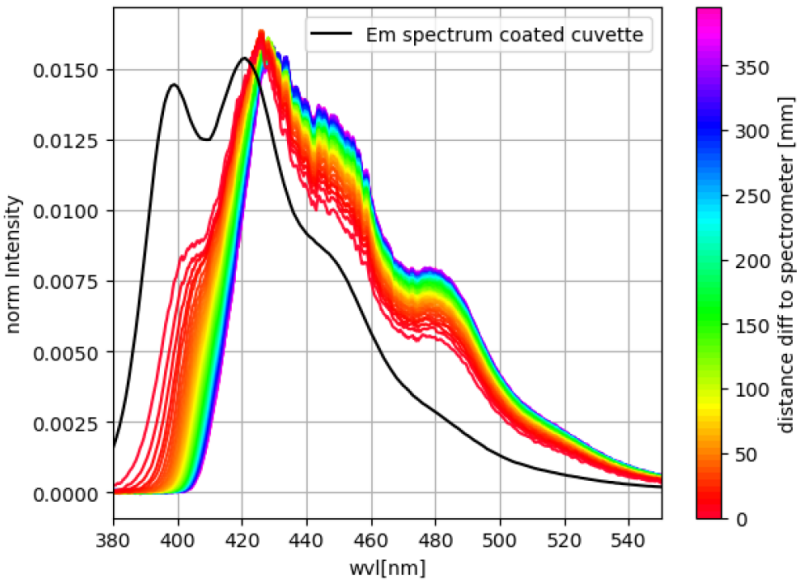

Fig. 4.17.: **Change of WLS paint emission spectrum for different distances [74].** The emission spectrum of the WLS paint is shown in black. The spectrum was read out by a spectrometer at the end of a coated rod. We notice the spectrum being cut off with increasing distances below $100\,\mathrm{mm}$.

analytical derivation and work on simulating this systematic can be found in [74, 107].

Comparing the self-absorption modeling with the flattened model in Fig. 4.18 outlines better fitting results for the self-absorption model for small distances. There is ongoing work to implement the self-absorption into the ALGO simulation by separating the tube and paint layer to have a fast and more complete framework for simulating the WOM.

4.5.4 Flattened Timing Model

Similar to the flattened efficiency model we can describe the timing of the tube by the **flattened timing model** [108]. Again, we "flatten" the tube to a cuboid which height equals the tube's wall thickness (see Fig. 4.19). We simplify photons getting total internally reflected on the outer side as photons propagating in a straight line in the cuboid[7].

[7]This is reasonable approximation, if the tube's radius is much larger compared to the curvature.

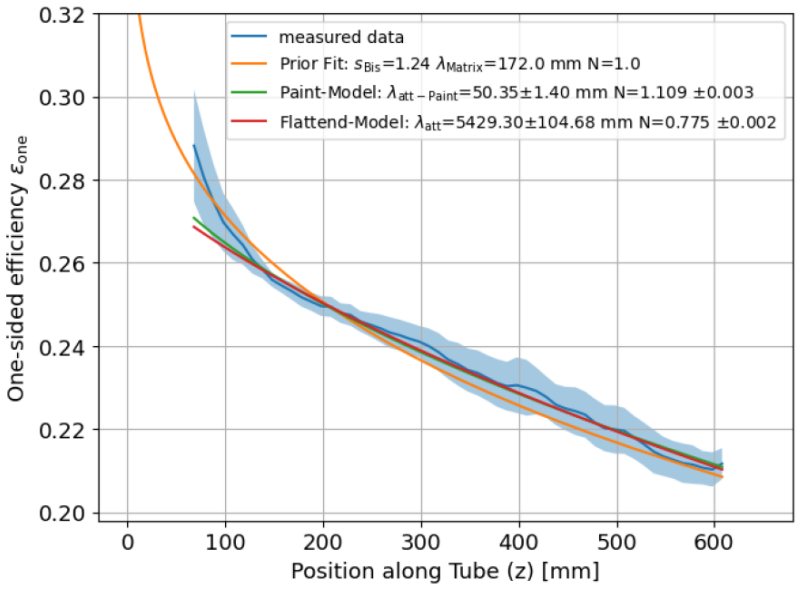

Fig. 4.18.: **Fitting the flattened model and self-absorption model to an efficiency measurement of a coated tube [74].** We notice that the self-absorption model (orange) fits much better to the efficiency at small distances compared to the flattened model (red). However, we need to consider the large error bars on the measured values.

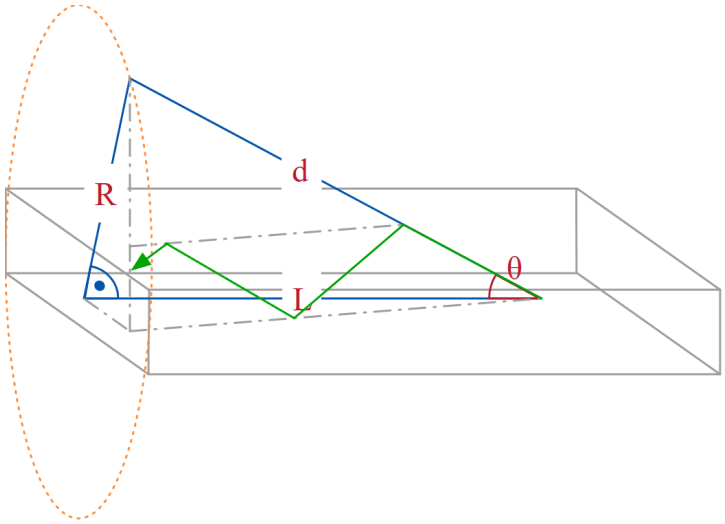

Fig. 4.19.: **Photon propagation in the flattened timing model[108].** The tube is rolled out to a cuboid and photons originally reflected by TIR go in straight lines.

We consider a photon at a horizontal distance L from the tube's end traveling a total distance d at an angle θ relative to the surface. From Fig. 4.19 we can see that

$$\begin{aligned} d^2 = R^2 + L^2 = L^2 \cdot (\tan^2\theta + 1) \\ \iff \theta = \arctan\left(\sqrt{\frac{d^2}{L^2} - 1}\right). \end{aligned} \tag{4.5}$$

The photons are emitted isotopically by the WLS paint located on the outer side of the tube. Therefore, we use angular distribution for isotropic emission from one half-hemishere

$$P(\theta) = \sin\theta \tag{4.6}$$

which is normalized to 1. We get the distance dependent distribution by applying the substitution

$$\begin{aligned} &\int_0^{\pi/2} P(\theta)\,\mathrm{d}\theta = \int_0^{\infty} P(\theta(d))\frac{\mathrm{d}\theta}{\mathrm{d}d}\,\mathrm{d}d \\ \text{with} \quad &\frac{\mathrm{d}\theta}{\mathrm{d}d} = \frac{L}{d\cdot\sqrt{d^2 - L^2}}. \end{aligned} \tag{4.7}$$

Combining everything and simplifying we get following expression for the distant dependent probability distribution:

$$\begin{aligned} P(d) = P(\theta(d)) \cdot \frac{\mathrm{d}\theta}{\mathrm{d}d} &= \sin\left(\arctan\left(\sqrt{\frac{d^2}{L^2} - 1}\right)\right) \cdot \frac{L}{d\cdot\sqrt{d^2 - L^2}} \\ &= \frac{\boldsymbol{L}}{\boldsymbol{d^2}}, \quad \text{for} \quad d \geq L \end{aligned} \tag{4.8}$$

As L is the shortest distance between emission point and the tube's end $P(d) = 0$ for $d \leq L$. To consider the attenuation inside the glass we need to add an exponential term according to Eq. 2.3 resulting in a probability distribution of:

$$P(d) = \begin{cases} \frac{L\cdot e^{-\frac{d}{\lambda_{att}}}}{d^2} & d \geq L \\ 0 & d < L \end{cases} \tag{4.9}$$

The model can be partly verified by comparing it to simulation results from ALGO for different injections points (see Fig. 4.20). We notice a good agreement at the start before the simulation's distribution drops below the model's expectation. As our flattened model simplifies the tube's geometry by not cutting out photons

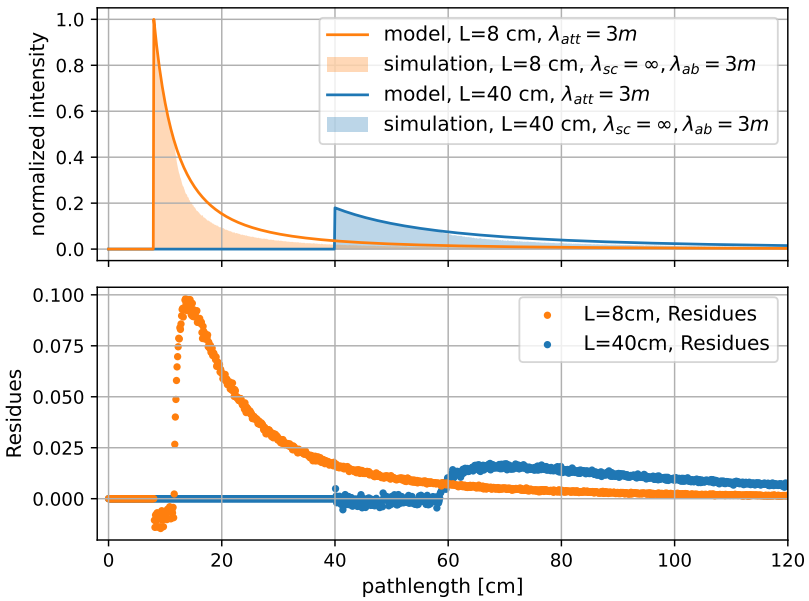

Fig. 4.20.: Comparison between flattened timing model and ALGO simulation. The simulation was run for a quartz tube of outer radius $90\,\mathrm{mm}$ in air. To highlight the simulation to model agreement the distributions were normalized to the maximum for L=$8\,\mathrm{cm}$.

outside the TIR angle we run into a disagreement as soon as totally reflected photons dominate. At the start, most of the detected photons reach the end of the tube without being reflected on the tube first which can be properly described by our analytical model. Photons with longer pathlengths are reflected on the tube's wall before reaching the end. The model assumes photons of all θ angles to be reflected inside the tube resulting in more photons with longer pathlengths reaching the tube's end. Comparing the deviations for different distances L shows that the agreement persists over a longer range of pathlengths for higher L , because small changes in directions result in larger change of total pathlength d while still exiting the tube without being reflected[8]. For a better agreement between simulation and model one would need to filter out all photons with $\theta < \theta_C$.

4.6 Tube Evaluation Testing Stand

To evaluate the absolute efficiency of coated WOM tubes we use the efficiency test stand visualized in Fig. 4.21. The coated tube is coupled between two PMTs with optical gel [109] which are enclosed in mu-shields to shield them from the earth's

[8]Obviously, the absolute number of "direct hits" is larger for small distances.

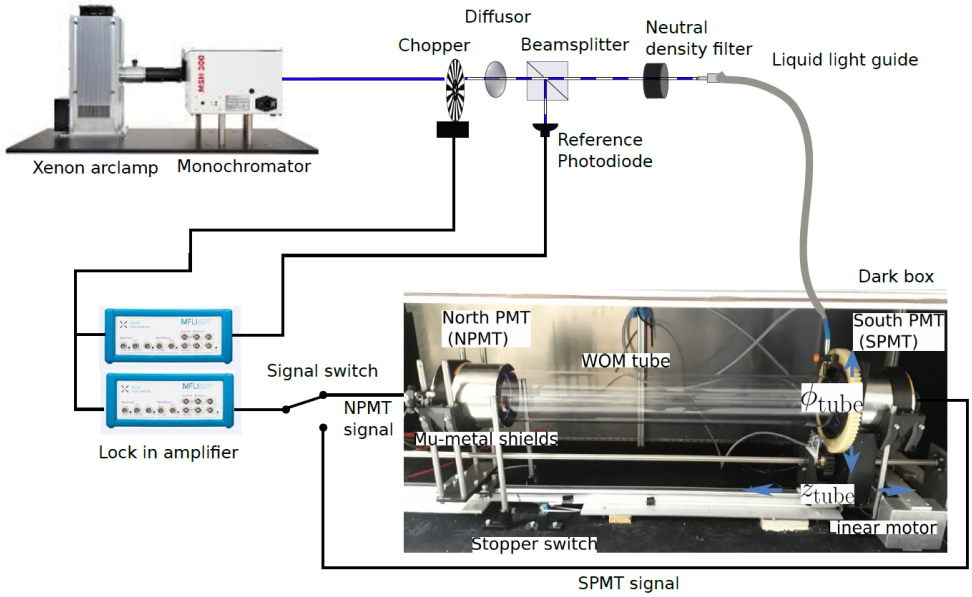

Fig. 4.21.: **Schematic of the WOM tube evaluation test stand [71].** Monochromatic light is injected onto different distances z_{tube} and azimuth angles ϕ_{tube} on the tube which is located inside an aluminum dark box coupled to a PMT from each side. The photocurrent of the PMT and reference photo diode to correct for intensity fluctuation of the light source are read out using lock-in amplifiers.

magnetic field. The light is injected into the tube at different distances to the PMTs z_{tube} and different azimuth angles ϕ_{tube} using a linear and an angular stepper motor. This part of the setup is located inside a closed off aluminum box which functions as a Faraday-cage shielding the PMTs from external electric fields.

The light source is a Xenon arclamp [110] connected to a monochromator [111] set up so the outgoing light has a spectral Full Width at Half Maximum (FWHM) of $1.5\,\text{nm}$. The light then hits a beam splitter which directs parts of it towards a reference photo diode [112]. This diode takes data throughout the whole measurement cycle and is used to correct for intensity fluctuations of the lamp caused by either the increased temperature over time or fluctuations of the supply current. The remaining light is then guided into the dark box onto the tube using a Liquid Light Guide (LLG) [113].

The photodiode and PMT are read out using lock-in amplifiers [114], which perform background subtraction on the signal. This is achieved by placing a chopper behind the monochromator's output and feeding its adjusted frequency into the lock-in amplifiers. The rotating chopper modulates the signal into a square wave, alternating between measuring background + signal and background only. The

lock-in amplifiers use this phase-sensitive detection to isolate the modulated signal and subtract the background, resulting in a clear signal even for inputs with a low SNR. The background-subtracted photocurrent is then used to determine the tube's efficiency.

4.6.1 Determining the absolute Efficiency

The efficiency is the ratio between the ingoing and outgoing signal. The amplitude of the outgoing signal is determined by the ratio between the PMT's intensity I_{sig} and the intensity measured by the reference photo diode I_{ref}. This correction leads to eliminating the time dependence of the light source

$$A_{sig}(\lambda, z_{tube}, \phi_{tube}) = \frac{I_{sig}(t, \lambda, z_{tube}, \phi_{tube})}{I_{ref}(t, \lambda)}. \tag{4.10}$$

The amplitude of the ingoing signal, $A_{ref}(\lambda)$, is measured by illuminating the PMT directly at its center while leaving the rest of the setup unchanged. As we are only interested in the tube's efficiency all other influence is eliminated by correcting the tube measurement with this reference measurement. A_{ref} is determined in the same manner as A_{sig}.
From this, we can calculate the efficiency of the tube as measured by the lock-in amplifiers

$$\epsilon_{lock-in}(\lambda, z_{tube}, \phi_{tube}) = \frac{A_{sig}(\lambda, z_{tube}, \phi_{tube})}{A_{ref}(\lambda)}. \tag{4.11}$$

However, there are two corrections to be performed on this quantity:

- The PMT is illuminated at its center in the reference measurement which is not where the tube is coupled to. This is corrected by a surface corrections factor S_{surf} determined by performing a surface sensitivity scan on the PMT (see Section 5.1.2).

- In the tube measurement, the PMT sees the WLS paint's emission spectrum contrary to the single wavelength in the reference measurement. This is corrected by $S_{wvl}(\lambda)$ using the PMT's acceptance spectrum $S_{\text{PMT}}(\lambda)$ weighted with the emission spectrum of the paint $w_{em}(\lambda)$

$$S_{wvl}(\lambda) = \frac{\frac{1}{300\,\text{nm}} \int_{300\,\text{nm}}^{600\,\text{nm}} S_{PMT}(\lambda') w_{em}(\lambda') d\lambda'}{S_{PMT}(\lambda)}. \tag{4.12}$$

Therefore we can conclude the following formula for the **one-sided** efficiency of the coated tube [71]:

$$\epsilon_{one}(\lambda, z_{tube}, \phi_{tube}) = \frac{A_{sig}(\lambda, z_{tube}, \phi_{tube})}{A_{ref}(\lambda) \cdot S_{\text{surf}} \cdot S_{\text{wvl}}(\lambda)}. \tag{4.13}$$

The total, both-sided efficiency is the sum of the efficiency curves measured by the PMTs from both sides, namely NPMT and SPMT

$$\epsilon_{both}(\lambda, z_{tube}, \phi_{tube}) = \epsilon_{one}^{\text{NPMT}}(\lambda, z_{tube}, \phi_{tube}) + \epsilon_{one}^{\text{SPMT}}(\lambda, z_{tube}, \phi_{tube}). \tag{4.14}$$

As we would expect no change in the efficiency with the azimuth angle ϕ_{tube} due to cylindrical symmetry, we average over all angles to determine a statistical error on the measurement.

4.6.2 Correction of Light Guide Systematics

Measurements performed in [115] showed a systematic in the setup related to the LLG connecting the beam splitter setup and the dark box. It was noticed that the bending of the LLG throughout the measurement caused uncontrollable intensity changes which were not corrected by the photodiode reference as they happened after the beam splitting. This is corrected for by moving the beam splitting setup inside the dark box just before the light hits the tube (see Fig. 4.22). Like this, the bending systematic is corrected by the photodiode reference.

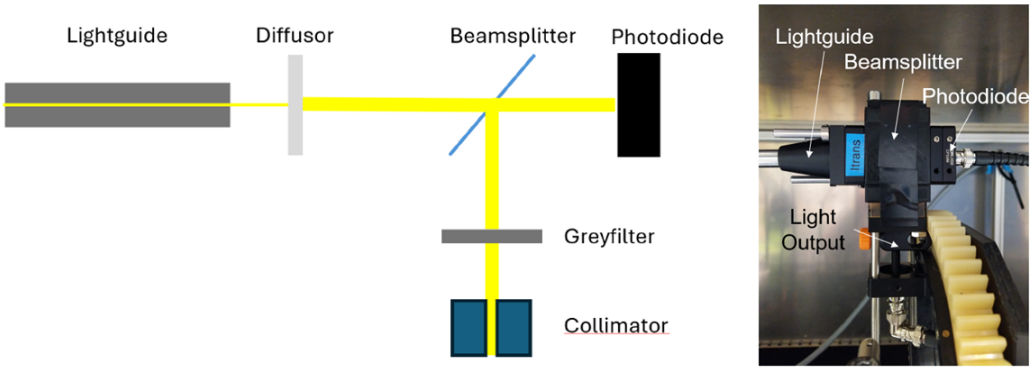

Fig. 4.22.: **Schematic (left) and photo (right) of the LLG correction for the WOM evaluation setup [115].** The box the the beam splitting and photodiode reference is now located directly above the tube so the efficiency is not affected by the bending of the LLG.

We compare an efficiency scan over all z_{tube} and ϕ_{tube} before and after the modification of the setup (see Fig. 4.23). We notice an angular systematic before the modification which significantly decreased after the modification. Further, the maximum relative difference between efficiencies decreased from 25% to 10% and to a standard deviation of 1.2%.

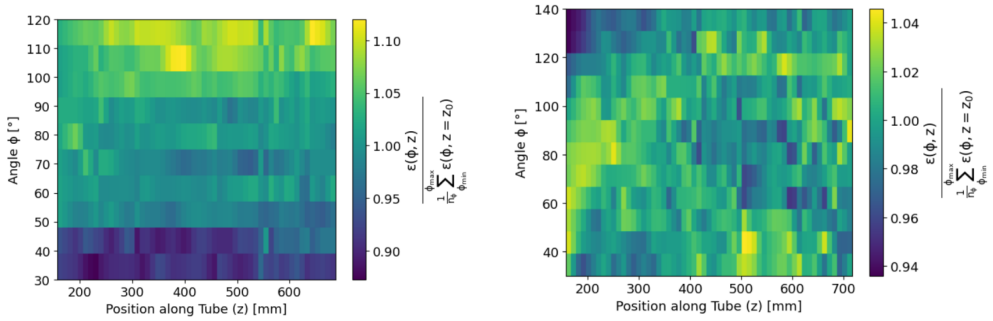

(a) Before modification, deviation: 25%.

(b) After modification, deviation: 10%.

Fig. 4.23.: **Tube efficiency scans before and after setup modification [115].** The efficiency was calculated for every point and normalized for every z_{tube} to correct for attenuation effects. We notice the angular systematic disappear after the modification and a significant decrease in the efficiency spread as a function of ϕ and z.

4.7 Application for Upgrade and Gen2

As shown in Fig. 4.24 the arrangement of the WOMs in the Upgrade geometry consists of a 5 WOM cluster close to 2 WOMs arranged vertically in the deep region and 3 WOMs in the shallow region. The cluster of WOMs in the deep physics region would be able to be operated in coincidence which will serve as a proof of concept for event reconstruction with WOMs. The UV-flashers will be used to calibrate the ice for WOM sensitive wavelengths and the relative positioning of the WOMs. The low-radioactive quartz glass enables studies on the radioactivity of the ice which are not possible with other modules as they are dominated by noise of the pressure vessel's glass.
The three WOMs in the shallow region would focus primary on ice calibration studies on the operation of the modules at different environmental temperatures ($-40\,^{\circ}\mathrm{C}$ in the shallow layer vs. $-15\,^{\circ}\mathrm{C}$ in the physics region).

As UV-light has an attenuation length of only several meters in the ice [19] standalone WLS modules are not expected to yield a high efficiency in Gen2. However, a possible application of WLS technology there could be the concept of a tubic WLS

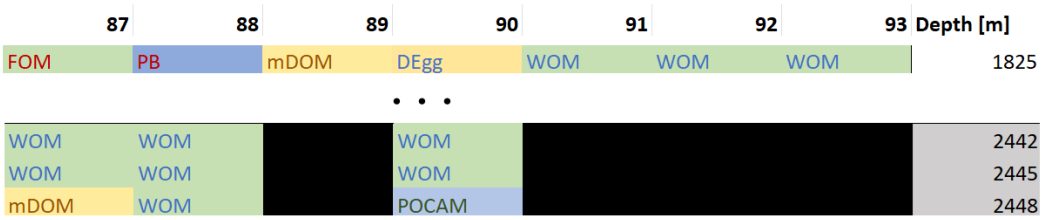

Fig. 4.24.: **Placing of WOMs on the strings in the IceCube Upgrade geometry [116].** All the other Upgrade modules are hidden for visualization purposes. The modules on the strings 87, 88 will be deployed first and needed therefore to be shipped in 2024 already.

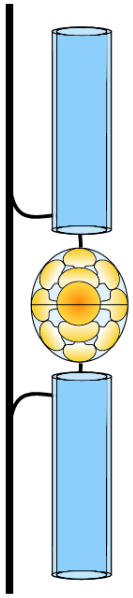

Fig. 4.25.: **Visualization of the WOMTrap for Gen2 [117].** It would feature a $\sim 2\,\mathrm{m}$ WLS plastic tube located vertically between two Gen2 optical modules. On top of the light normally received by the modules it will additionally collect, shift and focus UV-Cherenkov light onto the modules.

light collector (working title: **WOMTrap**) positioned between two optical modules as shown in Fig. 4.25. This extension would work the same way as the inner tube of the WOM providing a cost-efficient way to increase the detector's sensitivity as there is no need for PMTs, a pressure vessel or electronics. This tube would have an increased length and thickness to cover most of the vertical space between modules and withstand the pressure of the freezing process.

Simulation studies were able to show that Gen2 would be able to observe small-scale modulations in the light curve of core-collapse supernovae and give insight in the hydrodynamics of the process. The addition of WLS in the detector would add a small improvement which could be more significant for fainter light signals. [117] As the WOMTrap is still only in its conceptual phase it will not be discussed in much detail in this work.

After the WOM and all of its components have been introduced we will now focus on the characterization and optimization of the module as well as the evaluation of its performance.

5 Optimization and Characterization of Components

Throughout the development process of the WOM different production processes and parameters of components were optimized and characterized. This chapter will talk about the most significant optimizations including characterization measurements of PMTs at different temperatures, studies on the geometry of the inner tube and the coupling between the inner tube and PMT.

5.1 PMTs

A total of 26 ET9390B Series PMTs were originally considered for the WOMs. This section will feature PMT characterization measurements which include determining each PMT's Quantum Efficiency (QE), surface scans of the photocathode as well as studies on the temperature dependency of Gain and Dark Rate.

5.1.1 Quantum Efficiency

The PMT's Quantum Efficiency (QE) is an important property of an optical IceCube module, which is used to determine the full module's efficiency necessary for a proper event reconstruction. The experimental setup to measure the QE of the WOM PMTs [118] is shown in Fig. 5.1. We use a pulsed light source guided through a monochromator producing adjustable monochromatic light. The light is guided towards the PMT using an optical fiber mounted on a 2-axis linear stage to perform a surface scan. An absolute calibrated photodiode is located beside the PMT to determine the number of photons exiting the fiber. The current of the PMT is read out between the cathode and first dynode pin using an ampere meter which measures the current of the electrons released from the photocathode before the first multiplication stage. Therefore, the PMT is operated with a low HV of $250\,\mathrm{V}$ which ensures that all emitted electrons from the cathode are accelerated towards the first dynode and detected.
For each PMT a wavelength scan at its center in the range of $200\,\mathrm{nm}$ to $800\,\mathrm{nm}$

is performed followed by a XY surface scan at fixed wavelength of $375\,\mathrm{nm}$ which denotes the wavelength for peak QE. Before each PMT measurement cycle we take a reference measurement of the photodiode to determine the QE.

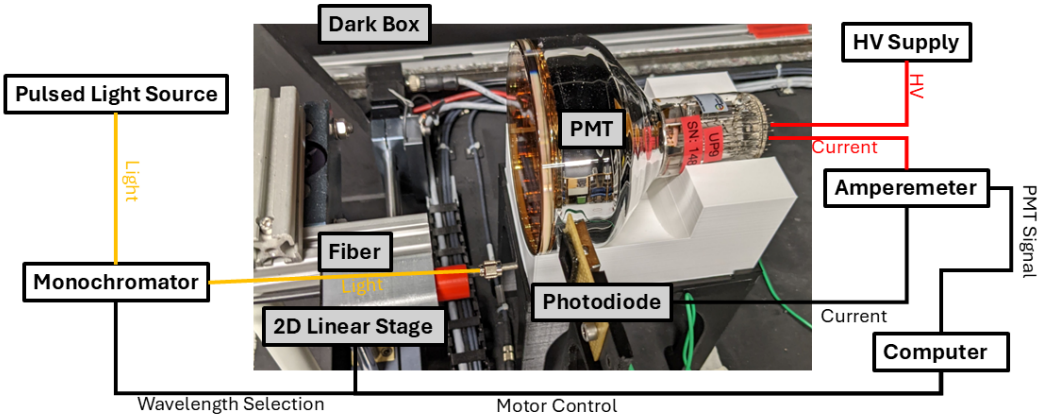

Fig. 5.1.: **Setup to measure the QE of WOM PMTs.** We measure the current of released electrons before the first amplification for different wavelengths and xy-positions of the cathode. An absolute calibrated photodiode is used to determine the number of photons hitting the cathode.

The resulting wavelength dependent QE of each PMT is shown in Fig. 5.2. One observes that the curves scatter around the QE curve given by the datasheet [79]. The QE reflects the probability of a photon being absorbed by the photocathode and the emitted electron being able to escape the cathode to hit the dynode. Both probabilities depend on the thickness of the cathode which has some variation caused by the limited precision of the PMT's manufacturing process. Further, the normalized QE curves show a very similar shape between each other and relative to the reference curve. The shape of the curves depend on the material of the cathode and the glass cover which is the same over all PMTs of the same model. However, we notice the large spread for different PMTs ranging between peak values of 12% until 42%. We observe three PMTs with peak QE values of bellow 20%. As we want to have a high efficiency for our module we would prefer not to use these sensors for the deployed WOMs assuming there are enough spares left.

5.1.2 Surface Sensitivity

As the WLS-tubes have a small wall thickness of $2.5\,\mathrm{mm}$ and a radius of $115\,\mathrm{mm}$ shifted light will hit the PMT only around a ring on the outer part. The photon distribution on the cathode does not depend directly on the incident angles of the

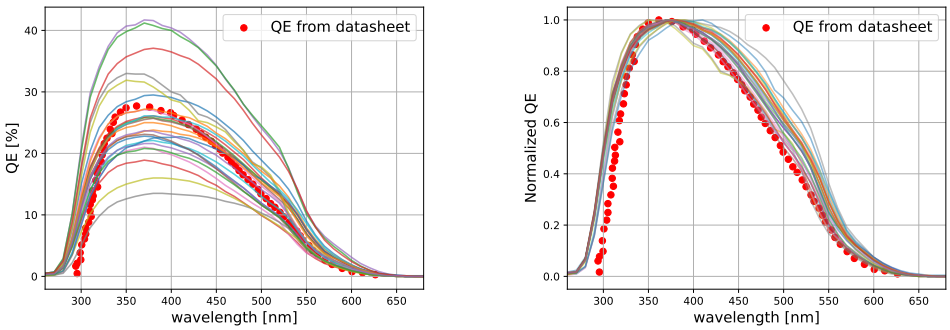

(a) Quantum Efficiency (QE) curves for 26 PMTs. **(b)** Relative QE curves normalized to peak value.

Fig. 5.2.: Measured QEs of all WOM PMTs with respect to the wavelength (data from [118]). The QE curve taken from the datasheet [79] is shown for comparison. To create the normalized curves each QE value was divided by its peak value.

UV-photons relative to the inner tube, but on the radius of the tube and distance between injection point and PMT. As we simulate the propagation of the photons through the inner tube one can predict the photon distribution on the cathode with respect to the point of interaction between the UV-photons and the WLS-paint. To characterize the WOM's efficiency we want to determine the PMT's QE considering the underlying emission spectrum as well as the expected cathode distribution. For this we measure the **Surface Sensitivity** (or surface efficiency) for each PMT.

The surface scan measurement setup is shown in Fig. 5.3. The PMT is fixed inside a mu-metal shield from the PMT manufacturer [@119] which shields the sensor from external magnetic fields. The light source is a pulsed laser [120] with a wavelength of $(375 \pm 10)\,\mathrm{nm}$ with a variable attenuator. The laser is mounted onto a 3-axis stepper motor which scans the photocathode in the xy-plane in $2\,\mathrm{mm}$ steps[1]. The PMT's signal is read out by an ADC [121] with a sampling rate of $1\,\mathrm{GHz}$ which gets its trigger signal from the laser and is therefore triggered on every light pulse at a rate of $20\,\mathrm{kHz}$. To prevent interference of the PMT signal with external electric fields as well as additional background light all electronics are located outside the dark room. The HV of the PMT is set to a gain of 10^7 which will be the gain the WOM PMTs will be operated at after deployment. For every xy-position of the motor we take a total of 1000 waveforms of $256\,\mathrm{ns}$ length, corresponding to xy samples.

From the recorded waveforms we extract the photocurrent by integrating over all recorded waveforms. As we operate the PMTs at a high gain we want to isolate

[1]This is motivated by the laser beam having a diameter of $2\,\mathrm{mm}$.

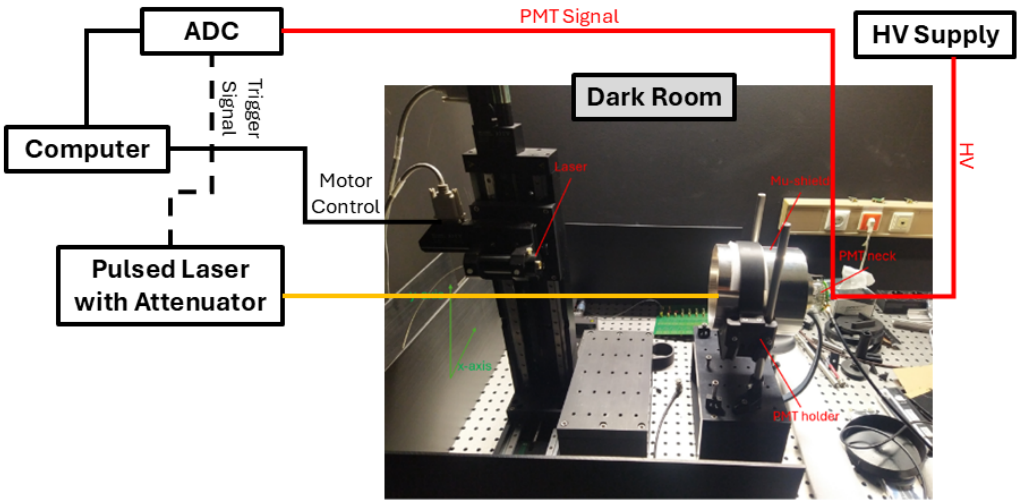

Fig. 5.3.: **Setup for PMT Surface Scans.** A pulsed light source is moved along the PMT's surface generating a trigger signal on every pulse. Every point on the surface is scanned with 1000 light pulses which will be added up to determine the relative efficiency.

the light signal from dark rate hits by cutting on the signal's height and time interval[2]. Details on the data processing and background subtraction can be found in [115].

Complimentary to the measurement mentioned above, the surface dependent QE was measured using the setup shown in Fig. 5.1. As we compare these two measurements for the same PMT (see Fig. 5.4) we notice that the measurements have a significant deviation. Especially, the efficiency on the outer ring relative to the center is decreased. This is explained by the different quantity being read out. The QE is measured by reading out the PMT's signal between the cathode and the first dynode while the PMT is being read out over the whole dynode chain in the surface scans. For this reason the QE measurement results are also independent on the HV as it mostly influences the multiplication of released electrons which we do not measure there. Electrons emitted far from the center of the photocathode eventually hit the first dynode at an edge which could result in the emitted electron missing one of the following dynodes. Obviously, this effect would not be observed while measuring the photocurrent between cathode and first dynode only.

The optimization of the inner tube diameter was done considering the PMT's surface scans using the full dynode chain as well as the measured wavelength-dependent quantum efficiency $\epsilon_{\mathrm{QE}}^{\mathrm{center}}(\lambda)$ at the center of the photocathode, see Section 5.2.

[2]While the attenuator dims the laser so we do not saturate the ADC we are not nesecary working with a single photon setup here. Therefore dark rate hits can be cut on their height. This assumes a QE high enough so the laser signal is above 1 PE.

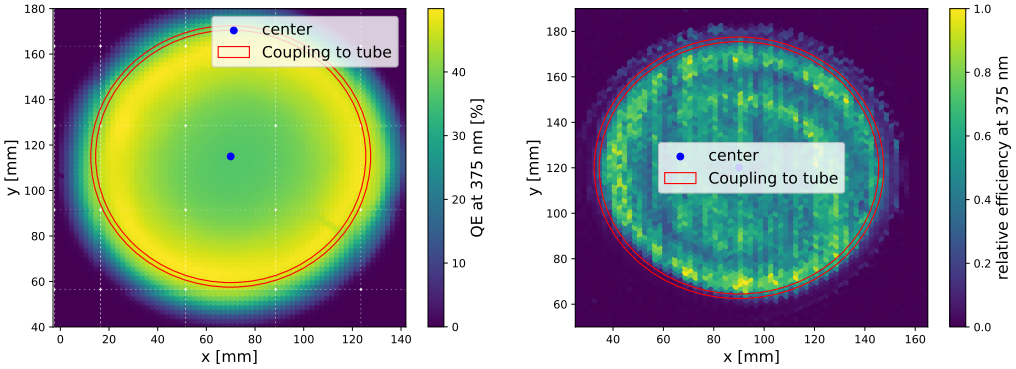

(a) QE Surface Scan.

(b) Surface sensitivity Scan using the full dynode chain, HV=1655 V.

Fig. 5.4.: Comparison of different surface scans for PMT UP9. The PMT orientation was not the same for both measurements, so the surface structure could be rotated by some angle. However, all surface sensitivity scans and QE surface scans were performed in the same orientation withing their own setup.

5.1.3 Temperature Measurements

As outlined in Section 2.5, certain PMT properties are anticipated to vary with changes in environmental temperature. In this section, we provide a detailed characterization of the temperature dependence of the Gain and Dark Rate for all WOM PMTs.

The measurement setup is shown in Fig. 5.5. The covered PMT is placed face down inside a climate cabinet [122] which can run pre-defined temperature cycles, as well as adjust the air humidity. To monitor the temperature of the PMT, a thermocouple is fixed onto its outer surface using tape. As the PMT is considerably small the temperature should equalize over the full sensor within minutes. The signal is read out by a **PicoScope** [123] which features the functionality of an oscilloscope combined with fast storage speed to read out waveforms at a high frequency. The PicoScope is operated using custom software [124] which implements the infrastructure for long term measurements and simple analysis. The PicoScope is triggered internally by a threshold trigger on the voltage's signal height.

The PMT is operated at the nominal gain of 10^7. The trigger threshold should be below 0.25 PE, resulting in a threshold of $3\,\mathrm{mV}$. As no light source is used in this setup the triggers result exclusively from the dark rate. To determine the gain and adjust the HV accordingly we fit a Gaussian to the 1 PE peak of the SPE spectrum (see Section 2.5 for details, instead of histogramming the charge we histogram the gain by dividing through the elementary charge e) at room temperature (see

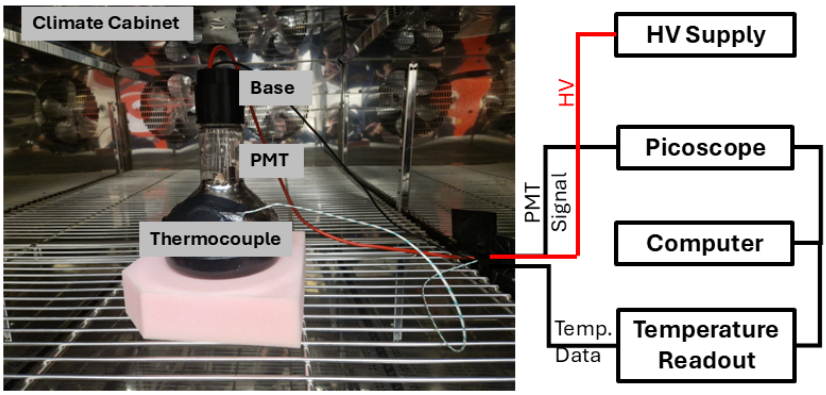

Fig. 5.5.: **Setup for PMT temperature measurements.** The PMT is located inside the climate cabinet. Hardware for HV-supply, readout and temperature monitoring is located outside of light-tight cabinet.

Fig. 5.6). As the PicoScope outputs the voltage, we first divide by its input impedance of $50\,\Omega$ to determine the current. The mean of the fitted Gaussian μ corresponds to the determined gain. The temperature cycle set by the climate cabinet between $20\,°\mathrm{C}$ and $-40\,°\mathrm{C}$ is shown in Fig. 5.7. The air humidity is set to be as close to 0 as possible to prevent damaging exposed electronics.

The gain of the PMT is monitored throughout the temperature cycle in steps of $20\,\mathrm{min}$. The change of the gain over the time shown in Fig. 5.8 shows an increase of the gain for lower temperatures. This is a property of the secondary electron emission on the dynodes. At higher temperatures the lattice vibrations of the phonons increase which reduces the energy for the emission of new electrons effectively increasing the dynode's work function with increasing temperature. The temperature-to-gain correlation (see Fig. 5.9) shows a linear behavior where the gain falls by 0.6% per $1\,°\mathrm{C}$ temperature difference. This value varies between different PMTs in the range of 0.2 - 1.3%/°C (see Section A.1).

To determine the dark rate the PicoScope determines the trigger rate by measuring the time it takes to get a certain amount of triggers. For most dark rate measurements this value was set to 10,000 resulting in getting a dark rate value as well as a timestamp every $10\,\mathrm{s}$ to $20\,\mathrm{s}$. As the trigger is set below the IceCube conventional trigger threshold of 0.25 PE we need to perform a subsequent SPE cut. The resulting dark rate is calculated by dividing the number of recorded waveforms between two timestamps by their distance in time. The resulting time dependency on the dark rate is shown in Fig. 5.10. At the start of the measurement, we notice an immediate very steep fall in the rate. This was caused by the prior activation of the PMT as it was stored in a not completely dark environment before. Then, the dark rate decreases with lower temperatures. As the dark rate is dominated by

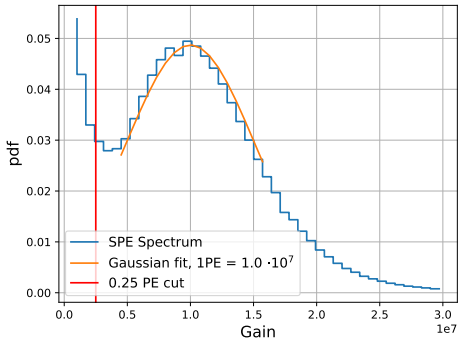

Fig. 5.6.: Gain of PMT UP15 at $1400\,\mathrm{V}$ at room temperature. The Gain is determined by a Gaussian fit to the 1 PE peak. Further, we observe that the 0.25 PE cut cuts into the noise peak a little which suggests this being a more noisy PMT.

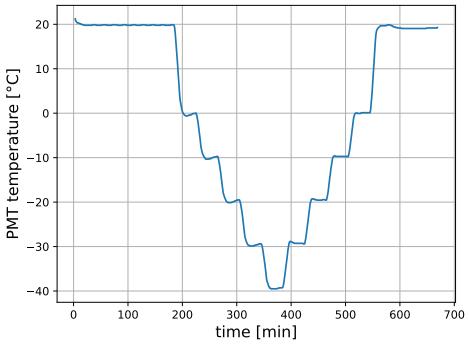

Fig. 5.7.: Temperature cycle for PMT Dark Rate measurements. Measured data by thermocouple. A temperature value was recorded every minute. We notice that the $30\,\mathrm{min}$ per temperature value are enough for the PMT to adjust to the temperature.

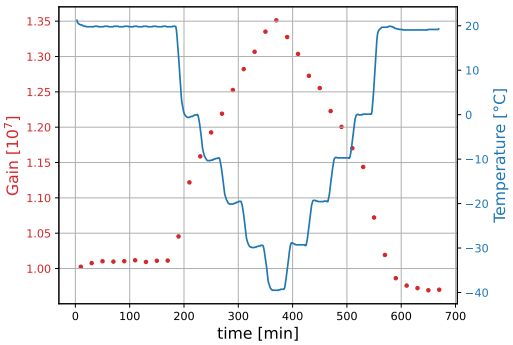

Fig. 5.8.: Gain drift of UP15 while temperature cycle. The gain was determined for every $20\,\mathrm{min}$ time frame.

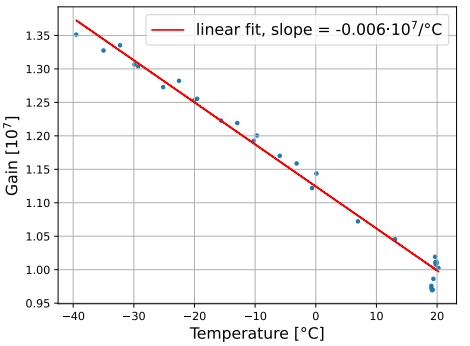

Fig. 5.9.: Correlation between gain and temperature of UP15. The gain increases linearly with decreasing temperature, but the effect varies for each measured PMT.

thermionic emission first, this contribution goes down with decreasing temperature. However, at dark rates low enough a different contribution, which increase with the temperature, becomes the more dominant effect. These effects contain afterpulsing due to ionization of the residual gasses inside the PMT and radioluminescence of surrounding materials such as the cover glass or PMT support structures. Another possible explanation would be the increasing relative air humidity at low temperatures which impacts the operation of the electronics (especially of the PMT Base). The air humidity regulation of the climate cabinet is probably too slow to keep the humidity at zero throughout the full measurement cycle. As this increase in the dark rate happens at temperatures below $-30\,^{\circ}\mathrm{C}$ a final possible reason for this effect could result from going below the minimal rated temperature for these PMTs. However, we do not expect operating the WOMs at temperatures this low so the risk of malfunction due to cold remains unlikely.

Fig. 5.11 shows the correlation between dark rate and temperature. Comparing the down and upcycling curve we notice a deviation especially in the region above $0\,^{\circ}\mathrm{C}$. The downcycling curve has higher values and is taking *longer* for the dark rate to decrease while the upcycling curve stays approximately flat at low dark rates before suddenly jumping up at the end. This discrepancy is caused most likely by the fact that the internal part of the PMT needs longer to heat up again (as we measure only the surface temperature). Like this, it would take longer for the dark rate to rise again. Overall, this shows that the temperature cycle and single temperature steps are too short to properly characterize the PMT's temperature behavior. However, this level of precision is sufficient for the goal of this study, which was to determine whether the PMTs are able to reach the nominal gain of 10^7, getting an estimation for the dark rate in the ice and identifying broken or bad performing PMTs which would be potentially discarded.

According to measurement data from the deployed IceCube modules [125] the ice temperature increases with the depth. The WOMs deployed in the shallow region are expected to be exposed to approx. $-35\,^{\circ}\mathrm{C}$ while the WOMs in the physics region will be at around $-18\,^{\circ}\mathrm{C}$. From our dark rate data we can determine the expected dark rates $R_{\text{shallow}}, R_{\text{physics}}$ at these temperatures for the underlying PMT considering the up and downcycle to determine a systematical error:

$$R_{\text{physics}} = (609 \pm 24 \pm 23)\,\text{Hz} \quad R_{\text{shallow}} = (693 \pm 29 \pm 16)\,\text{Hz} \tag{5.1}$$

Over all measured PMTs we get mostly minimal dark rate values between $350\,\mathrm{Hz}$ and $800\,\mathrm{Hz}$ (see Section A.2). However, one needs to consider that the electronics of the module itself would produce additional heat resulting in an uncertainty on the

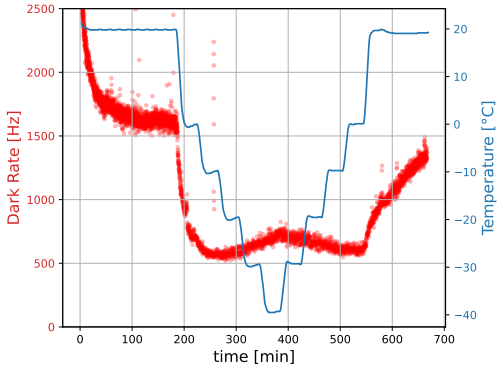

Fig. 5.10.: **Dark Rate of UP15 during temperature cycle.** The rate was calculated after a SPE cut to 0.25 PE. A value is determined after every 10000 triggers.

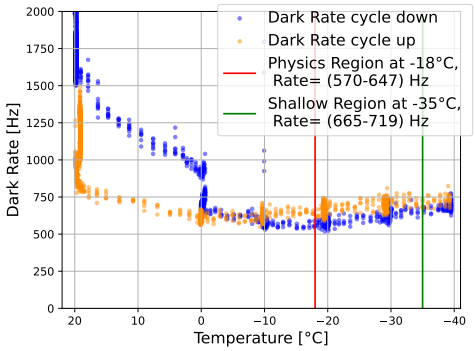

Fig. 5.11.: **Temperature correlation of dark rate of UP15.** The two temperatures expected in the shallow and physics region in IceCube are highlighted. We observe a strong deviation between the up and downcycle curve most likely caused by the measurement routine.

temperature. Further, additional noise contributions need to be considered for the WOM.

5.2 Inner Tube Optimization

To optimize the dimensions of the inner tube we use the results from the PMT surface scans as well as the ALGO ray tracing simulation to predict the cathode's photon distribution. This section will explain the simulation and the results for the optimal dimensions of the inner tube.

5.2.1 Simulation Setup

In the simulation, the light ray is injected from the top (in the direction $-\vec{e_y}$). We choose the source to be always a few cm above the tube ($y = 7\,\mathrm{cm}$) emitting a total of 1,000,000 photons. We run the simulation for different diameters, wall thicknesses and lengths of the tube. For every parameter set we use multiple injection points along the tube with $10\,\mathrm{cm}$ horizontal distance from each other. Previous measurements with coated HSQ300 tubes estimated the attenuation length to be about $3\,\mathrm{m}$ [6]. For simplicity, we assume that the attenuation is dominated by

absorption therefore setting the absorption length to $3\,\mathrm{m}$ and the scattering length to infinity[3]. The simulation is run for air (n=1.0) and PFPE (n=1.33) as the outer material.

The simulation outputs the two angles θ and φ for each photon which are visualized is Fig. 5.12. θ is the angle relative to the z-axis (which is the longitudinal axis of the tube) and therefore describes the forward movement of the photons. φ is the polar angle within the xy-plane and models the circular movement of the photons within the plane. The end surfaces of the tube are located at z-coordinates $z = 0$ and $z = l$, l being the length of the tube (default: l=76 cm).

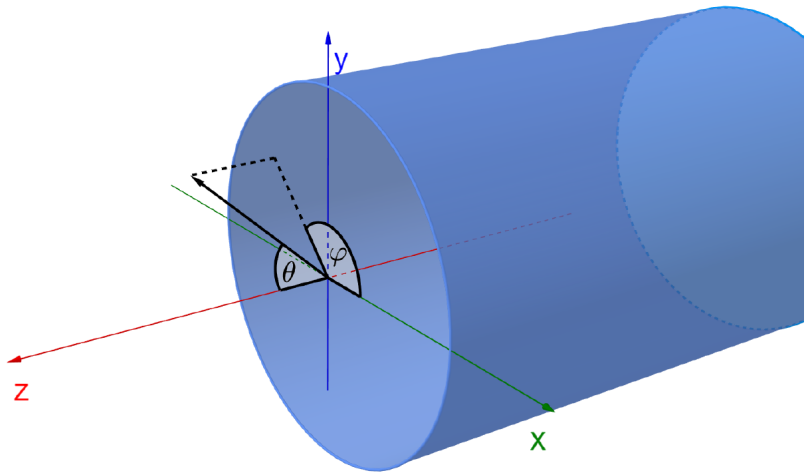

Fig. 5.12.: **Definition of output angles from ALGO [77].** θ is the forwarding angle relative to the z-axis while φ is the polar angle within the xy-plane.

Before hitting the photocathode the photons exiting the tube need to transverse the $6.5\,\mathrm{mm}$ thick glass cover of the PMT. As the PMT glass cover is made out of borosilicate glass [79] we first calculate the refraction between $n_{\text{quartz}} = 1.46$ and $n_{\text{borosilicate}} = 1.49$ using θ as the incidence angle. Let $\vec{r}$ be the vector pointing to the new coordinates of the photon on the cathode. It can be expressed by using the coordinates of the photon at the tube's exit $\vec{r_0}$ and its direction $\vec{e}$ expressed in

[3]The conceptional difference between absorption and scattering in this context is the chance of a scattered photons to remain within the TIR angle and still reach the end of the tube changing the angular distribution a little. However, this can be considered a minor effect. Further, there are many different possible combinations of absorption and scattering length resulting in an overall attenuation length of $3\,\mathrm{m}$. Studies on that are performed in Chapter 6.

spherical coordinates (θ_{ref} being the refracted angle inside the borosilicate glass of the PMT determined by applying Snell's law on θ):

$$\vec{r} = \begin{pmatrix} x_{\text{PMT}} \\ y_{\text{PMT}} \\ z_{\text{PMT}} \end{pmatrix} = \vec{r_0} + s \cdot \vec{e} = \begin{pmatrix} x \\ y \\ z \end{pmatrix} + s \cdot \begin{pmatrix} \sin\theta_{ref} \cos\varphi \\ \sin\theta_{ref} \sin\varphi \\ \cos\theta_{ref} \end{pmatrix} \tag{5.2}$$

As we know the thickness of the glass $z_{\text{PMT}} - z = 6.5\,\text{mm}$ we can determine the scaling factor s by using the z-component of Eq. 5.2.

$$s = \frac{z_{\text{PMT}} - z}{\cos\theta_{ref}} = \frac{6.5\,\text{mm}}{\cos\theta_{ref}} \tag{5.3}$$

x_{PMT} and y_{PMT} are then determined by inserting s into Eq. 5.2 and calculating the x and y components.

The resulting PMT cathode distribution of photons for two different injection points ($z = 20\,\text{cm}$ and $z = 40\,\text{cm}$) is shown in Fig. 5.13. For small distances like in Fig. 5.13a there is spot at the top with a significantly increased number of photons. As we inject the photons from the top this is caused by **direct hits** of shifted photons that exit the tube without hitting a wall first and therefore do not require to fulfill the TIR criteria. The fraction of direct hits increases with lower distances. Further, we notice semi-discrete rings in the top and bottom part. These are be formed by photons performing a discrete number of revolutions within the tube.
As all shifted photons originate from the same point they need a certain initial θ angle to perform a revolution loop before reaching the end. To perform two full revolutions, the angle would have to be much steeper, which would result in these photons being clearly separated from the one loop photons on the cathode. As more revolutions result in a longer trajectory the signatures of these photons are more faint, because a large fraction is lost due to attenuation.
For larger distances of the injection point from the end of the tube as in Fig. 5.13b the number of discrete circles increases and the spot from direct hits becomes fainter as more photons are now able to perform more revolutions within the available distance. Increasing the distance even further results in the discrete structure completely smeared out and forming a homogeneous distribution.
For both injection points we can also see that there is a spot at the bottom of the tube footprint where no photons reach the cathode. To reach the bottom part, photons need to perform at least half a revolution, which requires a relatively steep angle. This angle would cause the photon to fly out of the tube's footprint while traversing the PMT cover glass. We see for Fig. 5.13b the photons hitting the cathode much closer to the tube's footprint as a longer distance requires the angle to be less steep

to perform half a circle.
For a WOM deployed in IceCube the photon distributions for different z and azimuth angles will overlap as the module is illuminated by a Cherenkov cone forming a homogeneous photons distribution on the cathode. For the simulation setup this corresponds to having large z of $30\,\mathrm{cm}$ or higher.

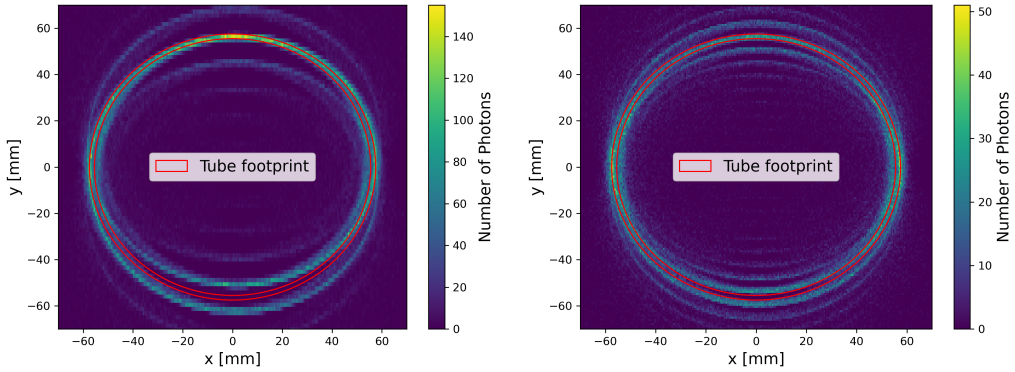

(a) $z = 20\,\mathrm{cm}$. **(b)** $z = 40\,\mathrm{cm}$.

Fig. 5.13.: Photon distribution on cathode for different distances z between injection point and PMT. Outer diameter: $115\,\mathrm{mm}$, wall thickness: $2.5\,\mathrm{mm}$, length: $760\,\mathrm{mm}$, outer material: PFPE (n=1.33). We notice a semi-discrete pattern which smears out with increasing distance.

The simulated cathode distribution can now be used to optimize the inner tube's outer diameter.

5.2.2 Outer Diameter and Wall Thickness

Previous simulation studies have shown the photons to be mostly reflected on the outer side inside the tube [77]. Consequentially, the tube's efficiency and photon distribution at the end changes only marginally with respect to the wall thickness. To save on material costs a relatively thin wall thickness of $2.5\,\mathrm{mm}$ was chosen which is just enough to keep a long tube stable and ensure a smooth manufacturing process of the glass tube.

To optimize the outer diameter we use the PMT's surface sensitivity measurement over the whole dynode chain as we are only interested in the relative efficiency for different tube diameters. Fig. 5.14 shows the previously calculated photon distribution on the PMT's cathode. We notice that most photons hit the PMT on the outer area. However, some photons entirely bypass the cathode.

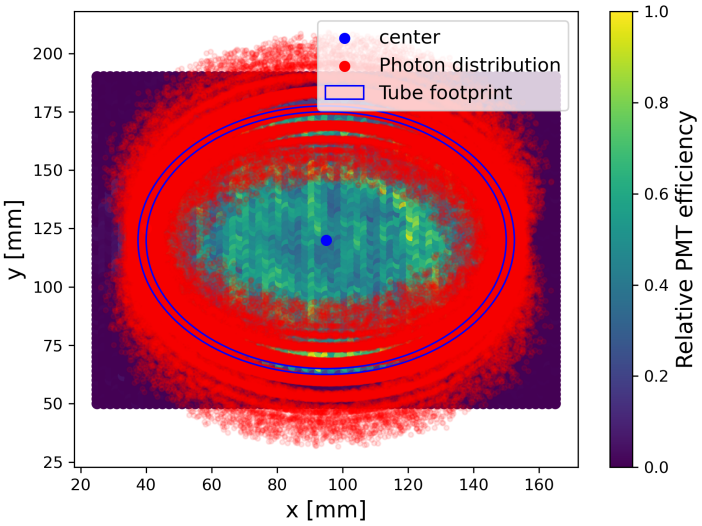

Fig. 5.14.: Photon distribution on cathode of PMT UP9. Tube outer diameter: $115\,\mathrm{mm}$, wall thickness: $2.5\,\mathrm{mm}$, z=$30\,\mathrm{cm}$. The PMT surface sensitivity was measured using the full dynode chain.

The efficiency ϵ for the underlying photon distribution is determined by averaging over the surface sensitivity $S(x, y)$ of all photon hits (photons which miss the cathode contribute with a value of 0):

$$\epsilon = \frac{1}{N} \sum_{i=0}^{N} S(x_i, y_i) \tag{5.4}$$

with x_i, y_i being the coordinates of each simulated photon on the cathode and N being the number of simulated photons reaching the end of the tube at $z = 0\,\mathrm{cm}$. Out of 1,000,000 total simulated photons about 350,000 reach the corresponding end. We use an injection point distance of $z = 30\,\mathrm{cm}$. The outer tube diameter d_{tube} is varied in the the range between $90\,\mathrm{mm}$ and $119\,\mathrm{mm}$ in steps of $1\,\mathrm{mm}$. For each diameter the relative efficiency ϵ for the underlying simulated cathode distribution is calculated. As the diameter contributes linearly to the photosensitive area (which is the outer surface area of the tube) and therefore to the effective area we want to optimize the value $\boldsymbol{\epsilon \cdot d_{\mathrm{tube}}}$. This procedure is done for a total of 26 PMTs which are considered to be included in the deployed WOMs. The optimization curves of some representative PMTs are shown in Fig. 5.15. We notice a strong variation between the curves of each PMT considering the position of the maximum as well as its height. Furthermore, also the shape changes.

To determine the average optimal tube diameter, we use the mean out of all 26 optimization curves (see Fig. 5.16). As noted before, the variation between each

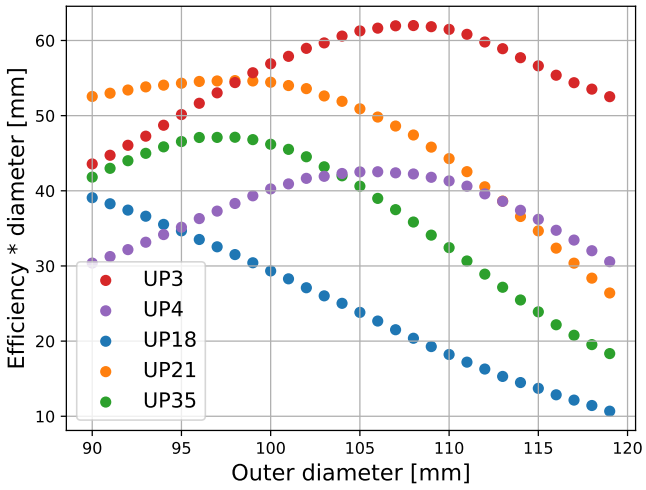

Fig. 5.15.: Outer diameter optimization curves for different PMTs. Wall thickness: $2.5\,\mathrm{mm}$, distance between injection point and PMT: $30\,\mathrm{cm}$. The numbering of the PMTs is arbitrary and does not reflect the allocation of PMTs to each WOM. Due to the large number of simulated photons the Poissonian errors are negligible.

curve is quite large resulting in large error bars. The optimal diameter would be at $99\,\mathrm{mm}$, but due to the large errors and flat behavior around the peak, diameters between $90\,\mathrm{mm}$ and $105\,\mathrm{mm}$ would result in the effective area to be within 1σ of the peak value. A small tube diameter also increases the amount of PFPE needed to be filled into the WOM (also seen in Fig. 5.16). The mass of required PFPE at room temperature is

$$m_{\mathrm{PFPE}} = \rho_{\mathrm{PFPE}} \cdot \pi \cdot h \cdot ((d_{\mathrm{vessel}}/2)^2 - (d_{\mathrm{tube}}/2)^2). \tag{5.5}$$

ρ_{PFPE} being the density of PFPE of $1.77\,\mathrm{g\,cm^{-3}}$ [82], d_{vessel} the inner diameter of the pressure vessel of $145\,\mathrm{mm}$ and h being the height of the inner tube of $760\,\mathrm{mm}$.

For economic reasons and weight constrains, it was decided to set an outer tube diameter of $115\,\mathrm{mm}$. This reduces the amount of PFPE needed by almost $2.5\,\mathrm{kg}$ which would result in a decreased cost of 500€ per module. However, the efficiency is reduced by about 20% on average. Using the surface sensitivity scans and the simulated photon distribution the exact efficiency can be determined for every PMT and WOM individually for a better performance characterization of the modules (see Section 8.5).

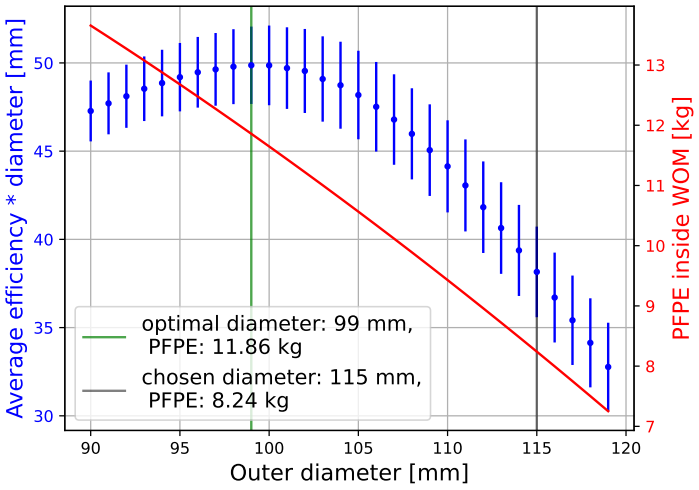

Fig. 5.16.: **Average tube diameter optimization curve and required amount of PFPE for filling.** The large error bar indicate a large variation between the single PMT curves. As $5\,\mathrm{kg}$ of PFPE cost about 1000€ a compromise between light efficiency and price was adopted in the end.

5.3 PMT Coupling to the Tube

An imperfect coupling between the inner tube and PMT leads to having a layer of either PFPE or air in the photon's path. Instead of being directly coupled into the PMT, a fraction of photons would be reflected on the interface resulting in a loss, which can be up to 50% in air[4] [16]. The use of optical glue is the preferred option here as it is able to achieve optical and mechanical coupling at the same time. This section motivates the choice of the glue, explains the gluing procedure and analyzes the resulting light losses.

5.3.1 Optical and Mechanical Requirements

The optical glue needs to fulfill certain requirements:

- Optical coupling between quartz (n=1.46) and borosilicate (n=1.49) requiring a refractive index between these two materials as well as transparency in the wavelength range of $400\,\mathrm{nm}$ - $600\,\mathrm{nm}$.

[4] We would expect a smaller loss in PFPE, because of its higher refractive index. But it would be still a significant loss, additionally to the PFPE flooding the insider of the inner tube reducing the transmission efficiency of the WOM.

- Strong mechanical bound to withstand vibration and forces from pressure differences.

- Temperature resistance in the range of $-40\,°\mathrm{C}$ to $50\,°\mathrm{C}$.

- Leak tight against PFPE to keep it from filling the tube and therefore save on the amount of needed filling material.

To couple optical components UV-curing glues are the optimal choice, because of their optical transparency, possibility of precise alignment, fast curing and minimal compression during curing to prevent misalignment of components. Throughout the WOM's development two possible UV-curing glues were studied in detail, namely **NOA61** [126] and **GA700H** [127]. A comparison of the most relevant properties of these adhesives is summarized in Tab. 5.1.

	NOA61	**GA700H**
Temperature Rating	$-150\,°\mathrm{C}$ - $125\,°\mathrm{C}$	$-40°$ - $265\,°\mathrm{C}$ (lower limit most likely even smaller)
Transmission for $400\,\mathrm{nm}$ - $600\,\mathrm{nm}$	95%	>92% for $1\,\mathrm{mm}$ thickness
Refractive Index	1.56	1.46
Viscosity at $25\,°\mathrm{C}$	$300\,\mathrm{m\,Pa\,s}$ (gel like)	$280\,\mathrm{m\,Pa\,s}$ (oily)
UV-Curing	$25\,\mathrm{min}$ at $2\,\mathrm{mW\,cm^{-2}}$	$10\,\mathrm{min}$ at $30\,\mathrm{mW\,cm^{-2}}$
Aging	1 week at $20\,°\mathrm{C}$	No aging required.
Solvent	Dichloromethane Cold (before aging)	Sulfuric acid or heat (no solvent mentioned by manufacturer)

Tab. 5.1.: Comparison of properties between two possible optical glues for the WOM. GA700H was tested for temperatures down to $-40\,°\mathrm{C}$, but there is no lower limit given for the temperature rating by the manufacturer. All the remaining data is given by the datasheets [126, 127]. We notice that for gel-like liquids a viscosity around 100,000 mPas would be expected contrary to the 100 times smaller value given in the datasheet of NOA61.

We notice that the difference in transparency results mainly from Fresnel losses, because we are dealing with a small glue layer thickness in the μm regime making absorption transmission losses neglectable. To determine the Fresnel loss for NOA61 we need to apply the Fresnel formulas for the transition of quartz to glue $(1.46 \rightarrow 1.56)$ and glue to PMT glass $(1.56 \rightarrow 1.49)$ to the simulated θ distribution at the end of the tube for for $30\,\mathrm{cm}$ distance to the injection point (see Fig. 5.17). Comparing

the resulting efficiency ϵ_{glue} to that of the direct transition 1.46 -> 1.49 (which would be the case if we use GA700H[5]) we get following results:

$$\begin{aligned} \epsilon^{\text{PFPE}}_{\text{NOA61}} &= 97.88\% & \epsilon^{\text{PFPE}}_{\text{GA700H}} &= 99.51\% \\ \epsilon^{\text{air}}_{\text{NOA61}} &= 97.63\% & \epsilon^{\text{air}}_{\text{GA700H}} &= 99.45\%. \end{aligned} \tag{5.6}$$

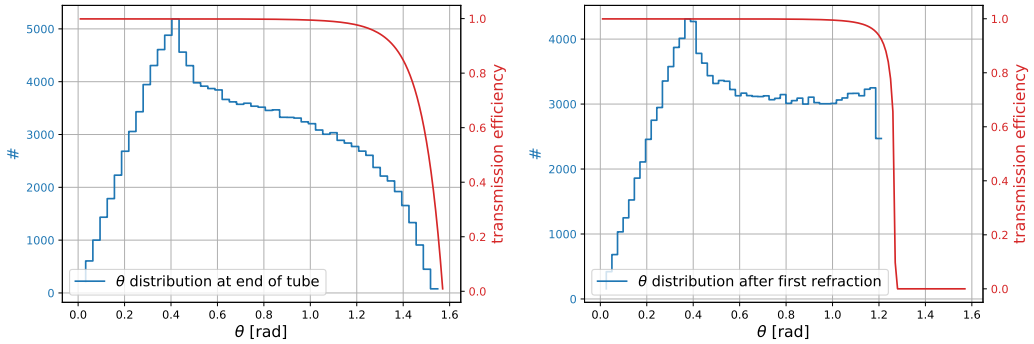

(a) Transition quartz to glue (1.46 -> 1.56), ϵ = 98.33%

(b) Transition glue to PMT glass (1.56 -> 1.49), ϵ = 99.53%

Fig. 5.17.: θ **distributions and Fresnel losses for NOA61 glue.** PFPE outside, 30 cm distance between PMT and injection point. The red curve shows the angle dependent transmittance calculated by the Fresnel formulas for the corresponding transition. In blue we see the simulated θ at the end of the tube. The loss in the second transition is lower, because the first refraction cuts out the large angle that would undergo TIR otherwise.

The Fresnel losses of NOA61 are noticeable higher, but still reasonable low at 2%. Due to the first refraction cutting off high angles, almost no photons undergo TIR in the second transition. While GA700H has lower transmission losses because of a better fitting refractive index, we can conclude that the loss factor resulting from using NOA61 is tolerable making this glue still a viable candidate.

Further, there are differences in the mechanical properties of both glues, especially in their viscosities. GA700H has a low viscosity resulting in an oily consistence. This needs to be considered while applying the glue as it makes the gluing process more challenging, especially applying and leveling the tube on the PMT (see Section 5.3). The low viscosity also enables every small unevenness in the tube's end surface or uncertainties in the leveling during the gluing process to have the potential to produce a leakage of PFPE, because of the glue's small thickness.
The testing resulted in limited success of achieving a leaktight gluing as the available

[5]GA700H is manufactured to have exactly the same refractive index as quartz having therefore no Fresnel losses between inner tube and glue.

equipment hardly allowed for the required precision in tube's evenness and leveling during the gluing process. This lead to either PFPE leaking inside or the PMT getting broken off during evacuation (see Section 5.3). The higher viscosity of NOA61 on the other side gives the adhesive a gel like consistence. Like this, it is able to compensate for small unevenness between the interface areas resulting in successful and leaktight gluing.
Its consistence and higher viscosity also simplifies the process of applying a glue layer thick enough due to stronger adhesion to the tube in its liquid state resulting in a consistent success. As the increased light loss of NOA61 is very minor it was chosen as the glue between inner tube and PMT.

The following section will give insight into the gluing process and corresponding challenges and adjustments to ensure a consistent coupling.

5.3.2 Vacuum Gluing

The gluing process is unique to each of the two PMTs in a WOM. The setup to glue the first PMT is shown in Fig. 5.18. The PMT is placed facing upwards in a holder constraining its movement and leveled to be even. The tube with glue applied on its end surface is placed onto the PMT, where it is centered a by 3D-print structure. The tube pressen onto the PMT with its own mass of $\sim 1.5\,\mathrm{kg}$. An UV-LED strip mounted on the inside of a plastic ring is placed around the tube at the bottom. As a small part of $5\,\mathrm{mm}$ lengt at both ends of the tube is not coated, the UV-light hitting the glue is not shifted, but lets the glue harden. After a curing time of $30\,\mathrm{min}$, another layer of glue is applied on the outside of the tube-PMT interface for additional adhesion, and to seal of potential remaining holes.

Gluing the second PMT in the same manner results in sealing off the inner volume of the tube at atmospheric pressure of $1\,\mathrm{bar}$. As later, the inside of the module will be evacuated to $0.3\,\mathrm{bar}$, we would get a pressure difference between inside and outside of the tube. This would result in a force of

$$F = \Delta p \cdot A = 0.7\,\mathrm{bar} \cdot 95.03\,\mathrm{cm}^2 = 665.2\,\mathrm{N} \tag{5.7}$$

with $A = \pi \cdot ((r_{\text{tube}}^{\text{outer}})^2 - (r_{\text{tube}}^{\text{inner}})^2) = 8.8\,\mathrm{cm}^2$ being the glued area and Δp the pressure difference between inside and outside the inner tube.
The small gluing area does not provide enough bonding strength. Therefore, the PMTs would be ripped off from the tube during the evacuation of the module resulting in

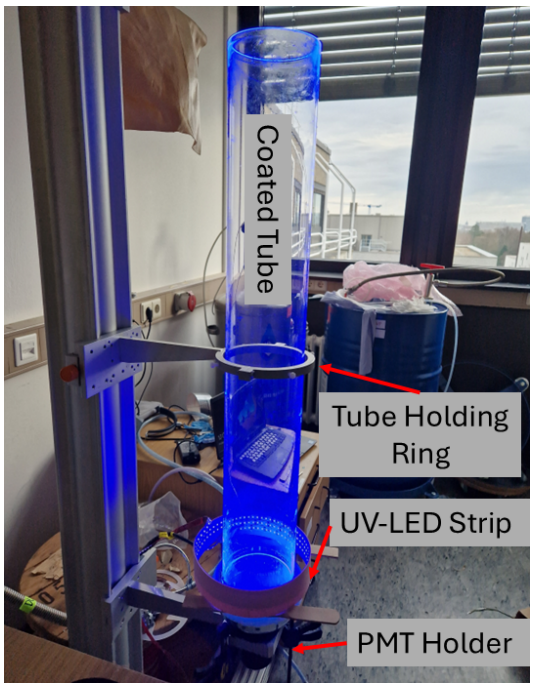

Fig. 5.18.: **First PMT gluing setup.** The tube is placed vertically, centered onto the PMT. The curing happens with an UV-LED strip mounted on the inside of a plastic ring.

1. PFPE flowing inside the tube,
2. worsening the optical coupling,
3. catastrophic damage if the PMT flies off.

To prevent creating this pressure difference the inside of the tube is evacuated before sealing it off with the glue. However, coupling the tube to the PMT while evacuating the inside can not be done manually as it needs to happen inside a vacuum chamber. A solution is the use of a **compensator**. It is a pipe made of rubber, which allows for a limited range of motion in a closed evacuated system. It is typically used to compensate for changes in length with temperature in pressure pipelines. The compensator is relatively stiff, which however can compress by about $1.5\,\mathrm{cm}$, if enough force is applied to it. This compression can be also achieved by a pressure difference from evacuating its inside. The application to our gluing procedure is illustrated in Fig. 5.19. The PMT to be glued is located inside. On top of the compensator a lid with a cup at the center is placed tightly. This cup is filled with silicone which presses against the PMT during evacuation and presses it down towards the tube. To prevent the compensator from compressing immediately, we initially secure it with nuts on threaded rods, allowing for a controlled release later.

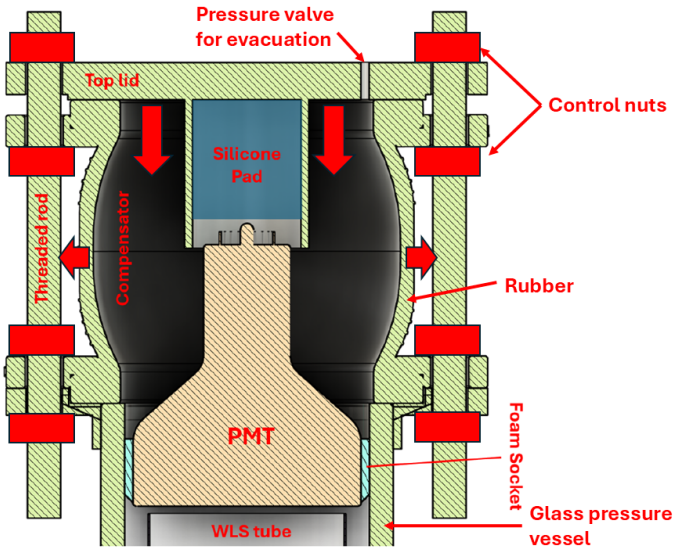

Fig. 5.19.: **CAD model of the compensator used for gluing [115].** The compensator is mounted on a pressure vessel, where the tube with one glued PMT is located. The PMT is initially held inside the pressure vessel by the foam sock applied to it previously. The arrows visualize the compression at evacuation.

The full gluing setup is shown in Fig. 5.20. The compensator is placed on top of the WOM pressure vessel[6] after the tube with one glued PMT was placed inside. To prevent the WOM tube to be pushed through the vessel by the compensator a plastic tube is placed at the bottom counteracting the pushing force. The high mass of the compensator of $15\,\mathrm{kg}$ and its soft rubber interface to the pressure vessel results in the system being airtight enough to keep a low pressure while the pump is running without needing additional sealing. As the module will be evacuated to a pressure of $300\,\mathrm{mbar}$ we want the pressure inside the tube to be lower than $200\,\mathrm{mbar}$. This ensures that the PMT is pressed against the inner tube at all times. But there is also no clear disadvantage to reduce the inner pressure even further, but limited by the available vacuum pump. To achieve a coupling good enough to contain the inner pressure, the PMT and tube are aligned to each other using centering structures. Once the desired inner pressure is reached the four nuts holding the compensator from below are released symmetrically to ensure the PMT is moving down evenly. After the PMT is properly coupled to the tube we let the glue cure for $30\,\mathrm{min}$ while keeping the pump running.

To evaluate the pressure inside the glued tube a small battery powered pressure sensor [92] mounted on a Arduino Nano [128] with Bluetooth interface was placed

[6]Using the WOM pressure vessel has the advantage of having a fitting inner radius for the procedure as well as UV-transparency to cure the glue.

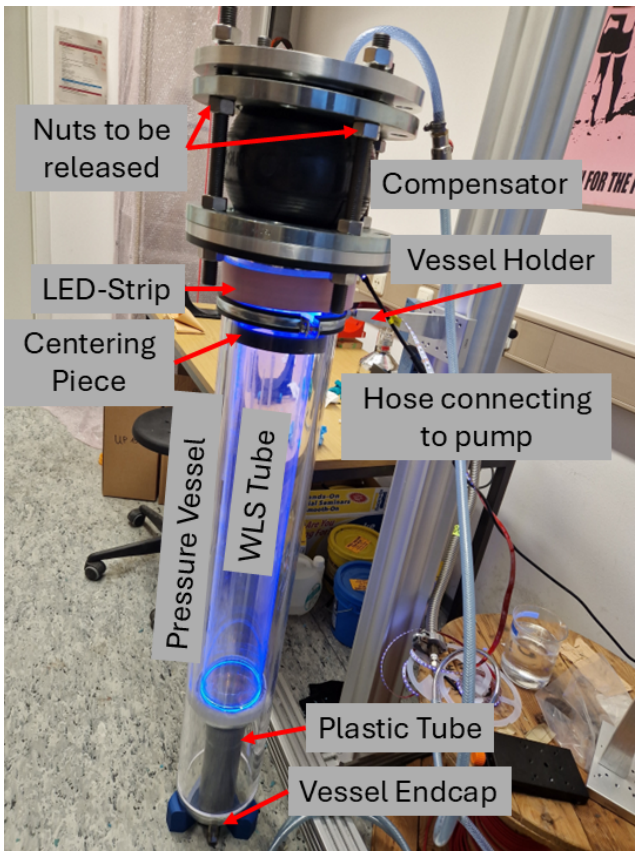

Fig. 5.20.: **Setup to glue the second PMT at underpressure.** We notice that the top nuts which were supposed to fix the lid to the compensator have some distance to the lid showing that the compensator got compressed during the gluing process.

inside the tube before gluing[7]. The inner pressure as well as the environmental temperature is monitored over several days. The results of one representative measurement are shown in Fig. 5.21. We see no significant increase in the inner pressure beyond $1\,\mathrm{mbar}$ over the course of 5 days. We notice fluctuations in the pressure which often can be correlated to environmental temperature changes. The temperature values do not reflect the exact temperature inside the tube as they were taken using a device outside the tube. Throughout many gluing attempts we were able to achieve consistent results of the inner pressure not increasing within 5 days.

To test if the underpressure gluing actually prevents the PMTs from being ripped off during evacuation the glued inner assembly was placed inside a pressure vessel and an evacuation test was performed. As seen in Fig. 5.22, the glue was able to

[7]Using a Bluetooth sensor has the advantage of having a readout without cables which is necessary to evaluate the pressure inside the sealed tube. This sensor is for testing purposes only and will not be inside the inner tube of the assembled WOMs.

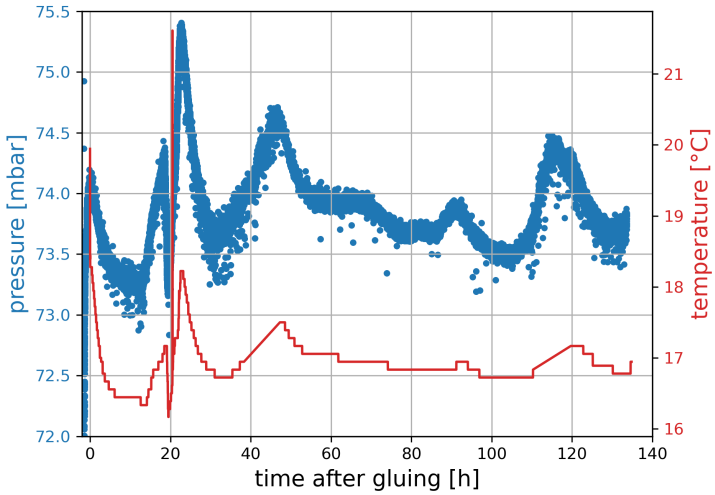

Fig. 5.21.: **Pressure evolution inside underpressure glued inner tube.** The temperature was measured outside the tube, therefore the temperature influence on the pressure is not perfectly reflected in the curve. The temperature spike at 20 h results from external interference with the temperature sensor.

withstand three evacuation cycles without the inner pressure increasing. Dips in the inner pressure curve follow the evolution of the pressure change outside the tube. This likely results from temperature changes in the vessel caused by the decreased pressure which also reflects on the pressure inside. As pressure sensors can not be installed inside the tubes for every produced WOM we use this evacuation test on each inner assembly to check if the gluing was successful. The test is repeated a few days after the gluing to consider for possible leakage during that time.
Over the first production phase glued inner assemblies stored at atmospheric pressure remained at underpressure even more than 6 months after gluing, marking the developed gluing procedure as consistently successful over long periods of time.

5.4 Summary

This chapter presented key characterizations and optimizations that enhanced our understanding of individual WOM components and their roles in overall module operation.

The PMTs were comprehensively characterized, including measurements of quantum efficiency, surface sensitivity, gain, and dark rate. These properties, together with the optimized diameter of the inner tube, provide a basis for evaluating key

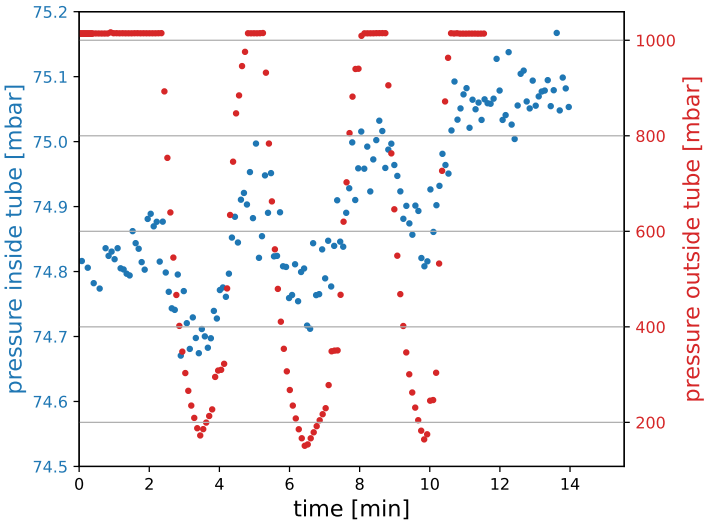

Fig. 5.22.: **Pressure curves for evacuation test of glued inner assembly.** Both pressures were taken using pressure sensors inside and pressure vessel. The slowly increasing pressure inside could result from heat produced by air friction resulting from the pumping.

performance aspects of the WOM, such as detection efficiency. These insights will inform the module's operation in the ice and the reconstruction of detected events.

To ensure both optimal optical coupling and mechanical integrity, a gluing procedure was developed and successfully tested. It involves the use of UV-curing optical adhesive and the evacuation of the inner tube to prevent pressure imbalances and resulting mechanical stress. This step marks significant progress toward a robust WOM production process and contributes to the mechanical stability required for deployment in the harsh IceCube environment.

Following this component-level analysis, the next chapter will focus on evaluating the overall performance of the WOM modules.

Timing Characterization

6

In this chapter, we perform a study on the timing of the WOM resulting from the propagation of shifted photons through the tube. We analyze the different contributions to the timing distribution and fit measured data to the ALGO simulation to determine attenuation properties of the coated tube.

6.1 Motivation

Timing resolution is a fundamental property of detectors like IceCube as timing information is used to reconstruct events in the detector. Each module's timing resolution directly affects the overall resolution limit of the reconstruction. Contrary to other optical IceCube modules, where the main timing contribution originates from the TTS of the PMTs, the WOM's timing behaviour is dominated by the propagation of shifted photons inside the tube. To properly characterize our detector's response, we want to measure and model the photon propagation which consists of different propagation modes (see Fig. 6.1).

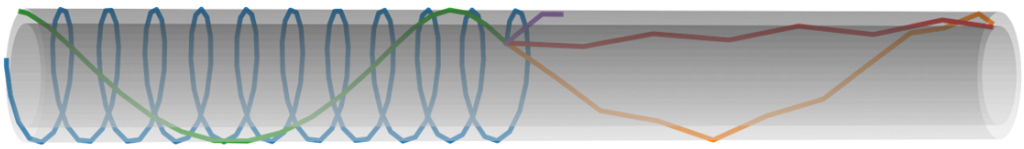

Fig. 6.1.: **Different photon trajectories in the WLS-tube.** Additionally, we need to consider photons exiting the tube directly without being reflected first. Data generated by WOMRaT [77].

Further, timing distributions can be used to determine the attenuation properties of the coated tube. The attenuation length of a coated quartz tube was measured to be $3\,\mathrm{m}$ [6]. This value can be independently confirmed through timing measurements, separate from the efficiency measurements done previously. Additionally, we can investigate the effects of absorption and scattering on the timing distribution and therefore determine the absorption and scattering separately and study their correlation.

6.2 Measurement Setup and Data Processing

To measure the timing distribution we use the setup shown in Fig. 6.2. Besides coated quartz tubes we also use a coated PMMA tube with $900\,\mathrm{mm}$ length and $90\,\mathrm{mm}$ outer diameter referred to as "Roadrunner". A picosecond light pulser [129] is used as a light source. It emits light pulses of about $170\,\mathrm{ps}$ width at a wavelength of $375\,\mathrm{nm}$. The light can be attenuated by a gray filter located outside the dark box. A small fraction of the tube at the top is coupled to the center of the PMT. The whole PMT is covered by black paper except a window of 3.6 x 1.8 cm at the center (see right of Fig. 6.2). This ensures the minimal TTS of the PMT (see Section 6.3.1). The other end of the tube is left open. Throughout this study besides the ET9390B PMTs, also a Hamamatsu R6231-100 PMT [@130] is used which proved to have a better accuracy to determine the properties of the tube. The PMT is read out by the same ADC already used for previous measurements [121] which gets its trigger on every light pulse. The position and angle on the light injection point into the tube can be adjusted by using two stepper motors.

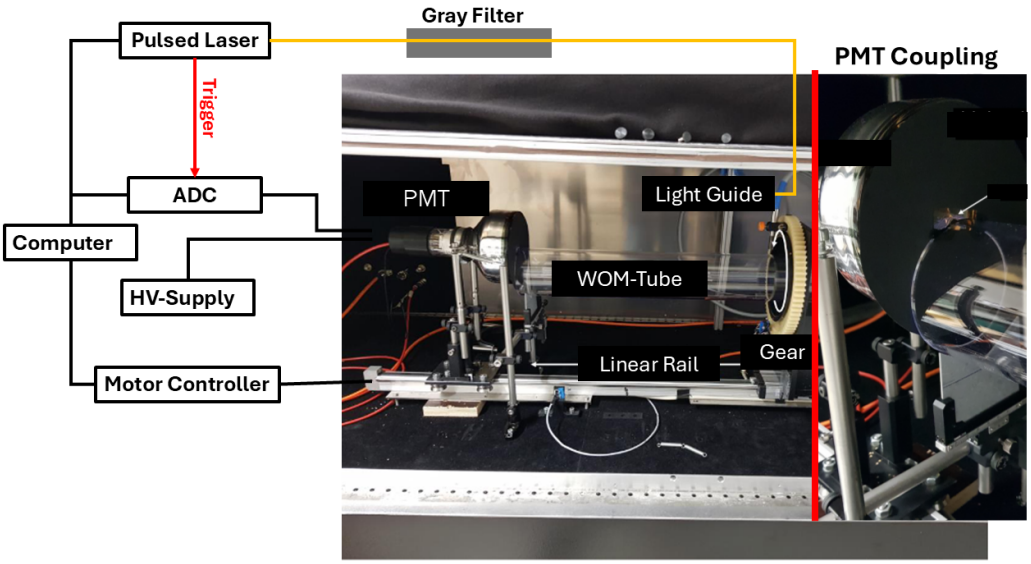

Fig. 6.2.: **General Measurement setup for WOM timing studies (adapted from [131]).** Throughout this study different tubes and PMTs are used. The coupling between tube and PMT is shown on the right side.

We record waveforms of $128\,\mathrm{ns}$ length with a sampling rate of $1\,\mathrm{GHz}$. To get a clean timing distribution we want to analyze only single photon hits. To ensure that only a single photon hit is present in each waveform, the gray filter is adjusted such that the occupancy (defined as the portion of the recorded waveforms containing a

signal) remains below 5%. If we only see a signal in 5% of the waveforms, the probability to see two photons would be $(5\%)^2 = 0.25\%$ which is considerably negligible for our purposes. Waveforms which contain signal are determined by an SPE-cut to the valley (see Fig. 6.3). We record 3,000,000 waveforms for each measurement with a frequency of $4\,\mathrm{kHz}$ which results in about 150,000 waveforms containing a signal. The effect resulting from the PMT's dark rate can be considered insignificant as the measured dark rates suggest occupancies below 0.1%. Furthermore, dark rate events produce a uniform timing distribution, which is subtracted afterwards.

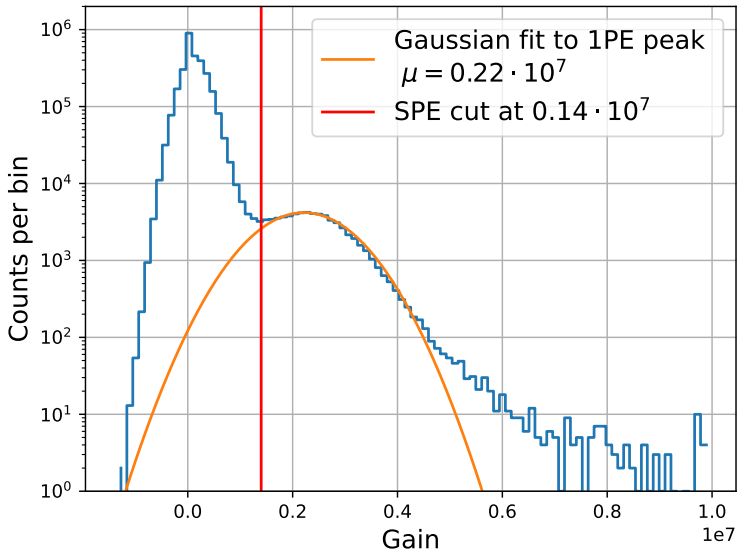

Fig. 6.3.: SPE cut for timing distribution for Hamamatsu R6231 PMT at 1490 V. The spectrum was taken using the pulsed light source triggering on every pulse. The cut is always set in the valley. The valles is very close to the SPE peak at 0.63 PE indicating a relatively high noise level.

6.2.1 Arrival Time Extraction

After filtering out "empty" waveforms, we want to determine the arrival time of each photon. Since the resolution is limited by the sampling rate, we perform a spline interpolation on the waveform to have a bin width of $0.2\,\mathrm{ns}$ for the resulting timing distribution. The interpolation range is chosen to be $\pm 15\,\mathrm{ns}$ around the minimum of the waveform to contain the full PMT pulse. The arrival time is extracted by applying a **Constant Fraction Discriminator (CFD)** to the interpolated falling edge of the pulse which determines the point in time, where the pulse's amplitude reaches 50% of its peak value (see Fig. 6.4). As the height of 1 PE pulses vary for each hit,

using a CFD ensures a more consistent arrival time determination compared to an absolute threshold discriminator. Using the position of the minimum could also distort the timing distribution as it is easily influenced by noise.

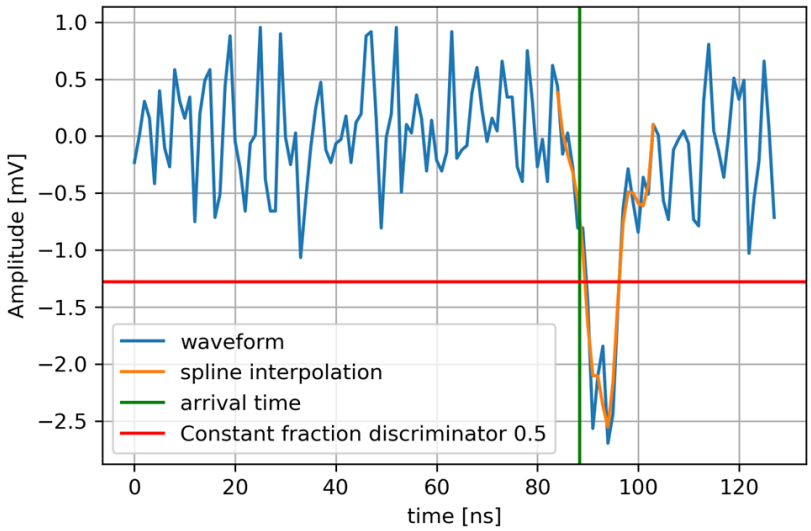

Fig. 6.4.: Arrival time extraction using Constant Fraction Discriminator. Waveform recorded from Hamamatsu R6231 PMT. We apply a spline interpolation on the waveform around the minimum and determine the time with a CFD of 0.5 on the falling edge.

Setting the CFD to a value of 0.5 can be motivated by investigating the error on the arrival time for different CFD settings. Locally, the time dependent amplitude $A(t)$ of the interpolated waveform can be determined by

$$A(t) = s(t) \cdot t \tag{6.1}$$

with $s(t)$ being the slope of the curve for a given time t. Therefore the uncertainty on the time σ_t is given by

$$\sigma_t = \frac{\sigma_A}{|s(t)|} \tag{6.2}$$

assuming σ_s to be considerably small due to using the interpolated signal. σ_A is constant given by the dynamic range of the ADC. Therefore, we want to set our CFD so we get the minimal local slope[1]. The correlation between CFD setting and local slope (see Fig. 6.5) shows the minimal slope to be in the region around 0.5. In Fig. 6.6 we see the distribution of CFD settings resulting in the minimal slope

[1]This is also the motivation to use the CFD on the falling rather than the rising edge as the later is more flat

for every waveform in one datataking which confirms 0.5 as the optimal setting to minimize the the error on the extracted arrival time.

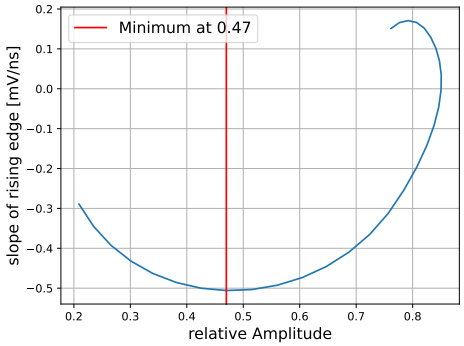

Fig. 6.5.: Slope for different CFD setting in one waveform. Measured by Hamamatsu R6231 PMT. The CFD setting and slope is determined for every interpolated sample. Having two different slope values for the same amplitude results from the pulse being not monotonically decreasing, because of a quite noisy signal.

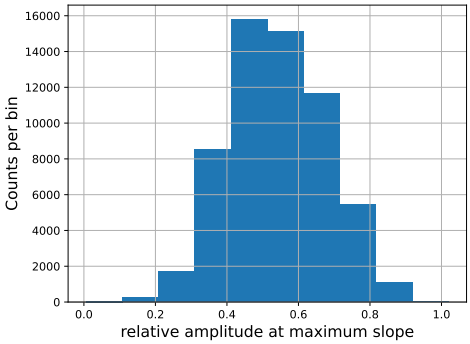

Fig. 6.6.: Distribution of relative amplitudes with minimal slope for all waveform of one datataking set. Measured by a Hamamatsu R6231 PMT. For every waveform we first determine the position of the minimal slope as shown in Fig. 6.5 and extract the relative amplitude at this point in time.

After having discussed the measurement and data extraction we continue by analyzing the timing distribution and its components.

6.3 Timing Contributions

The measured timing distribution contains the following main contributions:

- The **PMT's Transit Time Spread (TTS)** which results from different trajectories of the photo electrons. The TTS depends on the geometry of the PMT as well as the point of illumination on the photocathode. One also needs to consider the **angular distribution** of incoming photons as it contributes to an additional effect widening the distribution.
- The timing of the **wavelength-shifting** process which results from the time it takes for an excited molecule to fall down to its ground state.
- The timing of the shifted photons **propagating through the tube**. Here, we need to consider the tube's geometry as well as light attenuation due to

absorption and scattering. Therefore, we expect a change in distributions with the position of the injection point. To characterize the attenuation properties of the tube we want to keep the other contributions small to resolve tube's specific effects better.

Additionally, there are minor contributions resulting from the timing of the light source as well as broadening effects caused by the bending of the light guide and the ADC readout. Previous studies [132] showed these contributions to be negligibly small so they will not be discussed here in detail.
The measured timing distribution can be modeled by measuring the "background contributions" and then convolving them with the predicted timing distribution for the tube given by the simulation.

6.3.1 PMT Transit Time Spread

The TTS of the PMT is measured by directly illuminating the PMT using the pulser. TTS measurements of a Hamamatsu R5912 PMT at different injection points showed a clear increase from $1.72\,\mathrm{ns}$ up to $7.84\,\mathrm{ns}$ in the distributions standard deviation σ for injection points closer to the photocathode's edge [132]. We notice this effect being vastly different for other PMTs as a surface scan of a ET9390B PMT shows a mostly constant TTS (except on the very edges) with an average FWHM of $5\,\mathrm{ns}$ and therefore $\sigma = 2.1\,\mathrm{ns}$ (see Fig. 6.7) [71].

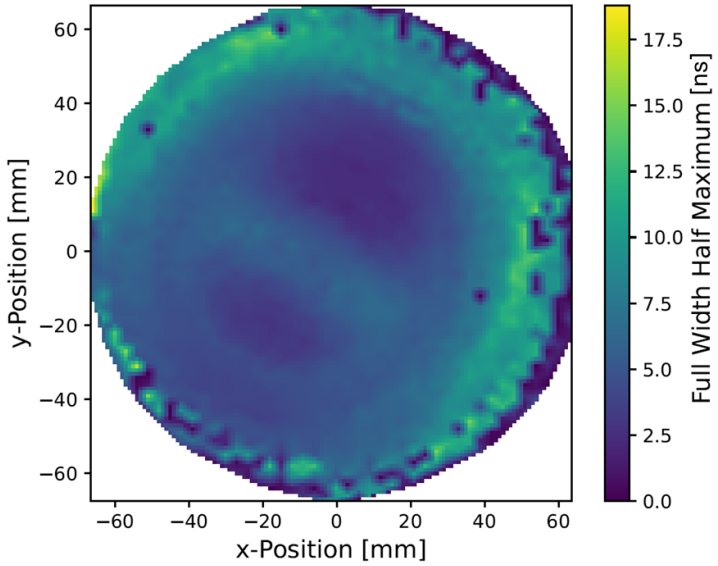

Fig. 6.7.: **TTS for different cathode positions for a ET9390B PMT at 10^7 Gain [71].** The same measurement setup as in Fig. 5.3 was used.

Multiple measurements of different ET9390B PMTs showed irregular behavior in their timing distributions. As shown in Fig. 6.8, both the shape and width of the timing distribution changes significantly under rotation of the PMT around its axis. This observation can be reproduced using different PMTs with the same orientation which leads to external magnetic fields (such as the earth's B-field) as a possible explanation. No mu-shield was used for this measurement which makes the PMT especially sensitive to these kinds of effects[2]. Using a smaller PMT, where the electrons move on shorter trajectories, would reduce the possible deviation induced by external B-fields. Performing the same measurement with a Hamamatsu R6231-100 2" PMT (see Fig. 6.9) shows almost no change in the timing distribution under rotation as well as a significantly smaller width of $\sigma \approx 1.25\,\mathrm{ns}$. To study the timing distribution from the photon propagation in the tube we want to minimize other background contributions which makes the smaller PMT the better choice here.

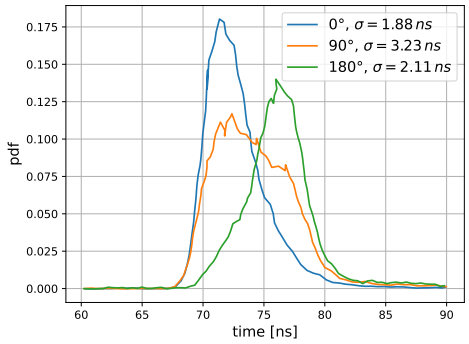

Fig. 6.8.: ET9390B PMT timing distributions for different rotations. HV=1500V. The PMT was illuminated at the center. Besides a rectangle of 3.6 x 1.6 cm the whole PMT surface was covered. σ was determined performing a Gaussian fit.

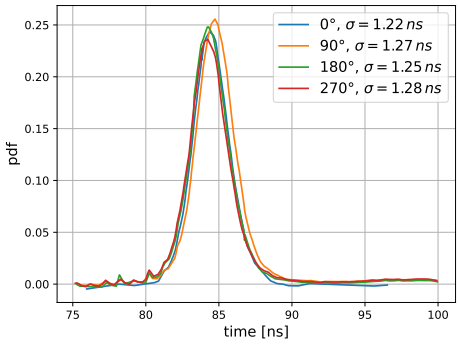

Fig. 6.9.: Hamamatsu R6231-100 PMT timing distributions for different rotations. HV=1400 V (1500 V max). Same illumination window as for ET PMT. We notice a much more constant and slimmer timing distribution.

6.3.2 PMT angular dependency

The PMT's timing distribution was measured by illuminating the PMT vertically which does not reflect the angular distribution of shifted photons exiting the tube.

[2]While using a proper mu-shield could help with this issue, one can not use it for the tube measurement while coupling the tube to the center of the sensor. The PMT needs to be fully enclosed in the mu-shield which is not possible, because the mu-shield would be in the way of the tube.

We want to estimate the change of the PMT's timing behavior with respect to the incident angle by comparing timing distributions taken under different angles. As shown in Fig. 6.10, we illuminate the PMT under a 45° angle. An angled prism out of plexiglass is coupled to the PMT with optical gel. Since it has the same refractive index as the PMT cover glass, the photons hit the cathode under the same angle without being disturbed by refraction.

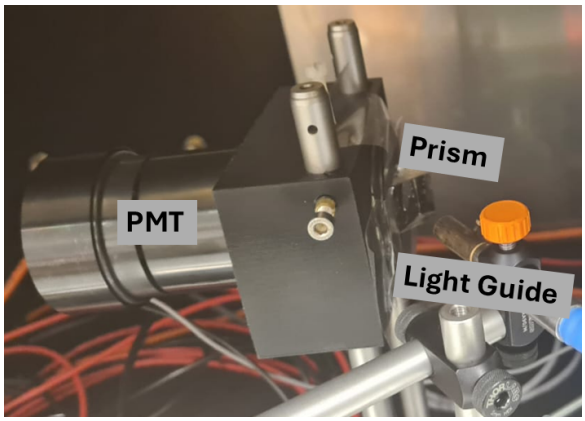

Fig. 6.10.: **Setup to measure the PMT's timing distribution under 45°.** We use a plastic prism to ensure the photons hit the cathode under 45°.

Comparing the timing distribution for 0 and 45° (see Fig. 6.11) we notice that both distributions have the same shape, but are shifted by $1.27\,\mathrm{ns}$. This would imply a path length difference of over $30\,\mathrm{cm}$ in vacuum and therefore can not be explained by irregularities in the setup. This leads to the possible conclusion of a shift in arrival time with respect to the incident angle. As we observe a broad angular distribution at the end of the tube the mix of different peak positions would lead to an overall broadening of the PMT's TTS. To consider this effect in the timing fit we convolute all other components with a Gaussian handling its width σ as a nuisance parameter. A more detailed study on the PMT's angular timing response is performed in Section 6.5.

6.3.3 WLS Paint

The timing of the wavelength-shifting process explained in Section 2.4 follows an exponential distribution

$$f_{\mathrm{WLS}}(t) = e^{-t/\tau} \tag{6.3}$$

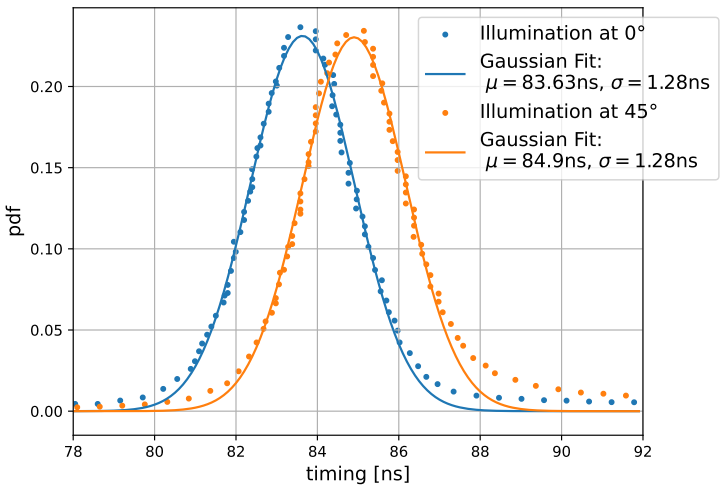

Fig. 6.11.: PMT timing distributions for different angles. We notice a shift by $1.27\,\mathrm{ns}$ between illumination under 0° and 45°.

with τ being the decay constant characterizing the time it takes an excited molecule to descent to one of its vibrational ground states. Measurements on the WLS timing conducted in [132] concluded in

$$\tau \approx 1.49\,\mathrm{ns}. \tag{6.4}$$

Fig. 6.12 shows the combined timing distribution compared to the PMT's TTS. We get a noticeably longer falling edge in the convolution compared to the almost symmetrical TTS of the PMT only.

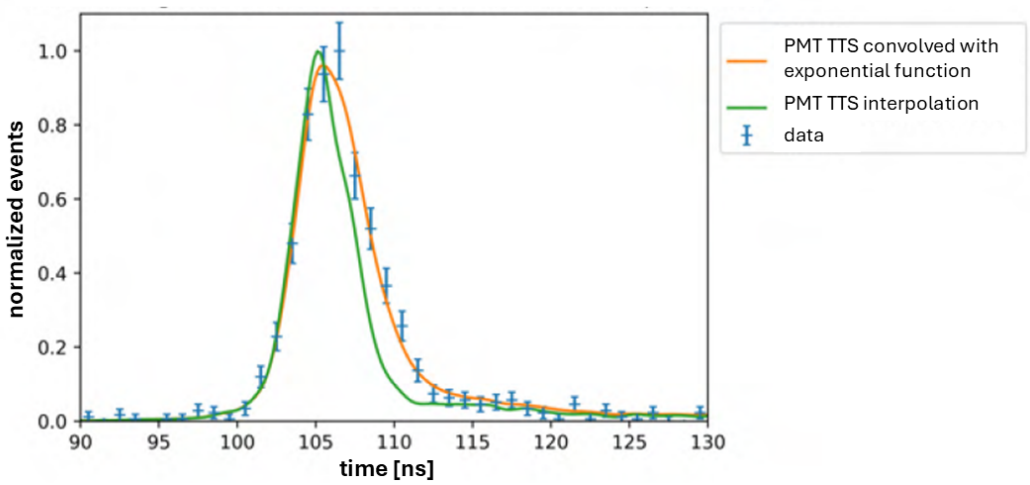

Fig. 6.12.: Timing of the WLS with PMT compared to the TTS of the PMT only [132]. Taken using a Hamamatsu R10806 PMT. The orange line was taken using a convolution between the interpolated TTS of the PMT and an exponential fit resulting in $\tau = 1.49\,\mathrm{ns}$. However, no error estimation was performed on it.

Only the Bis-MSB within the paint is sensitive to the wavelength of the pulser. Literature values suggest $\tau = 1.5\,\mathrm{ns}$ [31] which is considerably close to the measured value. However, the conducted measurements do not give us a proper error estimation. Different measurements taken previously and results from different publications resulted in values between $1.2\,\mathrm{ns}$ and $1.72\,\mathrm{ns}$ [131, 132] leaving us with a fairly large error range.

6.3.4 Tube Propagation

Because the analytical flattened timing model introduced in Section 4.5.4 does not reflect all effects as the simulation does, we will model the propagation inside the tube by using the simulation only. As previously mentioned, one end of the tube in the measurement setup is open which can lead to photon back-reflection at that end. To account for this in the simulation we use the setup illustrated in Fig. 6.13. We implement a tube with twice the length D of the tube actually used in the experiment, which can be read-out on both sides. The photons exiting on the right side have an effective distance of $2D - L$ which is also the effective distance of back-reflected photons. Additionally, we exclude photons exiting on the right side which do not fulfill the TIR criterion for back reflection of $\sin\theta > \frac{n_{\mathrm{air}}}{n_{\mathrm{PMMA}}} = \frac{1.0}{1.49}$. The resulting path length distribution is therefore the sum of these two contributions.

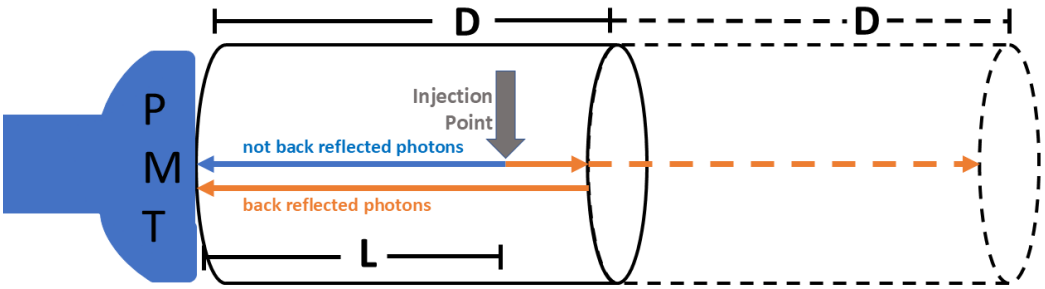

Fig. 6.13.: **Implementation of back-reflection in ALGO.** Back-reflected photons are considered by reading out photons exiting on right side of a tube with length $2D$ and cutting out all photons not satisfying the TIR criterion.

The simulation's output for different distances and attenuation lengths is shown in Fig. 6.14. The fractions of back-reflected photons generate a second, much smaller peak. Its height and position depend on the distance to the injection point L and the attenuation length of the tube. For small L, the two peaks have a larger separation as the path length difference increases. Further, the second peak gets smaller as the back-reflected photons travel a longer path increasing the number of absorbed and

scattered photons. The height of the back-reflected peak is particularly sensitive to the attenuation length as it disappears for attenuation lengths low enough. Using the peak from the back reflected photons increases the sensitivity of our fit with respect to the attenuation parameters. However, due to smearing out effects from the PMTs and WLS paint we will not be able to resolve the peak from the back reflected photons for high distances L.

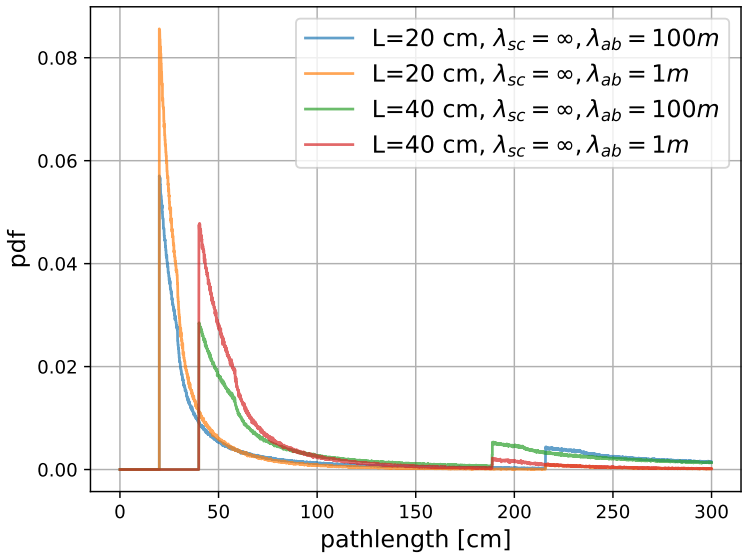

Fig. 6.14.: Simulated path length distributions considering back reflected photons. The simulation was done using a $2D = 180\,\text{cm}$ long PMMA tube with an outer diameter of $90\,\text{mm}$ in air. We notice the change of position and height of the second peak with respect to L and λ_{ab}.

6.4 Fit to Simulation

We want to fit our measured timing data to a model consisting of the contributions discussed in the previous section. The contributions are combined and fitted as already established in [131] using the convolution

$$(f * g)(t) = \sum_{t'} f(t')g(t - t'). \tag{6.5}$$

To perform the fit we generate a regular 2D grid of absorption and scattering coefficients μ_{ab}, μ_{sc}. The simulation generates a timing distribution from the tube's photon propagation considering the back-reflection at the open end. As the tube

is only read out in a window of $3.6\,\mathrm{cm}$ x $1.8\,\mathrm{cm}$, we exclude all simulated photons which do not exit the tube inside this window. These timing distributions are convolved with the PMT timing distribution discussed in Section 6.3.1 as well as with the contributions of the WLS paint and the PMT's angular effects. As the PMT's angular effect σ is not yet studied quantitatively and as the possible decay constants τ from the WLS timing cover a wider range, both of these effect are considered by nuisance parameters. A summary of all fitting parameters is shown in Tab. 6.1.

Parameter	**Range**
Absorption coeff. μ_{ab} [1/m]	[0.01, 0.5], 35 values
Absorption length λ_{ab} [m]	[2, 100]
Scattering coeff. μ_{sc} [1/m]	[0.02, 2.5], 35 values
Scattering length λ_{sc} [m]	[0.4, 100]
Gaussian width σ [ns]	[1.1, 2.2], 12 values
WLS decay constant τ [ns]	[0.8, 1.3], 6 values

Tab. 6.1.: **Ranges for fit parameters of timing fit.** A regular grid is used for μ_{ab} and μ_{sc} resulting in an irregular grid for $\lambda_{ab}, \lambda_{sc}$.

That leaves us with a 4-parameter fit which is performed for 8 different distances between photon injection point and PMT. One example fit result and its sensitivity to the absorption and scattering length is illustrated in Fig. 6.15. Relative to the best fit, we are changing one of these two fit parameters while keeping the other one constant. We observe the change in height of the first peak as well the sharpness of the second, back-reflection peak. While our best fit acknowledges back reflected photons as the distribution does not drop to 0 directly, many of them gets either absorbed or scattered out due to the relatively high attenuation.

Comparing to fits at larger distances (see Fig. 6.16) we are observing how the back-reflection peak slowly merges with the first peak, most likely effectively reducing the fit's sensitivity to the attenuation lengths. Further, we notice the wide range of fit parameters for different distances. To properly evaluate how consistent these different results are, we want to do an error analysis and sensitivity study.

6.4.1 Sensitivity Maps and Nuisance Parameters

To estimate the error on the fit parameters and visualize the correlation between absorption and scattering we use χ^2- **sensitivity maps**. For every set of fit parameters μ_{ab}, μ_{sc} the χ^2 is calculated while the two nuisance parameters are set to minimize the χ^2 for each data point. To better compare the two attenuation effects and later

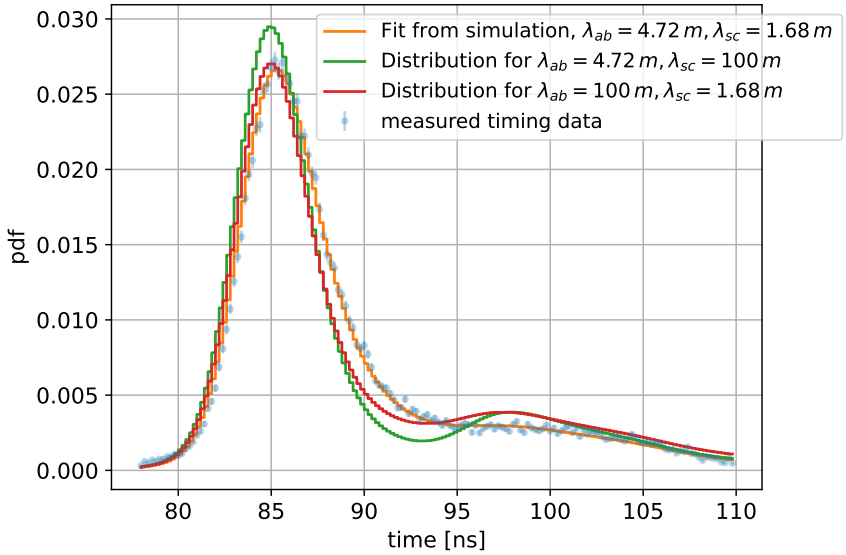

Fig. 6.15.: Best timing fit for $L = 8$ cm and comparison with different attenuation. σ=1.0 ns, τ =1.7 ns, χ^2/dof=2.4. The errors on the Probability Density Function (PDF) result from Poissonian errors on the number of hits. The errors on the fit parameters will be discussed later.

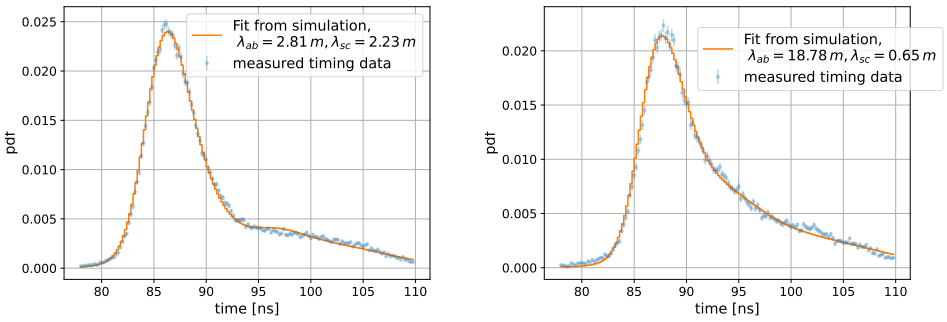

(a) L=20 cm, σ = 1.1 ns, τ = 1.6 ns, χ^2/dof= 2.7. **(b)** L=40 cm, σ = 0.9 ns, τ = 1.4 ns, χ^2/dof= 2.9.

Fig. 6.16.: Timing fits for different distances L. We notice the wide spread of λ_{abs} and λ_{sc}. Fits for other distances are shown in Section B.1.

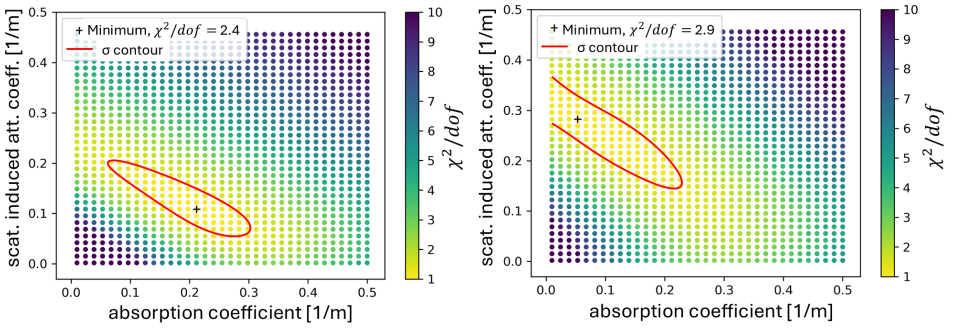

(a) L=8 cm (b) L=40 cm

Fig. 6.17.: Sensitivity maps and error contours for timing fits. The error contours are determined using the χ^2 error for a 2 parameter fit. The maps for other distances are shown in Section B.2.

combine them to one attenuation length the scattering length is converted into the **scattering induced attenuation length** $\lambda_{att,sc}$ which characterizes the lost photons due to scattering. Assuming uniformly distributed scattering angles only about 27% of scattered photons inside the tube will be lost while the rest will remain within the TIR angle. Therefore we get:

$$\begin{aligned} e^{-\frac{\lambda_{sc}}{\lambda_{att,sc}}} &= 1 - \left(\left(1 - \frac{1}{e}\right) \cdot 0.27\right) = 0.83 \\ \Leftrightarrow \frac{\lambda_{sc}}{\lambda_{att,sc}} &= \log\left(\frac{1}{0.83}\right) = \log(1.2) \\ \Leftrightarrow \boldsymbol{\lambda_{att,sc}} &= \boldsymbol{\lambda_{sc}/\log(1.2)}. \end{aligned} \tag{6.6}$$

The error contours are derived from the χ^2 error of a 2-parameter fit [131]:

$$\sigma_{\chi^2} = 2.3 \cdot \sqrt{2N_{dof}}. \tag{6.7}$$

N_{dof} is the number of degrees of freedom. For the error on the reduced $\chi^2 = \chi^2/N_{dof}$, we therefore get

$$\sigma_{\chi^2/N_{dof}} \approx 0.26. \tag{6.8}$$

Before constructing the sensitivity map, the errors of the Probability Density Function (PDF) are scaled to have $\chi^2/N_{dof} = 1$ for the best fit. The sensitivity maps for two different distances are shown in Fig. 6.17.

Considering the fits for all distances we can now perform a **combined fit**, where we sum up all χ^2 values to create the corresponding combined sensitivity map (see Fig. 6.18). The error contours show no clear correlation between absorption

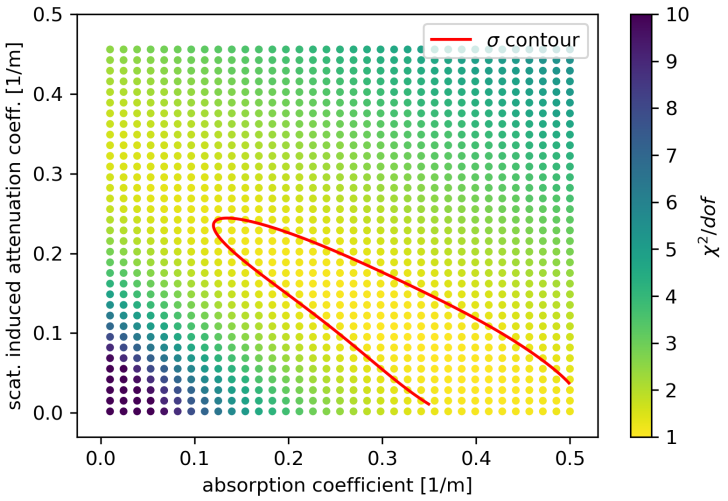

Fig. 6.18.: Sensitivity map of combined timing fit over all distances. The χ^2 values of all sensitivity maps were summed up and normalized to $\chi^2/N_{dof} = 1$ before drawing the error contour.

and scattering effects. However, the contours remain open toward small scattering coefficients which makes the attenuation effects being not fully constrained.
By combining absorption and scattering we derive an overall attenuation length of

$$\lambda_{att} = 2.33^{+0.56}_{-0.48}\,\mathrm{m} \tag{6.9}$$

which is compatible within 2σ with the value of $3\,\mathrm{m}$ determined by an efficiency measurement.

Fig. 6.19 shows the distributions of the two nuisance parameters corresponding to the best-fit points within the error contour in Fig. 6.18. While the σ distribution is almost limited to a single value of $1.0\,\mathrm{ns}$, the τ distribution features a wide spread of values above $1.6\,\mathrm{ns}$ even extending beyond the literature range of [1.3, 1.7] ns. We can try to explain this by remembering how the different contributions affect the overall timing distribution. Convolving a distribution with a Gaussian results in a symmetrical widening. We established previously that this can only result from a PMT effect. The contribution from the WLS on the other hand being an exponential, contributes similar to the timing of the tube propagation as both contributions feature an exponential dependence[3]. Therefore, these two contributions can not be fully decoupled leading to a lower sensitivity for both of them.

[3]The similarity increases even more for lower attenuation lengths resulting in an almost disappearing back-reflection peak.

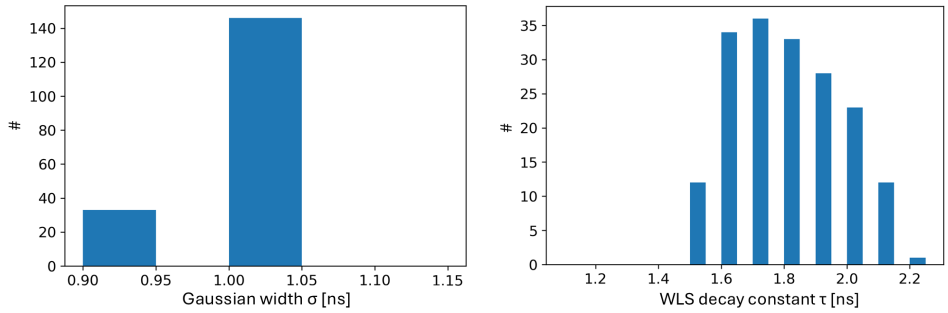

(a) Gaussian width σ distribution.

(b) WLS decay constant τ distribution. $\tau = (1.79 \pm 0.17)$ ns.

Fig. 6.19.: Distribution of nuisance parameters for combined timing fit. The distributions contain all used nuisance parameters over all fits for all 8 distances for the $\mu_{ab}, \mu_{att,sc}$ combinations located within the error contours shown in Fig. 6.18.

To estimate the mentioned systematic, we perform another combined fit while constraining τ to a value of $1.5\,\mathrm{ns}$ which was determined at previous measurements (e.g. [132]). The result (see Fig. 6.20) shows a noticeably smaller and closed error contour indicating an improved sensitivity for $\mu_{ab}, \mu_{att,sc}$. The resulting attenuation length of

$$\lambda_{att} = 2.60^{+0.45}_{-0.43}\,\mathrm{m} \tag{6.10}$$

is also consistent with the previously measured value of $3\,\mathrm{m}$.

6.4.2 Efficiency Fit

Complementary to the timing fit, we apply the same procedure to measure and fit the tube's efficiency. The measurement and data processing is performed as explained in Section 4.6. The simulation is performed over the same grid of $\lambda_{ab}, \lambda_{sc}$ values as for the timing fit. Instead of extracting the timing distribution, we use the ratio between the number of photons terminated at the tube's end and the number of injected photons (hereby the efficiency). We do not constrain the readout window at the tube's end in the simulation as well as in the measurement. One single fit (see Fig. 6.21) of efficiency as a function of the distance L is performed with the two fit parameters $\lambda_{ab}, \lambda_{sc}$ and the **scaling factor** s as a nuisance parameter to account for light losses within the measurement setup. Therefore we are expecting $s < 1$.

We notice an $s = 1.29$ clearly above the expectation of $s < 1$. Further, we observe a deviation for small distances. This systematic was already noticed in previous efficiency measurements [74, 115]. In Section 4.5.3 it was shown that this deviation can be explained by the **self-absorption model** which is not considered by

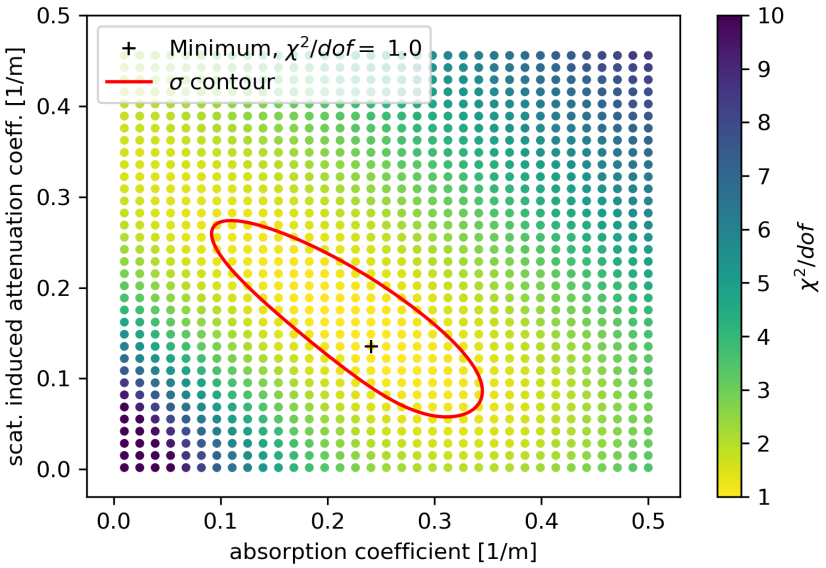

Fig. 6.20.: **Sensitivity map for combined timing fit for fixed $\tau = 1.5\,\mathrm{ns}$.** The contour shows a closed shape and increased sensitivity of the fitting parameters.

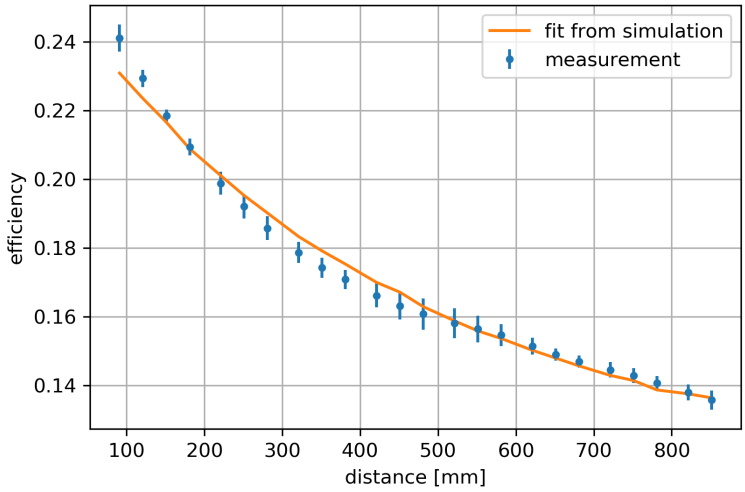

Fig. 6.21.: **Efficiency fit to simulation.** $\lambda_{ab} = 2.0\,\mathrm{m}$, $\lambda_{sc} = 35.05\,\mathrm{m}$, s=1.29, $\chi^2/N_{dof} = 1.5$. We perform one single fit with the absorption and scattering as fit parameters and the scaling factor s as a nuisance parameter to consider the losses within the efficiency setup.

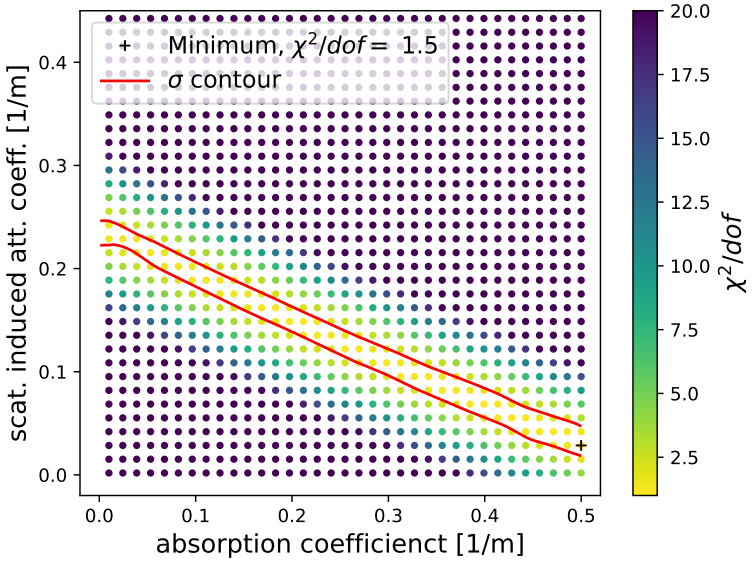

Fig. 6.22.: **Sensitivity map of efficiency fit to simulation.** We notice a clear correlation in the error contours. This results in a large error margin for the resulting attenuation length, but a very limited combination of $\lambda_{ab}, \lambda_{sc}$ for one fixed λ_{att}.

the simulation. Other possible explanations (or additional contributions to it) could be photons from the source hitting the PMT directly or propagating photons being scattered close to the exit and therefore hitting the PMT at the center. [115] was able to show a correlation between λ_{att} and s which prevents us from setting a hard constrain such as $s < 1$. The correlation would need to be studied in more detail to infer a more reasonable limit.

The sensitivity map in Fig. 6.22 displays a strong correlation between absorption and scattering contributions in contrast to the contours from the timing fit. The fit seems more constrained as there are less different contributions to it. Further, we are able to fit to absolute values here. As the shown correlation does not follow a 1:1 diagonal we get a large error margin for the resulting attenuation length of

$$\lambda_{att} = (2.69 \pm 1.49)\,\mathrm{m}. \tag{6.11}$$

This is a significantly worse sensitivity compared to the result from the timing fit and to the efficiency model fit with $\lambda_{att} = (3.041 \pm 0.191)\,\mathrm{m}$ from [6].

Finally, we can combine the results from the timing and efficiency fit in Fig. 6.23. We see that both error contours are compatible with each other. Overlapping

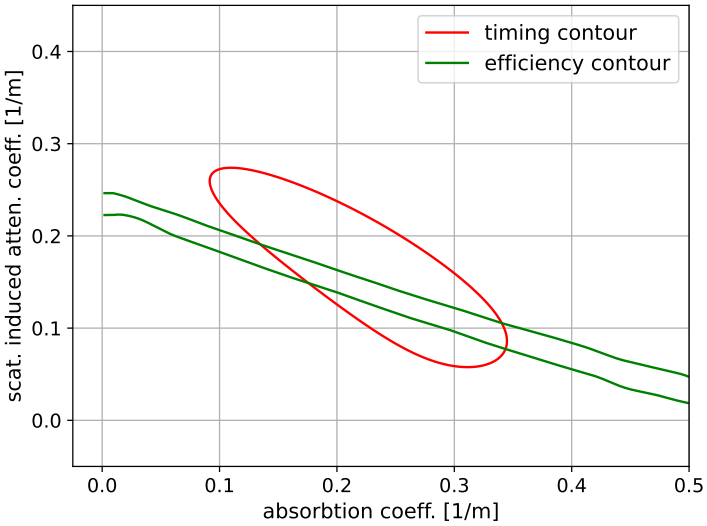

Fig. 6.23.: **Overlap between combined timing and efficiency fit to simulation.** We are using the combined timing fit with a fixed $\tau = 1.5\,\text{ns}$. The attenuation length resulting from the overlap of both curves is compatible with the results from the efficiency fit to the flattened model.

them constrains the correlation between the two contributions further. The final attenuation length from the two combined fit is given by

$$\lambda_{\text{att,combined}} = 2.65^{+0.38}_{-0.36}\,\text{m}. \tag{6.12}$$

Therefore, we observe consistent results between the timing and efficiency fit to the simulation as well as matching results between the combined timing and efficiency fit and the fit to the flattened efficiency model.

While these fits yielded positive results, there is still the PMT's angluar systematic left not fully characterized. In the following section, we want to make an attempt to study this contribution in more detail.

6.5 Angular Timing Response of the PMT

The distribution of the nuisance parameter σ shows an almost exclusive value of $\sigma = 1.0\,\text{ns}$, suggesting an underlying systematic there. We want to study the PMT's timing distribution for different incidence angles by using the setup explained in Fig. 6.24. Instead of the 2" Hamamatsu PMT, we are using a 5" ET9390B PMT as we are interested in characterizing the WOM PMTs and expecting to see a larger angular effect for PMTs with higher diameters. We measure both the efficiency and

timing distribution for different rotational positions of the PMT. The light source is focused onto the center of the PMT which is placed onto a rotational stage and turned by different angles. To cover a wide range of angles without being limited by refraction, a half-moon shaped prism made out of plexiglass with n=1.49 (same as the PMT glass) is coupled to the center of the PMT (not shown in photo). Its shape ensures a vertical incidence on the interface between air and prism and therefore no refraction between air and PMT glass. To measure the timing response we use the same light source and readout as for the tube timing measurement.

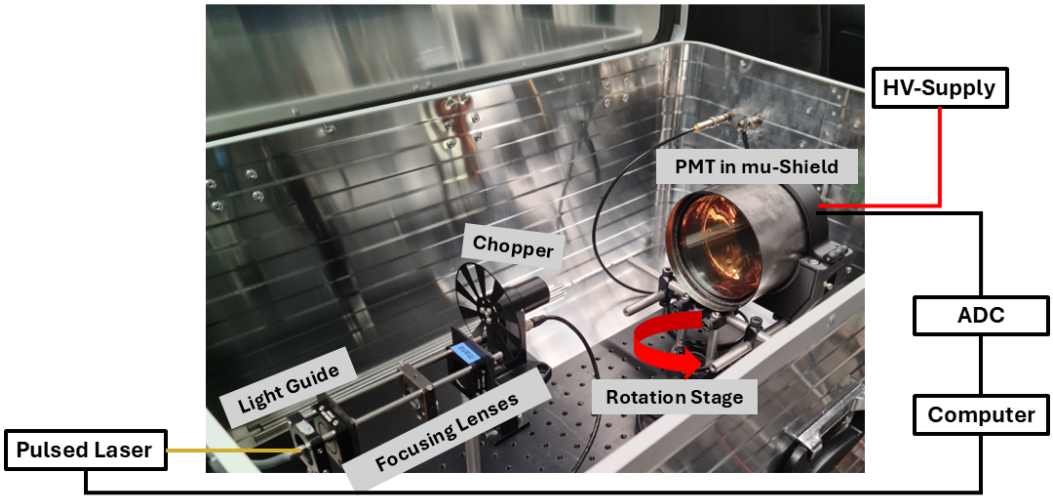

Fig. 6.24.: **Measurement setup for PMT's angle dependent timing response.** To measure the efficiency we replace the laser by the Xe-lamp and monochromator and use a Lock-in amplifier as readout (see Section 4.6).

The efficiency response showed an increase for steep angles suggesting an efficiency increase of about 8% the angular distribution at the tube's end (see Section 7.6 for details). The timing response at the center of the PMT[4] showed a shift in its distribution while the overall shape being unchanged, similar to the observations with the Hamamatsu PMT in Section 6.3.2. The correlation between the incidence angle and the mean of the resulting timing distribution, shown in Fig. 6.25, features several unexpected systematics. Although the measurement was taken symmetrically from both sides we notice a clear asymmetry in the height between positive and negative angles. Further, the minimum is located not in the center suggesting a shift along the x-axis. Additionally, there is a spike in the area around 0.52 (=30°) which is visible for several measurements of different PMTs. The mentioned systematics can be explained by uncertainties in the premature measurement setup like misalignment between light source and PMT or reflections

[4] A measurement on the outer ring, where the inner tube will be coupled, showed a constant shift over all angles about 5 ns higher than the average shift at the center.

inside the dark box. Although the measurement setup is still in an early stage of development and does not yet allow for a precise study of the angular response, the initial results already provide a valuable estimation of the upper limit of the contribution caused by this effect. To analyze this, we first interpolate the measured data using a linear relation to the steeper left side for angles below 0.

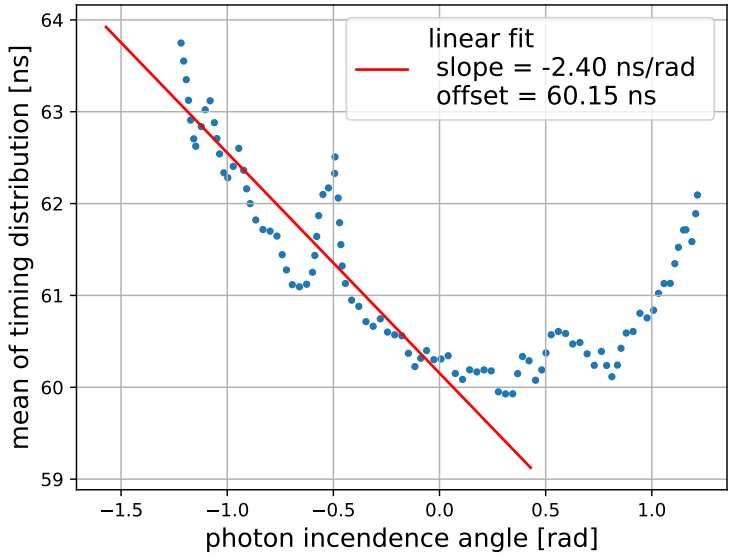

Fig. 6.25.: **Shift of PMT timing distribution with respect to the photon incidence angle measured at the center of the PMT (data from [133]).** As the PMT is located inside a mu-shield they are shadowing the light for high angles. We perform a linear fit to the steeper left side to get an estimation for the upper limit of this dependency.

To evaluate the effect of angular dependence on the WOM's timing distribution we need to weight the angular correlation with the angle distribution of photons exiting the tube. We get this θ distribution from our simulation of the inner tube considering back-reflected photons from the open end (see Fig. 6.26). For each θ value we get a timing shift value and therefore a timing distribution (approximated to be Gaussian) with a different mean μ and fixed standard deviation $\sigma = 1.88\,\text{ns}$.

We now sum up and normalize all Gaussians to get the timing distribution resulting from the PMT's TTS considering its angular response. The result is a Gaussian with $\boldsymbol{\sigma = 2.00\,\text{ns}}$ which is only a slight increase (see Fig. 6.27). Our fit result from Section 6.4 on the other hand, suggests a convolution with a Gaussian of $\boldsymbol{\sigma_{conv} = 1.0\,\text{ns}}$ which would result in a higher width of $\boldsymbol{\sigma = 2.13\,\text{ns}}$. However, we

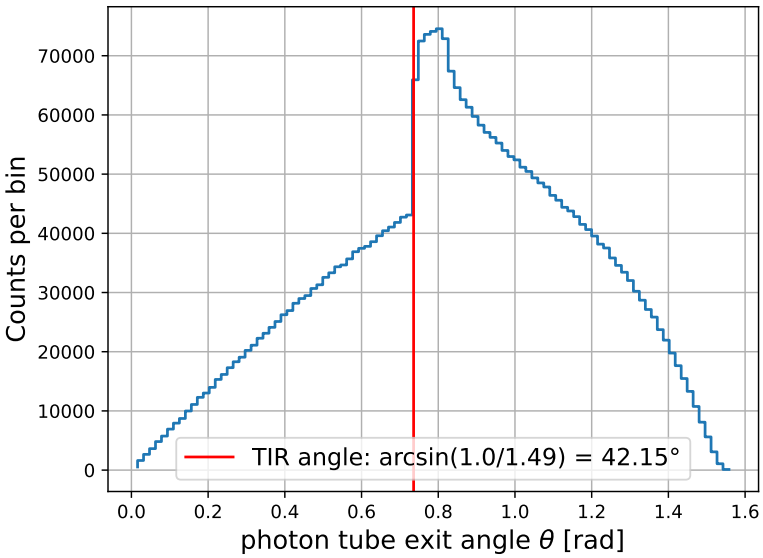

Fig. 6.26.: Simulated angular distribution of photons exiting the tube. D=90 cm, L=40 cm, $\lambda_{ab} = 3\,\mathrm{m}$, $\lambda_{sc} = \infty$. We notice a sudden increase starting at an angle of 42.15° which is the TIR angle between air and PMMA as there are no back-reflected photons for smaller angles. All exiting photons for $\theta < \theta_{\mathrm{TIR}}$ are therefore direct hits.

need to consider that the angular response can vary between different PMT models.

We can perform the same kind of estimation for the smaller Hamamatsu PMT using the two data points at 0 and 45° with a timing shift of $1.28\,\mathrm{ns}$ assuming a linear correlation. The resulting slope of $\boldsymbol{m = 1.65\,\mathrm{ns/rad}}$ is noticeably smaller compared to the measurement of the WOM PMT. Summing up all Gaussians with different timing shifts concludes in a timing width of $\boldsymbol{\sigma = 1.36\,\mathrm{ns}}$ compared to the initial width of $\mathbf{1.25\,ns}$. The expected width considering the nuisance parameter from the fit would be $\boldsymbol{\sigma = 1.60\,\mathrm{ns}}$. We can use the property of convolving two Gaussians with σ_1 and σ_2

$$\sigma = \sqrt{\sigma_1^2 + \sigma_2^2} \tag{6.13}$$

to infer the actually expected result for the nuisance parameter σ_{conv} taken the observed angular timing response of the used PMT.

$$\sigma_{\mathrm{conv}} = \sqrt{\sigma^2_{\mathrm{PMT+angle}} - \sigma_{\mathrm{PMT}}} = \sqrt{(1.35\,\mathrm{ns})^2 - (1.25\,\mathrm{ns})^2} = 0.51\,\mathrm{ns} \tag{6.14}$$

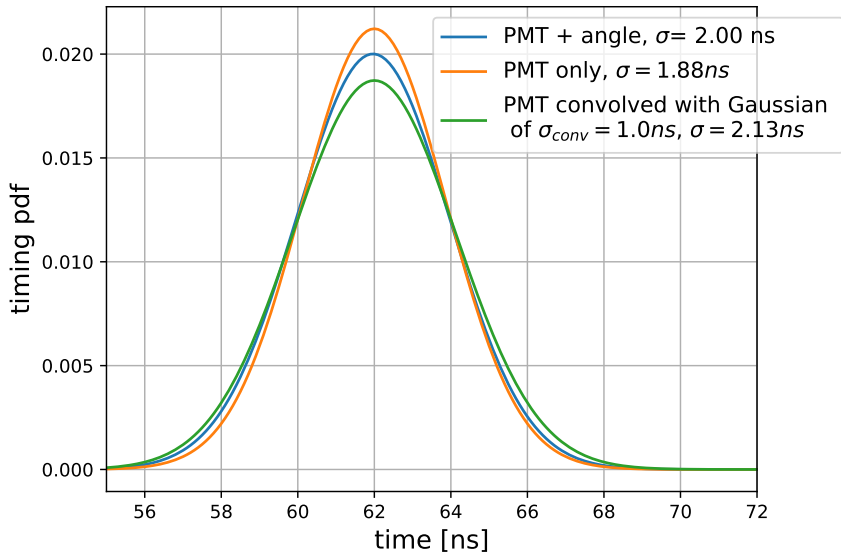

Fig. 6.27.: **Comparison between the timing distributions considering the PMT's angular response and the expectation based on the timing fit's nuisance parameter.** We compare the timing distributions of the vertical illuminated ET9390B PMT, the sum of the timing distributions under different angles and the initial timing distribution convolved with a Gaussian of $\boldsymbol{\sigma_{\text{conv}} = 1.0\,\text{ns}}$ which was suggested by the fit's result for the nuisance parameter.

Therefore, we can conclude a discrepancy between measurement and expectation. This could be caused either by an uncertainty in the angular response estimation or a yet unconsidered contribution to the overall WOM timing.

6.6 Timing of the Upgrade WOM

Finally, we measure the timing distribution of the full WOM as it will be constructed and deployed into IceCube to determine its timing resolution. We couple a coated quartz tube with a length of $D = 760\,\text{mm}$ and outer diameter $R = 115\,\text{mm}$ between two ET9390B PMTs. We measure the timing distribution for different positions on the tube (see Fig. 6.28a). We see the expected movement of the distribution to the right with increasing distance and the number of hits decreasing due to increased path lengths while the standard deviation σ of each distribution stays constant.
The overall timing distribution is obtained by summing over all individual distribu-

tions at the various distances (see Fig. 6.28b). Both PMTs used in the WOM show similar timing resolutions:

$$\sigma_{top} = 13.60\,\text{ns} \quad \sigma_{bot} = 13.17\,\text{ns}. \tag{6.15}$$

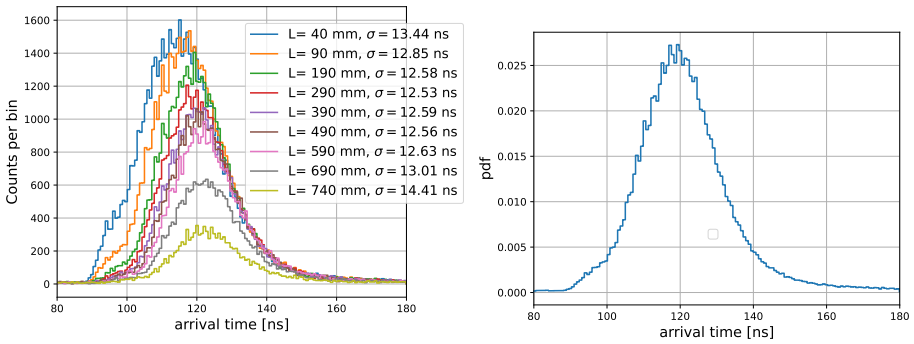

(a) Timing for different distances L to the PMT.

(b) Combined timing distribution over all distances, $\sigma = 13.17\,\text{ns}$.

Fig. 6.28.: Timing distribution of the full IceCube Upgrade WOM. The timing was measured for different distances using the optically fully assembled first constructed WOM reading out its bottom PMT. We do not expect significant timing contributions from the transmission through the pressure vessel and filling material.

Comparing the WOM's timing resolution to the TTS of other Upgrade modules like the mDOM with $\sigma_{\text{mDOM}} = 1.62\,\text{ns}$ and considering the requirement for Upgrade modules of $\sigma_{\text{req}} < 5\,\text{ns}$ [134], we find that the current WOM design results in a noticeably reduced timing performance.

6.7 Conclusion and Outlook

In this chapter, we established a method to extract attenuation properties of the WOM inner tube from its timing distribution, combining measurements, simulations, and analytical modeling. The observed distribution reflects contributions from the PMT, WLS processes, and photon propagation, all effectively captured in the combined approach.

While the timing fit yields consistent and independent constraints on absorption and scattering lengths and displays no clear correlation, the WLS decay constant τ remains a source of uncertainty due to its potential correlation with attenuation

effects. A separate efficiency-based fit confirms the timing-based results, and their combination yields an attenuation length of

$$\lambda_{\text{att,combined}} = 2.65^{+0.38}_{-0.36}\,\text{m} \tag{6.16}$$

in line with expectations, though with larger uncertainty than the efficiency fit to the flattened model. Building on the work initiated in [107], follow-up studies separating the attenuation effects of the tube and paint layer could deepen our understanding of the module and reveal new opportunities for optimization and application.

A dedicated measurement of the PMT's angular response revealed systematic effects, including asymmetries and deviations in the fitted widening parameter σ, suggesting that the current understanding of the PMT response remains incomplete. Improved experimental control will be necessary to fully quantify this contribution.

Overall, the developed method offers a complementary perspective on the inner tube's attenuation properties and enables an independent validation of its behavior. However, with a timing resolution of approximately $13\,\text{ns}$—limited by propagation effects rather than the PMT's intrinsic transit time—the WOM remains less competitive for timing-critical applications such as IceCube.

7 Effective Area of the WOM

The effective area A_{eff}, which is given by

$$A_{\text{eff}} = A_{\text{photo}} \cdot \frac{N_{\text{det}}}{N_{\text{hit}}} \tag{7.1}$$

can be used to evaluate an optical module's performance based on its efficiency, the number of detected photons N_{det} divided by the number of incident photons N_{hit}, and photosensitive area A_{photo}. This quantity is frequently used to compare the performance between modules. Because of the WOM's non trivial light propagation through the module (including absorption and re-emission) determining this value requires an extensive study considering a large variety of factors and their correlations.
In this chapter, we will determine the WOM's efficiency and effective area discussing its contributions. The results will then be used to evaluate the WOM's performance relative to other IceCube modules. We will use simulation and analytical calculations to make a prediction on the effective area to be verified by measurements in Chapter 8.

7.1 Overview of Contributions

As already introduced in Section 2.6, the effective area can be determined from the photosensitive area of the module A_{photo} and the efficiency for different wavelengths and angles $\epsilon(\lambda, \theta, \phi)$. For our application in IceCube we use the **effective cross-section area** averaged over all expected zenith and azimuth angles θ, ϕ:

$$A_{\text{eff}}(\lambda) = \frac{A_{\text{photo}}}{4\pi} \cdot \int_0^{2\pi} \int_0^{\pi} \epsilon(\lambda, \theta, \phi) \cos\theta \sin\theta \, d\theta d\phi = A_{\text{photo}} \cdot \epsilon_{\text{full}}(\lambda). \tag{7.2}$$

An ideal spherical detector of radius r would therefore have an effective cross-section area of $A_{\text{eff}} = \pi r^2$.

The efficiency results from several contributions at different stages of the light propagation inside the module:

$$\epsilon(\lambda,\theta,\phi) = \epsilon_{\text{trans}}(\lambda,\theta,\phi)\cdot\epsilon_{\text{WLS}}(\lambda)\cdot\epsilon_{\text{TIR}}\cdot\epsilon_{\text{att}}\cdot\epsilon_{\text{glue}}\cdot\epsilon_{\text{PMT}} + \epsilon_{\text{direct}}(\lambda,\theta,\phi). \tag{7.3}$$

We can separate these contributions into three categories:

- First, we have contributions happening **before wavelength-shifting** which include the transmission efficiency through the pressure housing and PFPE ϵ_{trans} and the absorption and shifting efficiency of the WLS paint $\epsilon_{\text{WLS, ab}}$. Both depend on the incidence angles θ, ϕ and/or the wavelength λ of the incoming Cherenkov light. As we can choose the WLS paint layer to be thick enough for the maximum absorption efficiency we do not expect an angular dependency in ϵ_{WLS}. Its wavelength dependency results in $\epsilon_{\text{WLS}} = 0$ for a wavelength λ outside the WOM's absorption spectrum shown in Fig. 4.3.

- The contributions **after the emission** of shifted light are independent on θ, ϕ and λ, as the wavelength-shifted photons are emitted isotropically and follow the same emission spectrum, independent on the wavelength of the initially absorbed photons. All the determined values are therefore already averaged over the emitted spectrum and solid angle. The factor ϵ_{TIR} is the probability of a shifted photon being captured inside the tube while ϵ_{att} considers the photon propagation loss inside the tube due to absorption and scattering. The last two factors describe the PMT coupling and detection. The factor ϵ_{glue} quantifies the glue transmission as discussed in Section 5.3. The value ϵ_{PMT} is the efficiency of the PMT determined by the QE measurements with corrections for the surface position and emission spectrum.

- Finally, there is a contribution **independent of the wavelength-shifting process**, which we refer to as **direct PMT hits**. This consists of either photons with a very steep zenith angle that hit the outer part of the PMT instead of the inner tube or photons that are not absorbed by the WLS and are directly detected by the PMTs.

As reference area A_{photo} we use the projected area of our module, where the transmitted photons would eventually hit the inner tube:

$$A_{\text{photo}}^{\text{proj}} = d_{\text{vessel}}\cdot h_{\text{tube}} = 1314.8\,\text{cm}^2. \tag{7.4}$$

Further, we can remove the ϕ dependency because of the underlying cylindrical symmetry as well as using only half the zenith range leaving us with following formula for the effective area:

$$\begin{aligned} A_{\text{eff}}(\lambda) =& A_{\text{photo}}^{\text{proj}} \cdot \left(\int_0^{\pi/2} \epsilon_{\text{trans}}(\lambda, \theta) \cos\theta \sin\theta \, d\theta \cdot \epsilon_{\text{WLS}}(\lambda) \cdot \epsilon_{\text{TIR}} \cdot \epsilon_{\text{att}} \cdot \epsilon_{\text{glue}} \cdot \epsilon_{\text{PMT}} \right. \\ &\left. + \int_0^{\pi/2} \epsilon_{\text{direct}}(\lambda, \theta) \cos\theta \sin\theta \, d\theta \right) \\ =& A_{\text{photo}}^{\text{proj}} \cdot \left(< \epsilon_{\text{trans}}(\lambda) > \cdot \epsilon_{\text{WLS}}(\lambda) \cdot \epsilon_{\text{TIR}} \cdot \epsilon_{\text{att}} \cdot \epsilon_{\text{glue}} \cdot \epsilon_{\text{PMT}} + < \epsilon_{\text{direct}}(\lambda) > \right) . \end{aligned} \tag{7.5}$$

In the following sections, these contributions will be determined and discussed in detail.

7.2 Transmission

Before hitting the WLS paint layer, the photons are transmitted through two layers, the pressure vessel and filling material. That is a total of three surface interactions, where refraction and Fresnel losses need to be considered (see Fig. 7.1). Further, we would expect losses due to photons "missing" the next layer, because of a smaller diameter (depending on each photon's incidence angle).

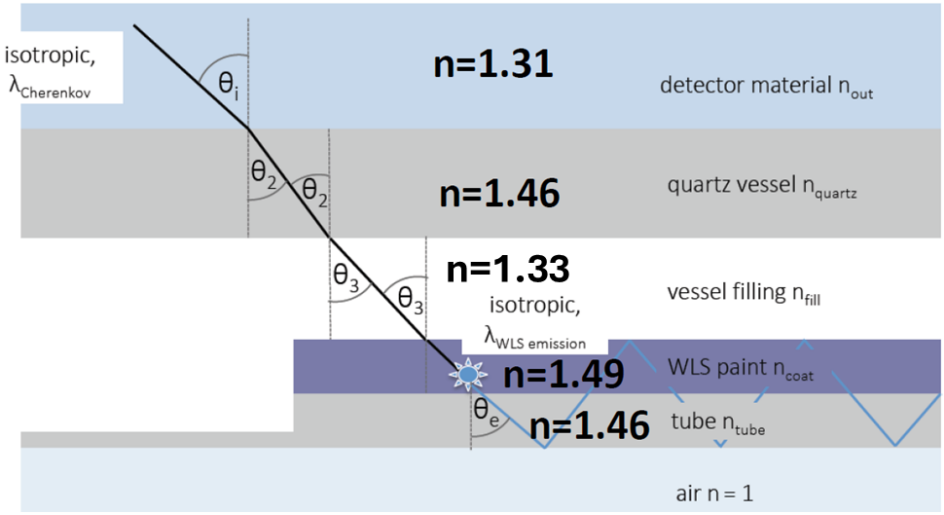

Fig. 7.1.: **Visualization of photon propagation through WOM transmission layers viewed from the side [135].** At each surface interaction, one needs to calculate refraction and Fresnel losses. We determine the efficiency for a deployed WOM with ice (n=1.31) as the detector material.

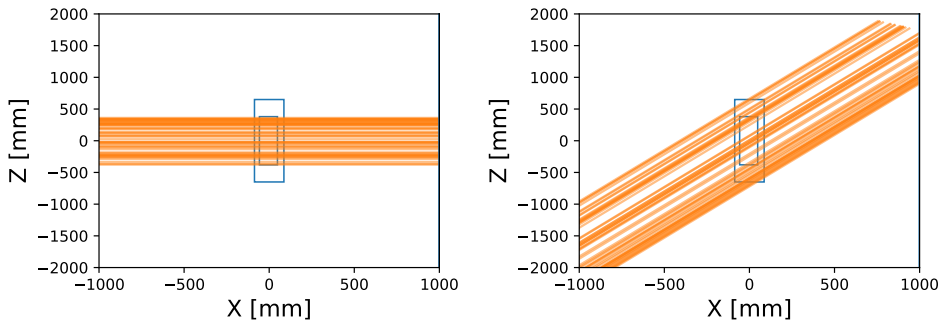

(a) $\theta = 0°$ (b) $\theta = 45°$

Fig. 7.2.: Visualization of generated photons for different zenith angles θ hitting the WOM. The WOM's pressure vessel and inner tube are shown for comparison. The direction of the photons is shown as straight lines without considering refraction due to layer transmission.

We want to determine the transmission efficiency using a customized python Monte-Carlo (MC) simulation [124]. It implements every transmission layer as a hollow cylinder located inside a certain detector material (chosen to be either ice or air). We use following values for the diameter d and height h for every layer:

$$\begin{aligned} d^{\text{outer}}_{\text{vessel}} &= 173\,\text{mm} \quad d^{\text{inner}}_{\text{vessel}} = 145\,\text{mm} \quad h_{\text{vessel}} = 1300\,\text{mm} \\ d^{\text{outer}}_{\text{filling}} &= 145\,\text{mm} \quad d^{\text{inner}}_{\text{filling}} = 115\,\text{mm} \quad h_{\text{filling}} = 760\,\text{mm} \\ d^{\text{outer}}_{\text{tube}} &= 115\,\text{mm} \quad d^{\text{inner}}_{\text{tube}} = 110\,\text{mm} \quad h_{\text{tube}} = 760\,\text{mm}. \end{aligned} \tag{7.6}$$

Photons are generated perpendicular to a plane of $A_{\text{plane}} = d_{\text{vessel}} \cdot h_{\text{tube}}(\theta)$ located at some distance from the WOM. This plane is then rotated around the WOM for different zenith angles θ in the range $[0, \pi/2]$[1] (see Fig. 7.2), adjusting the height so that all generated photons hit the outer layer of the WOM.

The distribution of generated θ angles follows a $\cos$-distribution to consider for the projected plane onto the WOM. This is illustrated in Fig. 7.3 showing the simulated distribution of $\cos\theta$. For runtime reasons, instead of generating many photons for each θ, we propagate a single photon randomly located on a plane for each θ sampled from a $\cos$-distribution. This produces enough statistics over all y, z, θ coordinates.

For every generated photon the simulation calculates its intersection point with the next layer. If such a point is found, we calculate the photon's refraction angle relative to the normal of the tangential plane at the intersection point as well as its transmittance $\epsilon^{\text{Fresnel}}(\theta, n_1, n_2)$ given by the Fresnel formulas. The ray

[1] Due to previously mentioned symmetry reasons we do not need to go through the whole range of $[0, \pi]$.

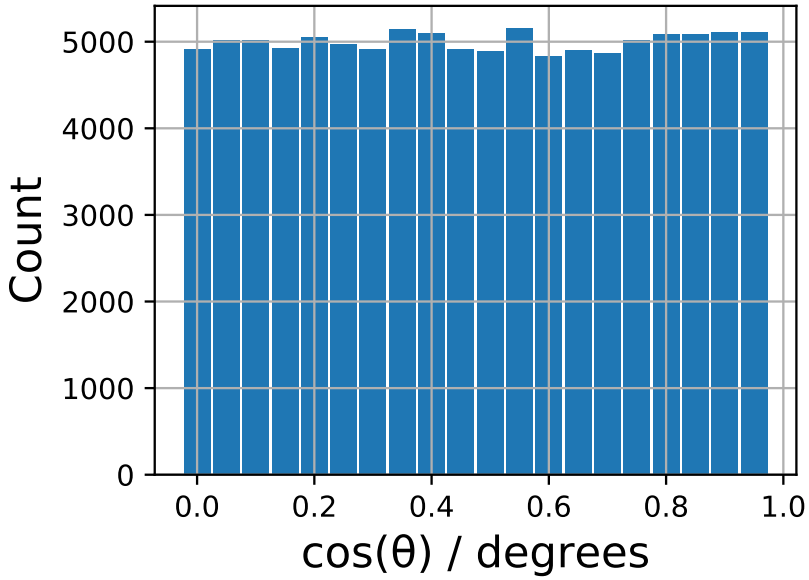

Fig. 7.3.: **Distribution of the cos of incident zenith angles θ [124].** We either weight our efficiency with $\cos\theta$ or sample θ from a $\cos$-distribution to consider for the plane's projected area of the WOM.

is then propagated further with its new direction until it either misses the next layer or reaches the inner tube. If it misses one layer, it contributes to 0, otherwise it is weighted by the product of all transmittances. In total, we calculate three intersections and efficiencies (ice $\rightarrow$ vessel $\rightarrow$ filling $\rightarrow$ tube). Therefore the efficiency considering all photons over all θ is given by:

$$< \epsilon_{\text{trans}} >= \frac{1}{N_{ph}} \cdot \sum_{ph(\theta)} \Theta_1 \epsilon_1^{\text{Fresnel}} \Theta_2 \epsilon_2^{\text{Fresnel}} \Theta_3 \epsilon_3^{\text{Fresnel}}. \tag{7.7}$$

Θ is the Heaviside function, contributing to 1, if the photon intersects with the next layer, and 0 otherwise. N_{ph} is the total number of generated photons chosen to be 10,000. $ph(\theta)$ follows a $\cos$-distribution in θ.
To evaluate the transmission for a fixed θ, we generate all photons originating from one plane and weight the efficiency with $\cos\theta$ to consider for the projected plane:

$$\epsilon_{\text{trans}}(\theta) = \frac{1}{N_{ph} \cdot \cos\theta} \cdot \sum_{ph} \Theta_1 \epsilon_1^{\text{Fresnel}} \Theta_2 \epsilon_2^{\text{Fresnel}} \Theta_3 \epsilon_3^{\text{Fresnel}}. \tag{7.8}$$

The θ dependent transmission efficiency in Fig. 7.4 shows a steady decline caused by photons missing the next inner layer on the z-axis due to angles being too steep.

Comparing the curves for ice and air as the detector material we see the same trend, but notice an increase of about 30% in air. Due to a larger difference in

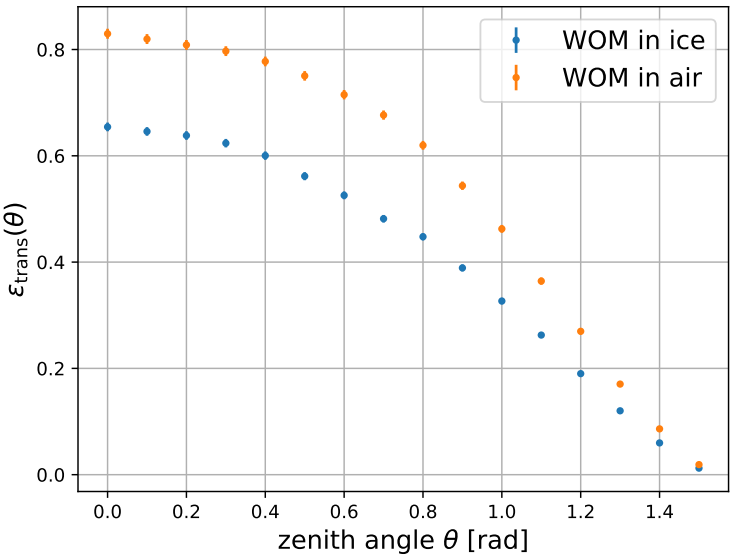

Fig. 7.4.: Simulated transmission efficiency in ice and air for different zenith angles. Calculation according to Eq. 7.8 with $N_{ph} = 10,000$. Errors result from poissonian errors on the counted photons.

refractive indices between n_{air} and n_{quartz} we get smaller refraction angles which result in a focusing effect towards the inner layers causing less photons to miss the next layer. The Fresnel losses are minor relative to the effect of photons missing the next layer.

In Fig. 7.5 we see the the transmission efficiency averaged over all angles for different refractive indices for the filling material n_{filling}. The best transmission is achieved for $n_{\text{filling}} = n_{\text{quartz}}$ as there will be no refraction and Fresnel losses for this transition in this case[2]. For PFPE with $n_{\text{PFPE}} = 1.33$ as the filling material compared to $n_{\text{air}} = 1.0$ we get for a WOM deployed in ice

$$< \epsilon_{\text{trans}}^{\text{PFPE}} >= 0.306 \pm 0.006 \quad < \epsilon_{\text{trans}}^{\text{air}} >= 0.094 \pm 0.003 \tag{7.9}$$

which shows a significant increase of more than factor 3 in the transmission efficiency when using the optimal filling material.

On top of the transmission efficiency at layer boundaries, we need to consider the absorption losses for the propagation through the vessel and filling material. For that, we first need to determine the expected value for the photon's path length

[2] However, ϵ_{TIR} would be 0 in that case.

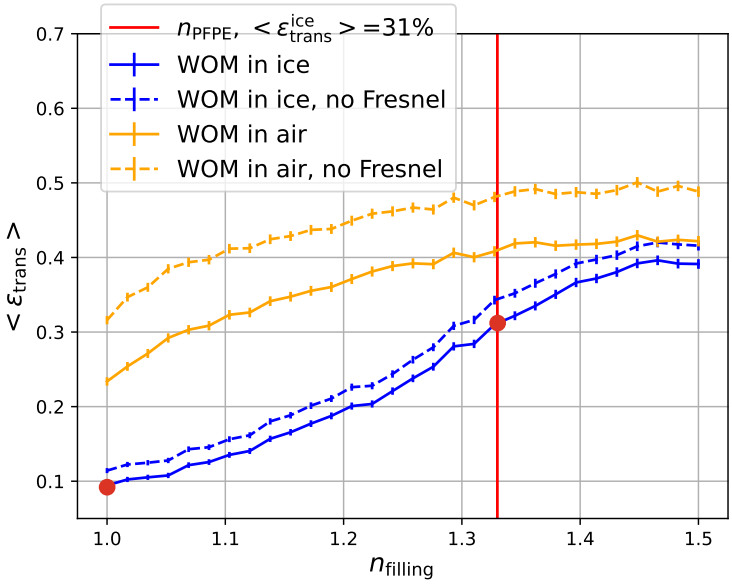

Fig. 7.5.: Combined transmission efficiency over all zenith angles for different filling materials. The zenith angles are sampled from a cos-distribution. We compare the curves in ice and air with and without considering the Fresnel losses to evaluate their contribution. We evaluate the efficiencies of a WOM deployed in ice (straight blue line) for PFPE and air filling (marked by red dots).

$< l >$ through a layer of thickness d. Given the angular dependent path length $l(\theta)$ and the normed density function of a cos-distribution $p(\theta)$[3]

$$l(\theta) = \frac{d}{\cos\theta} \qquad p(\theta) = 2\cos\theta\sin\theta \tag{7.10}$$

the expected path length $< l >$ is determined to

$$< l >= \int_0^{\pi/2} l(\theta)\cdot p(\theta)\, d\theta = 2d\int_0^{\pi/2} \sin\theta\, d\theta = 2d. \tag{7.11}$$

We apply that to the wall thicknesses of the pressure vessel and filling compartment and using the wavelength dependent absorption lengths from Fig. 4.7 to determine the full transmission efficiency shown in Fig. 7.6. We get peak values of $\epsilon^{\text{PFPE}}_{\text{trans}} \approx 0.3$ for $\lambda > 330\,\text{nm}$ and $\epsilon^{\text{air}}_{\text{trans}} \approx 0.095$ for $\lambda > 260\,\text{nm}$. As we assume no PFPE absorption losses in air get a notably lower UV-cutoff there.

[3]The sin term results for the differential of the solid angle and 2 is the normalization factor form $\int_0^{\pi/2} \cos\theta\sin\theta\, d\theta = \frac{1}{2}$.

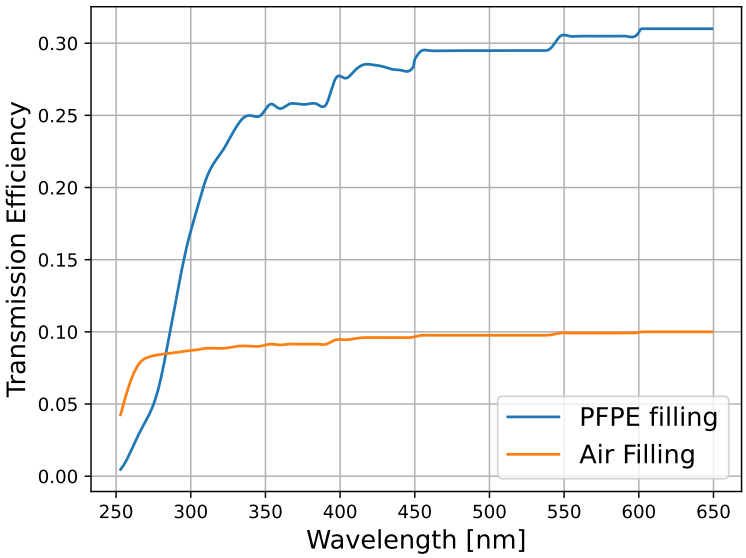

Fig. 7.6.: **WOM wavelength dependent transmission efficiency including absorption losses in quartz and PFPE.** The contribution from absorbtion was determined by applying the absorption coefficients from Fig. 4.7 to the expected value for the path length from Eq. 7.11.

7.3 Absorbtion and Wavelength-shifting

The absorption and shifting efficiency ϵ_{WLS} combines from from the factors

$$\epsilon_{\text{WLS}} = \epsilon^{\text{abs}}_{\text{WLS}}(\lambda) \cdot \epsilon^{\text{QY}}_{\text{WLS}}(\lambda). \tag{7.12}$$

The quantity $\epsilon^{\text{abs}}_{\text{WLS}}(\lambda)$ is the measured absorption spectrum of the WLS paint which has been shown to reach 100% for $\lambda = 280 - 380\,\text{nm}$ assuming high enough paint layer thickness [72, 73]. The value $\epsilon^{\text{QY}}_{\text{WLS}}$ is the absolute quantum light yield of the paint limiting its shifting efficiency. It was determined for the Bis-MSB to [136]:

$$\epsilon^{\text{QY}}_{\text{WLS}} = 0.926 \pm 0.053 \tag{7.13}$$

for $\lambda = 345 - 430\,\text{nm}$. To determine ϵ_{WLS} two different approaches can be used:

- We can measure $\epsilon^{\text{abs}}_{\text{WLS}}$ using a transmission measurement of a coated slide. The slide is illuminated at different wavelengths and the fraction of transmitted light behind the slide is measured. A transmission of 0 therefore corresponds to $\epsilon^{\text{abs}}_{\text{WLS}} = 100\%$ (see [73] for more details). This method however does not consider possible wavelength systematics for the re-emitted light.

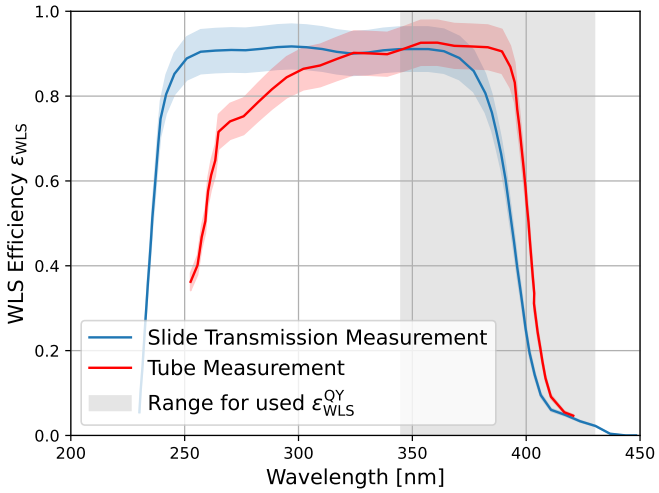

Fig. 7.7.: Wavelength-shifting efficiency ϵ_{WLS} determined by two different measurements. Both measurements produced relative efficiency curves which were scaled with ϵ^{QY}_{WLS} form Eq. 7.13. Data for transmission measurement taken from [73] and data for tube measurement from [6].

- The other approach would be measuring the relative curve for ϵ_{WLS} directly using a coated tube. The tube is illuminated with different wavelengths and the shifted and propagated photons are read out by a PMT coupled to its end (see Section 4.6). The curve is then scaled with ϵ^{QY}_{WLS} from Eq. 7.13 as the peak value located at $\lambda = 380\,\mathrm{nm}$ is expected to have an efficiency of 92.6%.

Comparing the results of both approaches in Fig. 7.7 we notice different shapes for both curves suggesting that ϵ^{QY}_{WLS} is not constant over the full wavelength range. While the absorption curve shows a plateau between $250\,\mathrm{nm}$ and $370\,\mathrm{nm}$ and cutting off beyond that, the curve from the tube measurement continuously falls of for $\lambda < 350\,\mathrm{nm}$ and cuts off earlier. Incident photons in the low UV-range are absorbed by p-Terphenyl and shifted into the absorption range of Bis-MSB, where they are shifted again. Both processes happen with an efficiency below 100% which reduces the detected fraction of photons with lower wavelengths (see [71] for details on the two wavelength-shifters). Additionally, while the slide measurements were performed for arbitrary high paint layer thickness to reach maximum absorption, this was not the case for the coated tube. Therefore, efficiency losses due to an insufficient paint layer thickness can not be excluded. We also notice the right falling edge being further shifted to higher wavelengths of about $390\,\mathrm{nm}$ for the tube measurement. This could either be an effect from the measurement procedure or another not fully characterized effect of either the paint or the tube geometry.

Since the results from the tube measurement reflect the actual situation in the WOM more closely, we will use these for the remaining analysis.

7.4 Capture by TIR

After transmission and wavelength-shifting, the photons need to be captured inside the tube to be further propagated towards the PMTs. Whether an emitted photon stays within the the inner tube is determined by the reflectance R resulting from the Fresnel formula for every interface interaction. For N interactions we therefore get [6]:

$$\epsilon_{\text{TIR}} = \frac{1}{2}\int_0^{\pi} (R(\theta))^N \sin\theta \, d\theta \tag{7.14}$$

with θ being the angle between the photon's trajectory $\vec{p}$ and the surface normal $\vec{n}$ with $\cos\theta = \vec{p}\cdot\vec{n}$.
As we assume a large number for N for most photons, all $R(\theta) < 1$ would eventually contribute to 0. Therefore we consider only photons with the the critical TIR angle $\theta > \theta_C$:

$$\lim_{N\to\infty} \epsilon_{\text{TIR}} = \frac{1}{4\pi}\int_{\Omega} \Theta(|\vec{p}\cdot\vec{n}| - \cos\theta_C)\, d\Omega. \tag{7.15}$$

Integrating over the solid angle Ω also considers for the curvature of the tube. [6]

The fraction of captured photons changes with the the emission point relative to the radius r_{tube} of the tube $x_0 = r_{\text{em}}/r_{\text{tube}}$. Fig. 7.8 illustrates the fraction of captured photons for different x_0 with respect to their polar θ and azimuth angle ϕ. If the photons are emitted from the center ($x_0 = 0$), all photons within θ_C are captured while the rest is lost, independent on ϕ. Moving x_0 further to the outside causes the angle between $\vec{p}$ and $\vec{n}$ to increase for a fixed ϕ which lets photons with $\theta < \theta_C$ with certain ϕ angles being captured (see bottom part of Fig. 7.8). Starting from $x_0 = \sin\theta_C$ even horizontally emitted photons with $\vec{p} \perp \vec{r_{\text{em}}} \perp \vec{z}$ perpendicular to the cylinder's z-axis would be captured resulting in capturing of photons over all θ for some azimuthal angles. This effect increases even further approaching $x_0 = 1$.

For $x_0 \to 1$ we can neglect the tube's curvature due to $r_{\text{tube}} - r_{\text{em}} \ll r_{\text{tube}}$ which simplifies Eq. 7.15 to

$$\epsilon_{\text{TIR}} = \frac{1}{2}\int_0^{\pi} \Theta(\cos\theta - \cos\theta_C)\sin\theta\, d\theta = \cos\theta_C. \tag{7.16}$$

This denotes the theoretical maximum for the capture efficiency. [6]

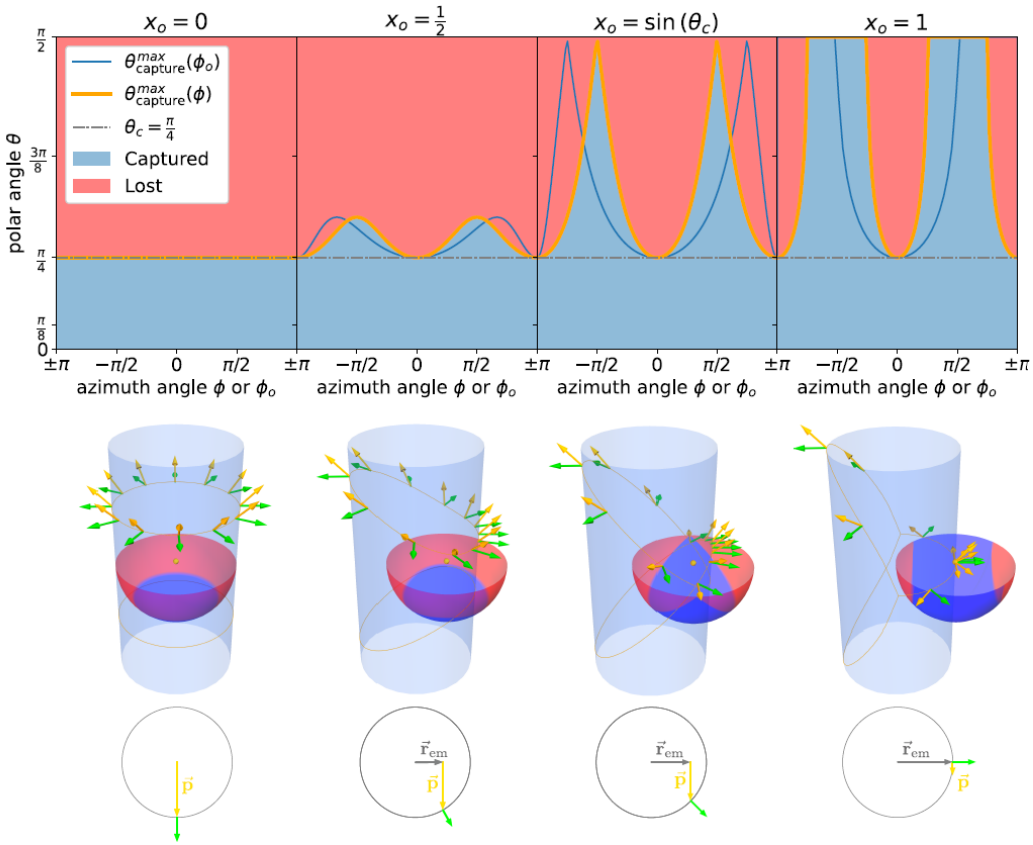

Fig. 7.8.: Illustration of captured photons for different emission points with respect to their polar and azimuthal angle [6]. θ_C is set to $\pi/4$. The top part shows the correlation between θ and ϕ for the captured photon. The two curves show the maximum θ for captured photons with respect to ϕ (relative to the emission point) and ϕ_0 (relative to the center). The bottom part visualizes the directions of emitted photons and the angle relative to the tube's surface.

The emission point can be set depending on the coating of the tube (outside or inside). Taking the WOM inner tube of $57.5\,\mathrm{mm}$ outer and $55\,\mathrm{mm}$ inner radius, Fig. 7.9 shows an increase in ϵ_{TIR} by about 14% for outside coating (relative offset $x_0 = 1.0$) relative to the inside (relative offset $x_0 = 0.96$) using PFPE with $n = 1.33$ as filling material making outer coating the preferable choice here. We get

$$\epsilon^{\mathrm{PFPE}}_{\mathrm{TIR}} = 0.41 \tag{7.17}$$

while the increase in air is comparably small. Coating the tube on the outer side however brings risk as the coating can be damaged or dirtied much easier. Further, one needs to use a filling material which does not dissolve the coating such as PFPE.

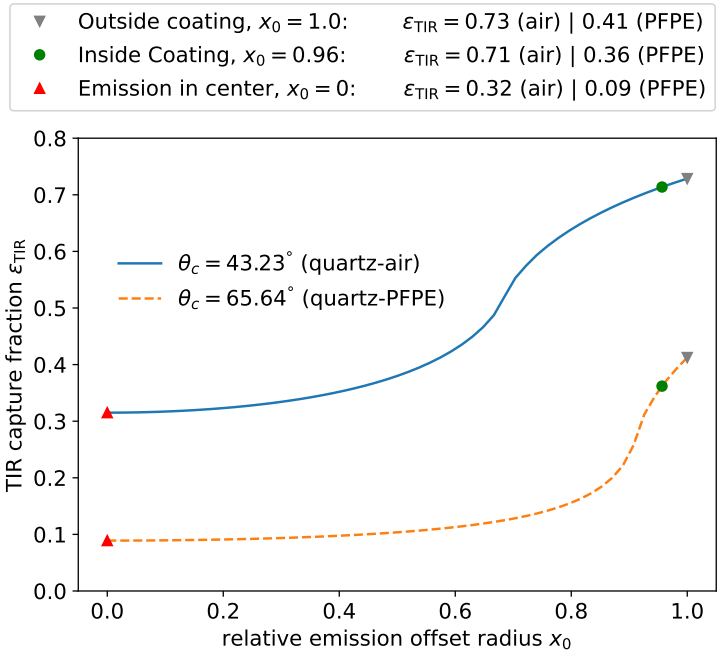

Fig. 7.9.: Capture efficiency for different remission point radii (adapted from [6]). We compare the value between emission from the center ($x_0 = 0$) and WOM tube coated on the inside ($x_0 = 0.96$) and outside ($x_0 = 1.0$) given the diameter of the inner tube.

Considering the previously determined transmission efficiency we can now determine the **combined capture efficiency** $\epsilon_{\text{comb}} =< \epsilon_{\text{trans}} > \cdot \epsilon_{\text{TIR}}$ for different filling materials. From Fig. 7.10 we can confirm PFPE as the best choice for a filling material[4] in terms of efficiency as we get the maximum at $n = 1.33$ with

$$\epsilon_{\text{comb}}^{\text{ice}} = 0.130 \pm 0.001. \tag{7.18}$$

Further, we note that no filling material (therefore air) would reduce our overall performance by almost 50%.

We are also observing that ϵ_{comb} in air as detector material is almost double the value in ice resulting form its significantly increased transmission efficiency. We are therefore limited in our module's performance by the environmental conditions in IceCube.

[4] While there are other possible filling materials with similar refractive indices such as ethanol, PFPE was the only filling which fulfilled all other requirements simultaneously such as being chemically inert to not dissolve the paint.

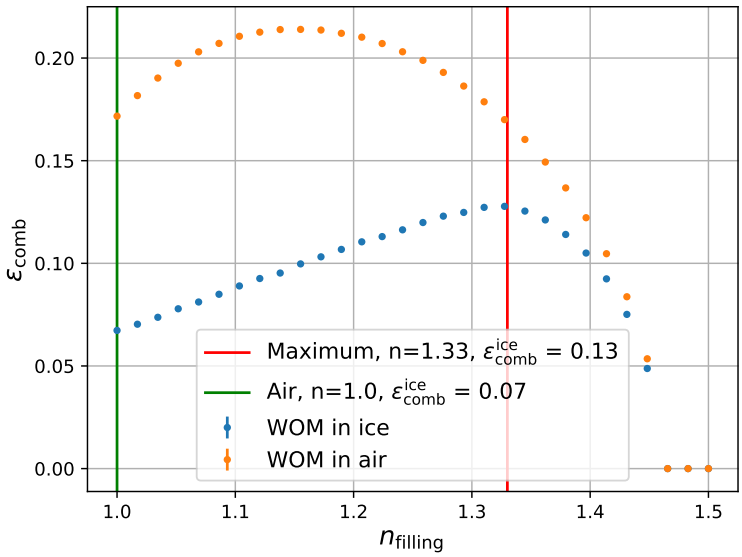

Fig. 7.10.: Combined capture efficiency for a WOM in different detector materials. Shown for $\lambda > 350\,\text{nm}$ so absorption losses during transmission are minor. ϵ_{TIR} was determined according to Eq. 7.16. Filling materials with $n \approx 1.33$ yield the highest efficiency for a WOM deployed in ice. In air that would be for $n \approx 1.15$ with almost double the efficiency. Transmission simulation was run for $N = 5 \cdot 10^5$ photons.

7.5 Propagation through the tube

After capturing, the photons propagate through the tube towards the PMTs while undergoing absorption and scattering. The combined capturing and attenuation efficiency $\epsilon_{\text{TIR}} \cdot \epsilon_{\text{att}}$ reading out one PMT can be approximated by the flattened model in Eq. 4.4. Considering both PMTs we get

$$\epsilon_{\text{TIR}} \cdot \epsilon_{\text{att}} = \langle \epsilon_{\text{flat}}(d, \lambda_{\text{att}}) \rangle = \left\langle \epsilon_{\text{flat, one-sided}}(d, \lambda_{\text{att}}) + \epsilon_{\text{flat, one-sided}}(L - d, \lambda_{\text{att}}) \right\rangle \quad (7.19)$$

for an inner tube of length $L = 760\,\text{mm}$ averaging over all distances d. We determine the efficiency of the tube in air and PFPE using following parameters for the TIR angles θ_C:

$$\theta_C^{\text{air}} = 43.23° \quad \theta_C^{\text{PFPE}} = 64.70°. \quad (7.20)$$

Fig. 7.11 shows ϵ_{flat} using air and PFPE filling for different attenuation lengths. Depending of λ_{att} we see a decrease in efficiency towards the center of the tube due to longer pathlengths. For our expected $\lambda_{\text{att}} = 3\,\text{m}$ we get a relative small variation of <5%. As we have no way to determine the light injection point on the tube

of a deployed WOM this dependency will be only considered by an uncertainty of $< \epsilon_{\text{flat}} >$ which increases for lower λ_{att}.

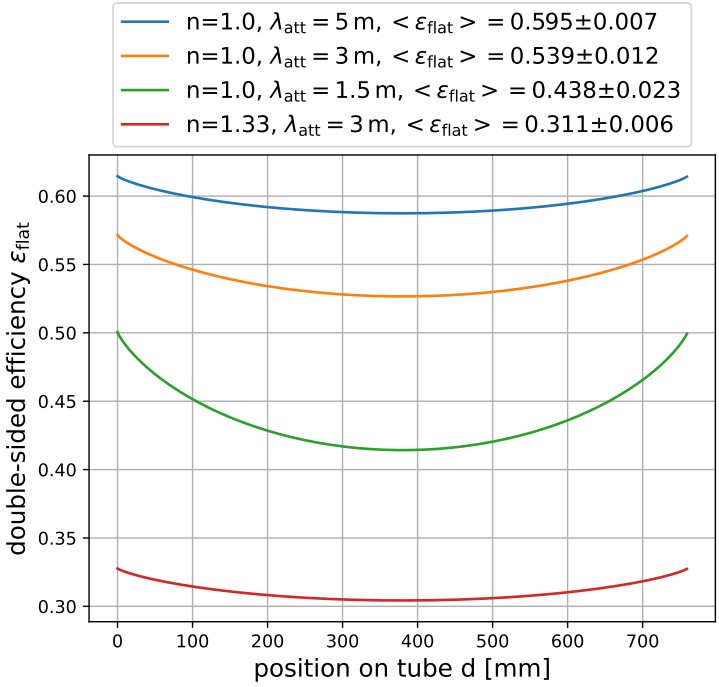

Fig. 7.11.: Inner tube efficiency in air and PFPE for different attenuation lengths according to the flattened model. The tube is read out at both ends at $d = 0$ mm and $d = 760$ mm. We see a drop in the efficiency towards the center of the tube. This distance dependency will be considered by an uncertainty on $< \epsilon_{\text{flat}} >$.

Now we can extract the contribution ϵ_{att} given by attenuation $\lambda_{\text{att}} = 3\,\text{m}$ only without the capture efficiency:

$$\epsilon_{\text{att}}^{\text{air}} = 0.738 \pm 0.016 \quad \epsilon_{\text{att}}^{\text{PFPE}} = 0.785 \pm 0.017. \tag{7.21}$$

We notice different values for tubes inside air and PFPE which results from different path lengths of photon trajectories caused by different θ_C.

7.6 Coupling into PMTs and Detection

Once the photons reach the end of the tube they are coupled into the PMT to be detected. First, they are transmitted through the glue layer. The combined Fresnel and absorption efficiency was already determined in Section 5.3 to be

$$\epsilon_{\text{glue}} \approx 0.930. \tag{7.22}$$

The detection efficiency of the PMT ϵ_{PMT} is given by:

- The wavelength dependent Quantum Efficiency (QE) of the PMT $\epsilon_{\text{QE}}^{\text{center}}(\lambda)$ measured at its center in Section 5.1.1.
- The surface correction factor S_{surf} to map the QE measurement onto the photon distribution on the cathode after exiting the tube. It is defined as the ratio between the relative efficiency over the cathode distribution and the efficiency at the center. It was determined from the measurement shown in Section 5.1.2 which measures over the full multiplication chain to consider for relative changes in lost electrons after the cathode emission[5].
- Correcting the PMT acceptance curve to the WLS emission spectrum $S_{\text{WLS,em}}(\lambda)$. We integrate the surface corrected QE weighted with the WLS emission spectrum over the emission's spectrum wavleength range of $400\,\text{nm}$ - $600\,\text{nm}$ (see Fig. 7.12).
- An angular correction S_{angle} resulting from steep photon emission angles at the end of the tube. A steep angle toward the cathode would cause the path length of the photon through the cathode to change eventually influencing the probability for absorption and emission. This needs to be considered as the QE measurements were performed under vertical incidence.

The PMT efficiency ϵ_{PMT} can be therefore determined by

$$\epsilon_{\text{PMT}} = S_{\text{surf}} \cdot S_{\text{angle}} \cdot \frac{\int_{400\,\text{nm}}^{600\,\text{nm}} \epsilon_{QE}^{\text{center}}(\lambda) S_{\text{WLS,em}}(\lambda)\, d\lambda}{\int_{400\,\text{nm}}^{600\,\text{nm}} S_{\text{WLS,em}}(\lambda)\, d\lambda}. \tag{7.23}$$

To estimate the angular correction we perform an efficiency measurement of the PMT for different incidence angles analogue to the angular timing measurements

[5] As we perform a relative measurement, we are missing information on the absolute loss of electrons which eventually miss the next dynode. However, this is considered for by adjusting the gain to a fixed value of 10^7. Photons missing hte first dynode are already considered in the QE measurement.

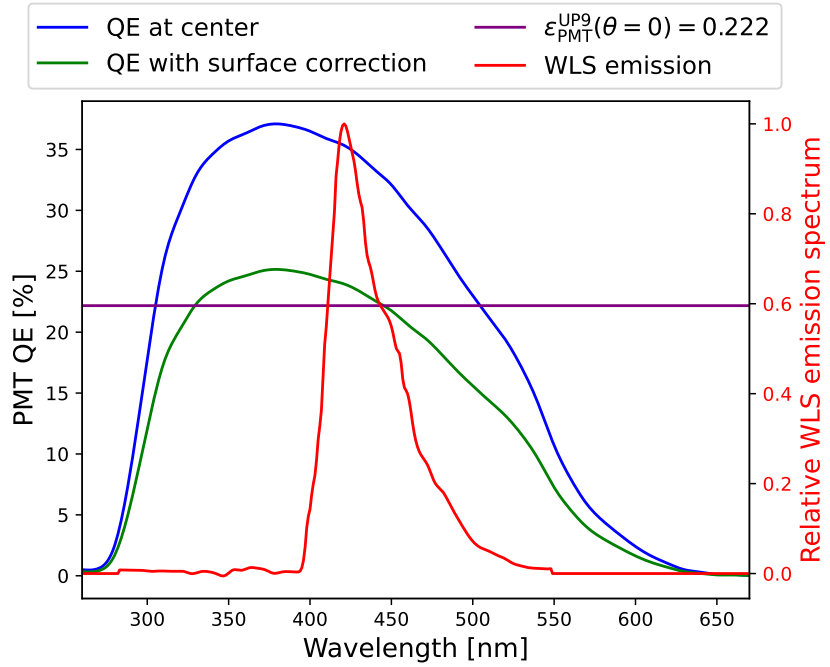

Fig. 7.12.: **Visualization of contributions for PMT efficiency of PMT UP9.** We see the QE curve at the PMT's center, the surface correction, the WLS emission spectrum (separate axis) and the overall PMT efficiency for vertical incidence (without angular correction). Given $S_{\text{surf}} = 0.678$, we get $\epsilon_{\text{PMT}}^{\text{UP9}}(\theta = 0) = 0.222$.

explained in Section 6.5 (instead of the pulser we use the lock-in amplifier setup as in the tube test stand shown in Section 4.6). Fig. 7.13 shows the relative angular efficiency change with the incidence angle θ for two measured PMTs UP13, UP15. We see a small increase towards larger θ which is however not symmetrical towards both sides. An increased efficiency can be explained by the photon taking a longer path through cathode increasing its absorption probability and therefore the QE. A similar effect was already observed in measurements using different PMT models [35]. However, the measured curve does only follow the $1/\cos\theta$ curve expected by this effect until $\pm 20°$ which indicates an additional, not yet considered effect.

We determine the angular correction factor S_{angle} by weighting the simulated θ distribution at the end of the tube with the measured efficiency curves, averaged over positive and negative θ.

$$S_{\text{angle}}^{\text{UP13}} = 1.126 \qquad S_{\text{angle}}^{\text{UP15}} = 1.040 \tag{7.24}$$

These values underlay certain measurement uncertainties. As the measurement was performed only for the two showed PMTs we can only make a rough estimation for the average angular correction of $S_{\text{angle}} \approx 1.08$.

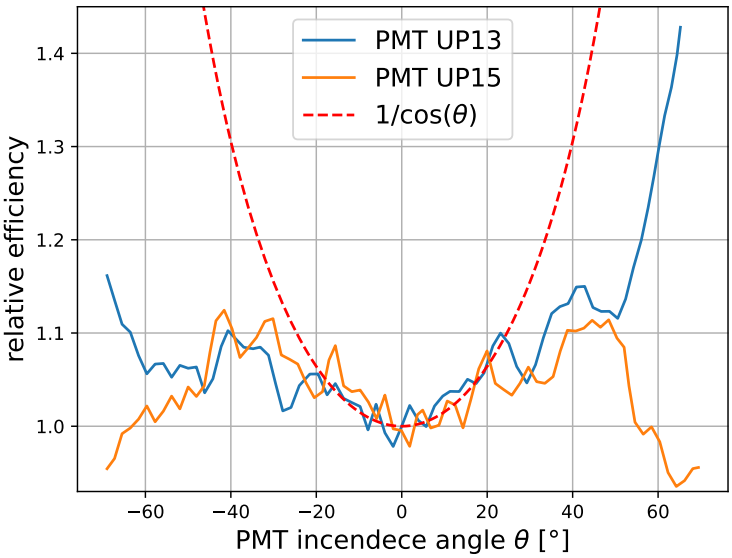

Fig. 7.13.: **Relative PMT efficiency for different incidence angles measured on outer ring, where the tube will be coupled (data from [133]).** We compare the data taken from two PMTs with a $1/\cos\theta$ expectation which would result from an increased path length of the photon thorugh the cathode. The strong increase towards positive θ for UP13 could result from a measurement uncertainty.

Calculating ϵ_{PMT} for every WOM PMT we get a distribution as shown in Fig. 7.14. We observe a wide spread between 11% and 27%. Especially low values result from either low QEs at the center (as already discussed in Section 5.1.1) or from low correction factors which happen due to blind spots in the surface scans.

We can therefore conclude an overall PMT efficiency of:

$$\epsilon_{\text{PMT}} = 0.188 \pm 0.047. \tag{7.25}$$

The given error results from different performances between the PMTs.

7.7 Direct PMT Hits

Following the discussion of contributions to the effective area including wavelength-shifting we will now focus on determining the amount of **direct PMT hits** which are photons detected by the PMTs without being absorbed by the WLS paint first. These consist either of photons with wavelengths outside the absorption spectrum of the WLS paint ($\lambda > 380\,\text{nm}$) which pass through the inner tube and eventually hit the

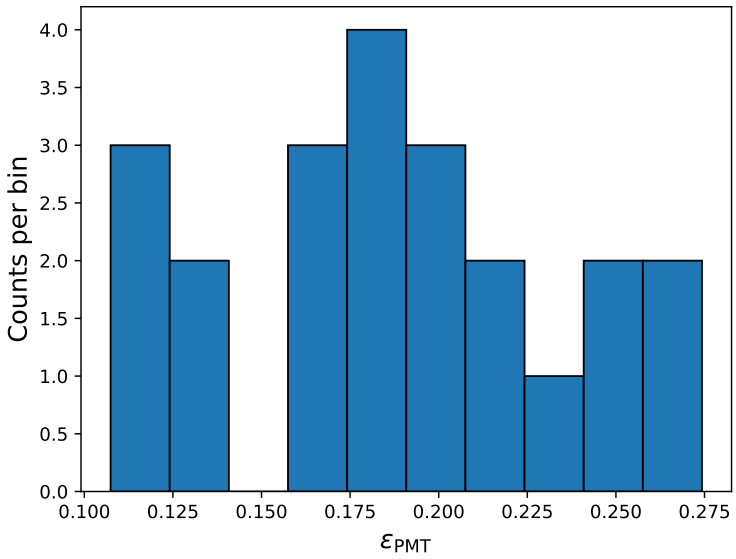

Fig. 7.14.: **Distribution of PMT efficiencies for all WOM PMTs.** We see a wide spread between 0.12 and 0.28 resulting from combined fluctuations in QE center measurements and surface scan corrections.

PMT, or photons of all wavelengths coming in under very steep angles to hit the part of the photocathode located outside the inner tube. However, the performed surface scans (see Fig. 5.4b) showed an efficiency close to 0 for hits at diameters above $115\,\text{mm}$ (this is also confirmed by the datasheet given an active diameter of $115\,\text{mm}$ [79]). Therefore we will focus only on photons hitting the PMT inside the inner tube.

We implement a simulation geometry in Zemax similar to the MC-simulation for the transmission from Section 7.2 as shown in Fig. 7.15. Every transmission layer is implemented as a hollow cylinder of the corresponding material. Further, we insert a CAD model of the WOM PMTs coupled to both ends of the tube. The detector area are the two PMT surfaces while the remaining PMT outer surface area is implemented as absorbing to filter out photons "passing though the PMTs". Further, we put absorbing surfaces on each end of the vessel as an additional filter for horizontal incoming photons. Just as in Section 7.2 the photons are generated perpendicular to a plane of $A_{\text{plane}} = d_{\text{vessel}} \cdot h_{\text{tube}}$ which is rotated by the zenith angle $\theta \in [0, \pi/2]$ simulating $n = 10,000$ photons for each θ. To consider for the projected are we weight with a $\cos\theta$ distribution.

For symmetry reasons we read out only one PMT as we only simulate half the range for θ. The efficiency of photons hitting the PMT with respect to θ is shown in

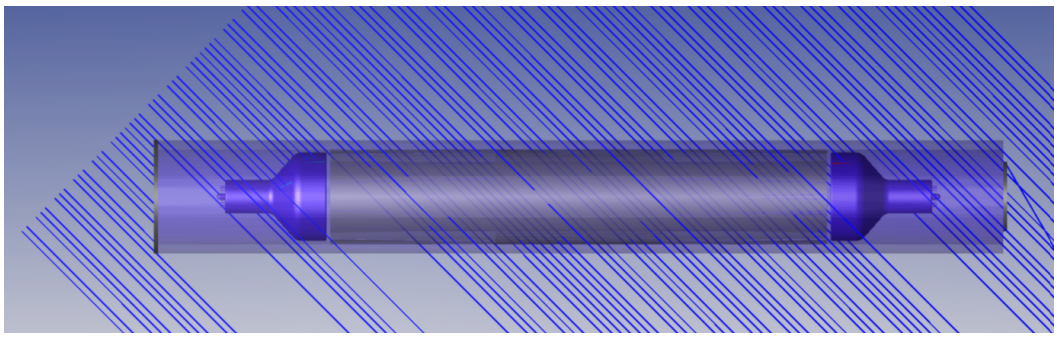

Fig. 7.15.: **Visualization of the simulation geometry for direct PMT hits in Zemax.** Zenith angle $\theta = 45°$. The rays are generated on a plane which is rotated around the WOM for θ in $[0, \pi/2]$. Rays go from top left to bottom right. The direct hits are detected of the front surface of the right PMT. The PMT outer surface areas are absorbing.

Fig. 7.16. We see the efficiency increasing with the larger θ until we see a sudden drop at around $\theta \approx 45°$. This is slightly above the TIR angle for the transmission between quartz and air. Therefore a large fraction of rays is getting reflected on the interface between inner tube and its center preventing them from hitting the PMT at its center (see Fig. 7.17)[6]. Eventually, the photons also get to θ_C between quartz and PFPE causing the to be captured inside the inner tube which increases to efficiency again.

Averaging over the $\cos\theta$ weighted efficiency we get a direct hit efficiency of

$$\epsilon_{\text{direct hits}} = 0.057. \tag{7.26}$$

This value needs to be corrected with the PMT's acceptance as already discussed in Section 7.6. The photon distribution on the PMT's surface follows a uniform distribution (see Fig. 7.18) contrary to the distribution of shifted photons. Therefore we can conclude that no surface correction is necessary as we have observed regular surface sensitivities of the used PMTs. Additionally, we correct for absorption losses through the vessel and filling (see Fig. 7.6), scaling the path length with a factor 2 already established in Section 7.2 to consider for steep angles.

The PMT being hit at steep angles would also result in a contribution of about $S_{\text{angle}} = 1.08$ for the PMT's angular sensitivity.

[6]The drop happens later as incident angle of the photons decreases due to the previous refraction towards optically denser materials.

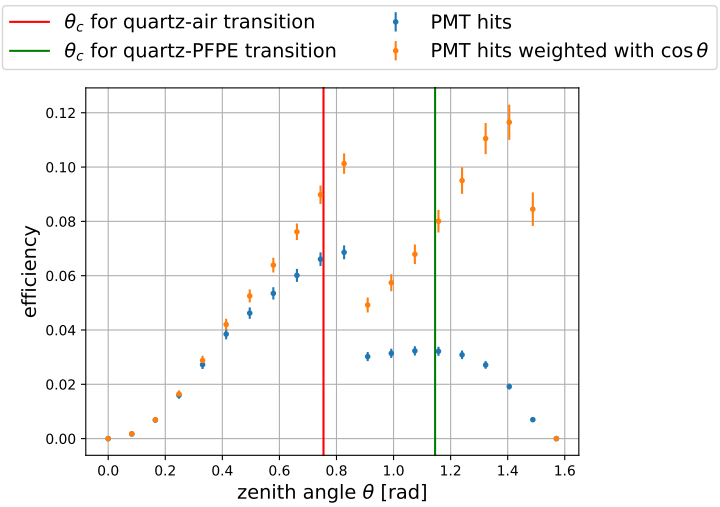

Fig. 7.16.: **Efficiency of direct PMT hits for different zenith angles.** Fresnel losses are also considered here. We notice a sharp a little after θ_C^{air} due to photons being reflected before hitting the PMT. Absorption losses still need to be applied.

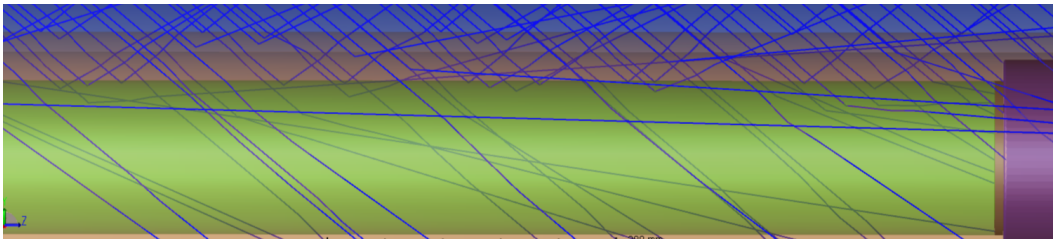

Fig. 7.17.: **Visualization of incoming photons being reflected on the interface between inner tube and the air inside.** $\theta = 60°$ We notice this effect as a sharp drop in the θ dependent efficiency. Due to the curved surface not all photons are reflected and some still hit the PMT.

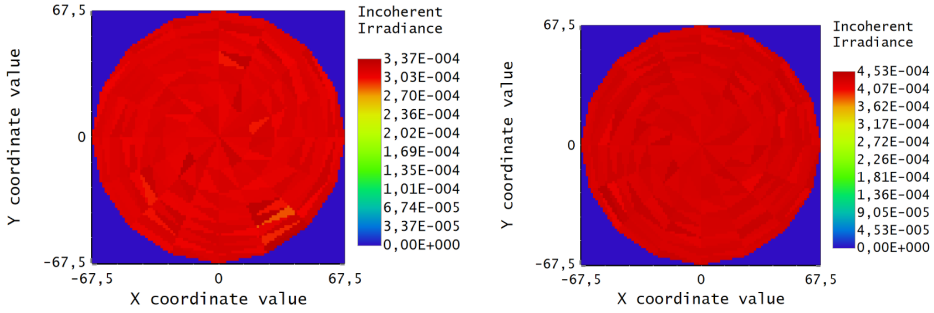

(a) $\theta = 45°$, Number of hits: 43870. (b) $\theta = 75°$, Number of hits: 59923.

Fig. 7.18.: **Distribution of direct PMT hits on the surface by Zemax simulation.** Number of simulated photons: 1,000,000, Number of pixels: 256. The WLS paint being transparent for high wavelength photons results in the full PMT being hit uniformly. The transmission though the PMT glass is not considered there.

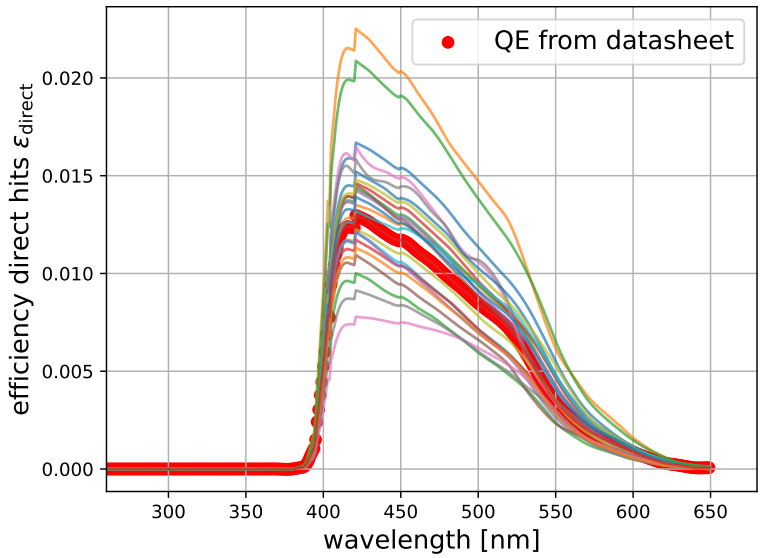

Fig. 7.19.: Direct hit efficiency for all QE measured WOM PMTs with PFPE filling. Wavelength dependent absorption transmission losses are considered here. The shape of the curves correspond to the acceptance spectrum from the QE measurements performed in Section 5.1.1 in the range $\lambda > 380\,\text{nm}$.

The final wavelength dependent contribution for direct hits $\epsilon_{\text{direct}}(\lambda)$ is determined by weighting the determined efficiency with QE curve for each PMT at its center:

$$\epsilon_{\text{direct}}(\lambda) = \epsilon_{\text{direct hits}} \cdot S_{\text{angle}} \cdot \epsilon_{\text{QE}}^{\text{center}}(\lambda). \tag{7.27}$$

The final results for all PMTs can be seen in Fig. 7.19. Just as the QE measurements we see a wide spread with peak values between 2.2% and 0.7%. The curve declines with higher wavelengths dropping to 0 for $\lambda > 600\,\text{nm}$.

Comparing the average peak value of 1.2% with the average contribution of shifted photons of

$$\epsilon_{\text{trans}}^{\text{abs}} \cdot \epsilon_{\text{WLS}} \cdot \epsilon_{\text{comb}} \cdot \epsilon_{\text{PMT}} \approx 0.019 \tag{7.28}$$

we observe a lower, but still noticeable contribution. However, while the shifted photon's contribution is constant over $\lambda \in [300, 400]\,\text{nm}$, ϵ_{direct} declines for higher wavelengths. Further, there could be other yet unconsidered systematics decreasing the effective contribution for direct hits.

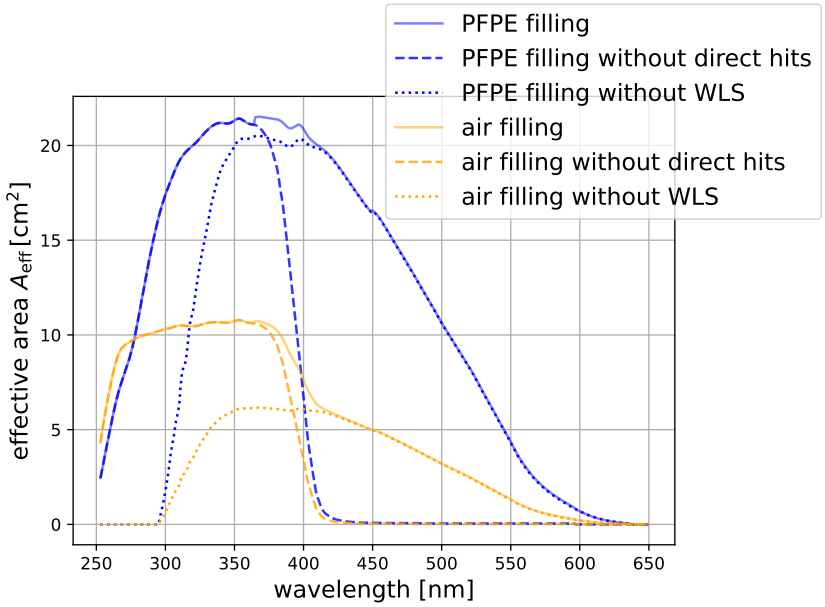

Fig. 7.20.: **Effective area of the WOM for different filling materials.** We compare the effective area with and without the contribution of direct hits and the WLS process. The shape of the curve is determined by the WLS absorption spectrum and the spectrum for direct hits which results from the PMT acceptance curve weighted complimentary of the absorption curve. The curve without WLS is given by the PMT's QE curve scaled with the direct hit efficiency.

7.8 Combined Effective Area and Performance Comparison

Finally, we will combine all discussed contributions to the effective area to evaluate the WOM's performance in IceCube and compare it to other modules. All contributions are summarized in Eq. 7.5. The resulting effective area over all wavelengths for the full module is shown in Fig. 7.20. We compare A_{eff} for air and PFPE as filling material and evaluate the contribution of the direct hits and wavelength-shifting towards the full effective area.

Because the WLS paint shows an absorption efficiency of $\sim 100\%$ for $\lambda < 380\,\text{nm}$, we get no contribution of direct hits until this point. Once the absorption spectrum starts to fall, A_{eff} is getting more and more dominated by direct hits following the PMT's acceptance spectrum until it eventually follows the QE curve when the absorption reaches 0. Comparing these curves for PFPE and air as filling materials we notice that for the later the direct hits contribute comparably less. For the falling edge of the absorption one observes a steep decline before the curve "catches up" with the PMT spectrum. This is caused by the significant higher transmission losses

in air by more than factor 3 (see Fig. 7.5). Further we see a steep decline in PFPE for $\lambda < 320\,\text{nm}$ caused by absorption losses in the PFPE which are not present with an air filling resulting in a plateau between $270 - 370\,\text{nm}$.

Comparing to the effective area ignoring wavelength-shifting, we get an increased number of direct hits as no photons are absorbed now. However, we are limited by the PMT's acceptance which goes to 0 for $\lambda < 300\,\text{nm}$. Comparing the curves for an air filling we see an increase of almost factor 2 in the peak value, if we introduce wavelength-shifting (additionally to the increased UV-sensitivity). This is caused by the considerably higher capture efficiency while direct PMT hits are suppressed by a lower transmission efficiency. The case with PFPE filling on the other side, shows a relative lower increase caused by wavleength-shifting, additionally to the low UV-sensitivity. Conclusively, the improvement resulting from wavelength-shifters is only significant given a high capture efficiency outperforming the transmission suppression which is not fully given in the current WOM design.

The wide spread of PMT efficiencies results in peak value ranges of

$$A_{\text{eff}}^{\text{PFPE}} = 14.2\,\text{cm}^2 - 31.3\,\text{cm}^2 \quad A_{\text{eff}}^{\text{air}} = 7.1\,\text{cm}^2 - 15.7\,\text{cm}^2. \tag{7.29}$$

In terms of effective area, the WOM performs considerably worse compared to other Upgrade modules like the DEgg and mDOM (see Fig. 7.21). The WOM's peak value is outperformed by almost 4 times by the DEgg and almost 6 times by the mDOM. While the WOM is unique in covering the wavelength range below $300\,\text{nm}$ this contribution is very small due to high losses in the transmission and the increased UV-sensitivity does not make up for the significant underperformance in the visible region. The overall effective area of the WOM is even below a normal IceCube DOM which exceeds the WOM by about 2 times in its peak value.

To quantify the module's performance inside the detector we need to consider the Cherenkov spectrum as well as the propagation of photons through ice. Scattered photons undergo a random walk effectively increasing their average pathlength until they hit a module therefore increasing their chance of being absorbed. We simulate IceCube events at different average distances from a module which emit light according to a Cherenkov spectrum. These photons are then propagated through the ice considering absorption and scattering (extending their pathlength). In Fig. 7.22 we see the spectrum of photons which reaches our modules for different event distances. For an average distance of $3\,\text{m}$ as we have it in the Upgrade we notice a uniform spectrum throughout the UV and optical range. As UV photons show a low scattering length [19] they undergo multiple scattering process before they

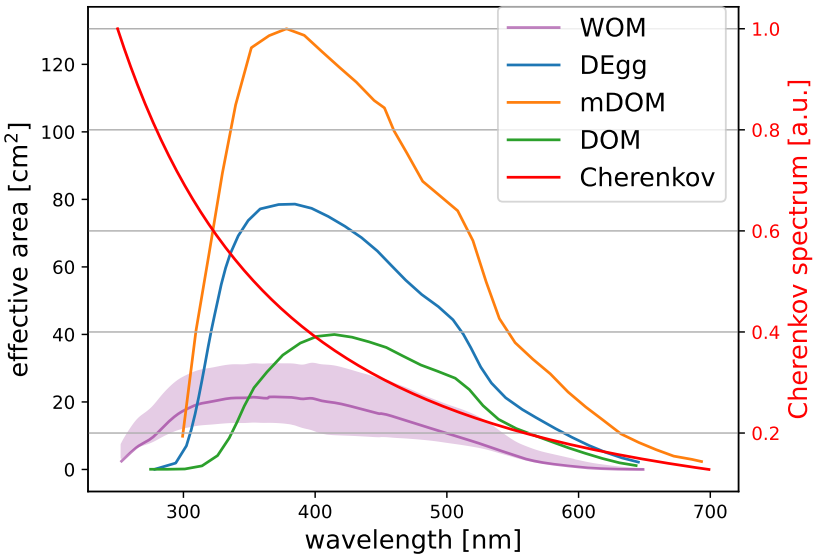

Fig. 7.21.: **Comparison of effective areas between different IceCube modules (data from [38, 41]).** The spread for different PMT performances is visualized for the WOM. The actual performance in the detector will be determined by considering the Cherenkov spectrum and the average distance between a neutrino event and a module.

reach the module which increases their absorption losses. As a result, the initially higher number of emitted UV Cherenkov photons is greatly reduced, eliminating the advantage of UV-sensitive modules. At larger distances, the suppression of UV light becomes even stronger, further reducing the effectiveness of UV sensors for future detector upgrades like Gen2. However, as we are dealing with much lower energies for supernova detection in IceCube the detection range for each module would be smaller than $3\,\mathrm{m}$, yielding an advantage due to the increased UV-sensitivity.

We will now compare and discuss the most import properties of the IceCube modules evaluating the WOM in its application in the detector. These include the averaged effective area in the wavelength range $250 - 600\,\mathrm{nm}$, the module's timing resolution defined as the standard deviation along the timing distribution σ_t, the dark rate R and the **Noise-to-Signal Ratio (NSR)** which we define as the dark noise per cm^2 of effective area NSR $= R/A_{\mathrm{eff}}$. These quantities are summarized for different modules in Tab. 7.1.

One notices the WOM being worse in nearly every comparison. Due to many different light losses it can not compare in terms of effective area. The module's dark rate is not low enough considering the effective area to get a low NSR. While the WOM seems to have a lower NSR than the mDOM we need to consider the possibility

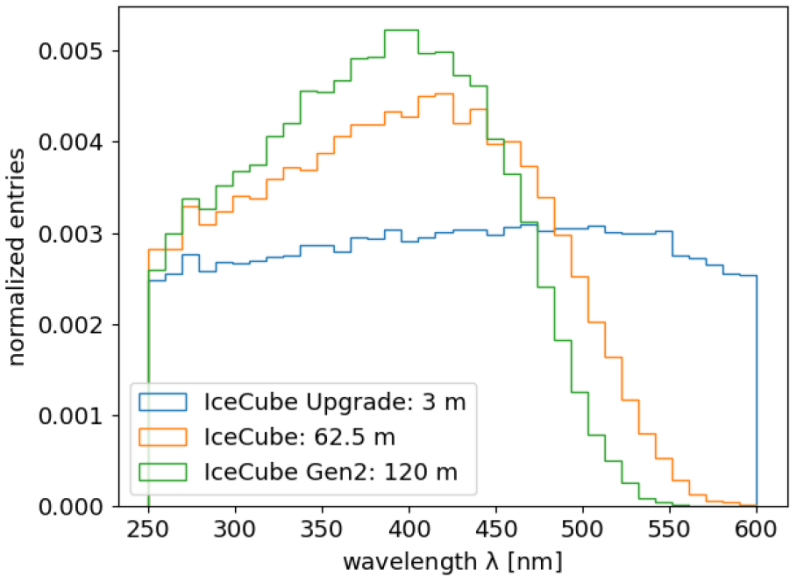

Fig. 7.22.: **Normalized number of Cherenkov photons for different event distances in IceCube [71].** We see a uniform distribution of Upgrade distances as the higher amount of originally emitted UV-photons is lost due to scattering and absorption. This effect increases further for higher distances such as in Gen2.

of lowering the rate in the mDOM using local coincidences between the different PMTs. The timing resolution suffers from the spread cause by the propagation inside the inner tube. Theoretically, one could use the timing signature from the direct hits which is only limited by the TTS of the PMT, but the amount to signal detected would be lacking.
Overall, the WOM's performance in IceCube is overshadowed by other, more potent modules.

7.9 Conclusion and Outlook

This chapter characterized the WOM's effective area and identified its key contributions and limitations. Due to its optical design, photons undergo multiple processes—transmission, absorption, wavelength shifting, and detection—which introduce significant efficiency losses compared to other IceCube modules. Transmission is strongly reduced by Fresnel reflections and UV absorption in quartz and PFPE, leading to a cutoff at shorter UV wavelengths.

The WOM reaches a peak effective area of $22\,\mathrm{cm}^2$ at $\lambda = 320 - 370\,\mathrm{nm}$, with sensitivity extending down to $250\,\mathrm{nm}$. While this UV-sensitivity is unique among Ice-

	$< A_{\text{eff}} > [cm^2]$	Timing σ_t[ns]	Dark Rate R[Hz]	NSR [Hz/cm^2]
WOM	11.7	WLS: 13.17 direct: 1.9	1400	119.7
mDOM	64.8	1.62	14400	222.2
DEgg	37.6	2.89	1800	47.9
DOM	17.9	1.7	870	48.6

Tab. 7.1.: **Comparison of sensor properties for different optical modules in IceCube (data taken [41, 134]).** We use average values for the modules. One can conclude the WOM being the significantly underperforming module compared to other Upgrade modules as well as already deployed IceCube DOMs.

Cube modules, it offers no advantage in practice for the reconstruction of events due to strong UV scattering in ice, even for small event distances like in the Upgrade.

Although outperformed in effective area and signal-to-noise ratio, the WOM offers a unique feature: two temporally separated signals from wavelength-shifted and direct photons. These could enable improved event reconstruction, provided the time difference is enhanced—e.g., by using a slower WLS.

The WOM design allows for increasing the photosensitive area by elongating the inner tube, although this is limited by the available space within IceCube. To address this constraint and further improve sensitivity, the WOMTrap has been proposed for Gen2: passive WLS tubes placed between modules to enhance the detection of faint light signals [117].

In summary, while the WOM demonstrates strong photon conversion and capture properties, its use in the IceCube Upgrade is limited by environmental and technical constraints. However, it may still be valuable in other detectors with higher signal rates and less demanding noise requirements.

We now proceed to the experimental characterization and production aspects of individual WOMs.

8 Production and Performance Evaluation

This chapter treats the WOM's production procedure and steps for performance evaluation and optical quality control. After going through an overview of every production step we will focus on the evaluation of the optical performance for coated tubes, glued inner assemblies and fully assembled WOMs. These results are used to determine the effective area for every produced WOM experimentally.

8.1 Summary of Production Steps

It total, 10 WOMs are produced to be deployed in the IceCube Upgrade which are separated into two batches of 5 modules each. We will focus on the first batch here which is already produced and shipped as this thesis is written. The order of the production steps is performed as follows:

1. Preparation and characterization of PMTs.
    - Quantum Efficiency (QE) measurements as explained in Section 5.1.1.
    - Surface scans at nominal gain (see Section 5.1.2) and calculation of the surface correction factor S_{surf}.
    - Temperature measurement of gain and dark rate as explained in Section 5.1.3.
    - Production of PMT foam socks as shown in Fig. 4.11.
2. Inner tube coating (see Fig. 4.4).
3. Inner tube evaluation which will be elaborated on in Section 8.2.
4. Inner assembly construction including evacuation testing to verify the vacuum gluing (see Section 5.3).
5. Inner assembly evaluation to verify the coupling and transmission efficiency of the glue which will be explained in Section 8.3.

6. Inserting the inner assembly inside the pressure vessel and apply the two-layer silicone sealing for top and bottom as shown in Fig. 4.12.

7. Filling in PFPE.

8. Electronic tests which includes connecting the set of electronics boards to two "reference" PMTs and verify basic functionality specifically taking data, checking the SPE spectrum and dark rate, reading out pressures and temperatures.

9. Inserting the electronics inside the module and verify the cable connections.

10. Closing and evacuation of the module. All cable connectors are fixed using epoxy resign preventing them from becoming loose during vibration and mechanical shocks. The modules in evacuation in both compartments at the same time. The target pressure is motivated in Section 9.2.

11. Installing the Harness as explained in Section 4.4.3.

12. Optical Final Acceptance Testing (FAT) of the modules using a wooded dark box (see Section 8.4).

13. Packaging and shipment.

Fig. 8.1 shows two fully assembled WOMs displaying improvements throughout the production phase.

In the following sections, we will discuss the single evaluation steps of the WOM production and compare the resulting performance parameters between each module.

8.2 Coated Tubes

The evaluation of the coated inner tubes serve as quality control for the paint layer and could provide an experimental verification for the performance determined in Chapter 7. We use the experimental setup and corresponding modifications and analysis procedure as explained in Section 4.6. For every tube, the same two "reference PMTs" are used to isolate the systematics to tube effects only. Every coated tube needs to pass established quality criteria for the paint layer thickness as well as distance and wavelength dependent efficiency. In this section, we will motivate these quality criteria and show the results of each coated tube.

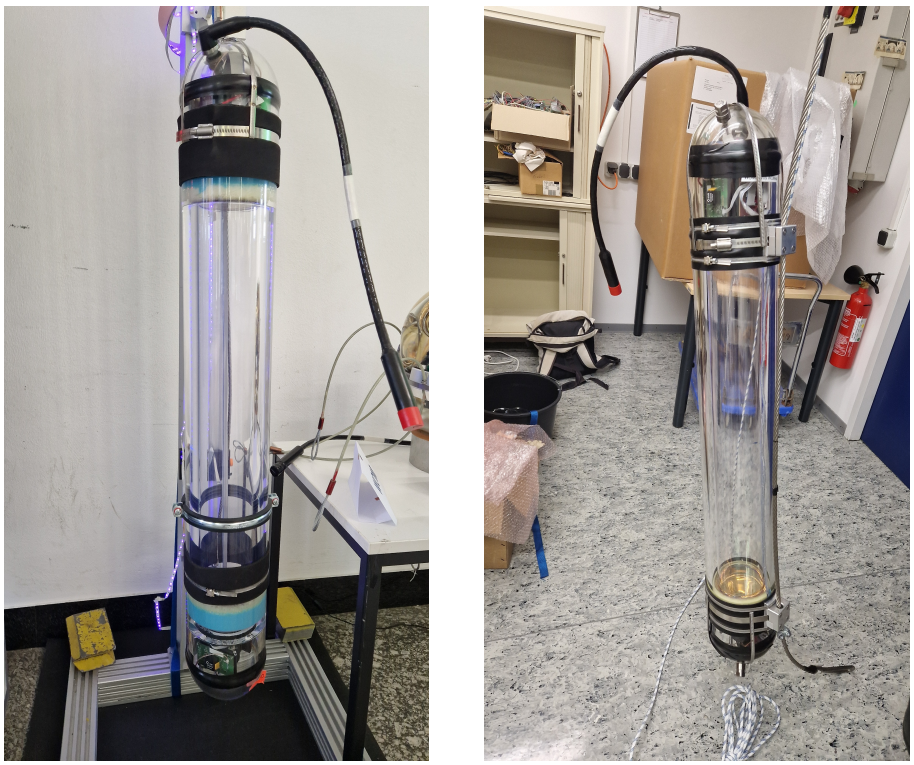

(a) First produced prototype "WOM1: WOM_Snow".

(b) WOM produced later in the production phase "WOM5: WOMderland".

Fig. 8.1.: Two fully assembled WOMs at different stages in the production. Between the assembly of the prototype "WOM1" and "WOM5" about 4 months has passed which were used to improve on the quality of several production steps like the sealing layers, cables routing and harness installation.

8.2.1 Paint Layer Thickness

The coating speed for all inner tubes was chosen to $U_0 = 2.9\,\text{mm/s}$ which results in an average paint layer thickness of $d \approx 12\,\mu\text{m}$. This number was chosen based on the results from [73] which displayed 100% absorption at $d = 25\,\mu\text{m}$[1]. Increasing the layer thickness has proven to worsen the paint layer quality and handling of the tube considerably.

The absolute value and relative homogeneity of the paint layer thickens can be measured over small distances using a profilometer (see Fig. 8.2). A paint layer variation of much bellow 1% was observed there.

The **paint layer homogeneity** can also be determined by an optical measurement. We perform an efficiency scan of all linear positions z and azimuth angles ϕ.

[1]The tube would have $d = 12\,\mu\text{m}$ on each side resulting in a total pathlength of $24\,\mu\text{s}$ of the photons through the paint.

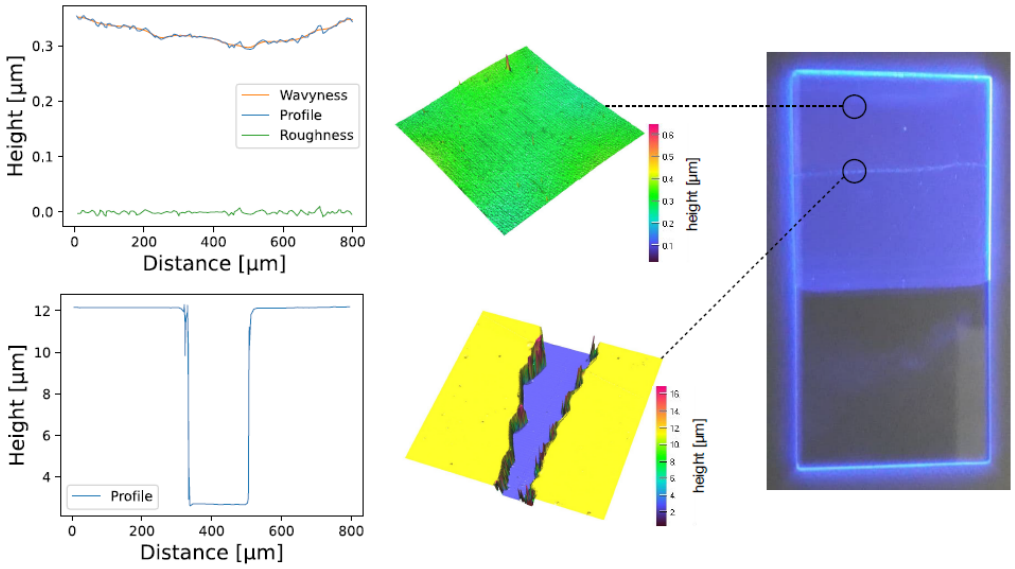

Fig. 8.2.: **Measurement of the paint layer thickness of a coated slide using a profilometer [6].** The absolute thickness is determined by cutting a valley through the paint and measure the relative difference. The measurement concluded a waviness of $50 - 100\,\text{nm}$ for a paint layer of $10\,\mu\text{m}$ thickness.

For each point we determine the efficiency ϵ relative to the efficiencies for other ϕ at a fixed linear position $z = z_0$. Therefore we measure the relative efficiency for each z and ϕ averaged within each z_0 to be not influenced by the attenuation losses:

$$\epsilon^{\text{real}}_{\text{paint}}(z, \phi) = \frac{\epsilon(z, \phi)}{\frac{1}{n_\phi} \sum_{\phi_{\text{min}}}^{\phi_{\text{max}}} \epsilon(z = z_0, \phi)}. \tag{8.1}$$

The measured variation in the efficiency could result from the following effects:

- Systematics from the measurement setup such as centering the tube inside the rotational stage or the bending of the light guide.
- Variation in the paint layer thickness resulting in a reduced absorption and shifting efficiency.
- Variation in the paint layer thickness potentially influencing the attenuation of photons propagation through the tube.

The systematics related to the measurement setup were characterized by the light source directed at a photodiode scanning through the same set of z, ϕ as it is used for the tube measurement [115]. It showed a normal distributed efficiency with $\sigma \approx 1\%$. As we expect a significantly lower contribution from the paint layer itself based on the profilometer measurement, we set a conservative requirement

of $\sigma < 5\%$. Further, $\epsilon^{\text{rel}}_{\text{paint}}$ needs to follow a normal distribution to ensure no z or ϕ dependent systematics.

For all evaluated tubes we observe an efficiency distribution similar to the one displayed in Fig. 8.3. We see a Gaussian distribution centered around 1 with little to no outliers with $\sigma = 1.3\%$. Taking the measurement with the opposite PMT resulted in no significant change.

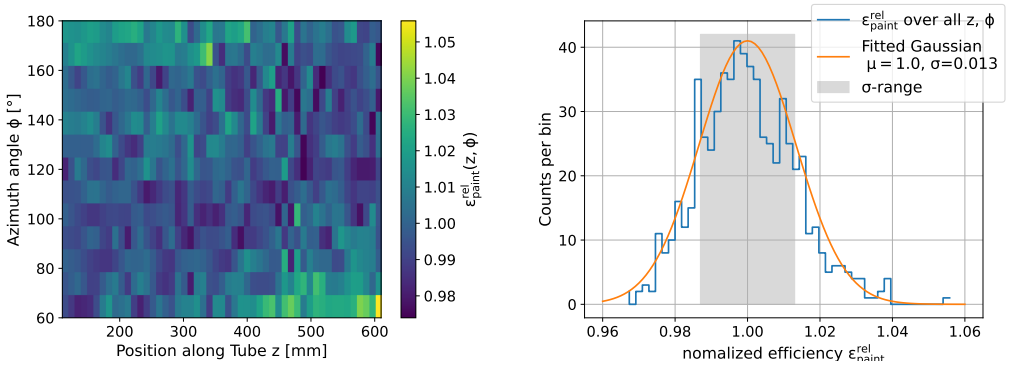

(a) $\epsilon^{\text{rel}}_{\text{paint}}$ over all z, ϕ.

(b) Histogram over all relative efficiencies.

Fig. 8.3.: Measurement of the paint layer homogeneity for WOM4 (data from [115]). Read out by the NPMT. Constrains within the test stand allowed for a ϕ-scan only between 60° and 180°.

The determined σ for the paint layer homogeneity will be further used as systematic errors for the measurement of the linear dependency on the absolute efficiency.

8.2.2 Linear Efficiency

We will now determine the absolute efficiency of the tube over all distances z between light injection point and PMT. The performed PMT reference measurement and the determined correction factors for surface and wavelength correct for all kinds of PMT effects, such as differences in gain, QE, surface sensitivity and wavelength acceptance, leaving us with the tube's performance only. The determined efficiency ϵ_{tube} therefore composes of the shifting efficiency of the WLS paint, the capture efficiency and the propagation efficiency of the shifted photons through the tube:

$$\epsilon_{\text{tube}}(z, \lambda) = \epsilon_{\text{WLS}}(\lambda) \cdot \epsilon_{\text{TIR}} \cdot \epsilon_{\text{att}}(z). \tag{8.2}$$

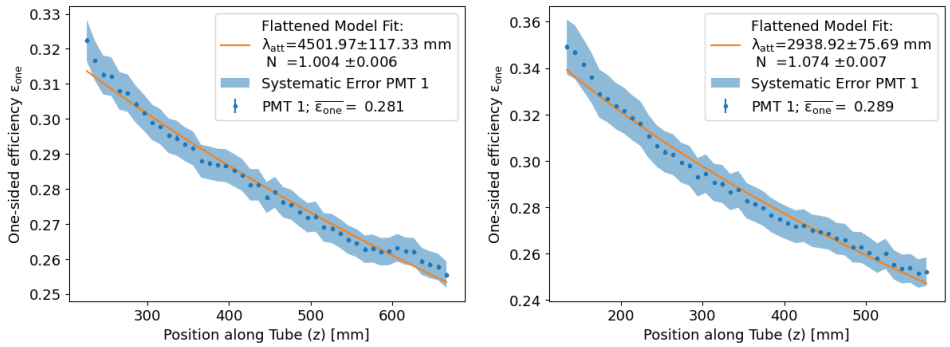

(a) Read out by NPMT, located on left side at $z_{\text{abs}} = 760\,\text{mm}$.

(b) Read out by SPMT, located on right side at $z_{\text{abs}} = 0\,\text{mm}$.

Fig. 8.4.: Linear efficiency fits to the flattened model for WOM4 [115]. z is the distance between PMT and light injection point. We measure the same tube on the same section from both sides using different PMTs and therefore expect similar fit results assuming all systematics were properly considered. We cut off the data points for close distances as these are dominated by self-absorption and can not be described by the flattened model (see Section 4.5.3).

For now, we perform the measurement at a fixed wavelength of $\lambda = 375\,\text{nm}$ which also denotes the maximum of ϵ_{WLS}. The wavelength-shifting contribution consists therefore only of the constant quantum light yield $\epsilon_{\text{WLS}}^{\text{QY}}$. As we neither observed nor expect an efficiency change with ϕ[2] we average for each z over all ϕ to get a statistical error and use the σ from the previous paint homogeneity measurement as a systematical error.

The resulting efficiency curves for both PMTs can be described by the flattened model (see Section 4.5.2). We fit this model to our data with two fit parameters being the **attenuation length λ_{att}** and the **scaling factor N** which considers the effect of $\epsilon_{\text{WLS}}^{\text{QY}}$ and losses on interfaces in the setup not covered by the photodiode reference. We therefore expect $N < 1$.

From the fits shown in Fig. 8.4 we notice a deviation from our expectations as N is above 1 for both read out PMTs. Additionally, there is a clear difference between the best fit parameter for NPMT and SPMT even though we would expect matching results. Reasons for that could lie within yet unconsidered systematics in the setup, but could also suggest a correlation between N and λ_{att}[3]. Instead of setting quality criteria to the fit parameters, we will use the both-sided efficiency for it as it is a more stable quantity to rely on. We set the lower threshold conservatively

[2] In Section 8.3 we will see that there is indeed a change in efficiency with ϕ for small z. These fluctuations however can not be precisely resolved with the setup. Additionally, small z are excluded from the fit as they are affected by self-absorption.

[3] These effects and possible explanations were studies excessively in [115]. We will only highlight the resulting consequences here.

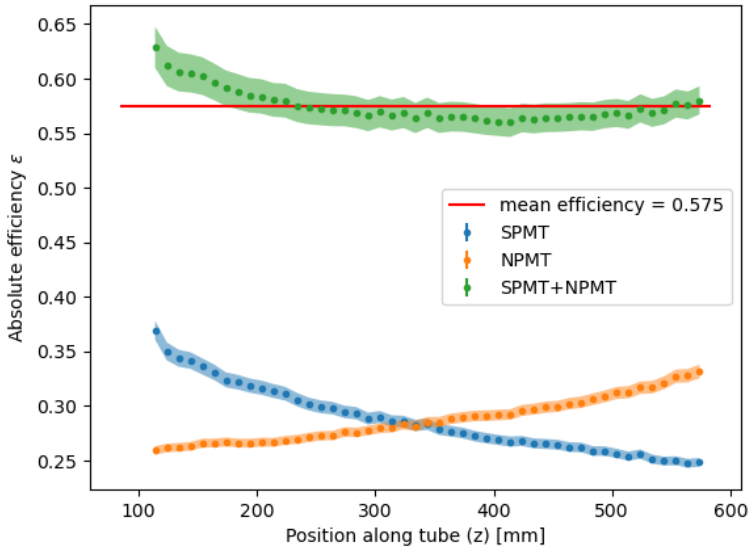

Fig. 8.5.: One- and both-sided efficiencies for WOM4 [115]. z is the absolute position on the tube with $z = 0$ being the position of the SPMT on the right side. The requirement of $\epsilon_{\text{tube}} > 0.4$ is evaluated on the mean over all z for the sum of NPMT and SPMT.

to an average efficiency of 40%. According to Fig. 7.11 this would correspond to a $\lambda_{\text{att}} < 1.5\,\text{m}$ therefore much below the expected value of $3\,\text{m}$ which would indicate severe issues in the coating and handling of the tube.

Fig. 8.5 shows an example of the efficiency curves which passes the requirement easily with $\epsilon_{\text{tube}} = 0.575$. Comparing the two one-sided efficiency curves we notice deviations in their courses and offsets (also reflected by the difference in fitting parameters). Detailed investigations suggest irregular magnetic fields in the dark box not completely shielded by the mu-shields as a possibles reason which however do not lower the integrity of out quality criteria significantly [115].

In Tab. 8.1 we see a summary of all evaluated coated inner tubes. We can confirm the deviation between NPMT and SPMT considering the best fit parameters and observe $N > 1$ frequently. The double-sided average efficiency is similar for most tubes at a value of around 55% easily surpassing the set 40% requirement. This leads to the consideration of this condition being too lax for our application. For future production a more strict condition of e.g. 50% would lead to a higher standard in quality control.

	$< \epsilon_{\text{both}} >$	λ_{att} [mm]	N	σ_{paint}
WOM2	0.517	2363 ± 24 2484 ± 81	0.953 ± 0.003 1.096 ± 0.011	0.029
WOM3	0.565	4447 ± 214 3471 ± 72	1.032 ± 0.009 0.949 ± 0.005	0.023
WOM4	0.575	4502 ± 117 2939 ± 76	1.004 ± 0.006 1.074 ± 0.007	0.013
WOM5	0.569	3752 ± 121 2802 ± 59	0.969 ± 0.007 1.131 ± 0.007	0.018
WOM6	0.472	2386 ± 50 2257 ± 56	0.894 ± 0.006 1.010 ± 0.008	0.030
WOM7	0.565	3623 ± 84 2429 ± 40	1.099 ± 0.006 1.032 ± 0.005	0.015
WOM8	0.584	3755 ± 85 3014 ± 37	1.072 ± 0.006 1.058 ± 0.003	0.017

Tab. 8.1.: **Results from linear efficiency and paint homogeneity measurements of WOM tubes (data from [115]).** λ_{att} and N are shown for NPMT and SPMT. While only 5 WOMs were assembled in the first batch tubes for 7 WOMs were already coated and evaluated. We exclude WOM1 as the setup and evaluation procedure were adjusted afterwards.

8.2.3 Wavelength Scan

The wavelength scans are used as quality control to ensure a paint layer thick enough to provide the optimal absorption and shifting efficiency. As there is no distance dependence in the wavelength acceptance according to Eq. 8.2 we can measure the relative ϵ_{WLS} for each distance individually. We measure the efficiency for different distances and injection wavelengths at a single angle ϕ. For each distance z we normalize the curve setting the value at $\lambda = 380\,\text{nm}$ to 1 as we would expect the maximum efficiency there[4]. The resulting curves for different distances are shown in Fig. 8.6.

We see similar curves for all distances which display a slightly falling slope in the region between $300\,\text{nm}$ and $380\,\text{nm}$ and quickly going down to zero for wavelengths below. We therefore do not see wavelength coverage below $300\,\text{nm}$ as the PMT's efficiency cuts off there [79].

For an optimized WOM performance we require ideally a flat wavelength acceptance. As increasing the coating speeds makes the paint layer prone to deformation during handling we tolerate the slight slope by setting the condition to an average

[4]Normalizing the curve to its maximum value showed to eventually result in artifacts due to unreliable reference measurements at low wavelengths.

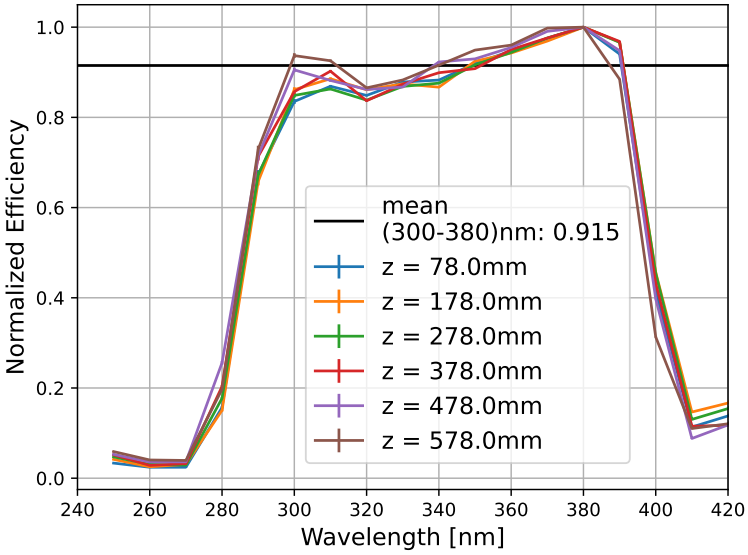

Fig. 8.6.: **Wavelength scan at different distances for WOM4 [115].** The measured efficiency values are normalized for each distance to 1 at $\lambda = 380\,\mathrm{nm}$. Therefore we would expect the same curve for each distance.

relative efficiency above 85% in the region $300\,\mathrm{nm}$ to $380\,\mathrm{nm}$. Comparing the average curves of all measured tubes in Fig. 8.7 we see very similar shapes and all WOMs passing the 85% mark even going above 90% which confirms that we have paint layers thick enough for each WOM. We also notice the rapid decline for $\lambda < 300\,\mathrm{nm}$ corresponding with the decrease of the PMT's acceptance to 0.

Comparing the recent measurements to a previous measurement we can conclude that it is possible to see the full WLS spectrum with our setup. Instead of taking the reference measurement with a PMT we would perform the reference measurement with an UV-sensitive photodiode instead. As it is sensitive for $\lambda < 300\,\mathrm{nm}$, we are able to see the absorption spectrum down to $250\,\mathrm{nm}$. Additionally, we see a slightly higher efficiency towards $\lambda = 400\,\mathrm{nm}$ which was already highlighted in Fig. 7.7.

8.3 Optical Tube Coupling

The next step in the WOM's production process is gluing the PMTs to the tube and evaluating the resulting inner assembly. After the gluing and mechanical verification

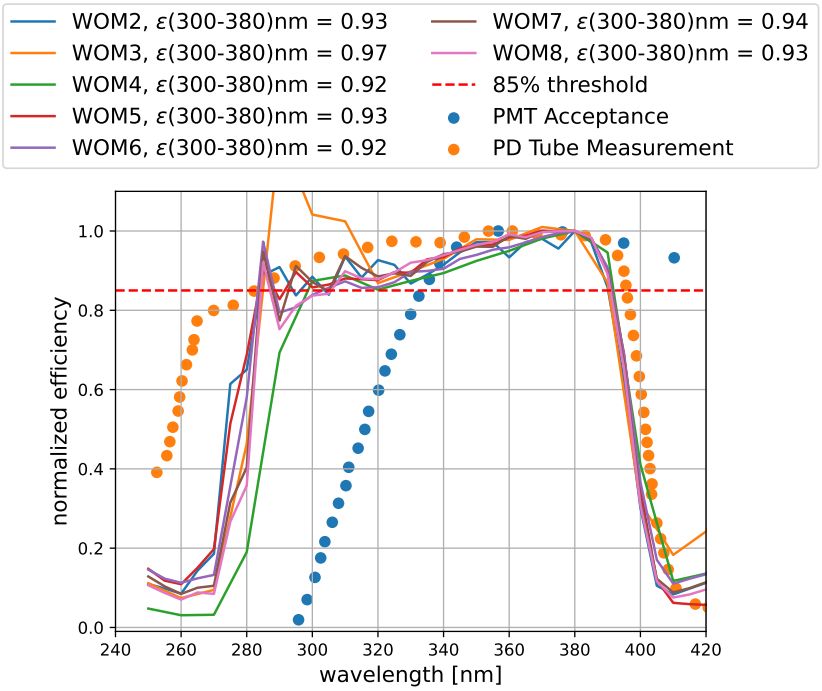

Fig. 8.7.: **Mean wavelength efficiencies for all WOMs compared to a previous tube measurement using a photodiode instead of a PMT in the reference measurement (data from [71, 115]).** For wavelengths below $300\,\mathrm{nm}$ the WOM measurement do not give reliable results due to the PMT's sensitivity falling down to 0.

process has been discussed in Section 5.3, we want to focus on evaluating the optical coupling and estimate the possible efficiency loss in case of "bad gluing".

8.3.1 Loss Expectation

First, we will estimate the possible measurable systematics which could result from partly bad coupling considering the azimuth injection angle, the simulated photon distribution at then end of the tube and on the photocathode as well as the PMT's surface sensitivity.

We define "bad coupling" as having an air layer between tube and PMT's surface. This could be caused by either a spot missing applied glue completely or by air bubbles inside the glue layer. As we were already able to confirm a mechanical bond for the consistent underpressure inside we can exclude the first possibility for a mechanically properly coupled, evacuated tube. Still for simplicity, we assume the phase transition quartz→air→PMT glass for a badly glued spot contrary to quartz→glue→PMT glass for good gluing. For a fully bad coupled (or completely

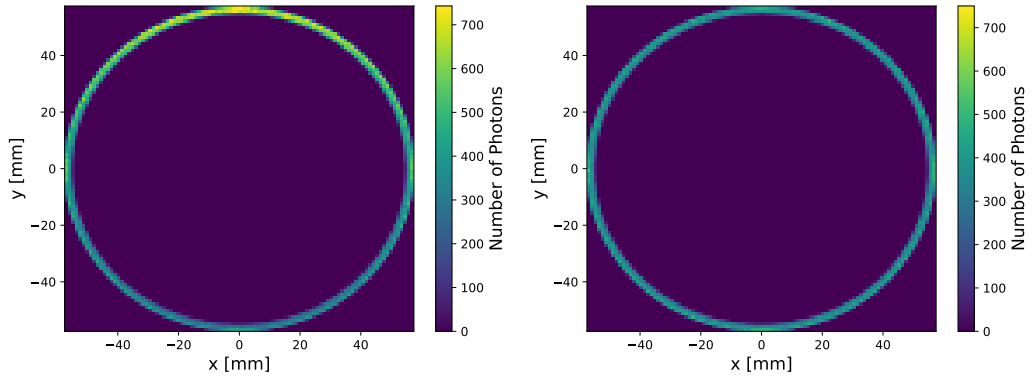

(a) Distance $d = 10\,\mathrm{cm}$.

(b) Distance $d = 30\,\mathrm{cm}$.

Fig. 8.8.: Simulated distributions at the tube's end in air for different distance d between photon injection point and PMT. Quartz tube of outer diameter $115\,\mathrm{mm}$ and wall thickness of $2.5\,\mathrm{mm}$ in air. The light was injected vertically from the top, where we also see an increased number of exiting photons. For increased d the distribution becomes more homogeneous.

uncoupled) tube we expect a transmission efficiency of 37% assuming an injection point far from the PMT readout[5] which is dominated by photons being reflected on the surface between quartz and air. This marks a huge loss compared to 98% efficiency for a perfectly glued tube (see Section 5.3).

As already mentioned previously and also displayed in Fig. 8.8 the photon distribution for close distances peaks around the azimuth injection angle, because photons of most emission angles can not go around the tube over this small distance to properly distribute over the full tube. Having bad coupling over a certain azimuth range could therefore result in a measurable systematic over the injection angle. As only vertical injection is implemented into ALGO we will rotate the photon distribution instead.

We investigate the extreme case of having bad coupling over half the coupling area for azimuth angles of $[-\pi/2, \pi/2]$ equivalent to exiting photons with $y > 0$. For these photons we calculate the transition through air while for photons with $y < 0$ we calculate the transition through the glue layer with $n = 1.56$. For photons not lost in this process we calculate the refraction and propagate them through $6.5\,\mathrm{mm}$ of PMT glass to determine the photon's distribution on the photocathode. The resulting photocathode distributions for different injection azimuth angles α is shown in Fig. 8.9.

[5] This value was determined similar to the glue loss in Section 5.3 by applying the Fresnel formulas to the θ distribution of a quartz tube in air using a distance of $30\,\mathrm{cm}$ between injection point and PMT.

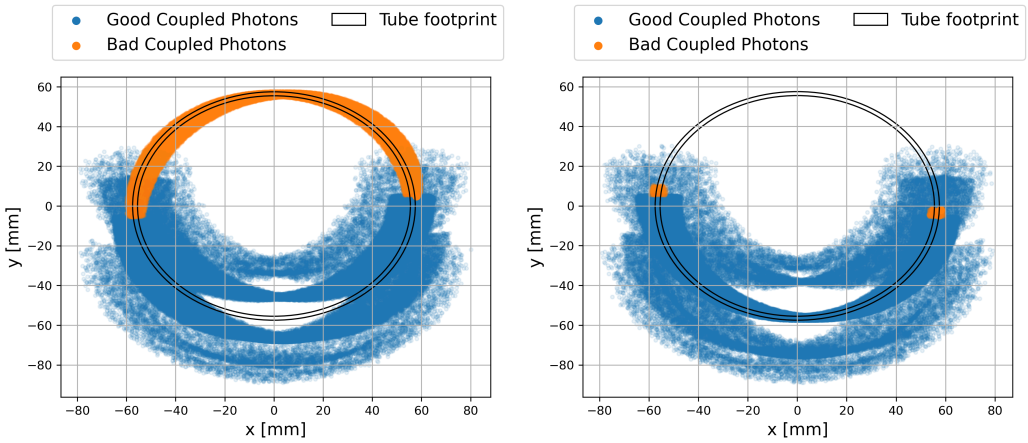

(a) $\alpha = 0$ (illumination from top). Coupling efficiency $\epsilon_{\text{couple}} = 0.783$.

(b) $\alpha = \pi$ (illumination from bottom). Coupling efficiency $\epsilon_{\text{couple}} = 0.617$.

Fig. 8.9.: PMT cathode distributions of simulated photons propagating through a tube partly halfway coupled to the PMT. For every azimuth injection angle α photons exiting the tube with $y > 0$ undergo transition through a layer of air while photons with $y < 0$ propagate through the glue. After calculating the refraction angles and TIR losses all photons are propagated through $6.5\,\text{mm}$ of PMT glass.

For $\alpha = \pi$ the contribution of photons exiting on the unglued side is strongly suppressed compared to $\alpha = 0$ resulting in an overall lower coupling efficiency. At short distances, photons need to be emitted at a steep angle in order to reach the opposite side of the tube relative to their injection point. As a result, almost all of these photons are reflected at the air layer in the uncoupled segment, as observed for $\alpha = \pi$. Therefore, the coupling efficiency consists almost exclusively of photons hitting the glued segment. For $\alpha = 0$ on the other hand, photons with steep angles reaching the bottom side of the tube (y<0) are not lost given the interface transition between quartz and glue. The photons hitting the uncoupled top side of the tube consist of many direct hits and overall photons with small angles which are not affected by the TIR loss between quartz and air resulting in an overall higher coupling efficiency.

This effect can be confirmed in Fig. 8.10 which shows the **coupling efficiency** $\boldsymbol{\epsilon_{\text{couple}}}$ defined as the fraction of photons hitting the PMT's surface containing photons propagated the the air N_{air} and glue layer N_{glue} relative to the number of photons exiting the tube on the corresponding side N_{tube}:

$$\epsilon_{\text{couple}} = \frac{N_{\text{air}} + N_{\text{glue}}}{N_{\text{tube}}}. \tag{8.3}$$

For a close distance of $d = 10\,\text{cm}$ we get the highest ϵ_{couple} for α being located at the center of the unglued segment as explained previously. Increasing the injection

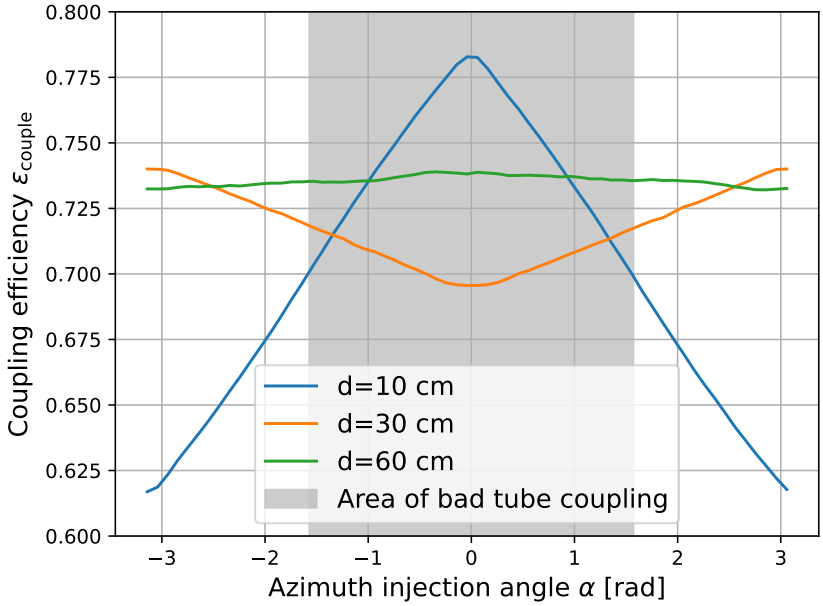

Fig. 8.10.: Simulated coupling efficiency of a tube half coupled to a PMT for different injection angles and distances. ϵ_{couple} is defined as the fraction between photons reaching the PMT's surface and photons reaching the tubes end (see Eq. 8.3).

point distance decreases the range for ϵ_{couple} until it becomes almost constant for $d = 60\,\text{cm}$ caused by the tube's end distribution becoming more homogeneous. For $d = 30\,\text{cm}$ we observe the opposite trend as for $d = 10\,\text{cm}$ marking $\alpha = 0$ as the minimum for ϵ_{couple}. With increasing distance the θ distribution along the tube's end is getting more and more smoothed out resulting in much less photons exiting the tube on the opposite side of the injection point being lost on the interface between tube and air layer. On the other hand, the photons exiting on the injection side show higher θ angles increasing the lost fraction there. As a small asymmetry still remains we do not see a constant relation yet.

Finally, we weight the determined cathode distribution with the measured surface acceptance of the PMT. Every propagated photon is weighted with the relative surface efficiency and we calculate the mean relative efficiency for each α. As the surface scans have displayed an asymmetric pattern we would expect to see a variation with α even without considering the unglued segment. This effect decreases with increasing distance and a more homogeneous cathode distribution.

This can be confirmed in Fig. 8.11. While we observe an angular dependency on the efficiency for $d = 10\,\text{cm}$ for both, a perfectly coupled tube and the partly glued tube, because of the highly asymmetric cathode distribution, both of these

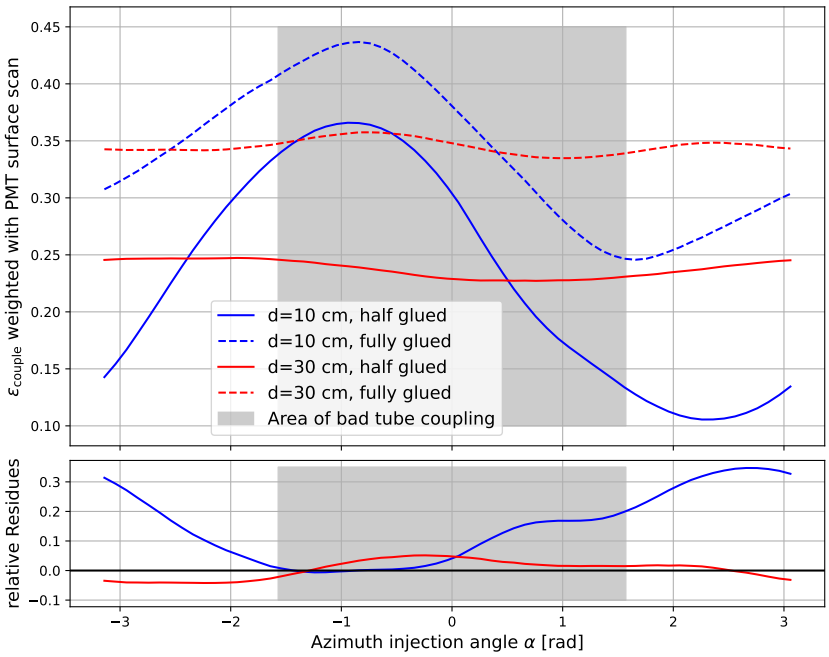

Fig. 8.11.: **Coupling efficiency weighted with relative surface sensitivity of PMT UP16.** We compare the efficiency for a tube badly coupled over half of the gluing area with a tube perfectly glued without any air segment for different injection point distances d. The **relative Residues** shown in the bottom plot are are the differences between the two curves for the same d normalized to their respective maxima to visualize their relative distance.

curves show a constant behavior for $d = 30\,\text{cm}$. It also shows a constant difference of relative 40% over all injection angles while for a close distance we observe a strong angular variation of the difference with a minimum deviation of 19%. This deviation becomes maximal in the injection area outside the the badly glued segment which is conclusive with the already discussed occurrences in Fig. 8.9.

If we therefore want to attempt a measurement on the quality of the gluing, we would need a reference measurement with a "perfectly coupled" tube which can be compared to the glued tube. Measurements at higher distances over all azimuth angles would show a constant efficiency with a possible constant difference in case of bad gluing while close measurements would show even a relative deviation increasing for certain angles.

8.3.2 Experimental Measurement

The inner assembly can not be evaluated as detailed as the inner tube due to the inability to determine the absolute efficiency. This is caused by the required foam

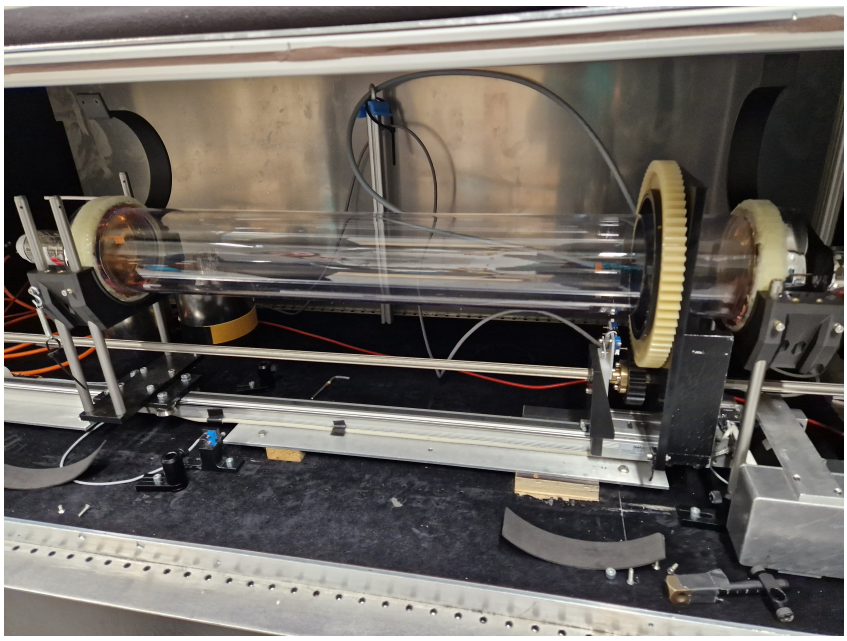

Fig. 8.12.: **Evaluation of the inner assembly using the tube evaluation test stand.** As we can not perform this measurement using mu-shields we try to evaluate the gluing quality based on a comparison of relative measurements before and after gluing.

socks around the PMTs, which need to be applied before gluing, preventing the PMTs to fit inside the mu-shields and therefore being unshielded from external magnetic fields. We therefore perform a relative measurement to estimate the coupling quality. After the inner tube evaluation, we couple one side of the tube to another PMT, which will be used in the corresponding inner assembly, using optical gel just as it is done for the inner tube evaluation. The PMT is explicitly not enclosed in a mu-shield. We measure the efficiency for a close and far distance over all azimuth angles ϕ. As we are not interested in absolute efficiencies we are using the ratio between signal and photodiode reference current without any PMT references and corrections. The same measurement in the same orientation is performed after constructing the inner assembly (see Fig. 8.12). According to Fig. 8.11 we would observe a clear decrease in the relative efficiency in case of significant bad coupling. As we are not changing the orientation and measurement setting between these measurements we would expect the same magnetic field influence assuming them being constant with time. However, the different surface sensitivities between PMTs add an uncertainty to the evaluation.

We want to verify the expectation derived in the previous section by performing the evaluation measurement with an inner assembly purposely glued only along half of the tube's area as we used for our expectation simulation. The measurement

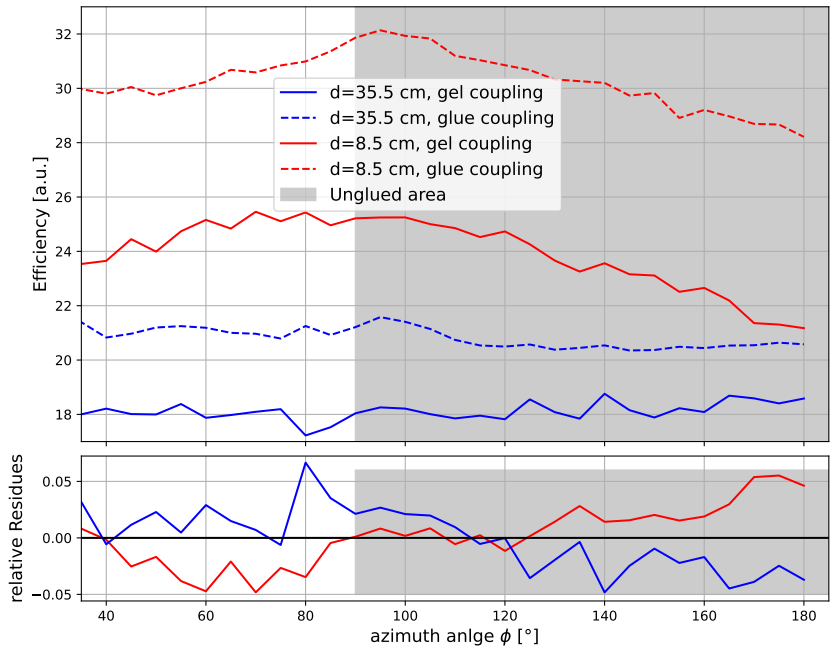

Fig. 8.13.: **Inner assembly evaluation of a tube glued over half of its end surface area to a PMT (data from [115]).** The same PMT was used as for the simulated expectation (UP16). The tube was unglued along ϕ of $90°$ to $180°$. Due to setup limitations we can not perform a full ϕ in one single measurement.

results before and after gluing shown in Fig. 8.13 deviate visibly from our expectation. We see about the same relative deviation between gel and glue coupling of 20%. While we observe a little bit of more structure for close distances it is much below the expectation. Further, the residues do not show the structural relative deviation, but more of a fluctuation bilaterally of the x-axis. Not being able to resolve these structures could be caused by different setup systematics. One possibility could be the distortion in PMT sensitivity, because of different inclination angles of the photons towards the PMT's surface. Despite these mentioned inconsistencies we can definitely see a clear decrease in efficiency pointing to a worsened coupling.

The inner assembly evaluation measurement for produced WOMs, where we would expect good optical coupling, yield vastly different results. Measurements like in Fig. 8.14a show similar efficiencies before and after gluing suggesting a successful gluing process resulting in optimal transmission. Efficiency like shown in Fig. 8.14b on other hand show a significant decrease for the inner assembly efficiency even similar to Fig. 8.13 suggesting an especially bad coupling. The vacuum gluing procedure and the following verification of a strong mechanical bound makes it very unlikely to get an optical coupling compared to half of the tube's area being not

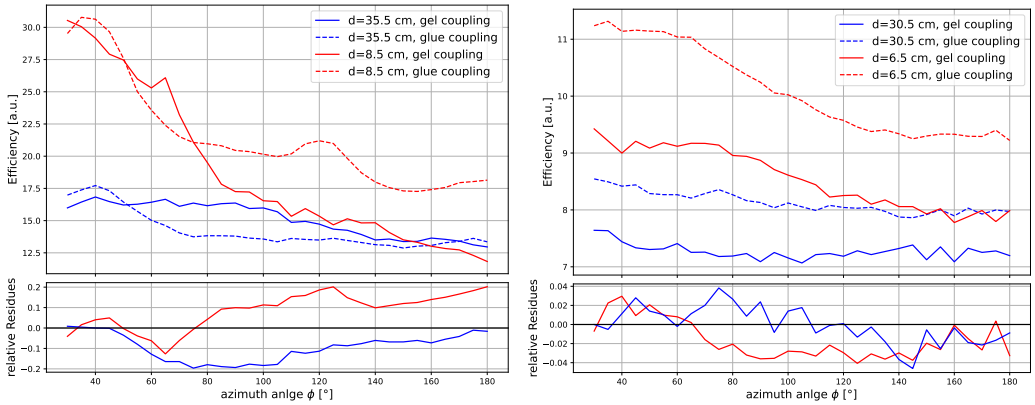

(a) WOM5 "WOMderland". (b) WOM4 "SchlickWOM".

Fig. 8.14.: Results of inner assembly evaluation measurements for produced WOMs (data from [115]). We observed vastly different results the coupling which are supposed to be similar due to a standardized procedure. This lead to not setting a quality control requirement on the inner assembly until the systematics are further investigated.

glued at all[6]. So we can make the conclusion of missing the required sensitivity in our measurement procedure to properly evaluate the coupling and separate it from other effects.

Isolating the effect of optical coupling has proven to be challenging especially while being exposed to external influences such as unshielded magnetic fields. Initial investigations from [115] observed a yet unexplained pattern of magnetic fields with our testing stand which needs to be investigated further. Additionally, the measured efficiency is influenced by different effects, one of them being the deterioration of the paint layer during tube handling. The lowered efficiency we observe can therefore be also caused by damage done to the paint during the gluing process. Properly decoupling the two fitting parameters in the flattened model fit could help us separate these effects as damaged WLS would show up most likely in the attenuation length only. All these approaches could help us optimizing and expanding on the optical quality control criteria for the WOMs which would lead to a more reliable and better characterized module.

[6]The underpressure on the inside result in the two PMTs being pressed towards the tube with almost 1 bar most likely increasing the optical coupling.

8.4 Final Acceptance Testing

After a WOM is fully assembled it undergoes **Final Acceptance Testing (FAT)** which verifies its overall functionality and identifies possible issues relevant for operating the module in the ice. Contrary to mass produced modules like mDOMs and DEggs we do not use the FAT to discard bad performing modules, but getting familiar with possible module specific issues and performance nuances only occurring while operating the full module. For the first batch of WOMs we performed only an **optical** FAT which would eventually be expanded on for the production of the remaining modules. Especially, we want to test the functionality of the PMTs, the WOM's signal output while being illuminated with external light and the functionality and visibility of the flashers.

8.4.1 Setup

The FAT setup (shown in Fig. 8.15) consists of a light tight wooden box with the WOM fixed inside using tension belts. To prevent light background, every interface area with possible gaps is covered with black compression and gaffa tape. Additionally, the whole box is enclosed in a black-out blanket. HV-control and readout is done by the electronics inside the WOM. The module is operated over the mini-Fieldhub located outside the dark box. A small hole is carved into the top lid of the box for cable routing.

We use the picosecond-pulser [129] as an additional external light source. We adjust its brightness with a filter wheel mounted directly behind it. The pulser is directed onto the WOM with a Liquid Light Guide (LLG). A total of 6 holes are drilled into the box to illuminate the module at 3 different height positions for 2 azimuth angles. The holes are located on the left side and front panel chosen to be close to each of the both PMTs and about in the middle between them to test the distance dependent module efficiency. While the diameter of the holes is adjusted to the size of the LLG we still get some movement there which provides a systematic to the setup which is increased by needing to change the insert of the light guide manually for each position.

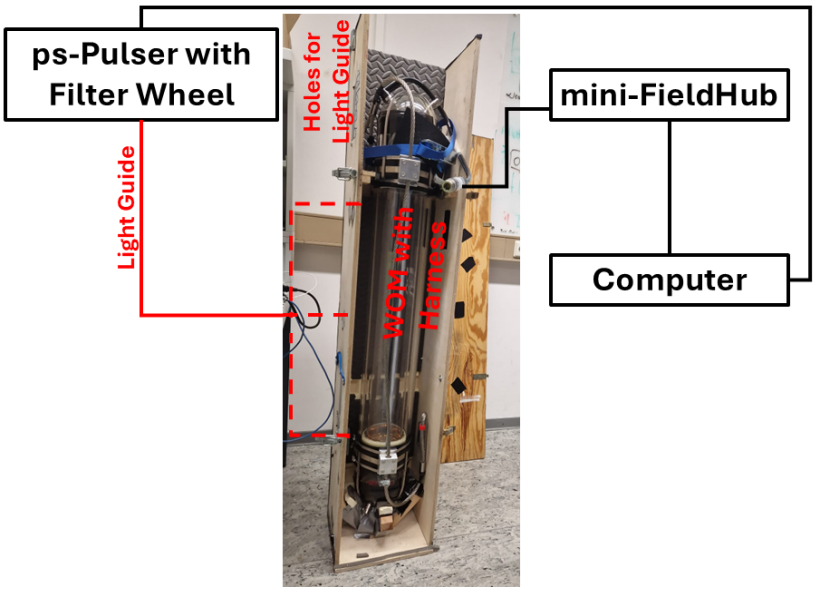

Fig. 8.15.: **Setup for the WOM's optical FAT.** The module is located inside a wooden dark box read out completely by the internal electronics. We illuminate the WOM using an external pulsed light source guided through 6 holes at different positions.

8.4.2 Gain and Trigger

We first want to calibrate the gain and trigger threshold for each PMT to set the module to nominal gain with a corresponding 0.25 PE trigger. The HV is set using the HV-board in units of DAC counts with a linear relation between counts and voltage with the maximum DAC value of 4095 corresponding to $2000\,\mathrm{V}$. We perform dark rate measurements for different HVs triggering on the pulse height.

The PMT signal is read out by the wuBase in units of ADC counts. The waveforms are calibrated to a photocurrent using calibration factors determined by an electronic simulation [137]. We can then calculate the charge SPE spectrum and determine the gain using a Gaussian fit (see Fig. 8.16).

We fit the determined gain values to the expected power-law from Eq. 2.15:

$$G(U) = A \cdot U^B. \tag{8.4}$$

From Fig. 8.17 we can determine the fit parameters A and B for both PMTs of WOM4:

$$\begin{aligned} A^{\text{top}}_{\text{UP13}} &= 10^{-21.5} \quad B^{\text{top}}_{\text{UP22}} = 8.98 \\ A^{\text{bottom}}_{\text{UP22}} &= 10^{-22.1} \quad B^{\text{bottom}}_{\text{UP22}} = 9.22. \end{aligned} \tag{8.5}$$

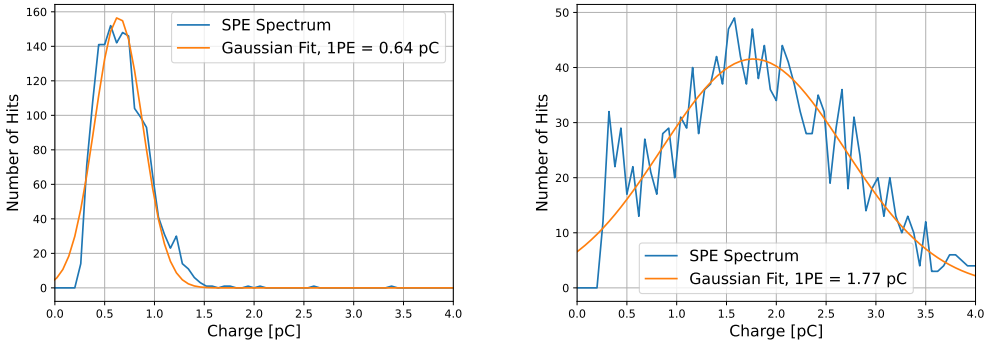

(a) HV=1285 V, 1PE=0.64 pC. **(b)** HV=1435 V, 1PE=1.77 pC.

Fig. 8.16.: SPE spectra for different HVs for bottom PMT, UP22 of WOM4. We use a constant trigger threshold of 900 DAC Counts for this measurements which can be noticed in the left spectrum being more cut off.

Comparing the voltages for the 10^7 nominal gain with the target voltages from the PMT dark rate measurements (see Section 5.1.3) of $U^{\text{old}}_{\text{UP22}} = 1235\,\text{V}$ and $U^{\text{old}}_{\text{UP13}} = 1316\,\text{V}$ we notice an increased required voltage of about $150\,\text{V}$. This is partly related to a manufacturing error for the PMT bases using the wrong resistors between dynodes resulting in a lower photocurrent. Further, one would need to verify the calibration constant for the ADC as it was determined for the LOM specific wuBase.

Setting the HV to a gain of $1.0\,\text{pC}$ $(0.625 \cdot 10^7)$[7] we will now calibrate the trigger DAC to be able to set the trigger properly to 0.25 PE for the data taking. Depending on the set trigger threshold we get a different cutoff in the SPE spectrum (see Fig. 8.18).

We determine the cutoff charge for every threshold by taking the earliest bin with more than zero entries. As we see in Fig. 8.19 the DAC counts to charge calibration follow a linear relation very similar between the two PMTs. We determine the slopes s to:

$$s^{\text{bottom}}_{\text{UP22}} = 7.2 \cdot 10^{-4}\text{pC/Count} \quad s^{\text{top}}_{\text{UP13}} = 7.1 \cdot 10^{-4}\text{pC/Count}. \tag{8.6}$$

We can therefore conclude that we will need to set a trigger threshold of 1000 DAC counts corresponding to a charge cutoff of $0.25\,\text{pC}$ while operating the PMTs at

[7] Because of the unexpected mentioned manufacturing issue some PMTs would eventually not reach the nominal gain of 10^7 so we performed the test at a lower gain. This will be adjusted for the second batch of WOMs.

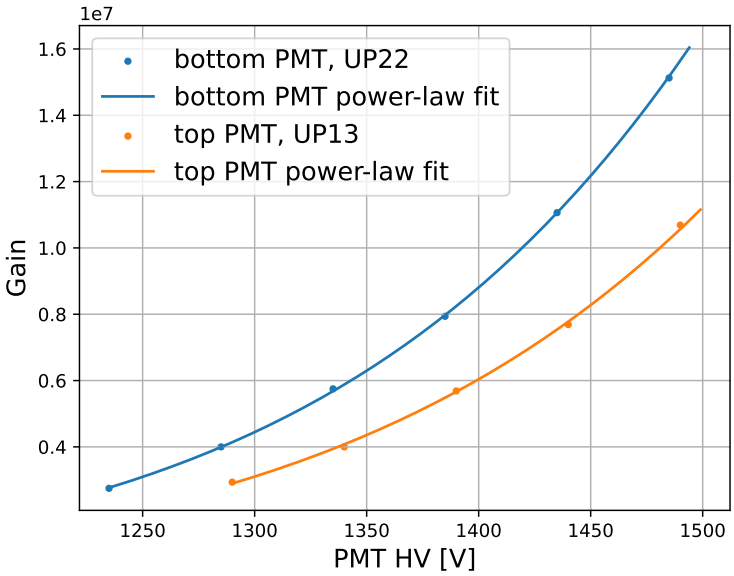

Fig. 8.17.: **Gain Calibration curves of WOM4 PMTs.** G=charge·e. We fit the power law from Eq. 2.15 to the gain curves of top and bottom PMT.

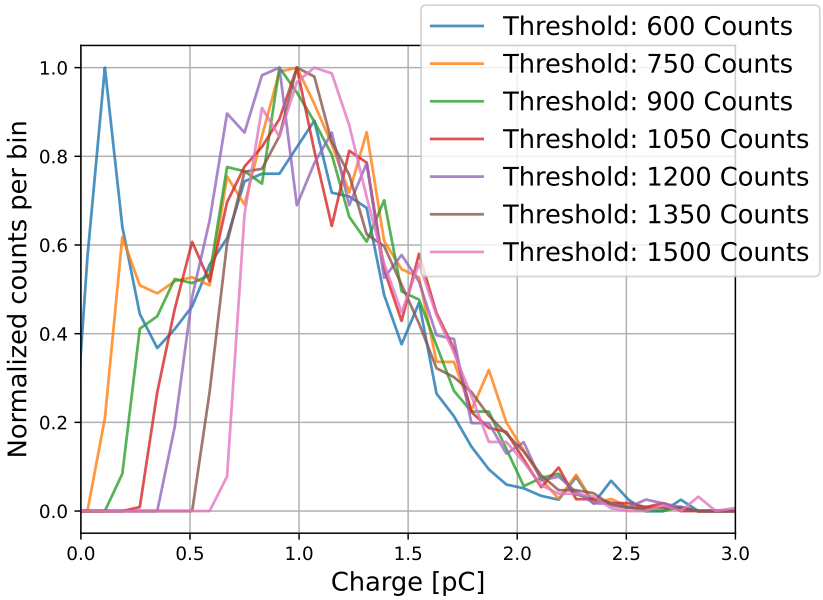

Fig. 8.18.: **SPE spectra of bottom PMT, UP22, of WOM4 for different trigger thresholds.** HV=1350 V. We see the cutoff charge increasing with the trigger threshold. Due to a limited bandwidth in the electronics we get less hits in the SPE peak for a low threshold as we see increased noise hits there.

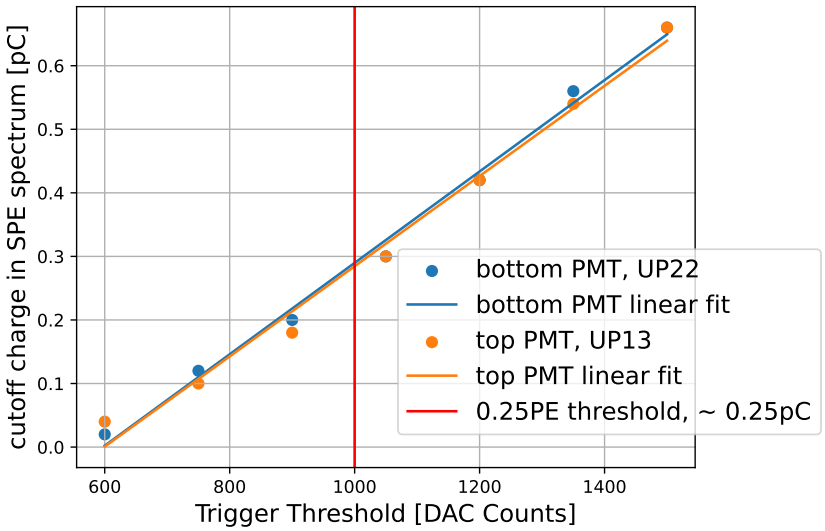

Fig. 8.19.: **Trigger DAC calibration for PMTs of WOM4.** The curves for both PMTs are very similar which is expected as the same DAC is installed on all wuBases.

a gain of $0.625 \cdot 10^7$. At the nominal gain of 10^7 we will need a threshold around 1150 counts.

8.4.3 Distance Efficiency

From our measurements in Section 5.2 we were able to confirm the wavelength-shifting functionality of the inner tube and determined its efficiency with respect to the distance between injection point and PMT. For FAT we want to verify the rudimentary tube properties by measuring the number of detected photons of light hitting the WOM at different spots.

We illuminate the module radially using the pulser and determine the number of detected photons by localizing the **Multi Photon Emission (MPE)** peak in the charge spectrum. The early development stage of the IceBoot software at that point resulted in a very limited bandwidth of transmitted hit data and therefore in triggering only on a small faction of photons reaching the PMT (up to $22\,\mathrm{Hz}$ per wuBase). Due to a high dark rate of up to $10\,\mathrm{kHz}$ per PMT at room temperature the less frequent pulses from the light source would not have enough presence to collect enough statistics. So the trigger threshold is increased to a value between 3000 and 4000 DAC counts which corresponds to a charge cutoff above 1PE eliminating a large fraction of the dark rate hits. We set the frequency of the pulser to either $1\,\mathrm{kHz}$ or $10\,\mathrm{kHz}$ and adjust the gray filter so the signal is bright enough to be seen, but still bellow the saturation threshold. To verify the correct brightness we check

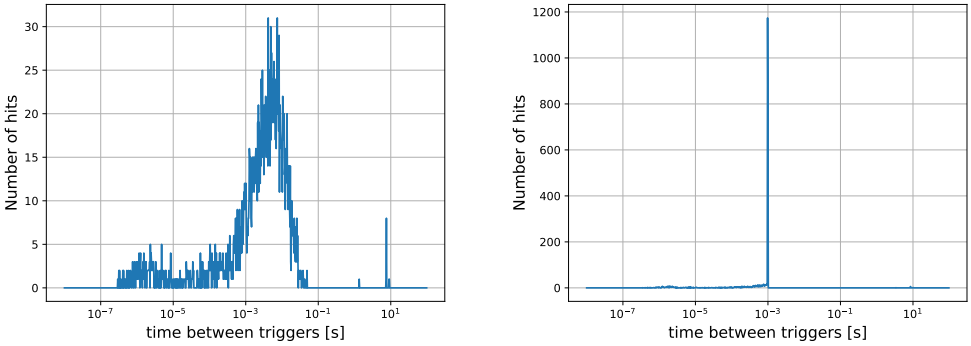

(a) Pulser turned off.

(b) Pulser flashing with 1000 Hz.

Fig. 8.20.: Timing distribution between triggers for bottom PMT of WOM4 with and without flashing pulser. HV=1350V, threshold= 3000 DAC counts. The pulser results in a sharp peak at $t = 1$ ms which corresponds to the set frequency. As we can not cut off the whole SPE peak with a maximum threshold of 4095 counts we are still seeing dark rate hits, but with a reduced frequency. We further see an excess at $t \approx 10$ s which marks the wuBase's deadtime after a certain number of triggers confirming that most photon hits are not recorded.

the distribution of times between triggers (see Fig. 8.20). For a turned on pulser we see a sharp peak at $t = 10^{-3}s$ corresponding to the set pulser frequency and almost no hits anywhere else. We can therefore confirm most of the recorded waveforms originating from the pulser's signal.

After having verified the pulser's signal, we determine the number of detected photons from the light pulse by localizing the corresponding MPE peak in the charge spectrum and determine its mean via a Gaussian fit (see Fig. 8.21). This is performed for all six injection points for top and bottom PMT.

From the measured charge we get the number of detected photons $N_{\text{ph, PMT}}$ which we correct with the surface correction S_{surf} and the measured QE at the PMT's center $\epsilon_{\text{QE}}^{\text{center}}$ for $\lambda = 375$ nm to determine the number of photons exiting the tube on both sides and its corresponding error:

$$N_{\text{ph, tube}} = \frac{N_{\text{ph, PMT}}}{S_{\text{surf}} \cdot \epsilon_{\text{QE}}^{\text{center}}} \qquad \sigma_{N_{\text{ph, tube}}} = \frac{\sqrt{N_{\text{ph, PMT}}}}{S_{\text{surf}} \cdot \epsilon_{\text{QE}}^{\text{center}}}. \tag{8.7}$$

The results for WOM4 (see Fig. 8.22a) show a trend of increasing efficiency with the illumination point being closer to the PMT. However, we see a huge discrepancy between the signal at the top and bottom PMT in terms of absolute values. The top PMT sees up to 350 photons for close distances while the number of photons for the bottom PMT stays below 50.

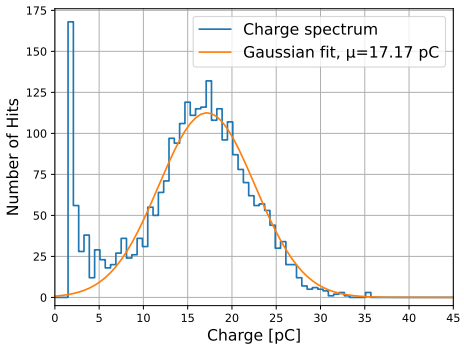

(a) Bottom PMT, UP22, HV=1350V.

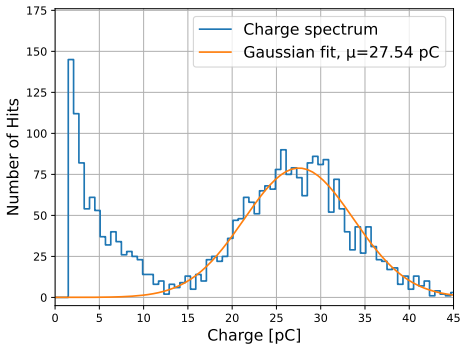

(b) Top PMT, UP13, HV=1400V.

Fig. 8.21.: MPE peaks from pulser light pulse in charge spectrum for bottom and top PMT of WOM4. The WOM is illuminated at the center point on the inner tube from the side ($\phi = 90°$). To confirm that this peak is actually caused by the light pulse we performed a reference measurement with the pulser turned off.

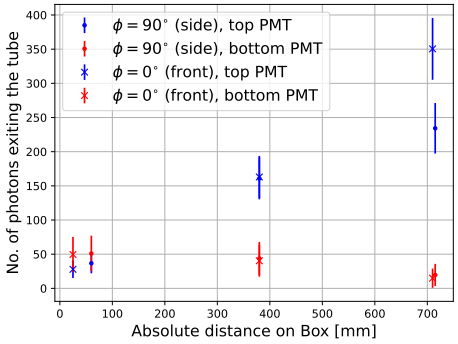

(a) WOM4 "SchlickWOM".

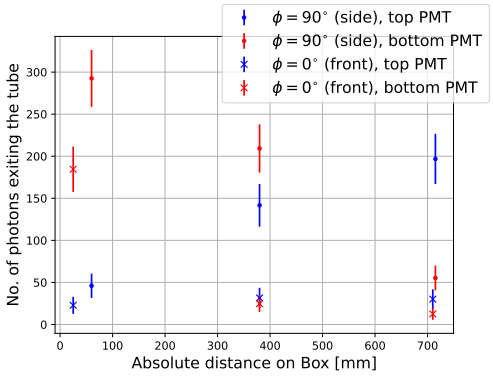

(b) WOM3 "Willy_WOMka".

Fig. 8.22.: Number of photons exiting the inner tube under illumination of a pulsed light source for different illumination spots on the WOM. We define $\phi = 0°$ for illumination using holes in the front panel and $\phi = 90°$ for illumination from the side. An absolute distance of 0 is the position of the bottom PMT and $7600\,\mathrm{mm}$ for the top PMT. The harness rope is located close to the front panel and could therefore block the incoming light.

WOM3 (Fig. 8.22b) shows much similar curves for top and bottom PMT while still not perfectly matching. But for $\phi = 0$ we see almost no change in N_{ph} with the distance staying at relative low values. This is most likely caused by the harness rope, located at the front panel, blocking most of the incoming light.

The observed inconsistencies point to a not yet fully optimized setup to perform a precise measurement. The light guide having too much movement within the holes could result in a strong variation of incoming light and misalignment between WOM and light source would cause irregularities the the measured efficiency curves. Additionally, the wooden box provides no shielding from external electrical nor magnetic fields which could contribute to distorting the PMT signal. To compare absolute values between PMTs and WOMs one would need to analyze and improve the systematics of the given setup while also collecting more statistics by measuring at more distances and azimuth angles.

8.4.4 Flasher Acceptance and PMT Linearity

We now want to test the functionality of the four flashers and later use these to test the photon linearity of the PMTs. As a reminder: There are four flasher boards located in the bottom compartment pointing radially outwards in $90°$ angles. The first three flashers on the chain (flasher 1-3) are equipped with UV-LEDs with $\lambda = 365\,\text{nm}$ while flasher 4 has an optical LED with $\lambda = 405\,\text{nm}$. The brightness can be adjusted over the bias voltage in DAC counts of 0-65535 which was calibrated to the absolute number of emitted photons per pulse (see Fig. 8.23) [138]. The time between two pulses is also set by a DAC with one count corresponding to $17\,\mu\text{s}$ [137].

We first want to check on the visibility and frequency of each flasher. For that, we flash each flasher individually setting them to the same frequency (which varies depending on the noise of the module) and about the same brightness for all four flashers. The emitted photons propagating outside the module are eventually back-reflected on the box's inner wall before they hit the WLS tube to be shifted and detected by the PMTs. We compare the time between two pulses extracted from the timing distribution with the expectation as well as the number of detected photons from the charge distribution as already explained for the pulser measurement.

As seen in Fig. 8.24, we get the same correct period length for all flashers seen in both PMTs for WOM2. This also applies to all other WOMs except WOM3, where the period length is lower by about 4-10 μs for flasher 4.

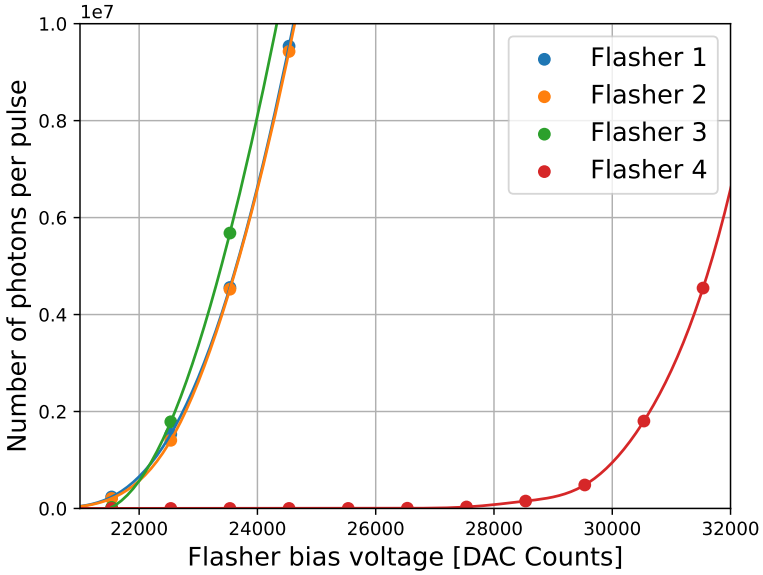

Fig. 8.23.: **Bias voltage calibration of flasher for WOM2 (data from [138]).** Shown in the relevant region for WOM FAT purposes. We see the single taken datapoints and a performed cubic interpolation between them. For FAT we use very low brightnesses to not saturate the PMTs and readout, where the bias calibration is not necessary linear.

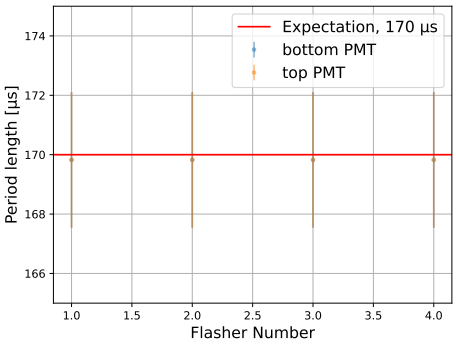

Fig. 8.24.: **Period length of flasher chain of WOM2.** The time between two flashes was set to 10 DAC counts which should correspond to $17\,\mu$s. The errors result from the arbitrary chosen bin width. The limitation on the resolution is the $60\,$MHz clock on the wuBase.

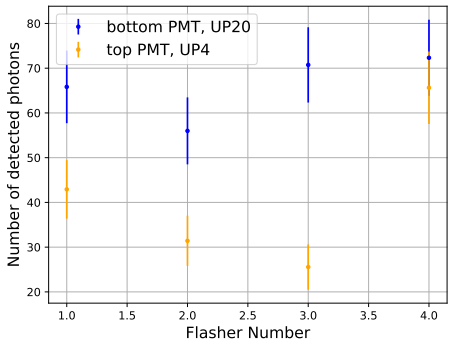

Fig. 8.25.: **Detected photons from all flashers by both PMTs of WOM2.** Bias for flasher 1-3: 23000 Counts, flasher 4: 30000 Counts. That corresponds to about the same number of emitted photons for all four flashers. We use Poissonian errors on the number of photons.

Comparing the detected flasher brightnesses in Fig. 8.25 we first notice consistent higher brightnesses for the bottom PMT which is because of its closer distance to the flashers. Further, we notice variations in the brightnesses of flasher 1-3 even through we would expect about the same number of emitted photons from them. During the installation process one could not prevent the LEDs from slightly bending to fit them properly into the pressure vessel. This different bending for each LED combined with the imperfect alignment of the module inside the box could cause the observed variations in photon losses. Finally, we notice the surprising increase in brightness for flasher 4 even though we would expect a decreased brightness there due to the WLS paint's absorption and re-emission efficiency at $\lambda = 405\,\text{nm}$ being decreased to below 20% relative to the value at $\lambda = 365\,\text{nm}$. One possible explanation would be the different behavior in reflection on the wooden box for different wavelengths. This needs to be properly studied by using a more well defined material in its reflectance.

After verifying the full functionality of the flashers we will use them to perform a linearity measurement on the PMTs. We determine the region, where the detected charge (or number of detected photons) scales linearly with the number of photons hitting the module before the waveforms start to saturate. This denotes the effective operating range of the WOM. For one selected flasher (like flasher 1 for WOM2) we perform a scan over a range of bias voltages using a fixed frequency. We determine the number of detected photons for both PMTs from the charge spectrum. Finally, we calibrate the range of set bias voltages to the number of emitted photons using Fig. 8.23 resulting in data shown in Fig. 8.26. We fit a linear slope to the first data points and determine a threshold, where the data deviates from a linear relation.

We determine slopes of

$$s_{\text{bot}} = 3.3 \cdot 10^{-5} \qquad s_{\text{top}} = 1.4 \cdot 10^{-5} \tag{8.8}$$

which describe the number of detected photons relative the number of flashed photons. The linear relation goes until an estimated number of 60 detected photons before the data points flatten out. The saturation can be also seen in the waveforms in Fig. 8.27, where we observe clearly clipped waveforms due to the saturation of the ADC. We can therefore confirm an operating range for the WOM of up to 60 PE. This number is bound to the set gain and the range of the readout ADC on the wuBase. Operating the module on the nominal gain of 10^7 would lower the threshold to about 38 PE. Due to the limited number of taken data points outside the saturated region we can only make a rough estimation on this value. One would need to increase the density of set bias voltages for a more precise result.

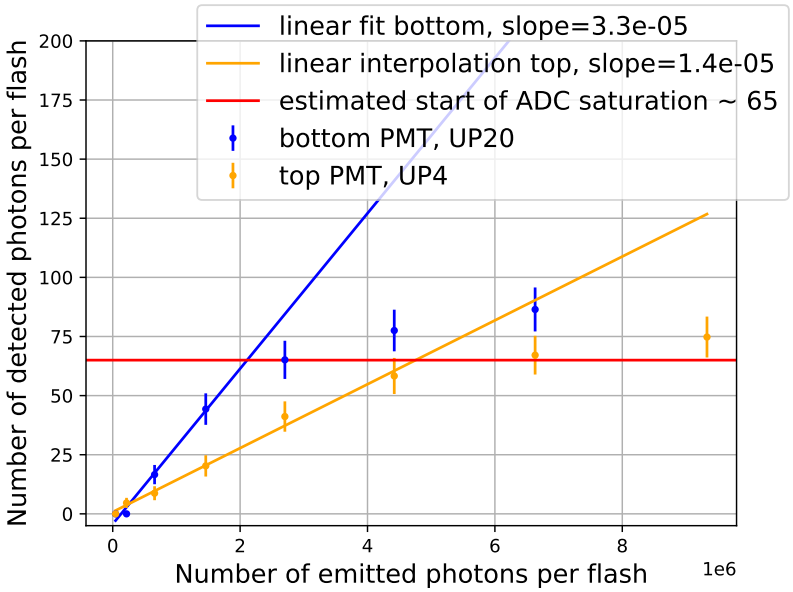

Fig. 8.26.: Photon linearity measurement of WOM2 using a flasher bias scan. Using flasher 1 with a period of $170\,\mu s$ and a trigger threshold of 4000 DAC counts. The set bias voltages are calibrated to the number of emitted photons per pulse.

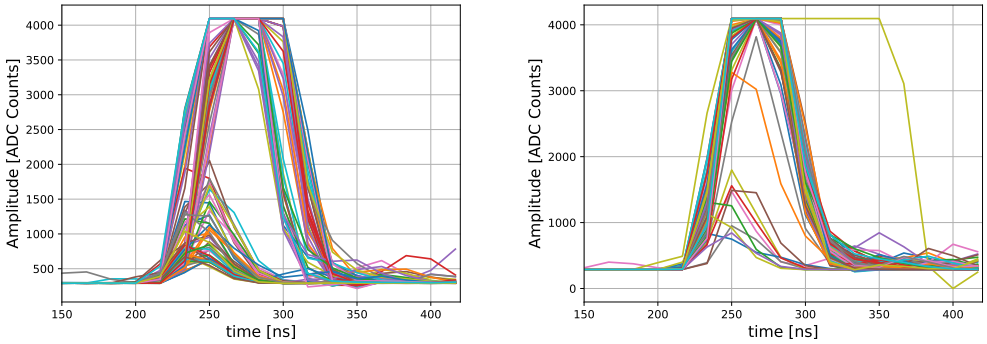

(a) Bottom PMT, bias=23000 counts. $N_{\text{ph, det}} = 65 \pm 8$.

(b) Top PMT, bias=23500 counts. $N_{\text{ph, det}} = 58 \pm 8$.

Fig. 8.27.: WuBase ADC waveforms of the first data point in the photon linearity measurement of WOM2 being outside the linear regime. We see many waveforms clipping off due to exceeding the ADC's range. The bottom PMT saturates earlier, because it is closer to the flasher.

8.4.5 Summary of Results

The goal of the performed FAT was to verify the basic functionality of the assembled and shipped modules and to identify issues that could become relevant during deployment and data-taking in IceCube. In many aspects, the tests yielded satisfactory results: no complete module failures were observed, and communication with the modules generally worked well.

However, severe issues arose during the testing of WOM4 and WOM6, which prevented the completion of the full test routine. Both modules exhibited frequent but irregular communication interruptions with the HV boards and wuBases. As a result, commands related to setting high voltage and data acquisition were not executed consistently. While WOM4 could complete the gain and trigger tests as well as the distance efficiency measurement and calibration, WOM6 failed to pass any FAT segment due to the high frequency of communication failures. Nevertheless, both modules were confirmed to have working PMTs and flashers. Since swapping components ruled out the possibility of individual faulty boards, potential root causes include internal cabling issues or the use of early-stage software at the time of testing.

No other issues of comparable severity were observed. The remaining modules performed as expected, albeit within the high uncertainty margin typical of our rather improvised test setup. Nonetheless, key behavioral trends—such as the expected increase in efficiency with increasing distance to the PMT—were confirmed. Minor deviations, such as the slightly off flasher period for WOM3 or the unexpectedly high brightness of one optical flasher, are not expected to significantly impact data-taking in the ice. See Appendix C for FAT results on all five shipped WOMs.

To improve the FAT procedure and enhance the reliability of the results, the following measures are recommended:

- Optimize the distance efficiency setup by ensuring proper mounting of the light guide to prevent random movement, which would reduce systematic uncertainties. Additionally, scanning over a wider range of distances would improve statistics. This could be achieved by replacing fixed mounting holes with a linear rail system. Shielding the module from external electromagnetic interference—e.g., using a Faraday cage instead of a wooden box—would also improve measurement quality.

- Refine the photon linearity test by increasing the number of data points and ensuring measurements are conducted at the correct nominal gain. This would

enable more accurate determination of the upper photon detection threshold and allows a study of the module's response to saturated waveforms.

- Include a test based on a physical signal, such as the detection of atmospheric muons producing Cherenkov light in the pressure vessel or PFPE. Such events would likely produce signals larger than 1 PE and might be observed in coincidence between both PMTs. However, the current triggering scheme does not support the detection of such signals, and the relatively low muon rate combined with sparse waveform recording limits observability. This could be addressed by implementing a low-gain channel for the WOM, similar to other optical modules.

- Introduce a temperature FAT as an additional segment, acting as a long-term stability test under cryogenic conditions. Modules would be placed in a freezer at $-40\,^{\circ}\mathrm{C}$ for one week, while monitoring gain and dark rate. This would test mechanical robustness and the long-term stability of optical properties. For the current batch, this test was only performed on one module, which will be discussed in Section 9.1.

While the current FAT setup and procedure allowed for a basic verification of module functionality and revealed some relevant issues, several aspects could be improved for the testing of the second production batch. Implementing the suggested adjustments would help to reduce uncertainties and make the results more robust, particularly in identifying subtle or intermittent issues early on.

8.5 Performance of produced WOMs

From all performed evaluation measurements we can now summarize and compare the performance parameters for our fully produced and shipped WOMs. We calculate the effective area of each module under use of individual experimental data with

$$A_{\mathrm{eff}}^{\mathrm{WOM}}(\lambda) = \epsilon_{\mathrm{trans}}(\lambda) \cdot \epsilon_{\mathrm{tube}}(\lambda) \cdot \epsilon_{\mathrm{glue}} \cdot \epsilon_{\mathrm{PMT}} + \epsilon_{\mathrm{direct}}(\lambda). \tag{8.9}$$

The tube efficiency ϵ_{tube} determined in Section 8.2 consists of the relative wavelength efficiency and the absolute linear efficiency averaged over all distances. This quantity accounts for wavelength-shifting, capturing and propagation efficiency in air:

$$\epsilon_{\mathrm{tube}}(\lambda) = \epsilon_{\mathrm{tube}}^{\mathrm{WLS}}(\lambda) \cdot \epsilon_{\mathrm{tube}}^{\mathrm{lin}} = \epsilon_{\mathrm{WLS}}(\lambda) \cdot \epsilon_{\mathrm{TIR}}^{\mathrm{air}} \cdot \epsilon_{\mathrm{att}}^{\mathrm{air}}. \tag{8.10}$$

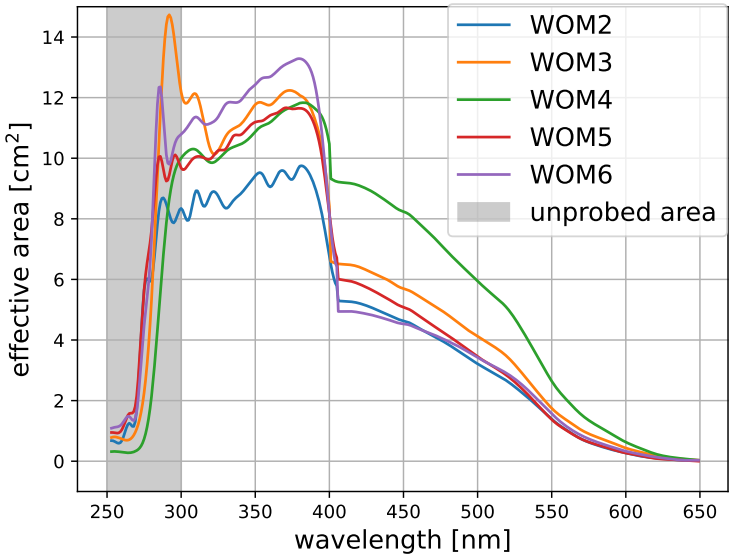

Fig. 8.28.: Effective area for the first batch of produced WOMs using experimental data from their evaluation. The first batch of WOMs was shipped without PFPE filling. The excess for WOM2 is most likely an artifact from the measurement. Due to the PMT cutoff for $\lambda < 300\,\text{nm}$ we do not have reliable experimental data there.

As the tube is coupled to the PMT with optical gel we still need to consider the different glue transmission. ϵ_{PMT} is determined from the QE and surface scans of each individual PMT used for the corresponding WOMs averaging over top and bottom PMT. Transmission and direct hit efficiency were taken from simulation data (the individual PMT corrections were still used for the direct hit contribution). However, due to several unresolved engineering challenges the first batch of WOMs had to be shipped without PFPE filling (see Section 9.4 for details) significantly reducing their effective area[8].

We see the effective areas for WOM2-6 in Fig. 8.28 displaying peak values fluctuating around $10\,\text{cm}^2$. Using a PMT reference measurement for the tube wavelength scan results in a cutoff for $\lambda < 300\,\text{nm}$ and therefore in an uncertainty for the performance in the low-UV. However, we can expect a behavior there similar to the curve shown in Fig. 8.7. For the next production batch, one would need to implement the mentioned photodiode reference measurement to inquire more information in the low-UV wavelength region.

[8]That also means, that the determined ϵ_{tube} for each WOM does not have to be corrected to the different filling material as these measurement were performed in air.

WOM No.	peak $A_{\text{eff}}[\text{cm}^2]$	dark rate [Hz]	NSR [Hz/cm^2]
WOM2 "WOMit"	9.74	1219	125.15
WOM3 "Wily_WOMka"	12.08	1084	89.74
WOM4 "SchlickWOM"	11.82	1073	90.78
WOM5 "WOMderland"	11.65	1377	118.20
WOM6 "Eisgekühlter_ WOMmerlunder"	13.29	1025	77.36

Tab. 8.2.: **Comparison of effective areas and dark rates for the first batch of produced WOMs.** The peak A_{eff} is defined as the effective area at $\lambda = 380\,\text{nm}$, where we would expect the highest value according to our wavelength scans. The dark rate is the sum over the dark rates of the single PMTs with an additional $120\,\text{Hz}$ to consider for the radioactive noise of the pressure vessel.

A comparison of the peak effective area and corresponding dark rate for the produced WOMs is summarized in Tab. 8.2. We notice that the different PMT performances result in a noticeable spread in efficiency and NSR. The distribution of the PMTs among the available modules has to be adjusted to the corresponding goal for the WOMs in IceCube. One could either ensure all modules having a similar SNR or having a few single "high performing" modules while the rest would perform worse than average. For a more precise characterization one would also need to measure the dark rate of the full modules at freezing temperatures of $-18\,^{\circ}\text{C}$ and $-35\,^{\circ}\text{C}$ expected in the ice as this was only done for the bare PMTs here.

8.6 Summary and Outlook

In this chapter, we introduced and applied quality control criteria for various optical components of the WOM across all stages of the production chain. These criteria are motivated by reproducible performance requirements that ensure a consistent quality standard for the final delivered and deployed modules.

A key focus of the evaluation was the inner tube, where paint layer quality directly impacts wavelength-shifting and photon propagation. Measurements of paint homogeneity and efficiency confirmed theoretical expectations and showed that all tubes met performance criteria, suggesting stricter thresholds—e.g. raising linear efficiency from 40% to 50%—are feasible. However, asymmetries likely caused by external magnetic fields warrant further study, potentially using Helmholtz coils for compensation [115]. Additionally, the current setup cannot probe wavelengths below $300\,\text{nm}$ due to PMT limitations—a gap that could be closed using a photodiode

for the reference measurement, as shown in earlier work [71]. Using the measurements to estimate the quality of optical coupling introduces too many uncertainties to serve as a reliable quality control criterion without further refinement.

Each completed WOM underwent FAT to verify basic functionality. While the improvised test setup limited detailed performance assessment, it allowed identification of key issues such as communication dropouts (WOM4, WOM6) and incorrect resistor placement on PMT bases, leading to reduced gain. To better assess long-term performance, future FAT procedures should include extended monitoring of gain and dark rate for temperatures down to $-40\,^{\circ}\mathrm{C}$. This could be implemented using a dedicated calibration module for continuous lab testing in the North.

Due to engineering constraints during the initial production phase, the first batch of five WOMs was assembled without PFPE filling. As a result, their effective area is limited to approximately $10\,\mathrm{cm}^2$, making them significantly less competitive compared to other modules developed for the IceCube Upgrade. Addressing this issue in future production runs—by enabling reliable PFPE integration—would allow for a substantial increase in effective area and improve the overall light collection performance of the modules.

The absence of PFPE is not merely a temporary compromise but reflects underlying engineering challenges related to the mechanical design, sealing, and thermal behavior of the modules. These challenges form the focus of the following chapter, which discusses **Design Verification Testing (DVT)**. In the following we will examine the technical limitations as well as the necessary design adaptations to ensure reliable, high-performance WOM modules in future deployments.

9 Design Verification Testing

Besides an optimized optical performance, the WOMs need to be mechanically robust to survive and perform under extreme conditions in the ice and during transportation. Studies to satisfy these requirements are referred to as **Design Verification Testing (DVT)**. DVT is performed for different temperatures, mechanical vibrations and shocks during transportation and for extreme outer pressures of $700\,\mathrm{bar}$. This chapter discusses the testing procedures and corresponding results on the complete module as well as on the single components, which result in corresponding improvements for the WOM's mechanical design.

9.1 Temperature Testing

The WOM needs to resist operation temperatures down to $-40\,^{\circ}\mathrm{C}$ which are expected inside the Antarctic ice, as well as storage temperature of up to $50\,^{\circ}\mathrm{C}$, which are present during plane transportation. Further, local temperature differences within the module need to be considered as the source for the heat is located at the plane's ceiling giving the WOM's upper compartment a higher temperature relative to the lower compartment. Further, the IceCube modules need to resist a **thermal shock**, which happens as the modules originally stored at $-40\,^{\circ}\mathrm{C}$ are dropped inside the melted ice at $0\,^{\circ}\mathrm{C}$.

The temperature DVT is performed in the climate cabinet already used for PMT testing in Section 5.1.3. As shown in Fig. 9.1 the module is placed horizontally in the climate chamber[1]. To prevent the PFPE from flowing inside the top compartment eventually damaging the electronics, the WOM is slightly inclined. Because, the module can not be placed hanging of the steel rope, we install a metallic spring between the two harness blocks. Fully tensioned the spring pulls the two harness blocks together with a force of $1500\,\mathrm{N}$ corresponding to five times the weight force of a WOM hanging on the rope. Assuming the harness would get loose due to thermal expansion, this would be noticed by a changed distance between the harness blocks[2].

[1] Vertical placement was not possible due to the limited size of the cabinet.
[2] The spring is not intended to be a part of the final harness design. It is used for testing purposes only.

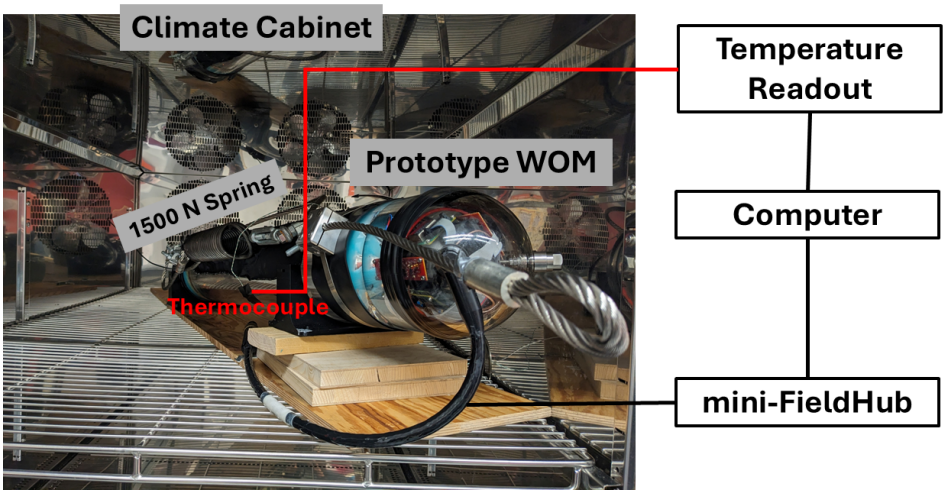

Fig. 9.1.: **Temperature testing setup for a fully assembled WOM.** The module is placed horizontally, slightly inclined inside the climate cabinet. Readout is happening via WOM electronics operated over the mini FieldHub located outside the climate cabinet. To simulate a hanging position of the module, a spring is installed pulling the two harness blocks together with $1500\,\mathrm{N}$.

During the test, the WOM is monitored using the internal pressure and temperature sensors as well as an external thermocouple measuring the temperature on the outer side of the pressure vessel.

9.1.1 Temperature Cycle

The module inside the climate cabinet undergoes a temperature cycle as shown in Fig. 9.2. First, the temperature is reduced slowly down to $-40\,^{\circ}\mathrm{C}$. Throughout this time, pressure and temperature values are taken each minute and datataking is performed every 15 minutes. After the WOM is operated at $-40\,^{\circ}\mathrm{C}$ for some time the module is completely turned off to stay at this freezing temperature for at least one day. This is supposed to test the robustness of the module for storage at the pole at $-40\,^{\circ}\mathrm{C}$. For the upcycle symmetric to the downcycle back to $20\,^{\circ}\mathrm{C}$ the monitoring and datataking is turned on again until the module reaches room temperature. This is followed by a further increase in the temperature to $50\,^{\circ}\mathrm{C}$ to test the module for transportation at high temperatures inside the plane and warehouses. As no operation will be performed at these temperatures the module is turned off for this testing segment.

Fig. 9.3 shows the taken pressure and temperature data for the down- and upcycle to $-40\,^{\circ}\mathrm{C}$ for WOM1. The data concludes that the temperature and pressure behaves as expected as the temperature of the thermocouple and on the MMB

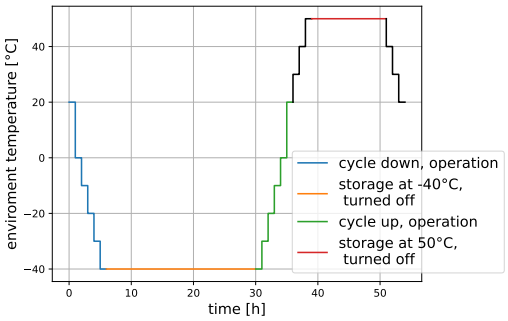

Fig. 9.2.: Temperature cycle for WOM DVT. The time axis is only supposed to give an idea for the relative time of each segment and does not reflect the actual length.

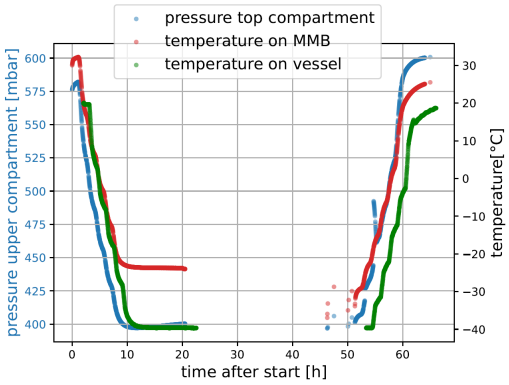

Fig. 9.3.: Pressure and temperature monitoring for DVT temperature cycle of prototype WOM1. The module was turned off for the most part while being at $-40\,^{\circ}\mathrm{C}$. There is only pressure data for the top compartment as the bottom pressure sensor was not yet implemented at this point in time.

match and the pressure changes linearly with the temperature. The structure of the temperature curve does not show clear steps for the up- and downcycle meaning that the set time of 1 h per $10\,^{\circ}\mathrm{C}$ temperature difference is not enough to properly cool or heat the complete module at the required temperature. Further, it needs to be considered that the electronic boards produce heat while in operation which is reflected in the MMB's temperature which only goes down to $-22\,^{\circ}\mathrm{C}$ instead of $-40\,^{\circ}\mathrm{C}$. Neither of the two measured temperatures reflect the proper temperature of the PMTs during the up- and downcycle, but only provide a rough estimate.

To investigate the change of the gain of the WOM we take the bottom PMT (UP15) as an example. Fig. 9.4 shows its gain over the course of the temperature cycle. The downcycle shows a steady increase with decreasing temperature before it suddenly drops down after the minimum temperature of $-40\,^{\circ}\mathrm{C}$ is reached. This second observation did not show up in the temperature evaluation of the single PMT (see Section 5.1.3). The upcycle, which is performed after the modules have been turned off for about one day, starts at a significant higher gain which then decreases with increasing temperature. As the turned off state of the module prevented the electronic boards to produce heat the PMTs were able to cool down properly over a longer time resulting in an increased gain.

As previously discussed, the direct PMT temperature can not be measured and is expected to be somewhere between the temperature read out by the sensor on the MMB and the temperature on the outer side of the pressure vessel. In Fig. 9.5 the

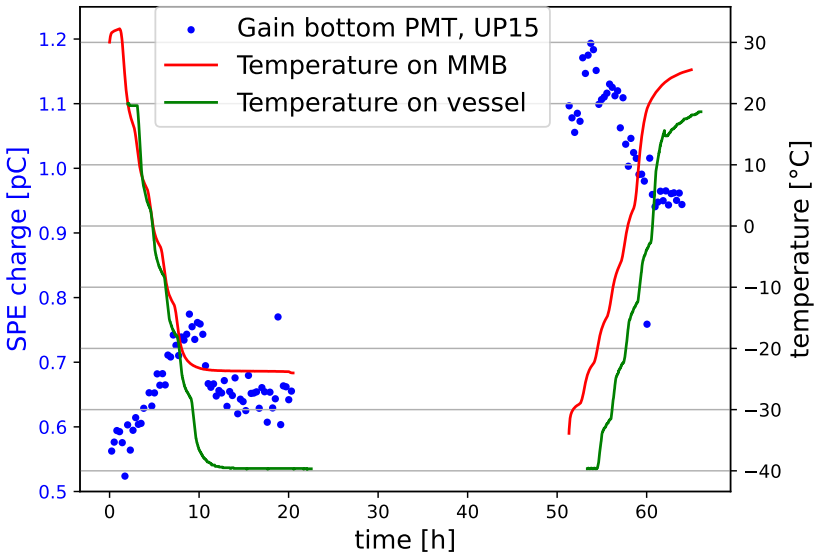

Fig. 9.4.: Change of gain for bottom PMT (UP15) of prototype WOM1 during temperature cycle. Data was taken every 15 minutes for 2 minutes. The SPE charge was determined from a Gaussian fit to the SPE spectrum of 2 minutes of data. Single outliers result from fitting artifacts.

correlation between gain for both temperatures is shown. We observe similar slopes for up- and downcycle.

As we operate the module at a different gain than the single PMTs from Section 5.1.3[3] we need to calculate the relative slopes s to compare them to the bare PMT measurement of UP15:

$$\begin{aligned} s^{\text{down}}_{\text{vessel}} &= 0.42\,\%/^{\circ}\text{C} \qquad s^{\text{up}}_{\text{vessel}} = 0.33\,\%/^{\circ}\text{C} \\ s^{\text{down}}_{\text{MMB}} &= 0.96\,\%/^{\circ}\text{C} \qquad s^{\text{up}}_{\text{MMB}} = 0.54\,\%/^{\circ}\text{C}. \end{aligned} \tag{9.1}$$

The discrepancy between up- and downcycle is larger compared to the bare PMT measurement and can denote to a systematical error:

$$s_{\text{vessel}} = (0.375 \pm 0.045)\,\%/^{\circ}\text{C} \qquad s_{\text{MMB}} = (0.75 \pm 0.21)\,\%/^{\circ}\text{C}. \tag{9.2}$$

The slope for the bare PMT measurement of $0.6\,\%/^{\circ}$C (see Section 5.1.3) is located between these two values as we would expect as the PMT's temperature should be somewhere between the MMB's and vessel's temperature. The PMT would be slightly affected by the heat produced by the boards. The pressure vessel's temperature is

[3] As already mentioned in Section 8.4 we see a different gain while operating the PMTs with the WOM electronics rather than the picoscope.

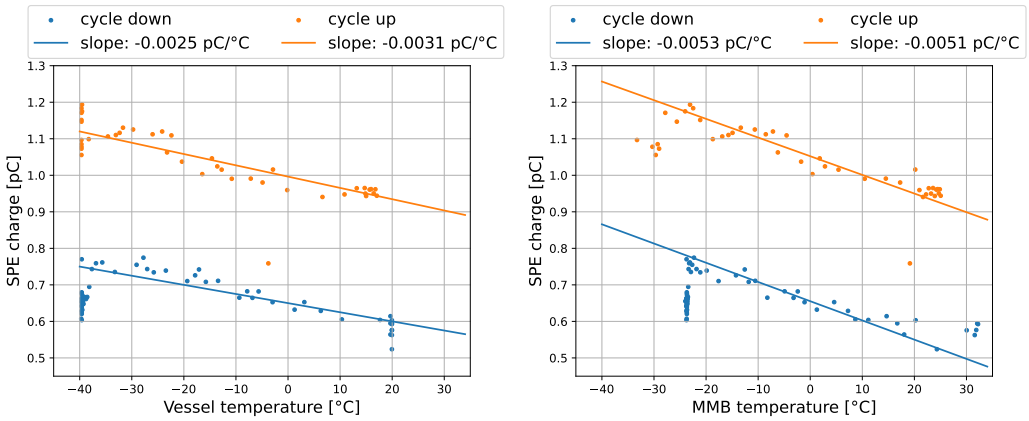

(a) Temperature measured on the outside of the pressure vessel.

(b) Temperature measured using the temperature sensor on the MMB.

Fig. 9.5.: Correlation between temperature and bottom PMT gain of WOM1. The slopes differ between the two temperatures as they change differently with time. Using the MMB temperature we get similar slopes for up- and downcycle while we see differences there while using the temperature on the pressure vessel.

also more stable as it only depends on the setting of the climate cabinet and not on the operation of the electronics. This explains the much higher discrepancy between down- and upcycle using the MMB's temperature. The module being turned off before results in a temperature increase not only because of the cabinet's setting, but because of the additional heat from the boards.
Conclusively, we get matching results with the bare PMT measurement using the picoscope as readout, but observe much higher systematic errors, because the temperature cycle is not long enough for the temperature to properly stabilize. Longer down- and upcycles would cause a better temperature equilibrium over the whole module and reduce systematic uncertainties.

Contrary to the picoscope measurement, the PMT's dark rate can not be determined from counting the number of hits due to the limited bandwidth. Instead, we will use the timing distributions for two consecutive hits (see Fig. 9.6). Random noise with an average rate R is a Poissonian process. Therefore, the underlying timing follows an exponential distribution given by the density function:

$$f(t) = R \cdot e^{-R \cdot t}. \tag{9.3}$$

While Fig. 9.6a shows one Poissonian peak, we can resolve a double peak structure in Fig. 9.6b. The right peak results from random distributed noise which we are primarily interested in (**uncorrelated hits**) while the left peak features

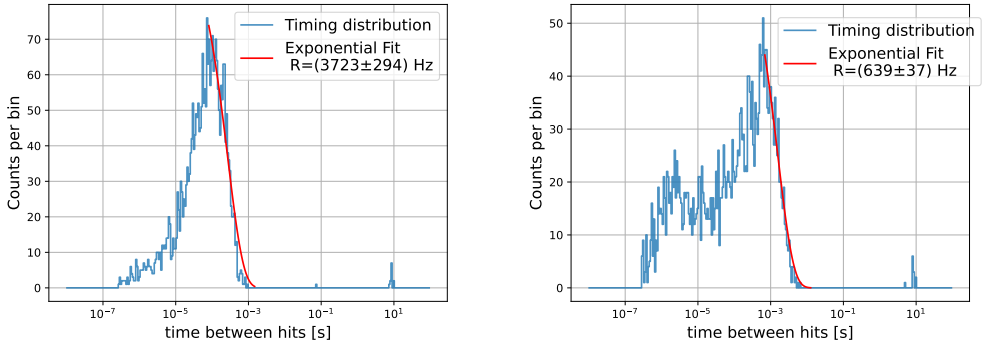

(a) $T = 20°$C. 14 minutes after starting the down-cycle.

(b) $T = -40°$C. 18 hours after starting the down-cycle.

Fig. 9.6.: Timing distributions of bottom PMT of WOM1 for different temperatures. The dark rate R is determined by fitting an exponential distribution given by Eq. 9.3 with a corresponding normalization factor. The error on the rate is given by the fit.

correlated effects such as afterpulses or oscillation photons from the radioactivity of the glass (PMT, pressure vessel and inner tube) [139]. These effects are also present at room temperature, but significantly suppressed. Further, they also showed up in the picoscope measurements from Section 5.1.3, where we observed a small increase in the dark rate at low temperatures after it had decreased before. The precise composition of correlated hits can be studied by using veto-detectors which detect the scintillation photons from the different WOM components as well as from the environment. To reduce the background of our module in the ice we can introduce a **deadtime** between hits which should be high enough to get rid of most background contributions while still keeping most of the signal hits. Setting the deadtime in the valley between the two peaks at $\lambda = 10^{-5}$ s gets rid of the major fraction of correlated background while still keeping about 50% of the signal.

The dark rate over the full temperature cycle is shown in Fig. 9.7. We see a clear decrease of the dark rate with the temperature and some fluctuations below $1000\,\mathrm{Hz}$ at $-40\,°\mathrm{C}$. The steep decline at the start of the cycle is further caused by the PMT's activation as it was exposed to light before testing. The rate seems to be relatively constant, but a long-term stability tests would need to be performed in the future while monitoring the module over a longer period of time at cold temperatures.

The temperature correlation plots in Fig. 9.8 visualize a fluctuation of the rate for temperatures between $-10\,°\mathrm{C}$ and $-40\,°\mathrm{C}$. We want to estimate the dark rate for this module being either located in the physics region at $T = -18°$ C or in the shallow region at $T = -35°$ C. The rate is determined by calculating the weighted

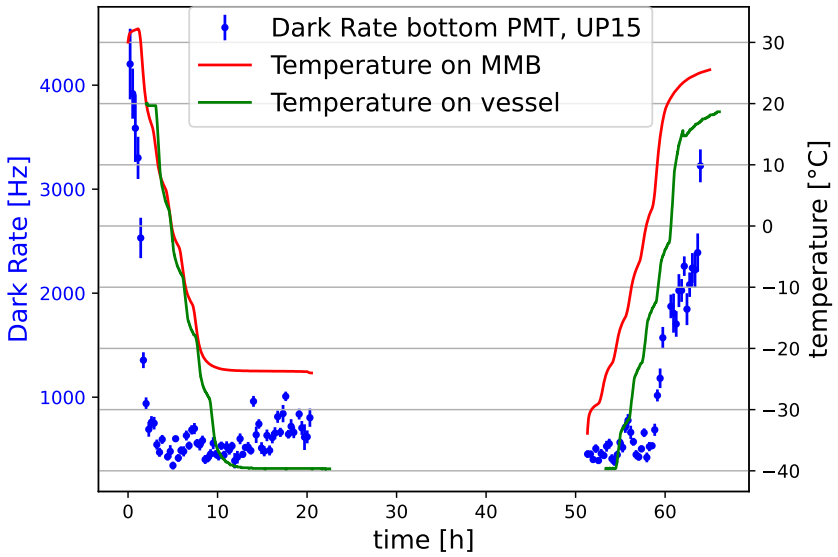

Fig. 9.7.: Dark rate of bottom PMT of WOM1 over the full temperature cycle. The mean and error are determined from an exponential fit to the timing distribution as illustrated in Fig. 9.6 from 2 minutes of data taken every 15 minutes.

mean over all datapoints being located within $4\,^{\circ}\mathrm{C}$ around the desired temperature. We use the temperature of the pressure vessel as it should be almost equal to the environmental temperature inside the climate cabinet. The resulting rates are:

$$R_{\text{physics}} = (597 \pm 28)\,\text{Hz} \qquad R_{\text{shallow}} = (513 \pm 24)\,\text{Hz}. \tag{9.4}$$

Comparing these numbers to the results of the bare UP15 PMT (see Fig. 5.11) we get a rate in the physics region within 1σ and a rate in the shallow region which is even below the rate of the picoscope measurement. However, we need to consider the lower gain of about 40% which would influence the dark rate slightly.

Assuming a similar dark rate for the top PMT[4] we can conclude a dark rate of about $1100\,\text{Hz}$ for WOM1 already including the radioactive noise from the glass of the pressure vessel. While we would expect the noise to slightly increase at higher gain, it can be confirmed that the base PMT measurements give a reasonable estimation on the dark rate of the fully assembled module.

[4]The dark rate of the top PMT (UP6) could not be properly determined as the trigger was set too low resulting almost only noise triggers. However, the bare PMT measurement of UP6 showed dark rate in around $600\,\text{Hz}$.

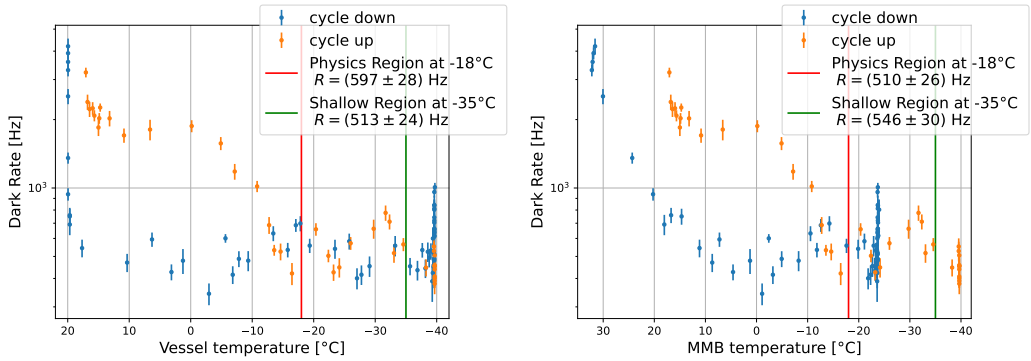

(a) Temperature measured on the outside of the pressure vessel.

(b) Temperature measured using the temperature sensor on the MMB.

Fig. 9.8.: Correlation between temperature and dark rate of WOM1 bottom PMT. We determine the dark rates for the expected temperatures in the physics and shallow region in the ice considering data from the down- and upcycle.

9.1.2 Thermal Shock

About one year before deployment, the IceCube modules are stored at the South Pole at a temperature of approximately $-40\,^{\circ}\mathrm{C}$. At deployment, the modules undergo a sudden temperature change while being dropped into the melted ice at $0\,^{\circ}\mathrm{C}$. This **thermal shock** could potentially cause mechanical deformation and therefore damage single components within the module. For the WOM possible damage could occur in the PMTs and their coupling to the tube as well as in the sealing.

To perform the thermal shock test we let the module cool down to $-40\,^{\circ}\mathrm{C}$ and keep in it in the climate cabinet for about one day while being turned off. The complete module is then quickly immersed into a bucket of water at room temperature[5] (see Fig. 9.9).

No visible mechanical damage was observed after the test. All electronic boards and both PMTs were fully operational before and after without changing their behavior. The module was tested without the Harness as it was already successfully tested before separately [118]. As this test was performed with a module not filled with PFPE no conclusion can be made about possible PFPE leakage during a thermal shock. This test therefore will have to be repeated for the second batch of modules with a WOM of improved design with filling material.

[5] To have a proper safety margin, we perform a shock test of $60\,^{\circ}\mathrm{C}$ temperature difference while we would expect a difference of $40\,^{\circ}\mathrm{C}$ at most during deployment.

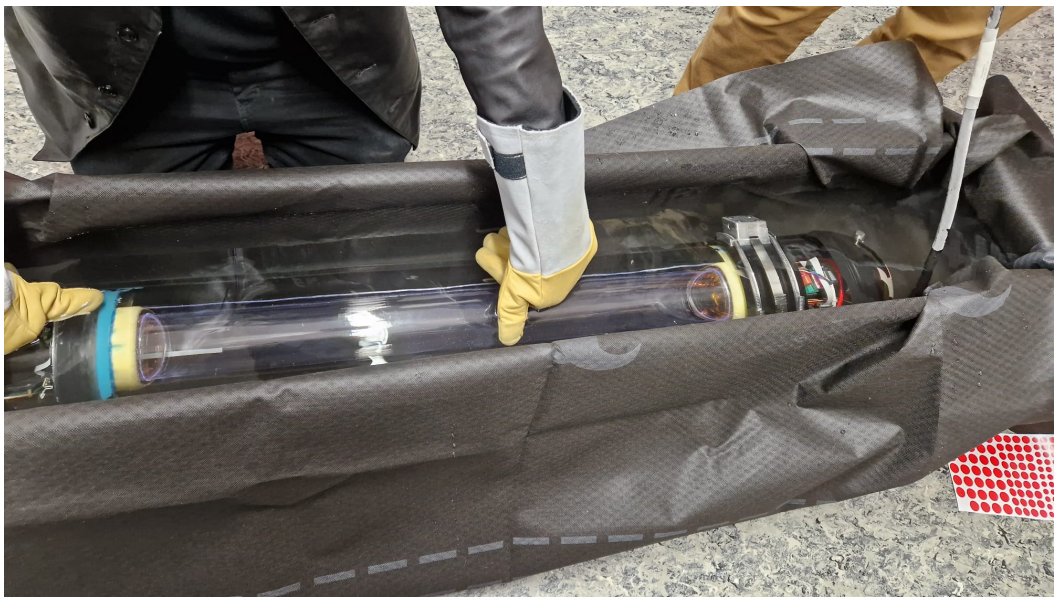

Fig. 9.9.: **WOM4 being immersed into a bucket of water after being cooled down to $-40\,^{\circ}\mathrm{C}$ to perform a thermal shock.** The thermal shock test was performed after the decision to build the first batch of WOMs without PFPE. Therefore the module does not contain the filling liquid. The prototype WOM1 was not used for this test, because of previous PFPE leakages caused by possible damage in the sealing (see Section 9.4).

9.2 Packaging and Transportation

IceCube modules undergo a long way on different transportation vehicles until they reach the South Pole. During transportation on ships, planes and trucks the devices are exposed to different fluctuating temperatures, outer pressure and different kinds of mechanical vibrations and shocks. This section will quantify the requirements for the WOM to survive the transportation and justify certain design decisions for the module and its corresponding transportation box.

9.2.1 Inner Pressure and Evacuation

The expected pressure inside a pressurized cabin is about $0.7\,\mathrm{bar}$. The LC-130 Hercules, which is used for cargo transport to the pole, is known to have have dips down to $0.65\,\mathrm{bar}$ in its cabin pressure setting the requirement to the inner pressure of the modules to below $0.6\,\mathrm{bar}$ [116]. For the WOM specifically, we need

to additionally consider the thermal expansion of the PFPE. For an optimal efficiency we want the central compartment's volume given by

$$\begin{aligned} V_{\text{PFPE}} &= \pi h_{\text{tube}} \cdot \left((r_{\text{vessel}}^{\text{inner}})^2 - (r_{\text{tube}}^{\text{outer}})^2 \right) \\ &= \pi \cdot 760\,\text{mm} \cdot ((72.5\,\text{mm})^2 - (57.5\,\text{mm}^2)) = 4.66\,\text{L} \end{aligned} \tag{9.5}$$

to be fully filled with PFPE. Due to filling material's thermal expansion of $0.0011\,\text{K}^{-1}$, $4.97\,\text{L}$ would need to be filled into the WOM at room temperature so the middle compartment is fully filled at $-40\,°\text{C}$ inside the ice. This additional amount would be located inside the top compartment before and flow down to the middle compartment as the PFPE compresses under low temperatures. Given a temperature of up to $50\,°\text{C}$ on the plane the filled PFPE expands by $0.16\,\text{L}$ relative to room temperature which increases the pressure in the top compartment due to a reduced gas volume. Using the ideal gas law with $\frac{pV}{T} = const$ we determine the required pressure in the top compartment at room temperature p_{lab}:

$$p_{\text{lab}} = \frac{p_{\text{plane}} \cdot V_{\text{plane}} \cdot T_{\text{lab}}}{V_{\text{lab}} \cdot T_{\text{plane}}}. \tag{9.6}$$

The value p_{plane} is given by the minimum pressure in the cabin of $0.6\,\text{bar}$ and V_{lab} is the initial gas volume of the top compartment already considering the extra filling of $0.31\,\text{L}$ of PFPE. We determine a maximum pressure of

$$p_{\text{lab}} = 0.48\,\text{bar} \tag{9.7}$$

for the pressure the WOM needs to be evacuated to under lab conditions. As an additional safety margin we choose a pressure of $0.3\,\text{bar}$ which is used for both compartments to prevent forces resulting from pressure differences inside. This estimation is quite conservative as it does not consider the mechanical compression of the pressure vessel due to the high pressure in the ice which effectively reduces the extra amount of needed PFPE increasing the allowed inner pressure at room temperature (see Section 9.3).

The top and bottom compartment are evacuated at the same time to the same pressure of $0.3\,\text{bar}$ to prevent any **push-pull forces** resulting from pressure differences inside the module. However, these effects can still occur during transportation caused for example by local temperature differences in the plane's cargo. As the heating pipes are only located at the plane's ceiling we would expect a considerable higher temperature in the top than in the bottom compartment (as the WOMs are being transported vertically.) A temperature difference of $50\,°\text{C}$ would cause a pressure difference about $0.15\,\text{bar}$ between the two compartments. An unlikely, but

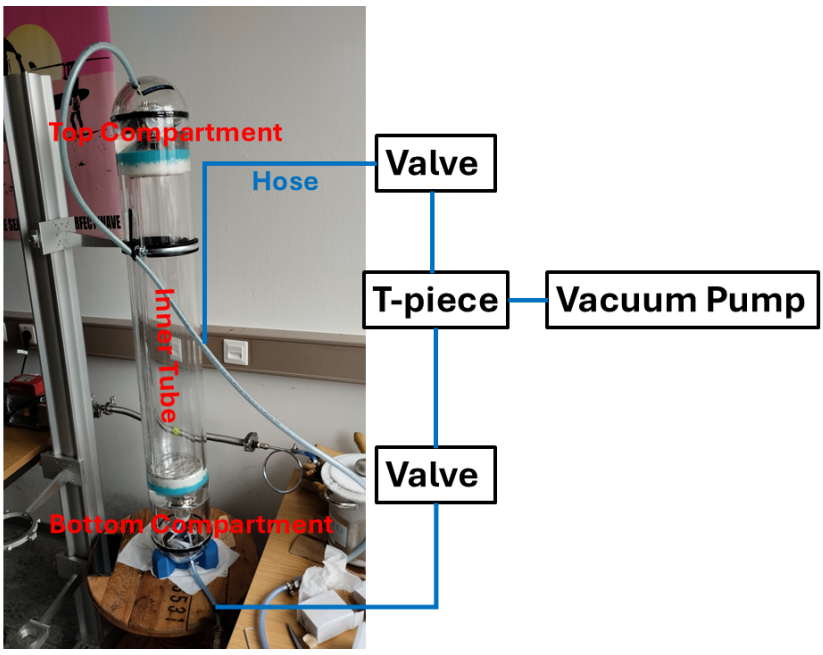

Fig. 9.10.: **Setup for push-pull test of a sealed inner assembly inside the pressure vessel.** The top and bottom compartment are connected to the vacuum pump using a T-piece. Both hoses can be closed off separately using valves so only one compartment is evacuated at the same time. The shown setup does not contain any PFPE filling, but the same test was also performed with PFPE inside with similar results.

existing possibility would be a small leak in either of the compartments creating the pressure difference.

To verify the sealing robustness against pressure differences we perform the **push-pull test**, where a pressure difference of $0.5\,\mathrm{bar}$ is deliberately created between the two compartments. As shown in Fig. 9.10 an inner assembly sealed in at the top and bottom side of the pressure vessel using the three layer sealing explained in Section 4.4.1. The top and bottom compartment are equipped with analogue pressure sensors and the corresponding endcaps are both connected to a vacuum pump. We create a pressure difference in both directions by evacuating either of the two compartments down to $0.5\,\mathrm{bar}$ while keeping the other one at $1\,\mathrm{bar}$ normal pressure. During the evacuation process both PMTs are closely monitored for any movement.

At a pressure difference of about $0.3\,\mathrm{bar}$ air bubbles start occurring on the MoldStar layer of the sealing (see Fig. 9.11). This indicates movement in that layer as the force of $184\,\mathrm{N}$ caused by the pressure difference is not compensated by friction between MoldStar and glass. As the ShinEtsu layer does not show any effects like this we observe compression of the MoldStar caused by this force. Up until a

Fig. 9.11.: **Blue silicon layer at top PMT during push-pull test at $0.3\,\mathrm{bar}$ pressure difference.** We see air bubbles along the MoldStar silicon layer indicating movement of it due to the pressure difference. This effect is not seen on the ShinEtsu layer, which has a much better glass adhesion.

pressure difference of $0.5\,\mathrm{bar}$ resulting in a push-pull force of $306\,\mathrm{N}$, no movement in the ShinEtsu layer is observed concluding a high enough glass friction to withstand expected pressure differences. Further investigations of a WOM filled with PFPE showed a movement resistance of pressure differences down to $0.7\,\mathrm{bar}$ with no PFPE leakage observed.

9.2.2 Vibration Test

In this section the vibration test is discussed which verifies the robustness of the module and its transportation box against mechanical vibration and shock.
The WOM is shipped in a custom transportation box made from a wooden frame with inner sizes of 302x300x1496 mm. As shown in Fig. 9.12 the WOM is placed vertically fixed with tension belts on the top and bottom. All sides are insulated with two-layer padding of styrodur and memory foam. This keeps the module in place and prevents damage resulting from vibration and shock in both directions (x and y-axis). The module stands on an insulated stand which is kept in place by multiple styrodur plates providing padding along the WOM's axis (z-axis). The large mass and fixation with tension belts prevent the module from jumping up and down even at high mechanical shocks along the z-axis. There is memory foam located between the rope and the removable front panel as well as between the harness, the steel rope and the pressure vessel to prevent the rope from scratching the glass. The box

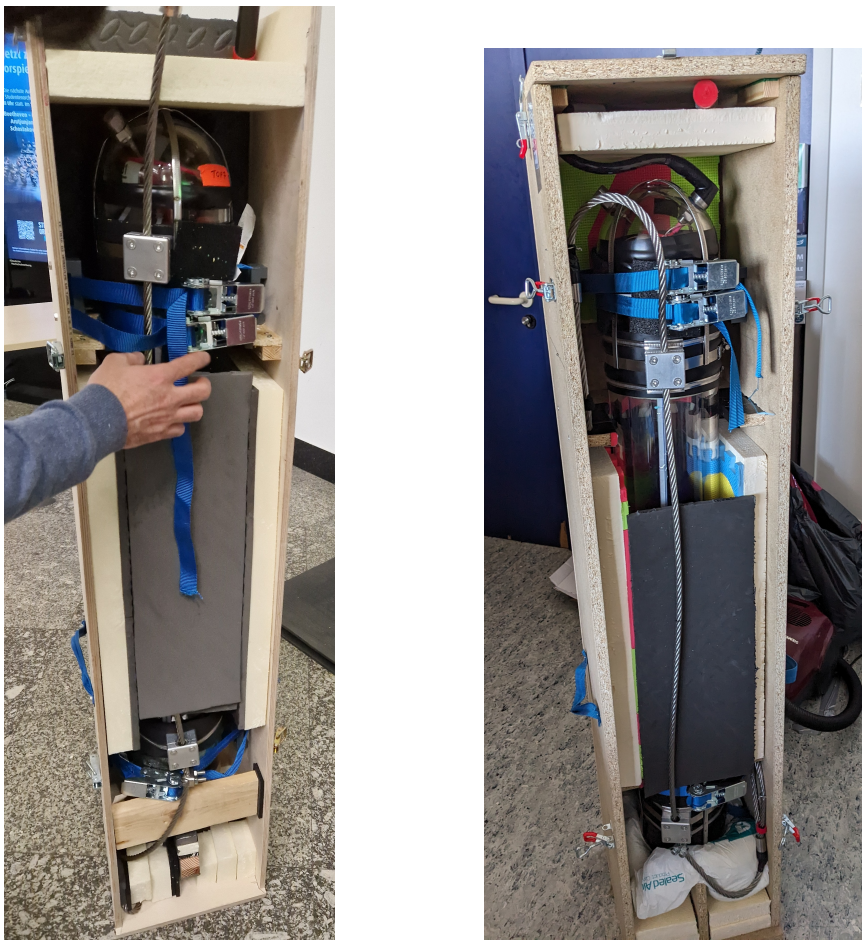

(a) Prototype box with WOM1 used for vibration testing.

(b) Final box design used to ship the modules to the South Pole.

Fig. 9.12.: **WOM transportation box prototype and final design.** Several improvements were implemented over time such as a thicker wooden frame, a change in the bottom stand and better fixation of penetrator and steel rope.

has a removable top lid to be able to access the penetrator to perform tests on the South Pole without opening up the whole box. The module is separated from the lid by two styrodur plates to cover the PMTs from light exposure while reading out the WOM.

The design of the box was improved over time to provide more safety during transportation. Thicker wood was chosen for better stability and the positioning of support structures was optimized. The bottom stand and its insulation was modified. Instead of using styrodur and memory foam, an expanding foam is placed there which adjusts itself to the shape of the bottom endcap providing a more reliable fixing. As the vibration test was performed with the first prototype box from

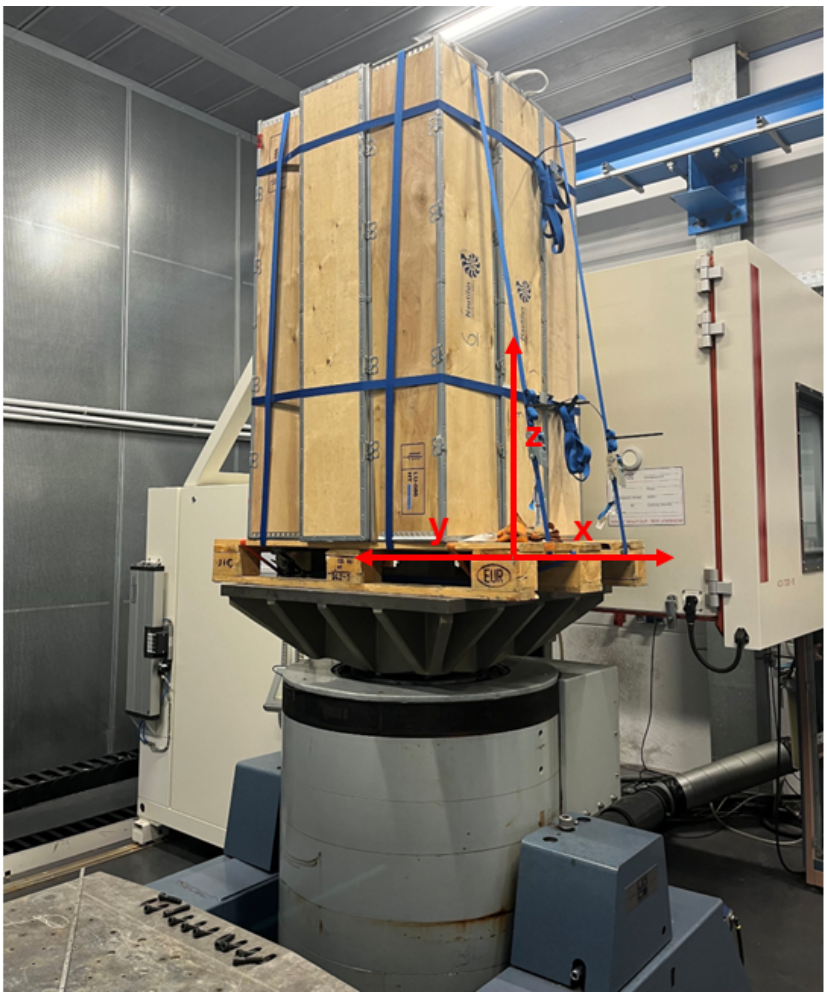

Fig. 9.13.: **Packed WOM strapped on pallet placed on vibration table.** The testing routine features vibrations at different frequencies and shocks along the x, y, z-axes.

Fig. 9.12a we can confirm that the final box design has similar or better insulation quality than the results from the vibration test.

For the vibration test performed by the company **AKUVIB** [@140], the packed WOM was strapped to a pallet surrounded by 8 similar empty boxes which then were placed on the corresponding vibration table (see Fig. 9.13). This resembles the shipping situation for a pallet of WOMs[6]. The testing routine kindly provided by the company includes vibration in three axes at typical frequencies expected from plane and truck transportation as well as mechanical shocks of 30G (see [141] for details).

[6] Five WOMs were shipped on a pallet, but placing the empty boxes asymmetrically around the packed WOM could result in issues due to irregular weight distribution.

The inspection of the module after the testing showed no obvious damages on the module. No movement of the inner assembly or PFPE leakage could be seen and no pressure change was determined. Communication with most electronic boards worked as before. However, the connection cable between penetrator and the MMB Power board became loose during the test resulting in no triggers during datataking. Opening up the module and fixing the cable resulted in restoring proper functionality. To prevent loose cables, all cable connectors are fixed with epoxy resin before closing and shipping the modules.
Overall, the vibration tests showed satisfying results with no unpreventable failures which makes it very likely for the WOMs to arrive at the South Pole safely.

9.3 Outer Pressure inside the Ice

During the deployment of the original IceCube DOMs, peak pressures of up to $550\,\mathrm{bar}$ were measured within the ice, resulting from both the hydrostatic pressure at depth and the pressure induced by the freezing process [116]. Therefore, all IceCube modules are required to withstand outer pressures of $700\,\mathrm{bar}$, which is achieved by the use of thick pressure vessels. This section discusses the effects of high pressures on the WOM's pressure vessel and its interior. Further, we perform a **pressure test** with the module to test its functionality under the conditions given deep inside the ice.

9.3.1 Deformation at Overpressure

The pressure vessel undergoes mechanical deformation while being exposed to high outer pressure. A mechanical simulation in **Autodesk Fusion** [@142] was performed to estimate the vessel's mechanical compression in height and diameter [108]. As seen from the results in Fig. 9.14 the maximum compression in inner radius is $0.44\,\mathrm{mm}$ ($0.88\,\mathrm{mm}$ in diameter) and a total of $2.8\,\mathrm{mm}$ ($1.2\,\mathrm{mm}$ for half a cylinder and $0.2\,\mathrm{mm}$ per endcap). This compression could potentially cause the interior (especially the PMTs) to either break or malfunction if not insulated properly.

The WOM PMTs are only rated for an overpressure of up to $1\,\mathrm{bar}$ [79]. Therefore, the sealing must be sufficiently soft to ensure that a compression of $1\,\mathrm{mm}$ in the inner diameter of the pressure vessel does not result in an overpressure exceeding $1\,\mathrm{bar}$ being applied to the PMT. We can estimate the required elasticity modulus

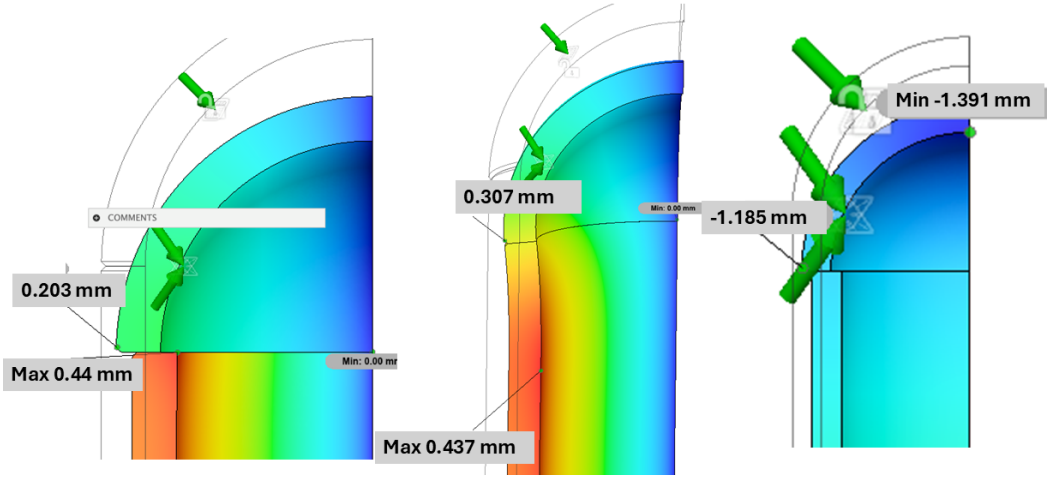

Fig. 9.14.: **Mechanical stress simulation of the WOM pressure vessel [108].** The properties of the glass were imported from the corresponding datasheet [81]. We assume the pressure being applied radially. Left: Radial compression close to the endcap. Center: Radial compression along the whole vessel. Right: Compression in height. The colorscale visualizes the amount of deformation with red being the highest. The results display a maximum compression of $0.88\,\mathrm{mm}$ in diameter and $2.8\,\mathrm{mm}$ in height.

E of the sealing by applying **Hooke's law** on the radial compression of a cylinder [143]:

$$\sigma_r = E \cdot \frac{\Delta r}{r} \tag{9.8}$$

with σ_r being the maximum allowed overpressure of $1\,\mathrm{bar}$ and Δr being the compression of $0.5\,\mathrm{mm}$ (considering some safety margin) of the inner pressure vessel's radius $r = 145\,\mathrm{mm}$. This concludes a required sealing material of $\boldsymbol{E < 14.5\,\mathrm{MPa}}$. This can be converted to a **Shore A hardness** of $\boldsymbol{S_A \approx 63}$ using an empirical model [144]. The Mold Star silicone having a Shore A hardness of 16 [101] concludes that the PMT sealing is clearly soft enough for the PMT to not get damaged by the compression of the pressure vessel[7]. Damaging the inner tube because of the height compression can be also excluded as the elasticity modulus of quartz glass with $\boldsymbol{E_{\mathrm{quartz}} \approx 73\,\mathrm{GPa}}$ [145] is much higher than that of the sealing, which would rather compress than break the tube.

To verify the estimation experimentally and further check for PFPE leakage under compression, we performed a **squeezing test**. A PMT inside a foam sock with a PFPE pressure equalization straw and cables routed through was placed inside a curved aluminum sheet held in place by three hose clamps set to an inner diameter of $145\,\mathrm{mm}$ (see Fig. 9.15). After the two layer silicone sealing is applied inside

[7] The foam layer is clearly softer than the MoldStar. Further, the mixing ratio for the ShinEtsu silicon was chosen to match the hardness of the MoldStar.

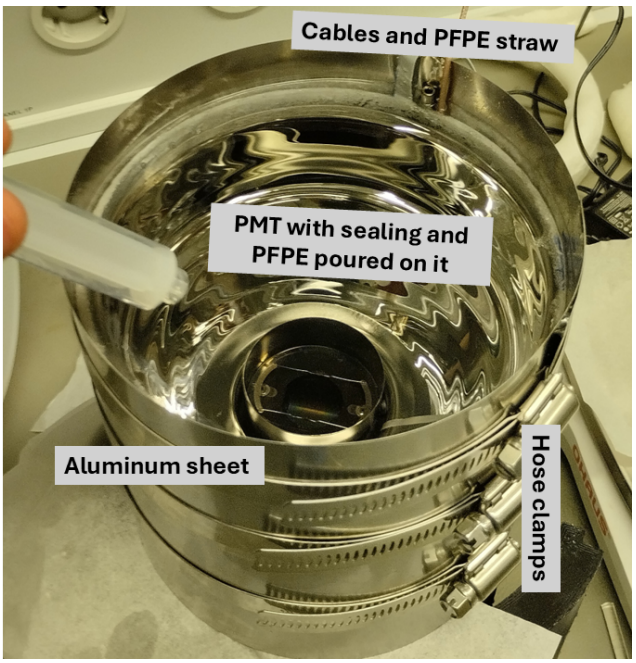

Fig. 9.15.: **Squeezing test for sealed PMT with PFPE straw and cables.** The PMT was sealed into an aluminum sheet of $d = 145\,\mathrm{mm}$. After the sealing dried, PFPE was poured on top of the PMT's surface area and the hose clamps were tightened to reduce the diameter by $1\,\mathrm{mm}$.

and cured, a layer of PFPE is poured onto the PMT's surface and the hose clamps are tightened by $3.14\,\mathrm{mm}$ corresponding to a compression of $1\,\mathrm{mm}$ in diameter. No physical damage was noticed on the PMT and also no PFPE leakage was observed. We note, that the silicon has a clearly worse adhesion to aluminum than to glass, which concludes that we would expect no worse results for the inner assembly sealed inside a quartz pressure vessel.

9.3.2 Pressure Testing

We test the fully assembled WOM at overpressure using a cylindrical hydraulic chamber of $700\,\mathrm{mm}$ inner diameter and $1400\,\mathrm{mm}$ height as shown in Fig. 9.16a at the facility of **Nautilus Marine Service GmbH** [@146]. The module is placed vertically standing inside the chamber kept in place by a rubber holding structure (see Fig. 9.16b). Due to the limited height the WOM can not to placed freely hanging inside the chamber. Therefore, we use the spring already introduced in Section 9.1 to simulate stress on the harness and monitor its movement resulting from the mechanical compression of the pressure vessel.

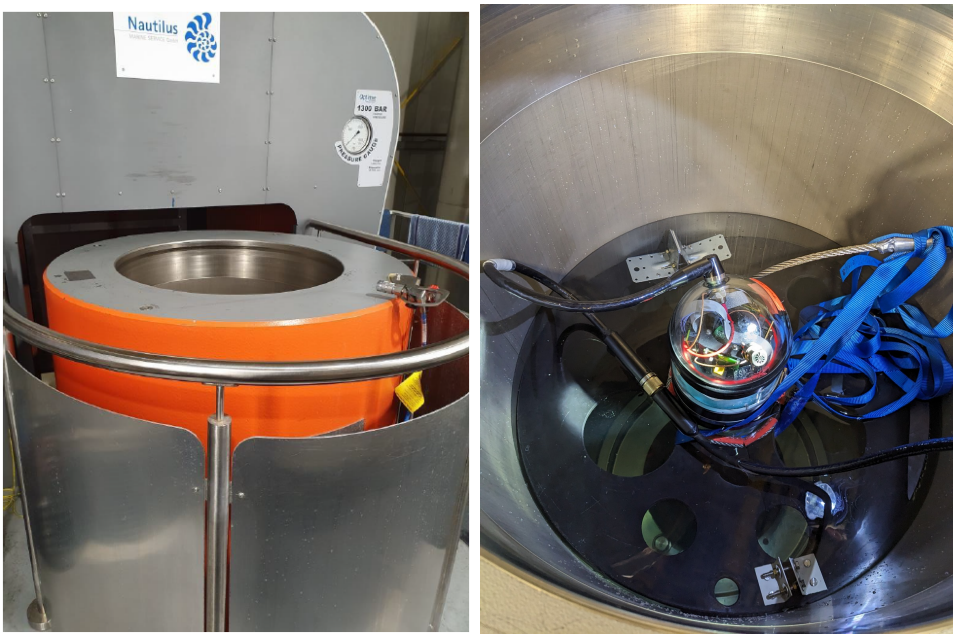

(a) Hydraulic chamber viewed from the side [147].

(b) Down view of the WOM placed inside the hydraulic chamber.

Fig. 9.16.: **Hydraulic chamber at Nautilus with the WOM placed inside.** The module is placed vertically standing inside the chamber fixed with a holding structure. To read out the module during testing we use an adapter cable routed through the top lid guiding to the mini-filedhub located in a neighboring room.

The executed pressure profile consists of three cycles of ramping up the pressure to $700\,\mathrm{bar}$, keeping it for one hour and ramping it down again having a total testing duration of about 6 hours. During this time the pressure and temperature on the MMB is monitored and 2 minutes of data is taken every 15 minutes. The inner pressure of the WOM during the pressure test, shown in Fig. 9.17, displays a shape similar to the executed pressure profile, increasing with increased outer pressure. The inner pressure increases because of the mechanical compression of the pressure vessel which reduces the inner volume. As this process scales linearly we would expect overlapping curves of inner and outer pressure. However, the height of the inner pressure curve differs between each of the three cycles pointing to irregularities in the process or potential leakages. Further, we observe what looks like a linear decrease in the inner pressure over the second and third cycle while the outer pressure remains constant. Finally, the pressure at the end of the test is more than $100\,\mathrm{mbar}$ below the initial pressure at the start.

We can predict the inner pressure value at the top of the curve (at $700\,\mathrm{bar}$ outer pressure) by calculating the relative gas volume change of the upper compartment based on the results displayed in Fig. 9.14. Additionally to the compression of

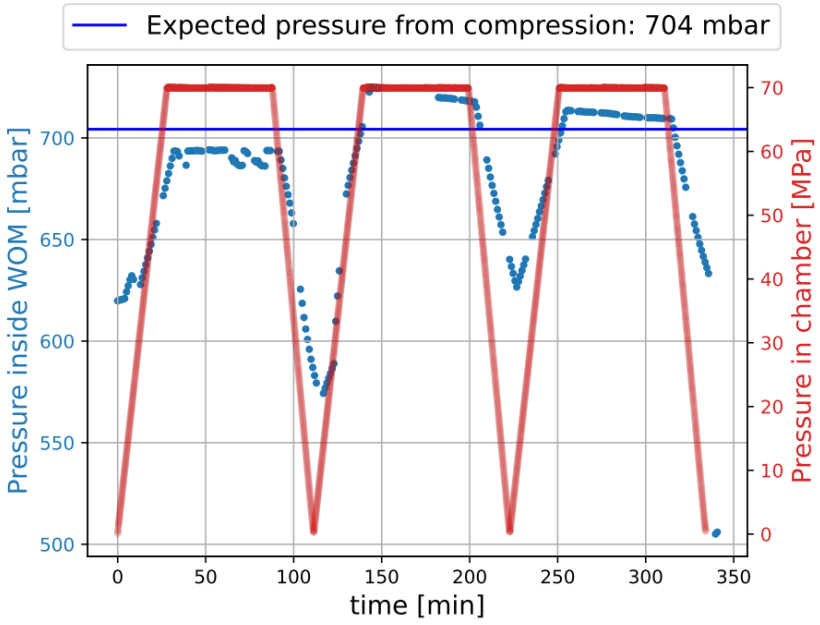

Fig. 9.17.: **Pressure inside and outside the WOM during pressure test.** The pressure inside the module is taken by the MMB in the top compartment. The temperature curve shows a constant relation with fluctuations of a few °C. The pressure outside the WOM was taken by the hydraulic chamber and provided by Nautilus.

the upper compartment, we also need to consider the compression of the center compartment, which results in PFPE being forced into the top compartment reducing its gas volume further. Taking the initial inner pressure of $620\,\mathrm{mbar}$ we predict a pressure at maximum compression of

$$p_{700\mathrm{bar}} = 704\,\mathrm{mbar}. \tag{9.9}$$

Fig. 9.17 shows this value being located between the peaks of the first and second cycle. This suggests a reasonable value within the large unexplained systematics of different peak height throughout the pressure cycles.

The continuous inner pressure decline observable over the second and third cycle could result from a leak between the evacuated inner volume of the inner tube and its outside. Breaking of the coupling between inner tube and PMT would result in a pressure equalization and therefore in a decrease of the pressure in the top compartment. The inner pressure values on the plateaus of the second and third cycle can be modeled by the exponential function

$$f(t) = c \cdot e^{-t/\tau} \tag{9.10}$$

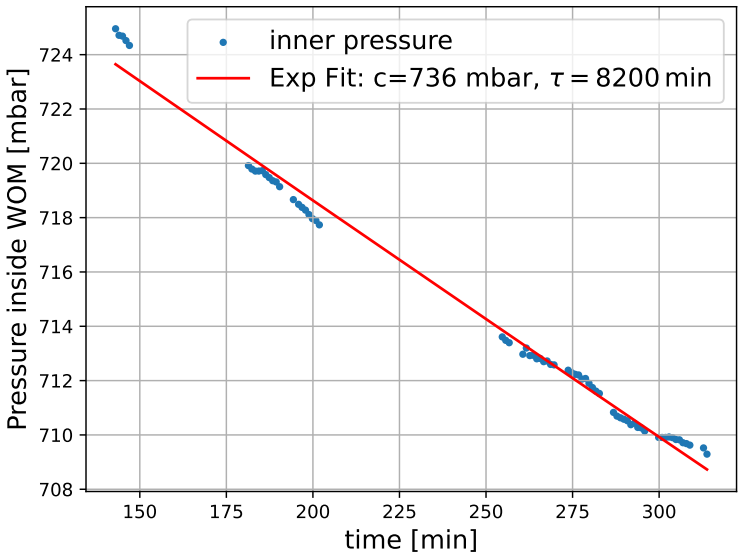

Fig. 9.18.: **Exponential fit to plateau values of inner pressure for the second and third pressure cycle.** We take only the plateau value for $p_{\text{outer}} = 700\,\text{bar}$. The lack of data between $t = 150\,\text{min}$ and $t = 180\,\text{min}$ results form a flasher test being performed at that point in time, so no pressure and temperature data could be taken.

which describes a pressure equalization process. However, this would indicate a very small leak which is not able to explain the sudden drop at the end of the pressure test down to $500\,\text{mbar}$. Additionally, the increase of the second plateau relative to the first one remains unexplained.

Besides the mentioned inconsistencies no other fatal errors were observed at first glance. The gain of the PMTs stayed constant fluctuating mostly within its errorbars (see Fig. 9.19). The dark rate in Fig. 9.20 shows a steady decline caused by light exposure of the module before testing. No correlation between rate and pressure can be observed and we see dark rate values expected at room temperature. All boards displayed full functionality after the test without any noticeable differences from before. A post-testing visual inspection showed no signs of damage or PFPE leakage. No significant movement of neither the harness block nor the spring took place.

Overall, we can confirm the WOM being robust against high outer pressure expected in IceCube. However, several inconsistencies in the monitor data points to not yet understood effects which need to be studied further to reduce the risk of unexpected malfunction.

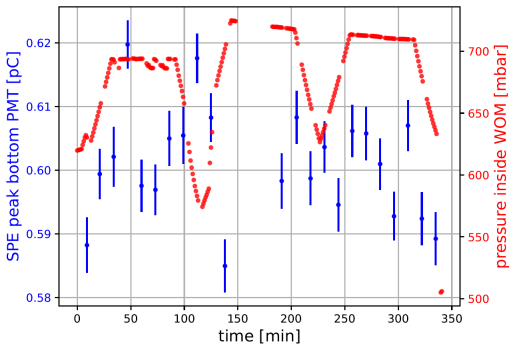

Fig. 9.19.: **SPE charge of bottom PMT, UP15 at HV=1420V during pressure test.** The charge was determined by fitting a Gaussian to the SPE spectrum. The top PMT could not be properly studied due to limited bandwidth and setting too low of a trigger threshold.

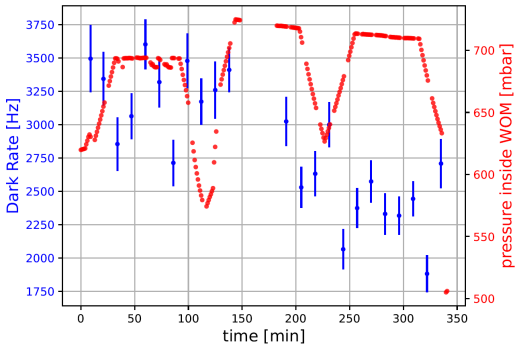

Fig. 9.20.: **Dark rate of bottom PMT, UP15 at HV=1420V during pressure test.** The rate is determined by fitting an exponential to the falling right edge of the timing distribution between hits.

9.4 Observed Weaknesses

Over the course of DVT several critical mechanical failures were observed, which could not be assigned to the consequences of one specific test. This section discusses these issues, evaluates impact on the functionality of the WOM and proposes consequences and possible improvements.

9.4.1 PFPE Leakage inside inner Tube

After the temperature cycle (which was performed after the vibration and pressure test) a small amount of liquid assumed to be PFPE was noticed inside the sealed inner tube (see Fig. 9.21). This amount was estimated to be around $8\,\mathrm{mL}$, increasing slightly to $18\,\mathrm{mL}$ over a few weeks, but not further. While this small amount of leakage does not worsen the performance or mechanical integrity of the module, it could point to an overarching design weakness with potentially more severe consequences in the future.

As this small amount of liquid is challenging to notice, it can not be said for sure which test caused its appearance. It also could have been caused by the pressure and/or vibration test. This observed leakage gives another explanation for the inner pressure decline form Fig. 9.18. Instead of assuming a pressure equalization we could

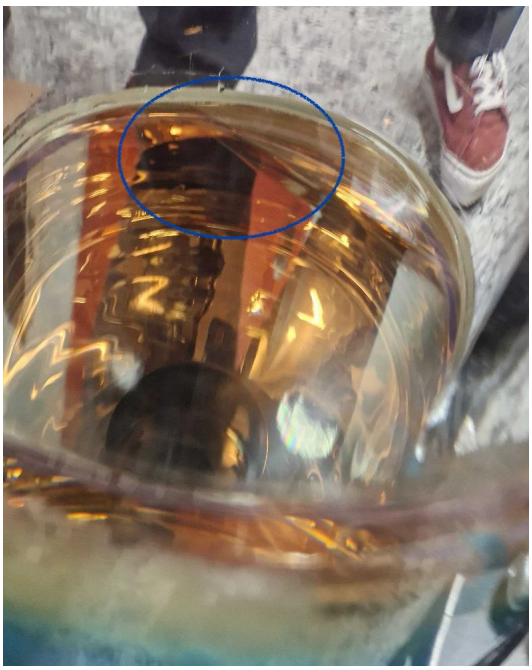

Fig. 9.21.: **Liquid observed inside inner tube of WOM1.** We can recognize the liquid faintly in the right fragment of the blue circle. Geometrical consideration can estimate its volume of $\approx 8\,\mathrm{mL}$. Its viscosity points to an oily liquid like PFPE more than water.

have a small hole in the gluing that lets PFPE leak into the inner tube decreasing the PFPE volume in the top compartment and therefore its pressure[8]. However, the observed pressure change from $725\,\mathrm{mbar}$ down to $709\,\mathrm{mbar}$ corresponds to a volume change of $31\,\mathrm{mL}$, which is significantly higher than the volume of PFPE observed inside the inner tube. The observed issue during the pressure test could also be a consequence of both mentioned effects: At $700\,\mathrm{bar}$ outer pressure PFPE is pressed through the small hole while at normal pressure the hole is not immersed in PFPE allowing for a pressure equalization partly explaining the pressure drop at the end of the test. Based on the ratio between the volume of the top compartment and the center of the inner tube

$$V_{\mathrm{top}} = 1.6\,\mathrm{L} \qquad V_{\mathrm{tube}} = 7.2\,\mathrm{L} \tag{9.11}$$

the pressures should equalize to a value close to $200\,\mathrm{mbar}$ which the inner tube was evacuated to. However, after pressure testing the inner pressure stayed constant at around $500\,\mathrm{mbar}$.

[8] Pressure equalization as explained before seems unlikely anyway, because at $700\,\mathrm{bar}$ both gluing spots would be immersed in PFPE due to the vessel's compression.

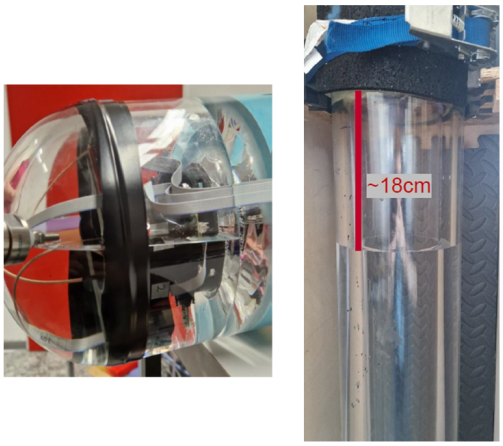

Fig. 9.22.: **PFPE leakage in bottom compartment of WOM1 after temperature cycle [148].** The leakage corresponded to a filling height reduced by $18\,\mathrm{cm}$ corresponding to a volume of $1.1\,\mathrm{L}$. Similar leakages were observed after subsequent temperature tests.

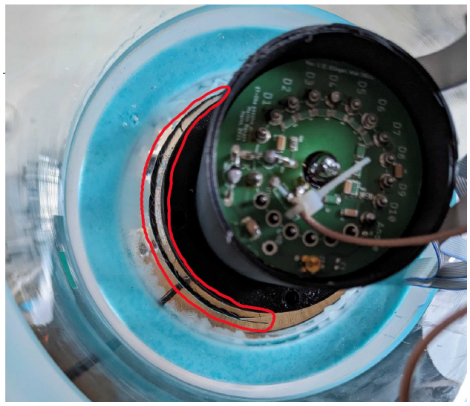

Fig. 9.23.: **Sealing of bottom PMT of WOM1 after leakage was noticed [148].** The crack is marked with the red line being located around the electronic holder made out of plastic.

9.4.2 PFPE Leakage in bottom Compartment

After a subsequent temperature cycle a large amount of PFPE leaked into the bottom compartment flooding it almost completely reducing the filling level in the center by $18\,\mathrm{cm}$ (see Fig. 9.22). While the leakage did not continue after the temperature cycle, it occurred again on a subsequent cycles after pouring the leaked PFPE back into the center compartment. Upon closer inspection of the bottom sealing a crack around the electronic holder was noticed (see Fig. 9.23) causing the PFPE to leak out.

Seeing the leakage continuously as a result of the temperature cycle makes it very likely to be caused by the difference in thermal expansion between silicone and glass. This could lead to cracks around the electronics holder as its coupling to the silicone is much worse compared to glass. Further, expanding and compressing air bubbles inside the ShinEtsu silicone would amplify this effect. The compression of the pressure vessel during the pressure test most likely also has a contribution to it as the sealing is also exposed to huge stress. A second pressure test with a different WOM module showed small amounts of several mL of PFPE leakage in the bottom compartment underlining this assumption [149].

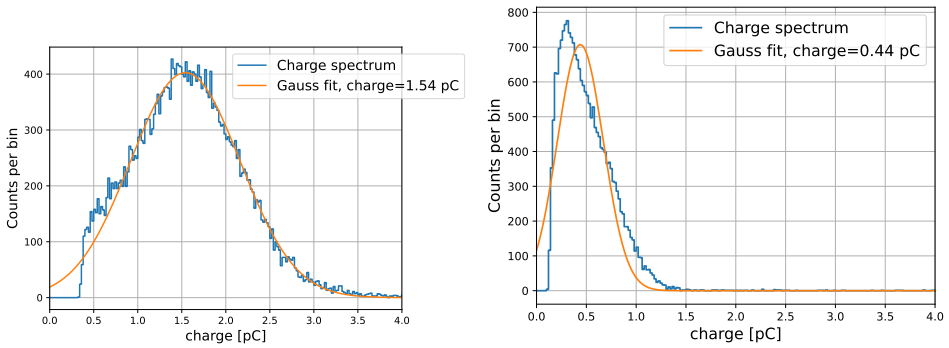

(a) Before being immersed in PFPE. Trigger: 1150 DAC Counts.

(b) While being immersed in PFPE. Trigger: 800 DAC Counts.

Fig. 9.24.: Charge spectrum of a PMT before and after being immersed in PFPE together with the whole electronic stack. PMT UP35, HV=1700V. For testing, a setup with two PMTs and the full electronics chain was prepared. Both PMTs with their corresponding electronic stacks mounted on them were immersed in two buckets of PFPE. 3 minutes of data was taken every 20 minutes over several days (see Appendix D for more details).

Not only does the PFPE leakage reduce the module's efficiency, but it also could potentially damages the bottom electronics. A long term measurement study was performed to determine the impact of the PFPE flooding on the functionality of the electronics. A full electronic chain with two connected PMTs was completely immersed into two buckets of PFPE while taking data over several days. This was compared to the same measurement without PFPE before. As seen in Fig. 9.24, the gain while immersed in PFPE is reduced to 25% of its nominal value and the SPE peak displays an unusual shape (see Appendix D for more details on the measurement). As an insulating material, PFPE helps prevent electrical breakdowns caused by short circuits. However, if it enters exposed electrical contacts—such as the connection between the PMT and its base—it can impede current flow, leading to reduced output from the PMT base and ultimately to lower gain. Not only would several PMTs not be able to reach the nominal gain like this, but it could also disturb their linear behavior.

These reasons along with other mechanical considerations such as the increased pressure in the bottom compartment due to reduced gas volume conclude that the WOMs would be at high risk of malfunction, if this issue is not treated accordingly.

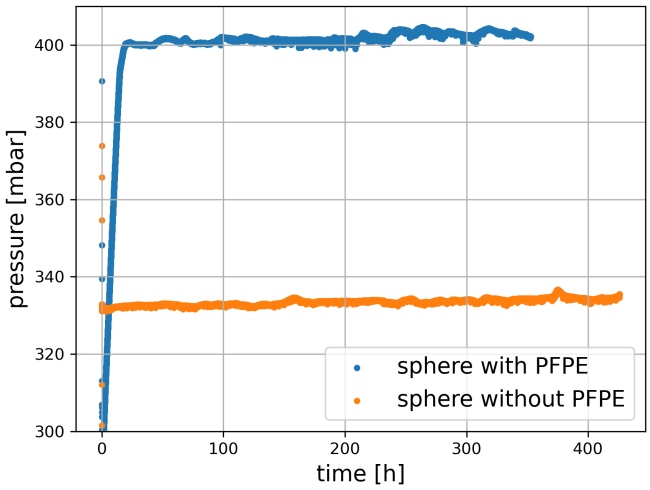

Fig. 9.25.: **Comparison of pressure evolution inside evacuated spheres with and without PFPE filling.** Two pressure vessel endcaps were used for the spheres resulting in an inner radius of $72.5\,\mathrm{mm}$. Both spheres were evacuated down to $300\,\mathrm{mbar}$. The initial increase over the first seconds results from the process of removing the pump and closing the vacuum port.

9.4.3 Pressure Leakage

Over the course of the development and testing period multiple cases of pressure leakage occurred leading to either partially or complete loss of underpressure inside the WOM over the course of several days. Quantitative studies were performed with two evacuated spheres made out of two pressure vessel endcaps each, one filled with $400\,\mathrm{mL}$ of PFPE. Both spheres were evacuated down to $300\,\mathrm{mbar}$ and their pressures were monitored using remote pressure sensors mounted on Arduinos [92]. As seen in Fig. 9.25 the PFPE filling influences the pressure curve. While the sphere without filling remained at a constant pressure around $330\,\mathrm{mbar}$ - mostly dominated by temperature fluctuations - we see a strong increase in pressure for the PFPE sphere over the first 10 hours before it stabilizes at around $400\,\mathrm{mbar}$.

PFPE can influence the vacuum sealing by evaporating due to low pressure and creeping through the endcap interface areas preventing the surface areas to couple properly [147]. While an inner pressure of $0.4\,\mathrm{bar}$ would still be acceptable to ensure the module does not open up during transportation the uncontrollability carries a huge risk here. A way to seal the interface areas from inside would be a preferable option.

A later performed monitoring of another evacuated PFPE sphere (see Fig. 9.26) showed surprisingly no such increase as discussed previously. The pressure is kept

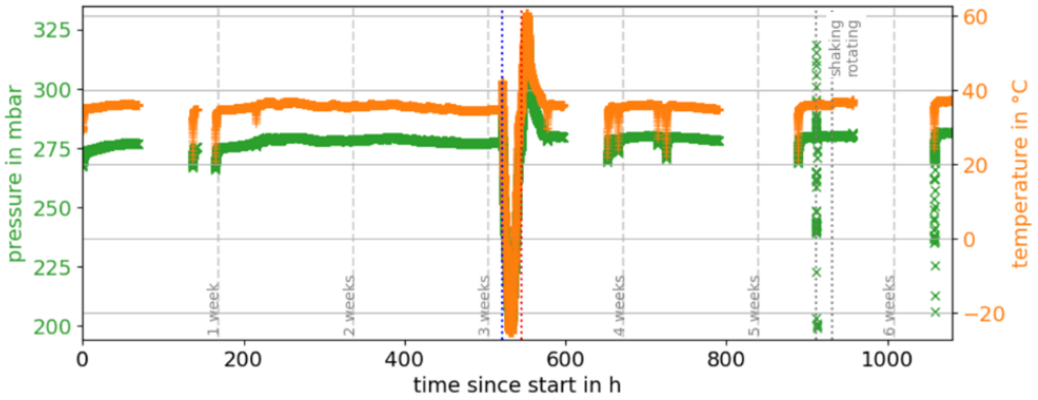

Fig. 9.26.: **Pressure and temperature evolution of a PFPE filled evacuated sphere [148].** The pressure and temperature was read out by a MMB placed inside read out with a mini-Fieldhub. This allows for longer monitoring as we are not limited by the sensor's batteries lifetime.

constant around $275\,\mathrm{mbar}$ over the course of more than 6 weeks. The sphere further underwent temperature cycling and stress tests by rotation and shaking without showing signs of air leaking in. This result suggests the previous pressure leakage to be a problem attributed to a lack of adherence to proper procedures.

9.4.4 Consequences on the Production of WOMs

While the PFPE inside the inner tube and the pressure leakage pose unfortunate but considerably mild issues, the leakage into the bottom compartment denotes a significant risk to the WOM's functionality and needs to be properly addressed before the modules can be deployed. Because of limited time for a proper redesign and testing, it was decided to ship the first batch of five WOMs without the PFPE filling. This decision reduces the efficiency of the deployed WOMs by about 50%, but on the other hand reduces the risk of malfunction and potential unexplained systematics in the data. Further, a hole was made through the bottom sealing to achieve a full pressure equilibrium between top, center and bottom compartment.

For an enhanced study on the effect of PFPE inside the WOM a second pressure test was performed, using three WOMs in total, one filled with PFPE. Because of time limitations the pressure profile was reduced to two cycles of up to $700\,\mathrm{bar}$. The updated electronics design allowed for pressure readout in the bottom compartment additionally to the MMB's pressure sensor. The results shown in Fig. 9.27 display

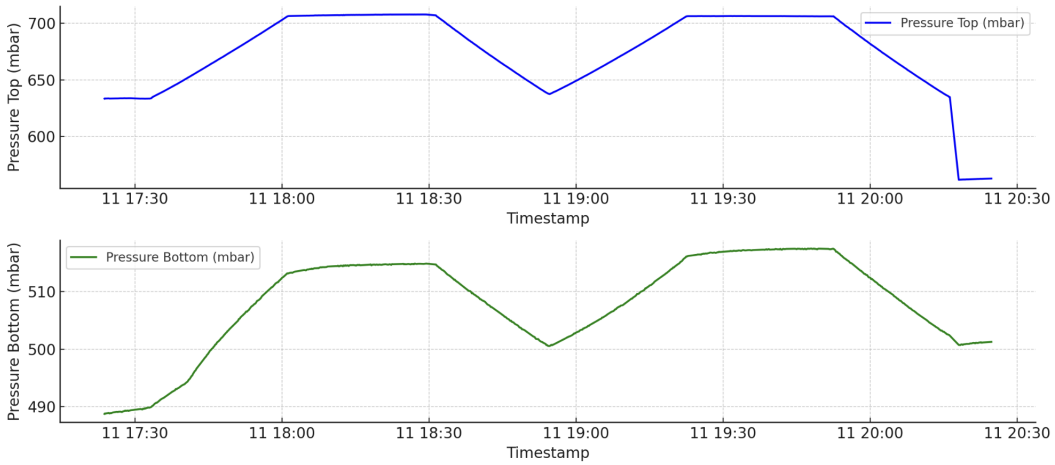

(a) WOM3 with PFPE.

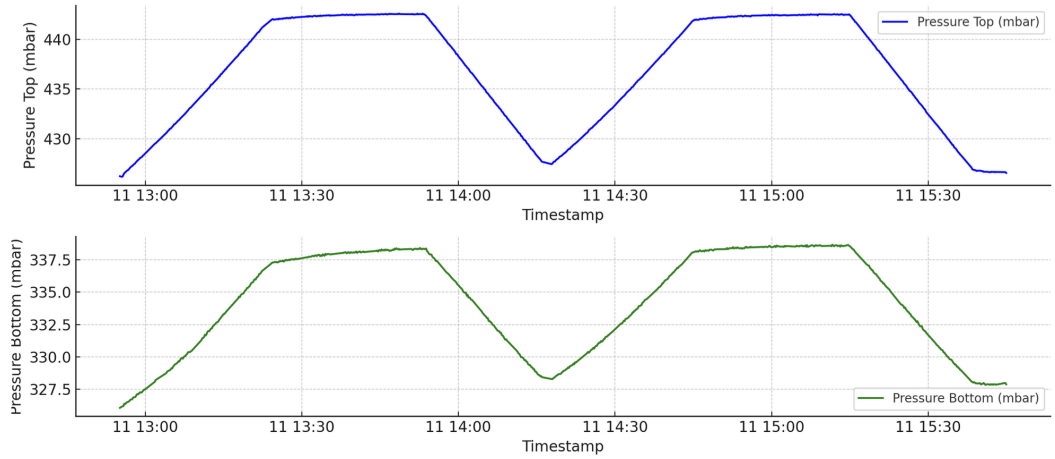

(b) WOM4 without PFPE.

Fig. 9.27.: **Monitor data of second pressure test [149].** The second pressure test was performed with three modules, WOM3 filled with PFPE and WOM4, 5 without PFPE filling. The pressure profile was reduced to two instead of three cycle. The inner pressure was monitored in the top and bottom compartment.

much cleaner pressure curves with the same height over both cycles in both compartments. For WOM3 filled with PFPE we observe a similar pressure drop as for WOM1 which is not seen for WOM4 and WOM5 without PFPE. This makes it very likely to be a systematic related to the filling which will not be an issue for the first shipped batch of WOMs. The two WOMs without filling do not display any unusual behavior and are therefore not expected to cause trouble related to overpressure.

Overall, the WOMs demonstrated satisfying robustness under various environmental conditions, including low and high temperatures, mechanical vibrations and shocks, and high external pressure. In most cases, the sensors exhibited behavior that aligned with expectations under these stress factors. Several failures could

be traced exclusively to the challenging handling of the PFPE filling, which was removed in the first batch of shipped WOMs.

To enable the use of PFPE filling in the second batch of modules, the bottom sealing design would need to be revised. One potential improvement could involve introducing a mechanism that applies force to press the silicone against the inner wall of the pressure vessel. This would counteract thermal and mechanical compression effects that lead to leakage. Such a modification would help retain the filling within the central compartment, ensuring optimal efficiency of the WOMs.

10 Conclusion and Outlook

The WOM is an UV-sensitive sensor designed to perform with a high Signal-to-Noise Ratio scheduled for deployment in the IceCube Upgrade during the austral summer of 2025/26. This thesis covered the development, characterization, production, and performance evaluation of the WOM, with a particular focus on its integration into the IceCube experiment. The first batch of five WOMs has been successfully produced and shipped, while a second batch featuring an improved design is currently produced to be shipped in summer 2025.

The individual components of the WOM were thoroughly characterized and optimized in their performance. This included detailed studies of the PMTs, focusing on quantum efficiency, gain, dark rate, and surface sensitivity under varying environmental conditions, particularly at low temperatures. The dark rate per PMT fluctuates around $650\,\mathrm{Hz}$ resulting in an overall dark noise about $1400\,\mathrm{Hz}$ per WOM considering the radioactive noise from the pressure vessel. The parameters of the inner tube and its coupling to the PMT were optimized to balance efficiency, cost, and mechanical robustness. Additionally, a vacuum gluing method was developed and integrated into the production pipeline, ensuring optimal optical coupling and mechanical stability.

The timing distribution reveals a complex structure resulting from additional contributions unique to the WOM, such as the timing characteristics of the WLS paint and photon propagation within the tube. These timing contributions were identified through measurements, simulations, and analytical models and combined into a unified timing and efficiency fit. This approach allowed for the extraction of the absorption and scattering lengths combining to an attenuation length about $3\,\mathrm{m}$ of the coated tube and their correlation, which marks these parameters as independent. Future studies could further separate the attenuation effects of the glass and WLS coating to gain deeper insights into the wavelength-shifting process, which could benefit other wavelength-shifting sensors. The propagation of wavelength-shifted photons significantly broadens the WOM's timing distribution ($\sigma \approx 13\,\mathrm{ns}$) compared to other IceCube modules ($\sigma < 5\,\mathrm{ns}$), presenting challenges for integration into applications requiring high-precision timing.

The effective area of the module was studied in relation to design parameters such as the choice of filling material, coating thickness, and systematic effects related to the PMTs. The effective area for UV photons decreases sharply below $300\,\mathrm{nm}$ due to strong absorption in the PFPE medium. Overall, the WOM exhibits a spectral sensitivity range consisting of shifted photons and direct PMT hits from $250\,\mathrm{nm}$ to $600\,\mathrm{nm}$, extending further into the UV than any other IceCube module which cuts off below $300\,\mathrm{nm}$. However, comparisons with Upgrade modules such as the mDOM and DEgg show that the WOM's effective area and signal-to-noise ratio are lower, in addition to its broader timing distribution. At short event distances ($3\,\mathrm{m}$), the UV sensitivity does not increase the number of detected Cherenkov photons, as UV light is strongly attenuated in the surrounding ice. Nevertheless, in scenarios like supernova detection, the enhanced UV sensitivity provides a small benefit.
The temporal separation between direct PMT hits and photons shifted by the WLS coating offers the potential to distinguish photon wavelengths. Utilizing the efficiency ratio between these contributions could improve distance estimations between events and modules. To achieve clearer timing separation, a wavelength shifter with a significantly longer decay time than the current $1.5\,\mathrm{ns}$ would be needed.

The WOMs to be deployed in the IceCube Upgrade underwent various optical tests, including evaluations of the inner tubes, assembled modules, and optical Final Acceptance Testing (FAT). These tests ensured quality control and confirmed that the effective areas of the modules were within theoretical expectations. The FAT was particularly useful for testing basic module functionality and identifying potential issues for in-ice operation. While effective, the FAT procedure could be further refined to provide more precise diagnostic data and better identify systematic variations between modules.

Environmental testing of the WOM prototype demonstrated its resilience to low temperatures, mechanical vibrations and shocks, and high external pressure. The module's optical performance mirrored that of the individual PMTs, which had been previously characterized. However, challenges arose in handling the PFPE under these conditions, as the liquid leaked into the inner tube and bottom compartment. To mitigate this risk, the first batch of WOMs was produced without PFPE filling. While this reduces the effective area by approximately 50%, it eliminates the risk of optical systematics or module failure. These issues will be addressed in the second batch to restore full efficiency.

The first batch of WOMs was successfully produced, packaged, and shipped to the South Pole (see Fig. 10.1). The production of the second batch will focus on improving the sealing to reliably contain the PFPE within the modules, with

promising initial results already achieved [148]. Simultaneously, development of the readout software continues, with the aim of introducing new features and reducing deadtime to enable higher trigger rates in the ice.
To ensure smooth deployment and operation, all modules undergo standardized acceptance tests at the South Pole prior to installation. This so-called South Pole Acceptance Test (SPAT), still in development for the WOM, is customized for each module type and validated with the IceCube infrastructure at the Northern Testing System (NTS). After the second batch is shipped, work will focus on integrating the WOM into the detector array, including developing the control software (xDOMApp) and implementing a full module simulation for data analysis.

Although the WOM may not fully meet the performance expectations within the specific constraints of the IceCube Upgrade, the underlying wavelength-shifting technology has shown great promise for a wide range of applications. Its ability to enable efficient detection in high-background or UV-sensitive environments makes it highly relevant for future experiments such as SHiP [150], NuDoubt^{++} [151], or Hyper-Kamiokande [@32]. Continued exploration and refinement of wavelength-shifting detector concepts — including but not limited to the WOM — represent an important step toward enhancing photon detection capabilities in next-generation particle and astroparticle physics experiments.

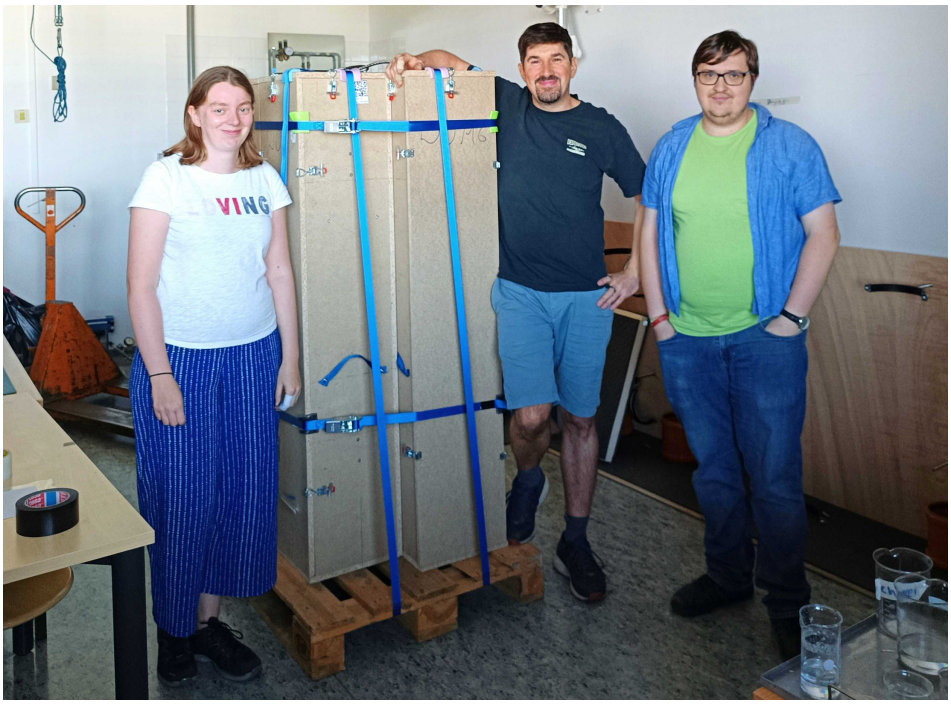

Fig. 10.1.: **First batch of WOMs, packed and strapped on a pallet ready to be shipped out.**

Appendices

PMT Characterization

A

This chapter shows additional plots for the PMT PicoScope measurements.

A.1 Temperature Dependency of PMT Gain

Fig. A.1 shows some additional selected correlation plots between the PMT temperature and its gain.

A.2 Temperature Dependency of the Dark Rate

Fig. A.2 shows additional correlation plots between the single PMT's dark rate and temperature.

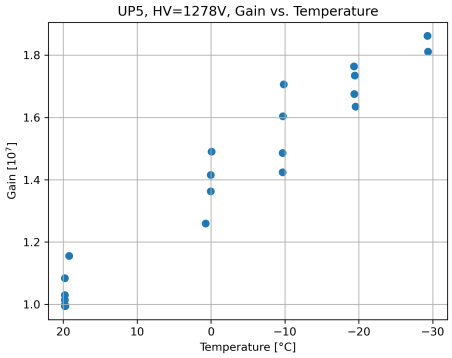

(a) UP5, HV=1278 V, slope= 1.3%/°C.

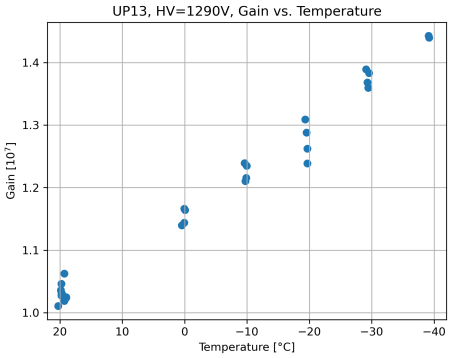

(b) UP13, HV=1290 V, slope= 0.75%/°C.

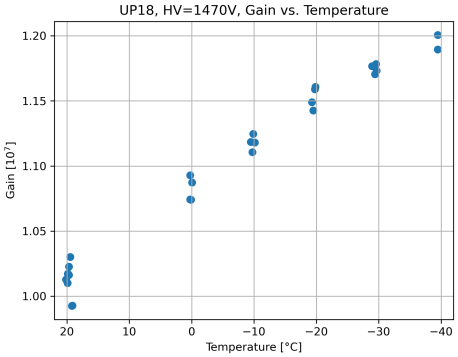

(c) UP18, HV=1470 V, slope= 0.33%/°C.

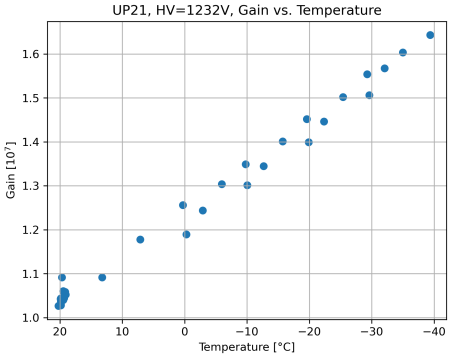

(d) UP21, HV=1232 V, slope= 1.1%/°C.

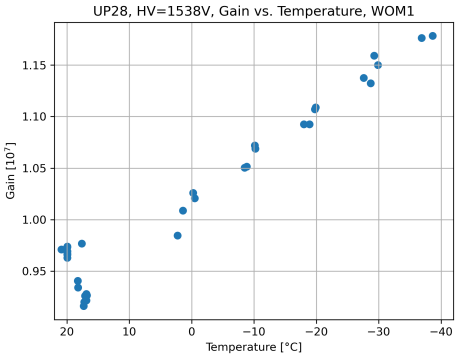

(e) UP28, HV=1538 V, slope= 0.28%/°C.

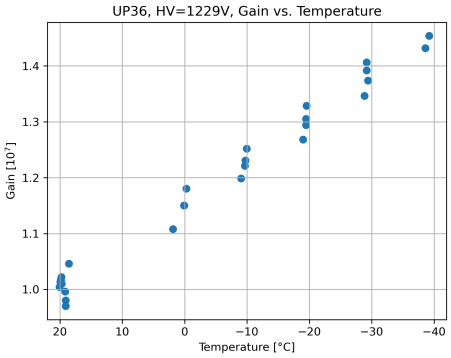

(f) UP36, HV=1229 V, slope= 0.75%/°C.

Fig. A.1.: Correlation between temperature and gain for some selected, representative PMTs. We get slopes in the range of 0.28 - 1.3%/°C.

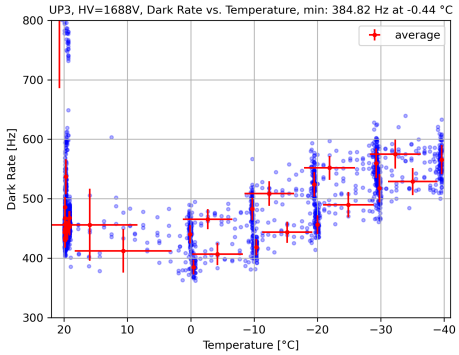

(a) UP3, HV=1688 V, minimum rate: 385 Hz at -0.44 °C.

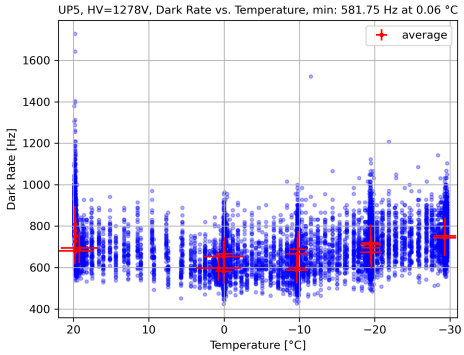

(b) UP5, HV=1278 V, minimum rate: 582 Hz at 0.06 °C.

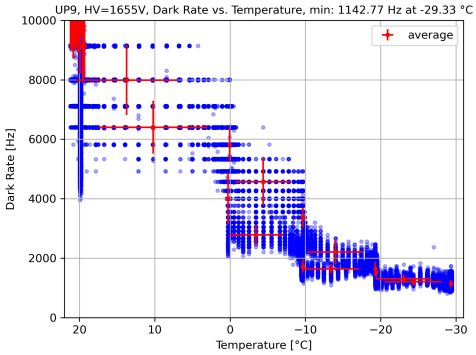

(c) UP9, HV=1655 V, minimum rate: 1143 Hz at -29.33 °C.

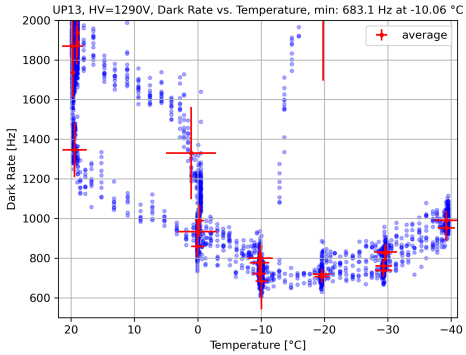

(d) UP13, HV=1290 V, minimum rate: 683 Hz at -10.06 °C.

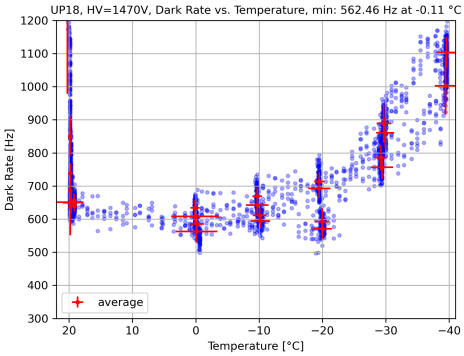

(e) UP18, HV=1470 V, minimum rate: 562 Hz at -0.11 °C.

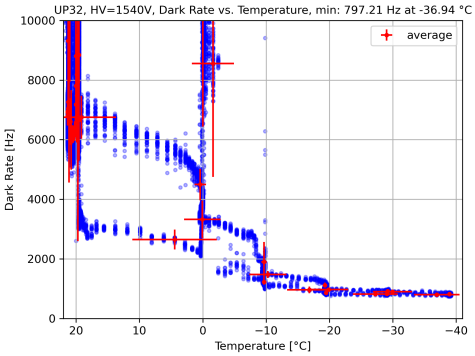

(f) UP32, HV=1540 V, minimum rate: 797 Hz at -36.94 °C.

Fig. A.2.: Correlation between temperature and dark rate for some selected, representative PMTs. We get minimal rate in the range of 350 - 800 Hz with some outliers above 1000 Hz.

Timing Distributions

B

This chapter shows fits to the measured timing distributions for distances not discussed in the main section.

B.1 Timing Fits

Fig. B.1 shows the fitted timing data for different distances L.

B.2 Sensitivity Maps

Fig. B.2 shows the sensitivity maps for the timing fits of different distances not featured in the main section.

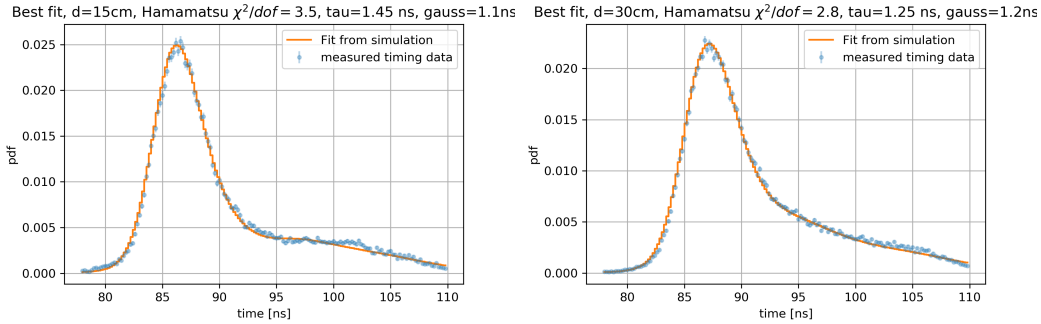

(a) $L = 15\,\text{cm}$, $\lambda_{ab} = 3.92\,\text{m}$, $\lambda_{\text{sc}} = 1.68\,\text{m}$.

(b) $L = 30\,\text{cm}$, $\lambda_{ab} = 9.01\,\text{m}$, $\lambda_{\text{sc}} = 0.68\,\text{m}$.

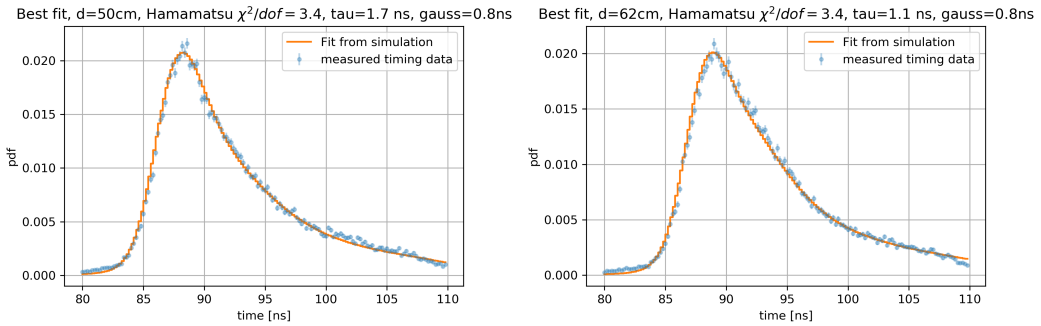

(c) $L = 50\,\text{cm}$, $\lambda_{ab} = 5.47\,\text{m}$, $\lambda_{\text{sc}} = 0.62\,\text{m}$.

(d) $L = 62\,\text{cm}$, $\lambda_{ab} = 7.16\,\text{m}$, $\lambda_{\text{sc}} = 0.71\,\text{m}$.

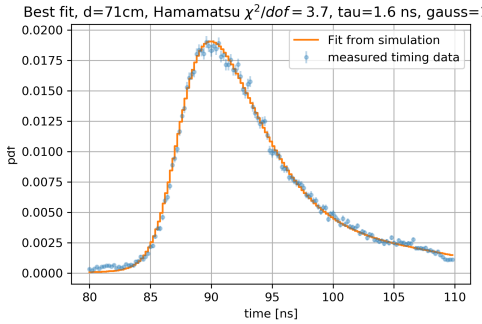

(e) $L = 71\,\text{cm}$, $\lambda_{ab} = 4.42\,\text{m}$, $\lambda_{\text{sc}} = 0.67\,\text{m}$.

Fig. B.1.: Fitted timing data for distances not shown in the main section. The fits were performed using τ and σ as nuisance parameters.

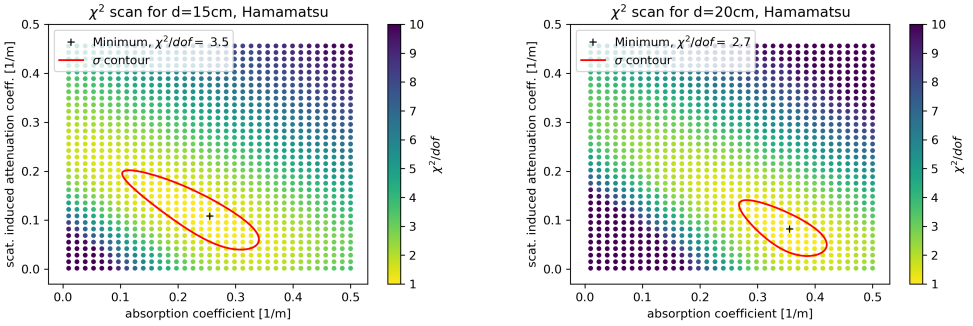

(a) $L = 15\,\text{cm}$.

(b) $L = 20\,\text{cm}$.

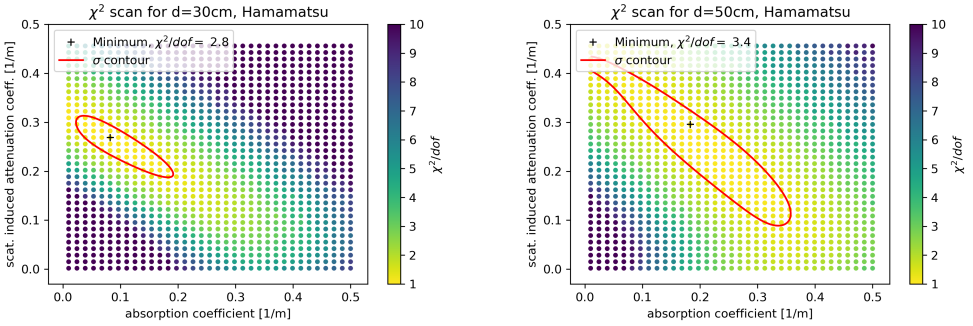

(c) $L = 30\,\text{cm}$.

(d) $L = 50\,\text{cm}$.

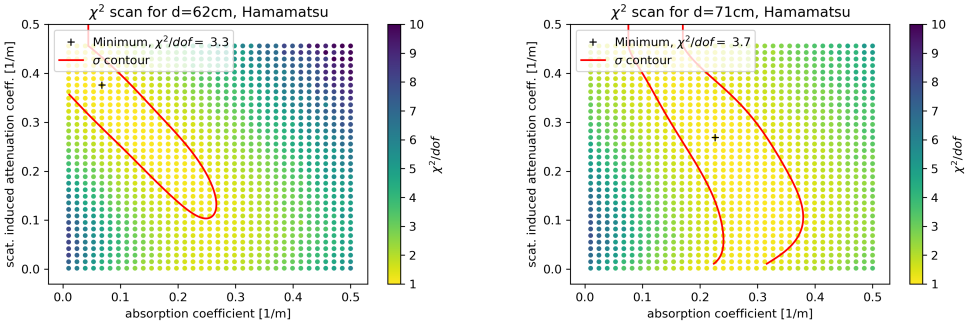

(e) $L = 62\,\text{cm}$.

(f) $L = 71\,\text{cm}$.

Fig. B.2.: Sensitivity maps for timing fits for different distances not shown in the main section. The χ^2/dof were normalized to 1 before drawing the error contour.

C FAT Results

This chapter displays the FAT results for all five shipped WOMs from the first batch. We show the results of the gain and trigger calibration, distance efficiency, and flasher tests.

C.1 Gain and Trigger

Fig. C.1 shows the gain of the WOM PMTs with respect to the set HV. Due to the wrong resistors being installed on the PMT bases we see lower gains than from the single PMT measurements. We see that some PMTs such as the top PMT of WOM2 (UP20) or the bottom PMT of WOM5 (UP28) are not able to reach the nominal gain of 10^7 at room temperature. However, the expected gain increase at low temperature could be able to compensate for it.

In Fig. C.2 we see the trigger threshold calibration curves. While there are small variations between the boards (due to tolerances on the specification on the single electronic components) we get overall similar slope values.

C.2 Distance Efficiency

Fig. C.3 shows the results for the remaining distance efficiency measurements of WOM2 and WOM5. As already discussed we notice discrepancy between data and expectation such as the efficiency of the bottom PMT of WOM2 not declining with increased distance.

C.3 Flasher Tests

This section shows the FAT results from tests using the WOM flashers. Due to issues discussed in the main section there is no data for WOM4 and WOM6.

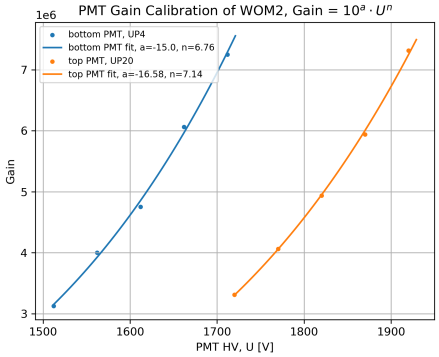

(a) WOM2.

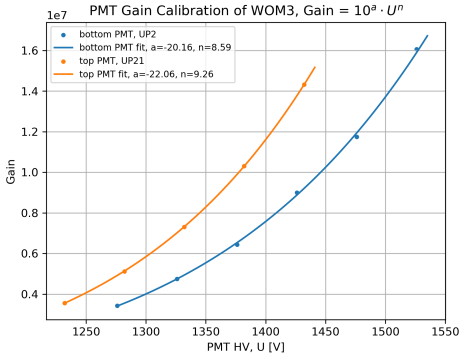

(b) WOM3.

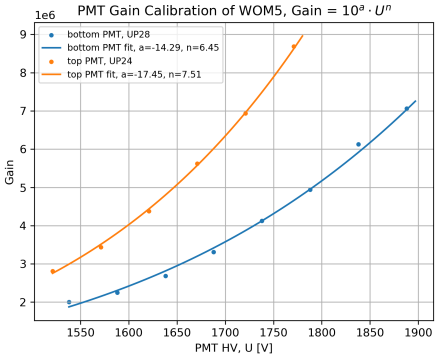

(c) WOM5.

Fig. C.1.: Gain to HV calibration at room temperature for shipped WOMs (not shown in the main section) during FAT. The calibration could not be performed for WOM6, because of issues discussed in the main section.

In Fig. C.4 we see the flasher bias calibration for the flasher chains installed in the WOMs. Flasher 1-3 having the same LED display a very similar behavior while flasher 4 with the visible LED deviates.

Fig. C.5 shows the measured time between two flashes. We notice small deviation form the set target value of $170\,\mu$s.

From Fig. C.6 we notice a discrepancy between data and expectation as flasher 4 with $\lambda = 405$ nm displays a higher than expected efficiency relative to flasher 1-3.

Fig. C.7 shows the results of the linearity measurements performed with one UV-flasher and read out by both PMTs. As already discussed in the main section only the first few data point are not affected by saturation of the ADC.

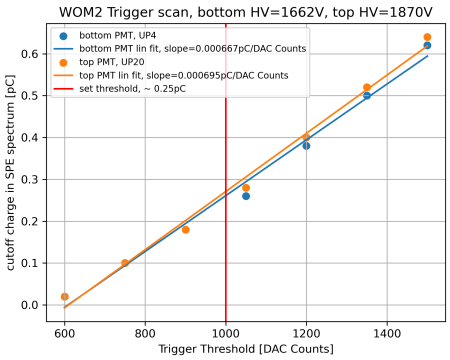

(a) WOM2.

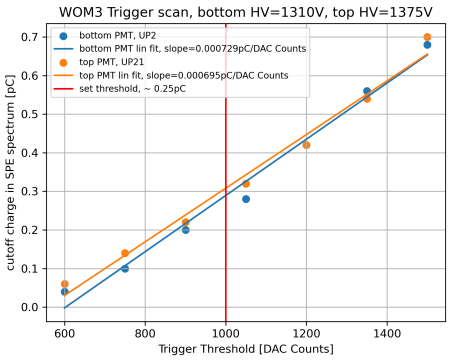

(b) WOM3.

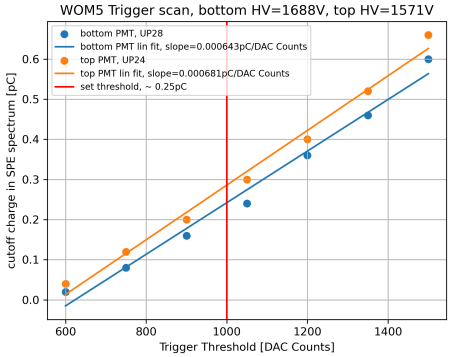

(c) WOM5.

Fig. C.2.: Trigger threshold calibration of WOMs from first batch not discussed in the main section. The calibration could not be performed for WOM6, because of issues discussed in the main section.

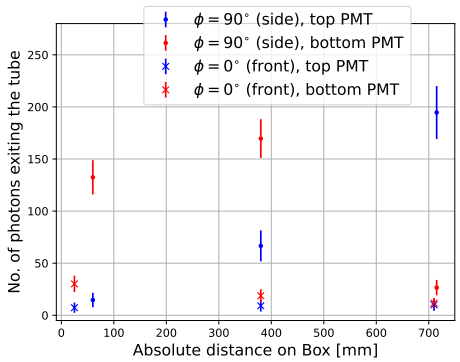

(a) WOM2.

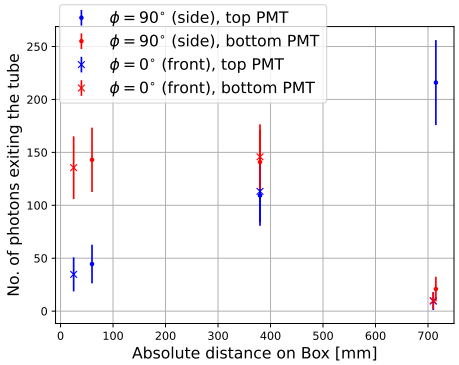

(b) WOM5.

Fig. C.3.: Distance dependent efficiency of shipped WOMs not discussed in the main section measured by both PMTs. The picosecond pulser was used as a light source illuminating the WOM at 6 different positions.

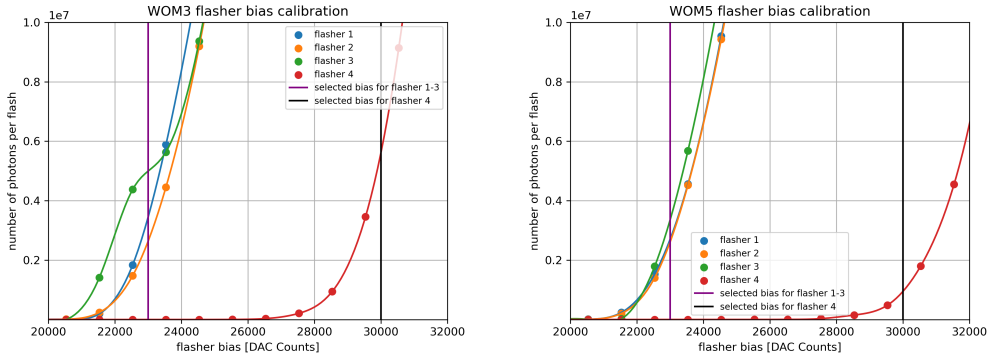

(a) WOM3. (b) WOM5.

Fig. C.4.: **Bias calibration of flasher chains installed in shipped WOMs from the first batch (data from [138]).** The flashers were absolutely calibrated using a dedicated setup before installing them in the modules.

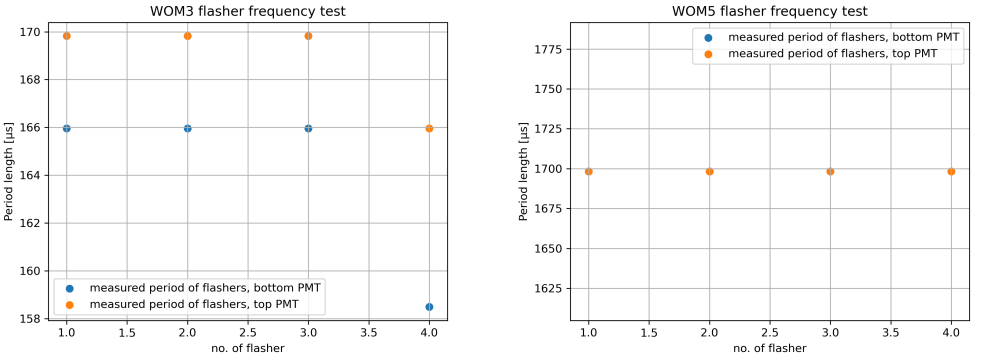

(a) WOM3. (b) WOM5.

Fig. C.5.: **Time between two flashes for every flasher on the chain.** The time was set to 170 μs and measured by taking the peak position from the timing distribution on both PMTs.

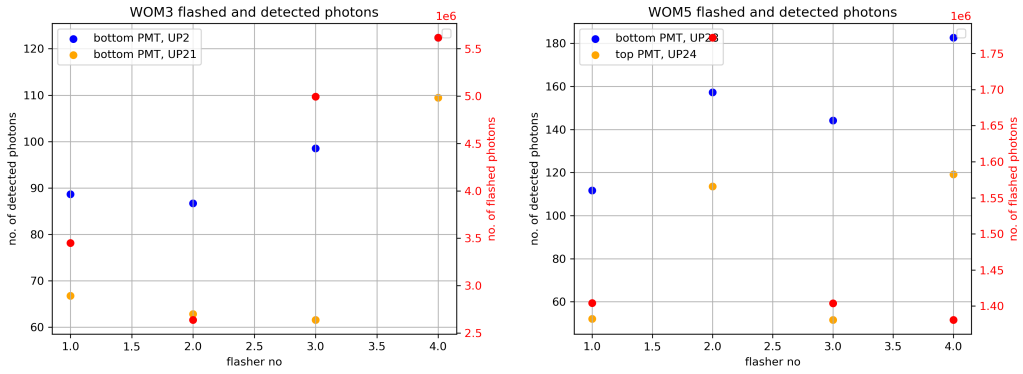

(a) WOM3. (b) WOM5.

Fig. C.6.: Number of photons detected by both PMTs per flash of each flasher. The right y-axis visualizes the number of flashed photons according to calibration data form Fig. C.4.

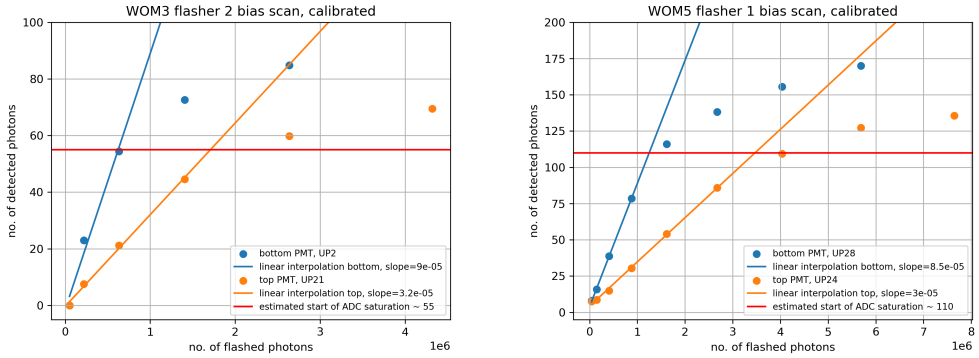

(a) WOM3. (b) WOM5.

Fig. C.7.: PMT linearity measurement performed using one UV-flasher. We varried the flasher's bias voltage and applied the bias calibration curves to get the number of flashed photons plotted on the x-axis. The number of detected photons was determined using a Gaussian fit to the measured MPE peak.

PFPE Long-Term Measurement

D

This chapter will give detailed insight into the long-term measurement to study the effect of PFPE on the WOM electronics. We will test the extreme case of the PMT and electronic stack being completely immersed in the liquid.
The setup shown in Fig. D.1 consists of the full WOM electronic chain with corresponding cable lengths connected to two PMTs (UP34 top, UP35 bottom). The setup is operated using the mini-FieldHub. The top and bottom electronic stack is mounted on the PMTs and immersed completely into buckets of PFPE. The measurement was run for about one day with 3 minutes of data taken every 20 minutes. The HV of both PMTs was set to a SPE charge of 1.6 pC.

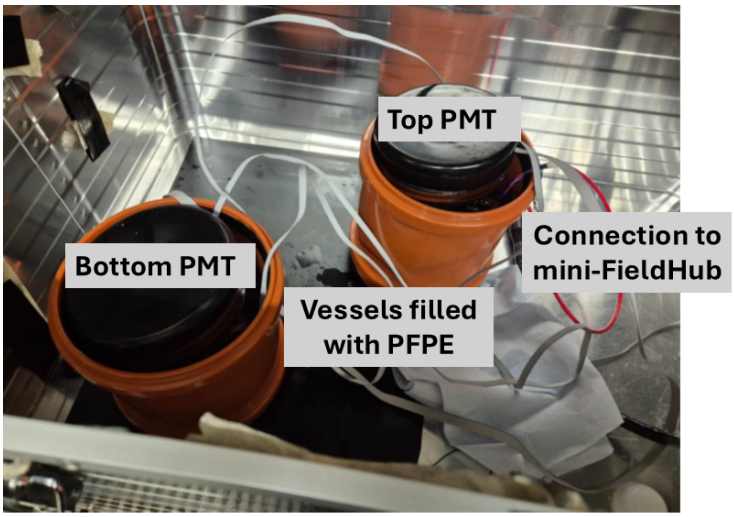

Fig. D.1.: **Setup to measured long-term effect of WOM electronics being immersed in PFPE.** The top and bottom electronic stack mounted to the PMTs are immersed into buckets filled with PFPE.

The change in gain already discussed in the main section is also visualized in Fig. D.2. We see the gain of both PMT decreasing from the original value of 1.6 pC. The decrease of the bottom PMT is much stronger.

After finishing the measurement the boards are removed from the PFPE and wiped with tissues and dried for about a day. The resulting SPE spectra for top and bottom PMT (without changing their HVs) are shown in Fig. D.3. The gain did

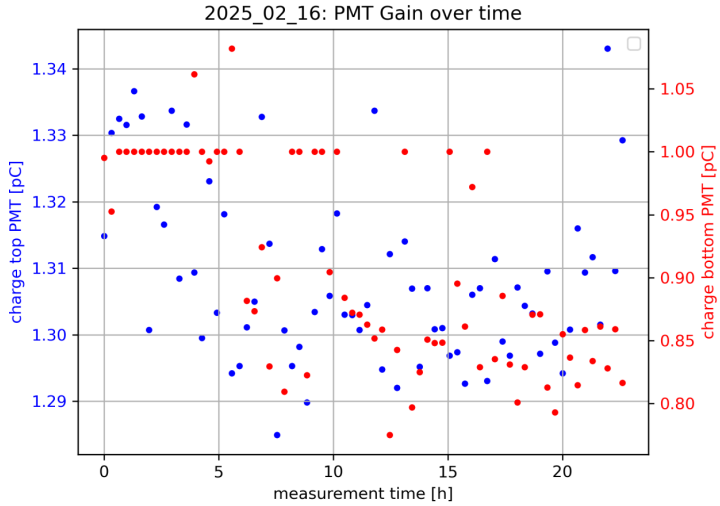

Fig. D.2.: SPE charge of top and bottom PMT during long-term measurement while being immersed in PFPE. The gain is calculated for each 3 minute datataking cycle. A charge of exactly 1.0 pC signifies a total of zero hits for the datataking cycle.

not regain its original value of 1.6 pC for both values. The top PMT is staying on a value around 1.3 pC while the gain of the bottom PMT increases to about 50% of its original value compared to its performance while immersed in PFPE. We still notice a non-Gaussian shape of the SPE peak.

Another observation during the measurement was the strongly decreased number of hits per datataking cycle. The limited bandwidth of the wuBase allows to record a maximum of about 10,000 waveforms per wuBase per minute which is considerably below the PMT's dark rate at room temperature[1]. However, while being immersed in PFPE the number of average hits per 3 minutes of datataking of clearly below the maximum value and displayed much less hits on average that the same measurement without PFPE before (see Fig. D.4). Drying the boards increases this number, but also does not restore the original number. This occurrence is partly related to bugs in the readout and data extraction software [137], but we can still conclude the PFPE having an influence on the operation of the electronics.

While small splashes of PFPE on the boards did not affect their operation, immersing the WOM electronics in the liquid could cause serious and potentially permanent contains in their performance. This could include a significantly reduced PMT gain or even the loss of data.

[1]This number used to be smaller in the older software version which was used to perform FAT on the first batch of WOMs.

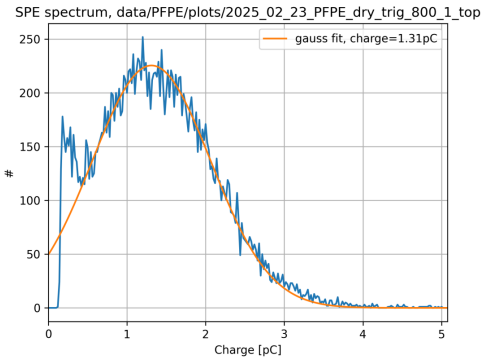

(a) Top PMT, UP34.

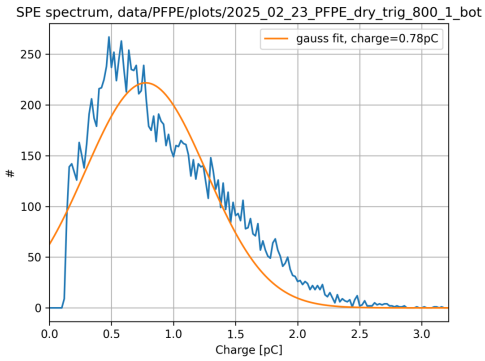

(b) Bottom PMT, UP35.

Fig. D.3.: SPE spectra of top and bottom PMT after taking boards out of PFPE and drying the for one day.

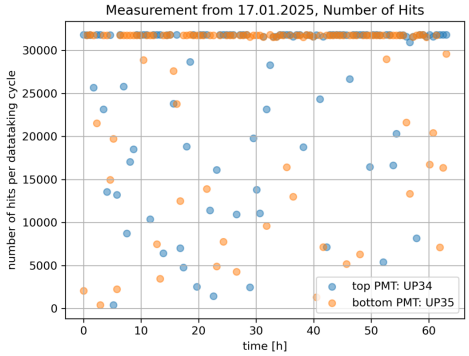

(a) Before PFPE immersion.

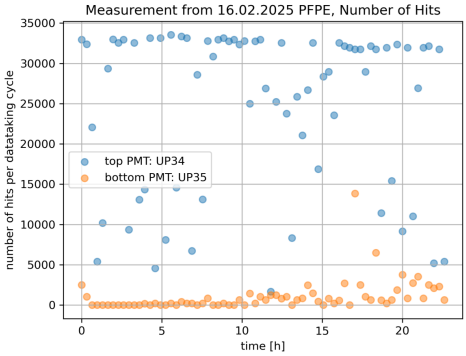

(b) During PFPE immersion.

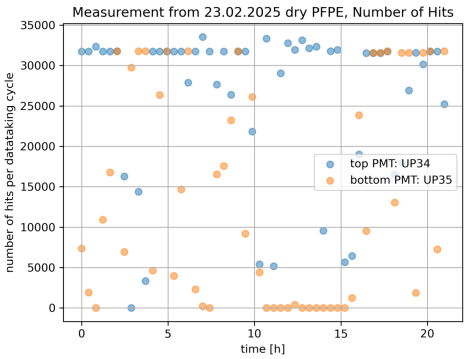

(c) After PFPE immersion and drying.

Fig. D.4.: Number of recorded waveforms per 3 minute datataking cycle before, during and after immersing the boards in PFPE. For both wuBases we count the number of extracted waveforms. Missing hits could result from corrupted files on software level.

Acknowledgments

Curriculum Vitae

Bibliography

[1] K. Hirata, T. Kajita, M. Koshiba, et al. “Observation of a neutrino burst from the supernova SN1987A”. In: *Phys. Rev. Lett.* 58 (14 Apr. 1987), pp. 1490–1493. DOI: 10.1103/PhysRevLett.58.1490 (cit. on pp. 1, 4).

[2] P. A. Čerenkov. “Visible Radiation Produced by Electrons Moving in a Medium with Velocities Exceeding that of Light”. In: *Phys. Rev.* 52 (4 Aug. 1937), pp. 378–379. DOI: 10.1103/PhysRev.52.378 (cit. on pp. 1, 5).

[3] M.G. Aartsen et al. “The IceCube Neutrino Observatory: instrumentation and online systems”. In: *Journal of Instrumentation* 12.03 (Mar. 2017), P03012. DOI: 10.1088/1748-0221/12/03/P03012 (cit. on pp. 1, 21, 22).

[4] Aya Ishihara et al. “The IceCube Upgrade - Design and Science Goals”. In: *Proceedings of 36th International Cosmic Ray Conference — PoS(ICRC2019)*. Vol. 358. 2019, p. 1031. DOI: 10.22323/1.358.1031 (cit. on pp. 1, 25).

[5] Sebastian Böser et al. “Detecting extra-galactic supernova neutrinos in the Antarctic ice”. In: *Astroparticle Physics* 62 (2015), pp. 54–65. DOI: https://doi.org/10.1016/j.astropartphys.2014.07.010 (cit. on p. 2).

[6] Benjamin Bastian-Querner, Lucas S. Binn, Sebastian Böser, et al. “The Wavelength-Shifting Optical Module”. In: *Sensors* 22.4 (2022). DOI: 10.3390/s22041385 (cit. on pp. 2, 29, 31, 35, 67, 83, 100, 117–120, 138).

[7] D. Griffiths. *Introduction to Elementary Particles*. New York, USA: John Wiley & Sons, 1987 (cit. on p. 3).

[8] C. L. Cowan, F. Reines, F. B. Harrison, H. W. Kruse, and A. D. McGuire. “Detection of the Free Neutrino: a Confirmation”. In: *Science* 124.3212 (1956), pp. 103–104. DOI: 10.1126/science.124.3212.103 (cit. on p. 3).

[9] Pablo Fernandez. “Neutrino Physics in Present and Future Kamioka Water-Cherenkov Detectors with Neutron Tagging”. PhD thesis. University Autonomous of Madrid, Feb. 2017. DOI: 10.13140/RG.2.2.19649.56169 (cit. on p. 3).

[10] K. Zuber. *Neutrino Physics*. Boca Raton, USA: CRC Press, 2020 (cit. on p. 4).

[11] Gabriel D. Orebi Gann, Kai Zuber, Daniel Bemmerer, and Aldo Serenelli. “The Future of Solar Neutrinos”. In: *Annual Review of Nuclear and Particle Science* 71.Volume 71, 2021 (2021), pp. 491–528. DOI: https://doi.org/10.1146/annurev-nucl-011921-061243 (cit. on p. 4).

[12] T. Wester, K. Abe, Bronner, et al. “Atmospheric neutrino oscillation analysis with neutron tagging and an expanded fiducial volume in Super-Kamiokande I–V”. In: *Phys. Rev. D* 109 (7 Apr. 2024), p. 072014. DOI: 10.1103/PhysRevD.109.072014 (cit. on p. 4).

[13] Maurizio Spurio. *Particles and Astrophysics. A Multi-Messenger Approach*. Astronomy and Astrophysics Library. Springer, 2015 (cit. on p. 4).

[14] John David Jackson. *Classical Electrodynamics*. Third Edition. New York, USA: John Wiley & Sons, 1999 (cit. on p. 5).

[15] I. M. Frank and Igor Y. Tamm. "Coherent visible radiation of fast electrons passing through matter". In: *Physics-Uspekhi* 93 (1937), pp. 388–393. DOI: 10.1007/978-3-642-74626-0_2 (cit. on p. 5).

[16] John Rack-Helleis. "Efficiency Determination of the Wavelength-shifting Optical Module (WOM)". https://butler.physik.uni-mainz.de/icecube/thesis/master_John_Rack-Helleis.pdf. MA thesis. Johannes Gutenberg-Universität Mainz, Oct. 2019 (cit. on pp. 6, 45, 46, 73).

[17] E. Hecht. *Optics*. Fifth Edition. Harlow, England: Pearson, 2017 (cit. on pp. 6, 7).

[18] A. Beer. "Bestimmung der Absorption des rothen Lichts in farbigen Flüssigkeiten". In: *Annalen der Physik* 162.5 (1852), pp. 78–88. DOI: https://doi.org/10.1002/andp.18521620505 (cit. on p. 7).

[19] M. Ackermann, J. Ahrens, X. Bai, et al. "Optical properties of deep glacial ice at the South Pole". In: *Journal of Geophysical Research: Atmospheres* 111.D13 (2006). DOI: https://doi.org/10.1029/2005JD006687 (cit. on pp. 7, 22, 55, 131).

[20] W. Demtröder. *Experimentalphysik 2 - Elektrizität und Optik*. 7th Edition. Springer, 2017 (cit. on pp. 8–10).

[24] A. Appel. "Some techniques for shading machine renderings of solids". In: *Proceedings of the April 30–May 2, 1968, Spring Joint Computer Conference*. AFIPS '68 (Spring). Atlantic City, New Jersey: Association for Computing Machinery, 1968, pp. 37–45. DOI: 10.1145/1468075.1468082 (cit. on p. 10).

[26] Glenn F. Knoll. *Radiation Detection and Measurement*. Fourth Edition. John Wiley & Sons, Inc, 2010 (cit. on pp. 10, 11).

[27] J. B. Birks. *The Theory and Practice of Scintillation Counting*. Pergamon Press, 1964 (cit. on p. 12).

[31] Marcin Kuźniak and Andrzej M. Szelc. "Wavelength Shifters for Applications in Liquid Argon Detectors". In: *Instruments* 5.1 (2021). DOI: 10.3390/instruments5010004 (cit. on pp. 12, 92).

[33] P. Bauleo, A. Goobar, and J. Rodríguez Martino. "UV-enhancement of photomultiplier response: a study of wavelength shifters for the AMANDA/IceCube detector". In: *Nuclear Instruments and Methods in Physics Research Section A: Accelerators, Spectrometers, Detectors and Associated Equipment* 443.1 (2000), pp. 136–147. DOI: https://doi.org/10.1016/S0168-9002(99)01007-4 (cit. on p. 13).

[34] A. Einstein. "Über einen die Erzeugung und Verwandlung des Lichtes betreffenden heuristischen Gesichtspunkt". In: *Annalen der Physik* 322.6 (1905), pp. 132–148. DOI: https://doi.org/10.1002/andp.19053220607 (cit. on p. 13).

[35] Hamamatsu Photonics K. K. *Photomultiplier Tubes - Basics and Applications*. Fourth Edition. 2017 (cit. on pp. 13–17, 124).

[37] Kimitsugu Nakamura, Yasumasa Hamana, Yoshihiro Ishigami, and Toshikazu Matsui. "Latest bialkali photocathode with ultra high sensitivity". In: *Nuclear Instruments and Methods in Physics Research Section A: Accelerators, Spectrometers, Detectors and Associated Equipment* 623.1 (2010). 1st International Conference on Technology and Instrumentation in Particle Physics, pp. 276–278. DOI: https://doi.org/10.1016/j.nima.2010.02.220 (cit. on p. 14).

[38] Martin Antonio Unland Elorrieta. "Development, simulation, and characterisation of a novel multi-PMT optical module for IceCube Upgrade with emphasis on detailed understanding of photomultiplier performance parameters". PhD thesis. Westfälische Wilhelms-Universität Münster, 2023 (cit. on pp. 15, 18, 19, 25, 132).

[39] *Photomultiplier tube basics*. https://psec.uchicago.edu/library/photomultipliers/Photonis_PMT_basics.pdf. Photonis (cit. on p. 17).

[40] A. G. Wright. *The Photomultiplier Handbook*. Oxford University Press, June 2017. DOI: 10.1093/oso/9780199565092.001.0001 (cit. on p. 17).

[41] R. Abbasi et al. "D-Egg: a dual PMT optical module for IceCube". In: *Journal of Instrumentation* 18.04 (Apr. 2023), P04014. DOI: 10.1088/1748-0221/18/04/P04014 (cit. on pp. 19, 24–26, 132, 134).

[43] IceCube Collaboration*†, R. Abbasi, M. Ackermann, et al. "Evidence for neutrino emission from the nearby active galaxy NGC 1068". In: *Science* 378.6619 (2022), pp. 538–543. DOI: 10.1126/science.abg3395 (cit. on p. 21).

[44] R. Abbasi et al. "Measurement of atmospheric neutrino mixing with improved IceCube DeepCore calibration and data processing". In: *Phys. Rev. D* 108 (1 July 2023), p. 012014. DOI: 10.1103/PhysRevD.108.012014 (cit. on p. 21).

[45] Donghwa Kang. "Recent results of cosmic-ray studies with IceTop at the IceCube Neutrino Observatory". In: *Advances in Space Research* 72.10 (2023), pp. 4613–4624. DOI: https://doi.org/10.1016/j.asr.2023.09.027 (cit. on p. 21).

[46] R. Abbasi et al. "Search for Galactic Core-collapse Supernovae in a Decade of Data Taken with the IceCube Neutrino Observatory". In: *The Astrophysical Journal* 961.1 (Jan. 2024), p. 84. DOI: 10.3847/1538-4357/ad07d1 (cit. on p. 21).

[47] R. Abbasi et al. "In situ estimation of ice crystal properties at the South Pole using LED calibration data from the IceCube Neutrino Observatory". In: *The Cryosphere* 18.1 (2024), pp. 75–102. DOI: 10.5194/tc-18-75-2024 (cit. on p. 21).

[48] R. Abbasi et al. "The IceCube data acquisition system: Signal capture, digitization, and timestamping". In: *Nuclear Instruments and Methods in Physics Research Section A: Accelerators, Spectrometers, Detectors and Associated Equipment* 601.3 (2009), pp. 294–316. DOI: https://doi.org/10.1016/j.nima.2009.01.001 (cit. on pp. 22, 23).

[49] R. Abbasi et al. “The design and performance of IceCube DeepCore”. In: *Astroparticle Physics* 35.10 (2012), pp. 615–624. DOI: https://doi.org/10.1016/j.astropartphys.2012.01.004 (cit. on p. 22).

[50] R. Abbasi et al. “Search for GeV-scale dark matter annihilation in the Sun with IceCube DeepCore”. In: *Phys. Rev. D* 105 (6 Mar. 2022), p. 062004. DOI: 10.1103/PhysRevD.105.062004 (cit. on p. 22).

[51] Sclafani, Stephen and others. “A Search for Neutrino Sources with Cascade Events in IceCube”. In: *Proceedings of 37th International Cosmic Ray Conference — PoS(ICRC2021)*. Vol. 395. 2021, p. 1150. DOI: 10.22323/1.395.1150 (cit. on p. 24).

[52] IceCube Collaboration*. “Evidence for High-Energy Extraterrestrial Neutrinos at the IceCube Detector”. In: *Science* 342.6161 (2013), p. 1242856. DOI: 10.1126/science.1242856 (cit. on p. 24).

[53] R. Abbasi et al. “IceTop: The surface component of IceCube”. In: *Nuclear Instruments and Methods in Physics Research Section A: Accelerators, Spectrometers, Detectors and Associated Equipment* 700 (2013), pp. 188–220. DOI: https://doi.org/10.1016/j.nima.2012.10.067 (cit. on p. 24).

[54] M.G. Aartsen et al. “Design and performance of the first IceAct demonstrator at the South Pole”. In: *Journal of Instrumentation* 15.02 (Feb. 2020), T02002. DOI: 10.1088/1748-0221/15/02/T02002 (cit. on p. 24).

[55] Turcotte-Tardif, Roxanne and Verpoest, Stef and Venugopal, Megha and others. “Estimation of Xmax for air showers measured at IceCube with elevated radio antennas of a prototype surface station”. In: *Proceedings of 38th International Cosmic Ray Conference — PoS(ICRC2023)*. Vol. 444. 2023, p. 326. DOI: 10.22323/1.444.0326 (cit. on p. 24).

[56] M. G. Aartsen et al. “Measurement of the cosmic ray energy spectrum with IceTop-73”. In: *Phys. Rev. D* 88 (4 Aug. 2013), p. 042004. DOI: 10.1103/PhysRevD.88.042004 (cit. on p. 24).

[57] Rasha Abbasi et al. “Design and performance of the multi-PMT optical module for IceCube Upgrade”. In: *Proceedings of 37th International Cosmic Ray Conference — PoS(ICRC2021)*. Vol. 395. 2021, p. 1070. DOI: 10.22323/1.395.1070 (cit. on pp. 24–26).

[58] Charlotte Benning, Jurgen Borowka, Oliver Gries, Simon Zierke, et al. “Performance Studies of the Acoustic Module for the IceCube Upgrade”. In: *Proceedings of 38th International Cosmic Ray Conference — PoS(ICRC2023)*. Vol. 444. 2023, p. 241. DOI: 10.22323/1.444.0241 (cit. on p. 24).

[59] Nikhita Khera, Felix Henningsen, et al. “POCAM in the IceCube Upgrade”. In: *Proceedings of 37th International Cosmic Ray Conference — PoS(ICRC2021)*. Vol. 395. 2021, p. 1049. DOI: 10.22323/1.395.1049 (cit. on p. 24).

[60] IceCube Collaboration. “Physics potential of the IceCube Upgrade for atmospheric neutrino oscillations”. unpublished. 2024 (cit. on p. 25).

[61] M.G. Aartsen et al. “Measurement of South Pole ice transparency with the IceCube LED calibration system”. In: *Nuclear Instruments and Methods in Physics Research Section A: Accelerators, Spectrometers, Detectors and Associated Equipment* 711 (2013), pp. 73–89. DOI: https://doi.org/10.1016/j.nima.2013.01.054 (cit. on p. 25).

[62] M G Aartsen et al. “IceCube-Gen2: the window to the extreme Universe”. In: *Journal of Physics G: Nuclear and Particle Physics* 48.6 (Apr. 2021), p. 060501. DOI: 10.1088/1361-6471/abbd48 (cit. on pp. 26, 27).

[64] G A Askar’yan. “COHERENT RADIOEMISSION FROM COSMIC SHOWERS IN THE AIR AND DENSE MEDIA”. In: *Zh. Eksperim. i Teor. Fiz.* 48 (Mar. 1965) (cit. on p. 27).

[65] Rasha Abbasi et al. “Sensitivity studies for the IceCube-Gen2 radio array”. In: *Proceedings of 37th International Cosmic Ray Conference — PoS(ICRC2021)*. Vol. 395. 2021, p. 1183. DOI: 10.22323/1.395.1183 (cit. on p. 27).

[66] Vedant Basu, Aya Ishihara, Markus Dittmer, Nobuhiro Shimizu, et al. “A next-generation optical sensor for IceCube-Gen2”. In: *Proceedings of 37th International Cosmic Ray Conference — PoS(ICRC2021)*. Vol. 395. 2021, p. 1062. DOI: 10.22323/1.395.1062 (cit. on pp. 27, 28).

[67] *HSQ 300/330 MF*. https://www.heraeus-conamic.com/media/Media/Documents/Products_and_Solutions/SEMI/EN/Solids_HSQ300_330MF_EN.pdf. Heraeus Conamic. 2022 (cit. on p. 31).

[68] *Paraloid B72*. https://www.preservationequipment.com/files/4ba8f3dc-85c1-44e4-9237-a3db00db1ef4/Paraloid%20B72%20Use.pdf. Preservation Equipment. 2021 (cit. on p. 31).

[69] *Bis-MSB*. https://exciton.luxottica.com/media/productattach/Datasheet/04210.pdf. Luxottica Exciton (cit. on p. 31).

[70] Manuel Grande and Gary R Moss. “An optimised thin film wavelength shifting coating for Cherenkov detection”. In: *Nuclear Instruments and Methods in Physics Research* 215.3 (Oct. 1983), pp. 539–548. DOI: 10.1016/0167-5087(83)90491-x (cit. on p. 31).

[71] John Rack-Helleis. “The Wavelength-shifting optical Module in the Context of the IceCube Upgrade”. unpublished thesis. PhD thesis. Johannes Gutenberg-Universität Mainz, 2025 (cit. on pp. 31, 33, 52, 54, 88, 117, 133, 144, 167).

[72] Lucas Sebastian Binn. “Charakterisierung von dünnen wellenlängenschiebenden Schichten”. https://butler.physik.uni-mainz.de/icecube/thesis/bachelor_Lucas_Binn.pdf. Bachelor’s thesis. Johannes Gutenberg-Universität Mainz, May 2018 (cit. on pp. 32, 116).

[73] Jonas Hümmerich. “Optisch aktive wellenlängenschiebende Beschichtungen”. https://butler.physik.uni-mainz.de/icecube/thesis/bachelor_HuemmerichJonas.pdf. Bachelor’s thesis. Johannes Gutenberg-Universität Mainz, Mar. 2022 (cit. on pp. 32–34, 116, 117, 137).

[74] Bastian Keßler. “Development of Wavelength-shifting Fibers with high Photon Capture-Rate”. https://butler.physik.uni-mainz.de/icecube/thesis/master_Bastian_Kessler.pdf. MA thesis. Johannes Gutenberg-Universität Mainz, Jan. 2024 (cit. on pp. 32, 47–49, 98).

[75] Emmanuelle Rio and François Boulogne. “Withdrawing a solid from a bath: How much liquid is coated?” In: *Advances in Colloid and Interface Science* 247 (2017). Dominique Langevin Festschrift: Four Decades Opening Gates in Colloid and Interface Science, pp. 100–114. DOI: https://doi.org/10.1016/j.cis.2017.01.006 (cit. on p. 33).

[76] Maximilian Bubeck. “Development of a Wavelength-shifting Optical Module”. https://butler.physik.uni-mainz.de/icecube/thesis/master_Maximilian_Bubeck.pdf. MA thesis. Johannes Gutenberg-Universität Mainz, Oct. 2020 (cit. on p. 34).

[77] Florian Thomas. “Light propagation simulation for the Wavelength-shifting Optical Module on CUDA GPUs”. https://butler.physik.uni-mainz.de/icecube/thesis/master_Florian_Thomas.pdf. MA thesis. Johannes Gutenberg-Universität Mainz, Oct. 2019 (cit. on pp. 34, 44, 46, 47, 68, 70, 83).

[78] Ronja Schnur. “Optimierung des adiabatischen Lichtleiters für das Wavelength-shifting Optical Module”. https://butler.physik.uni-mainz.de/icecube/thesis/bachelor_Ronja_Schnur.pdf. Bachelor’s thesis. Johannes Gutenberg-Universität Mainz, Feb. 2020 (cit. on pp. 34, 45).

[79] *9390B Series*. https://et-enterprises.com/images/data_sheets/9390B.pdf. ET Enterprises. 2014 (cit. on pp. 34, 60, 61, 68, 126, 142, 183).

[80] *Photomultiplier Tubes R877, R877-01*. https://www.hamamatsu.com/content/dam/hamamatsu-photonics/sites/documents/99_SALES_LIBRARY/etd/R877_TPMH1112E.pdf. Hamamatsu Photonics. 2014 (cit. on p. 35).

[81] *HLQ 210*. https://www.heraeus-conamic.com/media/Media/Documents/Products_and_Solutions/LAMP/EN/HLQ210_Datasheet_EN.pdf. Heraeus Conamic. 2021 (cit. on pp. 35, 37, 184).

[82] *Galden HT PFPE*. https://www.behlke.com/pdf/datasheets/galden_ht135.pdf. Solvay. 2014 (cit. on pp. 36, 72).

[83] John Rack-Helleis et al. “The Wavelength-shifting Optical Module (WOM) for the IceCube Upgrade”. In: *Proceedings of 37th International Cosmic Ray Conference — PoS(ICRC2021)*. Vol. 395. 2021, p. 1038. DOI: 10.22323/1.395.1038 (cit. on p. 37).

[84] IceCube Collaboration. *Mini-Mainboard - Design and Status Notes*. IceCube internal document. 2024 (cit. on p. 38).

[85] *STM32H742xI/G STM32H743xI/G*. https://www.st.com/resource/en/datasheet/stm32h743vi.pdf. STMicroelectronics. 2023 (cit. on p. 38).

[86] IceCube Collaboration. *Ice Comms Module (ICM) - Design and Status Notes*. IceCube internal document. 2024 (cit. on p. 38).

[87] *Spartan-7 FPGAs Data Sheet*. https://docs.rs-online.com/2179/0900766b815f303c.pdf. Xilinx. 2017 (cit. on p. 38).

[88] IceCube Collaboration. *LOM Fanout Board - Design and Status Notes*. IceCube internal document. 2024 (cit. on p. 38).

[89] IceCube Collaboration. *LOM wuBase (HV + Digitization) - Design and Status Notes*. IceCube internal document. 2024 (cit. on p. 38).

[90] Rasha Abbasi et al. "Electronics Design of the IceCube-Gen2 Optical Module Prototype". In: *Proceedings of 38th International Cosmic Ray Conference — PoS(ICRC2023)*. Vol. 444. 2023, p. 1039. DOI: 10.22323/1.444.1039 (cit. on p. 38).

[91] *SMHV Series - High-Precision Regulated HV DC to DC Converter*. https://www.hvmtech.com/_files/ugd/714c33_6182e99581dd42e1abc45ee4764f5d87.pdf. HMV Technology. 2017 (cit. on p. 38).

[92] *Adafruit MPRLS Ported Pressure Sensor Breakout*. https://cdn-learn.adafruit.com/downloads/pdf/adafruit-mprls-ported-pressure-sensor-breakout.pdf. Adafruit Industries (cit. on pp. 39, 78, 193).

[94] IceCube Collaboration. *XDOM Flasher - Design and Status Notes*. IceCube internal document. 2024 (cit. on p. 39).

[95] IceCube Collaboration. *Mini-Fieldhub - Design and Status Notes*. IceCube internal document. 2025 (cit. on p. 40).

[100] *FlexFoam-iT! Series*. https://www.smooth-on.com/tb/files/FLEXFOAM-IT_SERIES.pdf. Smooth-on (cit. on p. 41).

[101] *Mold Star 15, 16 and 30*. https://www.smooth-on.com/tb/files/MOLD_STAR_15_16_30_TB.pdf. Smooth-on (cit. on pp. 41, 184).

[102] *ShinEtsu X-32-3643-A Safety Data Sheet*. https://drive.google.com/file/d/1fgTHf2lRa8pSf-TYr-lQ7sum3C3zt2xZ/view?usp=sharing. Shin-Etsu Chemical Co., Ltd. 2020 (cit. on p. 42).

[103] *Teroson RB VII*. https://profiguide.teroson-bautechnik.com/media/teroson-rb-vii-tds-en.PDF. Teroson. 2014 (cit. on p. 43).

[104] *3M Scotchrap Tapes 50, 51 and Pipe Primer, 3M Scotchfil Electrical Insulation Putty*. https://multimedia.3m.com/mws/media/1275510O/scotchrap-50-51-and-pipe-primer-may-2013.pdf?&fn=Scotchrap%2050,%2051%20and%20Pipe%20Primer,%20May%202013.pdf. 3M. 2013 (cit. on p. 43).

[105] IceCube Collaboration. *WOM Harness*. IceCube internal document. 2024 (cit. on p. 44).

[107] Moritz Robin Strauß. "Detaillierte Modellierung von Absorption im Wellenlängenschiebenden Optischen Modul (WOM)". https://butler.physik.uni-mainz.de/icecube/thesis/bachelor_Moritz_Strauss.pdf. Bachelor's thesis. Johannes Gutenberg-Universität Mainz, Sept. 2023 (cit. on pp. 48, 107).

[108] Sebastian Böser. Personal Communication. University of Mainz, Germany, 2021–2025 (cit. on pp. 48, 49, 183, 184).

[109] *SILICONE GREASE EJ-550, EJ-552*. https://eljentechnology.com/products/accessories/ej-550-ej-552. Eljen Technology. 2021 (cit. on p. 51).

[110] *Xenon arc light sources 75-150 W*. https://qd-europe.com/fileadmin/Mediapool/products/lightsources/pdf/Xenon_arc_light_sources_75_150_W.pdf. Quantum Design. 2025 (cit. on p. 52).

[111] *Monochromator MSH-300 with variable slit*. https://qd-europe.com/fileadmin/Mediapool/products/Bentham/_pdf/MSH_300_with_variable_slit.pdf. Quantum Design. 2025 (cit. on p. 52).

[112] *Si photodiodes - S2281 series*. https://www.hamamatsu.com/content/dam/hamamatsu-photonics/sites/documents/99_SALES_LIBRARY/ssd/s2281_series_kspd1044e.pdf. Hamamatsu Photonics. 2025 (cit. on p. 52).

[113] *Liquid Light Guide, Ø5 mm Core*. https://www.thorlabs.com/drawings/df95f2388c67b511-9FBA7E28-CAFE-BBE2-FCF3EC9E039252D3/LLG5-4T-SpecSheet.pdf. Thorlabs. 2018 (cit. on p. 52).

[114] *MFLI Lock-in Amplifier*. https://www.zhinst.com/sites/default/files/documents/2021-12/zi_mfli_leaflet_v2.pdf. Zurich Instruments. 2018 (cit. on p. 52).

[115] Philipp Kern. "Characterisation and Development of the WOM for IceCube". MA thesis. Johannes Gutenberg-Universität Mainz, Oct. 2024 (cit. on pp. 54, 55, 62, 78, 98, 100, 138–144, 150, 151, 166).

[116] IceCube Collaboration. Internal Documentation (cit. on pp. 56, 177, 183).

[117] Jakob Beise et al. "Prospects for the Detection of the Standing Accretion Shock Instability in IceCube-Gen2". In: *Proceedings of XVIII International Conference on Topics in Astroparticle and Underground Physics — PoS(TAUP2023)*. Vol. 441. 2024, p. 159. DOI: 10.22323/1.441.0159 (cit. on pp. 56, 57, 134).

[118] Nick Jannis Schmeißer. Personal Communication. University of Wuppertal, Germany, 2021–2025 (cit. on pp. 59, 61, 176).

[120] *PILAS DX - Picosecond pulsed diode lasers*. https://contentnktphotonics.s3.eu-central-1.amazonaws.com/PILAS/ALS%20Pilas%20Datasheet.pdf. NKT Photonics. 2023 (cit. on p. 61).

[121] *ADQ14 Datasheet*. https://www.spdevices.com/en-us/Products_/Documents/ADQ14/14-1290-H%20ADQ14%20datasheet.pdf. SP Devices. 2021 (cit. on pp. 61, 84).

[122] *CTS-Climatic Test-chambers*. https://www.cts-umweltsimulation.de/images/produkte/ps-baureihe-c/download/CTS_Climatic_Test_Chambers_eng.pdf. CTS (cit. on p. 63).

[123] *PicoScope 6000 Series*. https://www.picotech.com/download/manuals/PicoScope6000ABSeriesDataSheet.pdf. pico Technology. 2014 (cit. on p. 63).

[124] Anna Pollmann. Personal Communication. Chiba University, Japan, 2021–2024 (cit. on pp. 63, 112, 113).

[125] IceCube Collaboration. *South Pole ice temperature data*. 2020. DOI: 10.21234/spice-temperature (cit. on p. 66).

[126] *Norland Optical Adhesive 61*. https://www.norlandprod.com/literature/61tds.pdf. Norland Products Incorporated (cit. on p. 74).

[127] *Adhesives for Optical Waveguides*. https://www.ofcconference.org/library/exhibits/OFC/2021/pdfs/909510-pb-productBrochure4.pdf. NTT AT. 2019 (cit. on p. 74).

[128] *Ardunio Nano*. https://docs.arduino.cc/resources/datasheets/A000005-datasheet.pdf. Arduino. 2025 (cit. on p. 78).

[129] M. Rongen and M. Schaufel. "Design and evaluation of a versatile picosecond light pulser". In: *Journal of Instrumentation* 13.06 (June 2018), P06002. DOI: 10.1088/1748-0221/13/06/P06002 (cit. on pp. 84, 152).

[131] Kyra Mossel. "Vertieftes Verständnis der Zeitantwort des Wellenlängenschiebenden Optischen Moduls (WOM)". https://butler.physik.uni-mainz.de/icecube/thesis/bachelor_MosselKyra.pdf. Bachelor's thesis. Johannes Gutenberg-Universität Mainz, Jan. 2022 (cit. on pp. 84, 92, 93, 96).

[132] Lea Schlickmann. "Zeitantwort des Wellenlängenschiebenden Optischen Moduls (WOM)". https://butler.physik.uni-mainz.de/icecube/thesis/bachelor_SchlickmannLea.pdf. Bachelor's thesis. Johannes Gutenberg-Universität Mainz, July 2021 (cit. on pp. 88, 91, 92, 98).

[133] Samyak Jain. Personal Communication. University of Wisconsin, Madison, USA, 2023 (cit. on pp. 103, 125).

[134] Sarah Mechbal, Nora Feigl, et al. "Characterization and testing of the IceCube Upgrade mDOM". In: *Proceedings of 38th International Cosmic Ray Conference — PoS(ICRC2023)*. Vol. 444. 2023, p. 1183. DOI: 10.22323/1.444.1183 (cit. on pp. 106, 134).

[135] Anna Steuer. Internal Presentation. University of Mainz, Germany, 2021 (cit. on p. 111).

[136] Xue-Feng Ding et al. "Measurement of the fluorescence quantum yield of bis-MSB*". In: *Chinese Physics C* 39.12 (Dec. 2015), p. 126001. DOI: 10.1088/1674-1137/39/12/126001 (cit. on p. 116).

[137] Chris Wendt. Personal Communication. University of Wisconsin, Madison, USA, 2024–2025 (cit. on pp. 153, 159, 218).

[138] Martin Rongen. Personal Communication. University of Erlangen-Nuremberg, Germany, 2024 (cit. on pp. 159, 160, 214).

[139] Martin Antonio Unland Elorrieta. "Studies on dark rates induced by radioactive decays of the multi-PMT digital optical module for future IceCube extensions". MA thesis. Westfälische Wilhelms-Universität Münster, Dec. 2017 (cit. on p. 174).

[141] *WOM Test Report*. https://drive.google.com/file/d/1VVTnQKNkHBLNWlVrn7Tqty2iPOc9_D_3/view?usp=sharing. AKUVIB - Engineering and Testing GmbH. 2024 (cit. on p. 182).

[143] S. Timoshenko and J. N. Goodier. *Theory of Elasticity*. 3rd Edition. London, United Kingdom: McGrawHill Book Company, 1970 (cit. on p. 184).

[144] David Labonte, Anne-Kristin Lenz, and Michelle Oyen. "On the relationship between indentation hardness and modulus, and the damage resistance of biological materials". In: *Acta Biomaterialia* 57 (May 2017). DOI: 10.1016/j.actbio.2017.05.034 (cit. on p. 184).

[145] John R. Rumble. *CRC Handbook of Chemistry and Physics*. 103rd Edition. Cleveland, Ohio, USA: CRC Press, 2022 (cit. on p. 184).

[147] Igor Krivopish. Personal Communication. Nautilus Marine Service GmbH, 2024 (cit. on pp. 186, 193).

[148] Lea Schlickmann. Personal Communication. University of Mainz, Germany, 2024–2025 (cit. on pp. 191, 194, 199).

[149] Enrico Ellinger. Personal Communication. University of Wuppertal, Germany, 2024 (cit. on pp. 191, 195).

[150] C. Ahdida, Atakan Akmete, Rj Albanese, et al. "The SHiP experiment at the proposed CERN SPS Beam Dump Facility". In: *The European Physical Journal C* 82 (May 2022). DOI: 10.1140/epjc/s10052-022-10346-5 (cit. on p. 199).

[151] Manuel Böhlers, Sebastian Böser, Magdalena Eisenhuth, et al. "Combining hybrid and opaque scintillator techniques in the search for double beta plus decays: A concept study for the NuDoubt^{++} experiment". In: *The European Physical Journal C* 85 (Jan. 2025). DOI: 10.1140/epjc/s10052-025-13847-1 (cit. on p. 199).

Webpages

[@21] Wikipedia, the free encyclopedia. *Behavior of a ray incident from a medium of higher refractive index n1 to a medium of lower refractive index n2, at increasing angles of incidence*. URL: https://en.wikipedia.org/wiki/Total_internal_reflection#/media/File:ReflexionTotal_en.svg (visited on Dec. 2, 2024) (cit. on p. 8).

[@22] Wikipedia, the free encyclopedia. *Power coefficients: air to glass*. URL: https://en.wikipedia.org/wiki/Fresnel_equations#/media/File:Fresnel_power_air-to-glass.svg (visited on Dec. 2, 2024) (cit. on p. 9).

[@23] Wikipedia, the free encyclopedia. *Power coefficients: glass to air (Total internal reflection starts from 42° making reflection coefficient 1)*. URL: https://en.wikipedia.org/wiki/Fresnel_equations#/media/File:Fresnel_power_glass-to-air.svg (visited on Dec. 2, 2024) (cit. on p. 9).

[@25] Wikipedia, the free encyclopedia. *The ray-tracing algorithm builds an image by extending rays into a scene and bouncing them off surfaces and towards sources of light to approximate the color value of pixels.* URL: https://en.wikipedia.org/wiki/Ray_tracing_(graphics)#/media/File:Ray_trace_diagram.svg (visited on Dec. 3, 2024) (cit. on p. 11).

[@28] Wikipedia, the free encyclopedia. *Diagram of the Stokes shift between absorption and emission light spectra*. URL: https://en.wikipedia.org/wiki/Stokes_shift#/media/File:Stokes_shift_diagram.svg (visited on Dec. 5, 2024) (cit. on p. 13).

[@29] *Deep Underground Neutrino Experiment*. URL: https://www.dunescience.org/ (visited on Dec. 5, 2024) (cit. on p. 12).

[@30] *DEAP-3600 - Dark Matter Experiment using Argon Pulseshape discimination*. URL: https://deap3600.ca/ (visited on Dec. 5, 2024) (cit. on p. 12).

[@32] *Hyper-Kamikande*. URL: https://www-sk.icrr.u-tokyo.ac.jp/en/hk/ (visited on Dec. 5, 2024) (cit. on pp. 12, 199).

[@36] Matsusada. *Construction of a photomultiplier tube*. URL: https://www.matsusada.com/application/ps/photomultiplier_tubes/ (visited on Dec. 6, 2024) (cit. on p. 14).

[@42] *IceCube - IceCube Neutrino Observatory*. URL: https://icecube.wisc.edu/ (visited on Dec. 9, 2024) (cit. on p. 21).

[@63] *IceCube-Gen2*. URL: https://icecube-gen2.wisc.edu/ (visited on Dec. 15, 2024) (cit. on pp. 26, 27).

[@93] ET-Enterprises. *Voltage Dividers*. URL: https://et-enterprises.com/products/voltage-dividers (visited on Dec. 26, 2024) (cit. on p. 39).

[@96] IceCube Collaboration. *IceCube Upgrade FieldHub data server - Github*. URL: https://github.com/WIPACrepo/fh_server (visited on Dec. 27, 2024) (cit. on p. 40).

[@97] IceCube Collaboration. *IceCube STM32 Code Repository - Github*. URL: https://github.com/WIPACrepo/STM32Workspace (visited on Dec. 27, 2024) (cit. on p. 40).

[@98] IceCube Collaboration. *STM32 code for WaveformMicroBase - Github*. URL: https://github.com/WIPACrepo/wuBase-stm32 (visited on Dec. 27, 2024) (cit. on p. 40).

[@99] IceCube Collaboration. *xDOMApp API interface definition framework - Github*. URL: https://github.com/WIPACrepo/xdomapp-api (visited on Dec. 27, 2024) (cit. on p. 41).

[@106] Ansys. *Ansys Zemax OpticStudio Comprehensive Optical Design Software*. URL: https://www.ansys.com/products/optics/ansys-zemax-opticstudio (visited on Dec. 31, 2024) (cit. on p. 45).

[@119] ET Enterprises. *Magnetic Shields*. URL: https://et-enterprises.com/products/magnetic-shields#contoured (visited on Jan. 19, 2025) (cit. on p. 61).

[@130] Hamamatsu Photonics. *Photomultiplier tube R6231*. URL: https://www.hamamatsu.com/us/en/product/optical-sensors/pmt/pmt_tube-alone/head-on-type/R6231.html (visited on Feb. 8, 2025) (cit. on p. 84).

[@140] *AKUVIB - Akkreditiertes Prüflabor nach DIN EN ISO/IEC 17025*. URL: https://www.akuvib.de/ (visited on May 5, 2025) (cit. on p. 182).

[@142] *Autodek | 3D Design, Engineering & Construction Software*. URL: https://www.autodesk.com/ (visited on May 6, 2025) (cit. on p. 183).

[@146] *Nautilus Marine Service*. URL: https://nautilus-gmbh.com/ (visited on May 6, 2025) (cit. on p. 185).

List of Figures

List of Tables